# CONFOCAL MICROSCOPY APPLIED TO THE STUDY OF SINGLE ENTITY FLUORESCENCE AND LIGHT SCATTERING

---

Dissertation

zur Erlangung des akademischen Grades des Dr. rer. nat.
im Fachbereich Chemie der Johannes Gutenberg-Universität Mainz

vorgelegt von

**Fernando D. Stefani**

**geboren in Buenos Aires, Argentinien**

**Mainz, Juli 2004**

| | |
|---|---|
| Dekan: | Prof. Dr. R. Zentel |
| 1. Gutachter: | Prof. Dr. W. Knoll |
| 2. Gutachter: | Prof. Dr. W. Baumann |
| 3. Gutachter: | Prof. Dr. B. Hecht - Universität Basel |

Mündliche Prüfung am 12. November 2004

Diese Arbeit wurde in der Zeit von September 2001 bis Juni 2004 unter der Betreuung von Prof. Dr. W. Knoll und Dr. M. Kreiter am Max-Planck-Institut für Polymerforschung in Mainz angefertigt.

Finanzielle Förderung: Bundesministerium für Bildung und Forschung - ,,Nano-Nachwuchsgruppe" Nr. 03N8702.

The work for this dissertation was carried out between September 2001 and June 2004 under the direction of Prof. Wolfgang Knoll and Dr. Maximilian Kreiter at the Max-Planck-Institute for Polymer Research in Mainz (Germany).

Financial support: Bundesministerium für Bildung und Froschung - ,,Nano-Nachwuchsgruppe" No. 03N8702.

# Contents


**1 Introduction** **1**

**2 The fluorescence and light scattering confocal microscope** **5**
2.1 The confocal principle . . . . . 5
2.2 Description of the home built confocal microscope . . . . . 8
2.2.1 Light sources and illumination . . . . . 8
2.2.2 Scanning . . . . . 12
2.2.3 Detection . . . . . 16
2.2.4 Time Correlated Single Photon Counting . . . . . 19
2.2.5 Computer control . . . . . 21
2.3 Alignment . . . . . 22
2.3.1 Light coupling into the single mode fiber . . . . . 22
2.3.2 Collimation of the illumination beam . . . . . 23
2.3.3 Alignment of the dichroic mirror and the microscope objective 25
2.3.4 Alignments in the detection . . . . . 26
2.4 Operation . . . . . 29
2.4.1 Sample requirements and mounting . . . . . 30
2.4.2 Imaging . . . . . 30
2.4.3 Time correlated measurements . . . . . 34
2.4.4 Spectra measurements . . . . . 37

**3 Single molecule fluorescence through a layered system** **39**
3.1 Description of the problem. . . . . 39
3.2 The emission . . . . . 41
3.2.1 Radiative decay rate to different regions of space . . . . . 42
3.2.2 Total electromagnetic decay rate . . . . . 44
3.2.3 Non-radiative electromagnetic de-excitation rate . . . . . 46
3.2.4 Detectable fraction of the de-excitation rate . . . . . 46
3.3 The excitation . . . . . 47
3.3.1 Electric field distribution near a geometric focus in a layered system . . . . . 47
3.4 Single molecule fluorescence signal . . . . . 54
3.5 Conclusions . . . . . 55

**4 Single molecule fluorescence through a thin gold film 57**
4.1 Introduction . . . 57
4.2 Experimental . . . 59
4.2.1 Sample preparation . . . 59
4.2.2 Measurement . . . 60
4.3 Single molecule fluorescence images through a thin gold film . . . 62
4.3.1 Full beam images . . . 62
4.3.2 Different illumination modes . . . 64
4.3.3 Influence of the separation distance to the gold film . . . 66
4.4 Modelling the experimental scheme . . . 68
4.4.1 Fundamental concepts . . . 68
4.4.2 Detectable fraction of the emitted fluorescence . . . 71
4.4.3 Excitation field at the chromophores position . . . 75
4.4.4 Theoretical fluorescence signal . . . 78
4.5 Conclusions . . . 81

**5 Single molecule fluorescence dynamics 85**
5.1 Electronic transition rates . . . 85
5.2 Kinetic traces analysis methods . . . 88
5.2.1 Autocorrelation analysis . . . 88
5.2.2 Trace-histogram analysis . . . 90
5.2.3 Comparison . . . 95
5.3 Experimental . . . 97
5.3.1 Sample preparation . . . 99
5.3.2 Measurement . . . 100
5.4 Influence of a nearby thin Au film on the electronic transition rates . 101
5.4.1 Influence on $\Gamma_{21}$ . . . 102
5.4.2 Influence on $k_{off}$ . . . 103
5.4.3 Influence on $k_{on}$ . . . 105
5.5 Conclusions . . . 106

**6 Photoluminescence blinking of $Zn_{0.42}Cd_{0.58}Se$ nano-crystals 109**
6.1 Brief Introduction and current status . . . 110
6.2 Experimental . . . 112
6.2.1 Sample preparation . . . 112
6.2.2 Measurement . . . 113
6.3 QD kinetic traces . . . 114
6.3.1 General characteristics . . . 114
6.3.2 Effect of the excitation intensity . . . 115
6.4 Modelling the QDs blinking . . . 123
6.4.1 Blinking model . . . 124
6.4.2 Monte-Carlo procedure . . . 124

6.4.3 Simulated blinking . . . . . 127
6.5 Conclusions . . . . . 132

**7 Light scattering from single metallic nano-structures 135**
7.1 Introduction . . . . . 135
7.2 Light scattering of individual colloidal gold nanoparticles . . . . . 136
7.2.1 Experimental . . . . . 136
7.2.2 Images of colloidal gold nanoparticles . . . . . 137
7.2.3 Spectra of colloidal gold nanoparticles . . . . . 139
7.3 Light scattering of individual C-shaped gold nanoparticles . . . . . 140
7.3.1 Experimental . . . . . 140
7.3.2 Images and spectra of C-shaped gold nanoparticles . . . . . 142
7.4 Conclusions . . . . . 143

**8 Summary 145**

**A Set-up control and data acquisition software 149**
A.1 AD-Basic routines . . . . . 149
A.2 Igor routines . . . . . 163
A.3 C++ routines . . . . . 180

**List of tables 187**

**List of figures 191**

**Abbreviations 193**

**Bibliography 195**

**Acknowledgements 205**

**Curriculum Vitae 207**

# Chapter 1

# Introduction

In 1974, Fleischmann and co-workers [1] wanted to perform experiments on pyridine by combining electrochemistry and Raman spectroscopy. In order to increase the Raman signal, they deposited the pyridine onto a roughened silver electrode. The idea was to increase the surface area of the electrode and therefore the amount of adsorbate on the sample. It worked; the Raman signal was indeed greatly increased. Three years later, Jeanmaire and van Duyne [2], as well as Albrecht and Creighton [3], recognized independently that the large intensities observed could not be accounted for simply by the increase in the number of scatterers present. They proposed that an enhancement of the scattered intensity occurred in the adsorbed state. Already at that time a surface plasmon enhancement mechanism of the scattered intensity was proposed [3, 4]. Since then, this effect was called surface enhanced Raman scattering (SERS) and captured the attention of chemists, physicists and engineers from around the world. It is not hard to see the motivation for such interest. The effect was large, completely unexpected, difficult to understand and of enormous practical utility if it could be understood and exploited.

The investigation of the SERS still continues and the understanding of the phenomenon has increased considerably. Nowadays, it is accepted that the SERS effect is caused by greatly enhanced electromagnetic fields generated by surface plasmon resonances (SPR) in certain *hot spots* of the rough substrate. At this point, it is important to note that such strong and localized electromagnetic fields do not only find applications in the SERS. For example, they can also be employed in optical tweezers and to modify radiative rates in a variety of processes such as molecular fluorescence. Recent advances in microscopy have made it possible to use single metallic particles as SERS substrates and to obtain the Raman spectra of single molecules adsorbed on them [5].

Almost simultaneously, the field that is today called nanotechnology developed, and thanks to that, it is possible to produce an enormous variety of structures in the sub-micrometer scale. In particular, metallic structures with nanometer size and different shapes can be manufactured and their surface plasmon resonances can

be tailored. These days, it is possible to think of a structure composed of metallic nanoparticles and a chromophore (or Raman scatterer) in a defined geometry in order to produce an ultra effective marker or to imagine a metallic nano-structure engineered to function as a nano-optical-tweezers. Even though such a nano-structure cannot be fabricated in a controlled manner yet, several research groups around the world are working on it, and it should not be long until this is achieved. The aim of this Ph.D. thesis is to settle the basis for the quantitative assessment of effects in individual such functional nano-structures.

The first step taken was the design and construction of a scanning confocal optical microscope (SCOM) that allows to measure, from the same diffraction-limited spot, time-resolved fluorescence and SERS with single molecule sensitivity and light scattering with highest resolution achievable with a far-field method (chapter 2). This instrument allows to investigate the surface plasmon resonances of individual metallic nanoparticles (chapter 7) and their influence on the Raman scattering and/or fluorescence processes.

Then, a model system was sought to realize the first systematic study. Surface plasmon resonances can be excited not only in metallic nanoparticles but also in planar surfaces. Such a simple geometry, although it provides a relatively small field enhancement, represents a very convenient platform for systematic studies because it is easy to fabricate, their geometric parameters can be controlled and a complete mathematical modelling is possible. The first studies were performed with fluorophores placed at a controlled separation distance from a gold film. The influence of the locally enhanced surface plasmon electromagnetic field on molecular fluorescence was investigated on a single molecule level.

First, a theoretical model was set-up to calculate the fluorescence signal of a single molecule in a plane layered system, including the electric field distribution in the focus of the SCOM and the emission rates of a chromophore (chapter 3). Second, the excitation and emission of single molecule fluorescence through a thin gold film was investigated experimentally and modelled (chapter 4). Third, the influence of the nearby gold film on the electronic transition rates responsible of the fluorescence process was studied (chapter 5).

If fluorescent markers are being considered, nanometer-size colloidal semiconducting crystallites, also known as quantum dots (QD) cannot be ignored. Since the middle 70s, the QDs have provoked a tremendous fundamental and technical interest. Owing to their size-dependent photoluminescence which is tunable across the complete visible spectrum, the QDs find application as light-emitting devices, lasers, and biological labels. However, the emission process in semiconducting QDs involves very complicated processes and the emitting state remains controversial. Recently, the advent of QD studies on a single dot level brought a new complication: the QDs present extremely complicated emission fluctuations that could not be explained until now. Even though surface enhancement effects were observed on QDs [6], the lack of knowledge about the blinking mechanism prevents an effective exploitation

of the effect. It is fundamental to understand the blinking of QDs before trying to improve their performance by other means such as locally enhanced fields. The photoluminescence blinking of QDs was experimentally investigated and modelled in order to gain some insight into the underlying physical processes (chapter 6).

The last experimental tool necessary for the investigation of field enhancements on a single nano-structure level is the capability of studying SPRs in individual metallic nano-particles. In order to fill this need, the home built SCOM was adapted for light scattering measurements and its performance was tested on spherical and C-shaped gold particles (chapter 7).

# Chapter 2

# The fluorescence and light scattering confocal microscope

A scanning confocal optical microscope (SCOM) was designed and constructed to perform local studies of fluorescence and light scattering, with diffraction-limited spatial resolution and single photon sensitivity. This instrument allows working with many different experimental schemes. The most distinctive characteristic is the possibility of measuring fluorescence and scattered light from the same focal spot.

The sections of this chapter are dedicated to detailed description of the microscope. The first section explains the confocal principle. The second section describes the different components and their functions. Finally, the last two sections explain how to properly align and operate the instrument.

## 2.1 The confocal principle

An ideal optical microscope would examine each point of the specimen and measure the amount of light scattered or absorbed by that point[1]. However, if many of such measurements were performed simultaneously, every point in the image plane would be clouded by aberrant rays of scattered light coming from other points of the sample. Marvin Minsky [7, 8] found in 1955 a simple and elegant solution for this problem: the confocal arrangement (see figure 2.1).

In the first place, it is possible to illuminate only one point of the specimen at a time by using a microscope objective to focus the light spread by an aperture pinhole (illumination pin-hole in figures 2.1.a and 2.1.b). As a consequence, the amount of light in the specimen is reduced by orders of magnitude, without reducing the focal brightness at all (fundamentally important to prevent photo-bleaching in single molecule fluorescence experiments). Still, due to multiple scattering, some extra rays

[1] In this context "point" means a diffraction limited spot.

coming from different points of the sample (dashed rays in figures 2.1.a and 2.1.b) could reach the detectors. However, it is possible to reject those rays using a second microscope objective to image on the same (confocal) point of the specimen, a second pinhole aperture (detection pinhole in figures2.1.a and 2.1.b) placed in front of the detector. Then, as shown in figure 2.1.a, an elegant, symmetric configuration is obtained consisting of a pinhole and an objective lens on each side of the specimen. The term confocal should be clear now, it is used to indicate that both illumination and collection pinholes (lenses) are focused on the same point of the object.

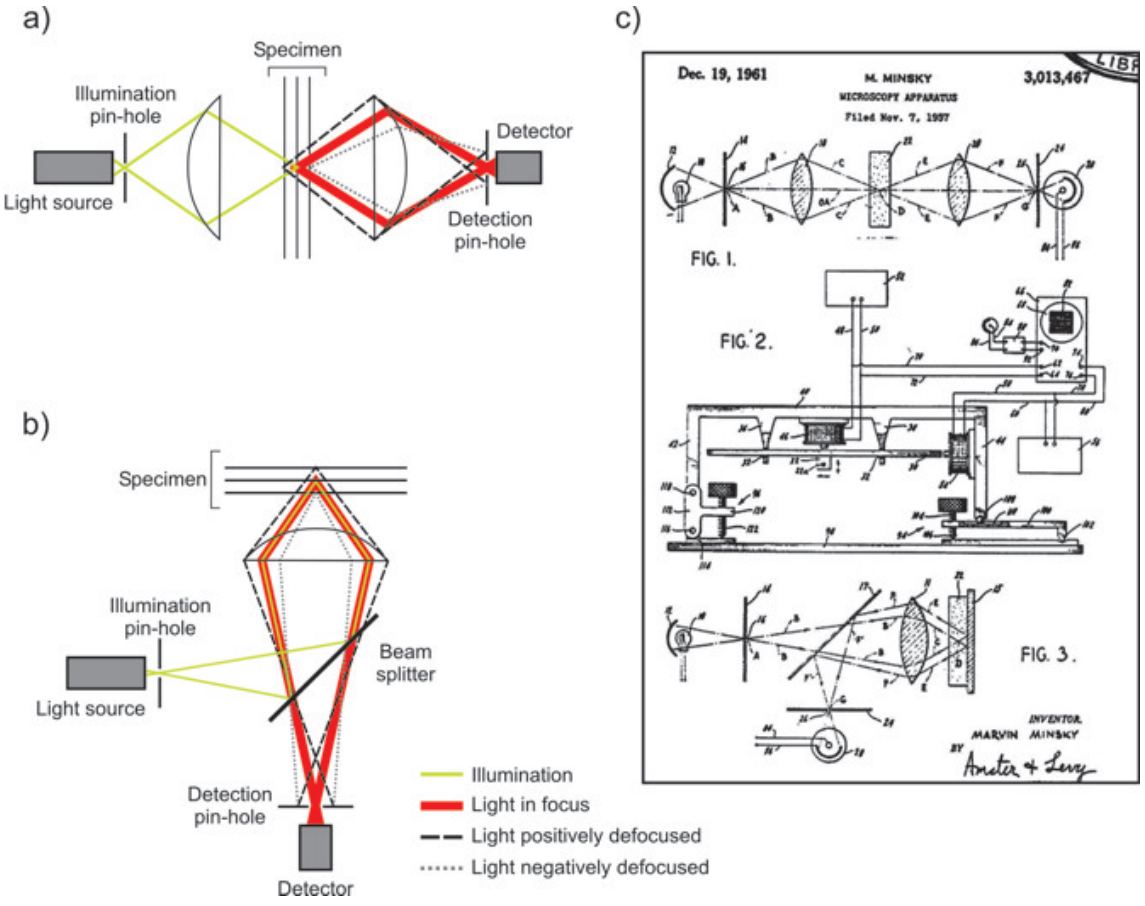


**Figure 2.1:** Confocal principle. c) Original sketches of the confocal principle from the patent by M. Minski (1957) [7]. a) and b) The original sketches are reproduced to better accompany the explanation in the text. FIG.2 in c) shows the original mechanical scanning stage by Minski.

The original drawing of the confocal microscope in the patent by M. Minski, from 1957, is shown in figure 2.1.c. The sketch named FIG.1 in figure 2.1.c shows the schematic of the configuration described in the previous paragraph (figure 2.1.a). In addition, Minsky also recognized the possibility of employing a reflected light scheme, as shown in the FIG.3 of figure 2.1.c, and reproduced in figure 2.1.b. In this case, only a single lens on one side of the specimen is used, and a half-silvered mirror separates the entering and exiting rays. This arrangement is equivalent to

the symmetric one in terms of resolution but much simpler in terms of alignment and operation. The price to pay for the simplicity is the fourfold brightness loss due to the beam splitter. However, in fluorescence measurements, the efficiencies of both configurations are similar because a dichroic filter can be used to spectrally separate the excitation and fluorescence light.

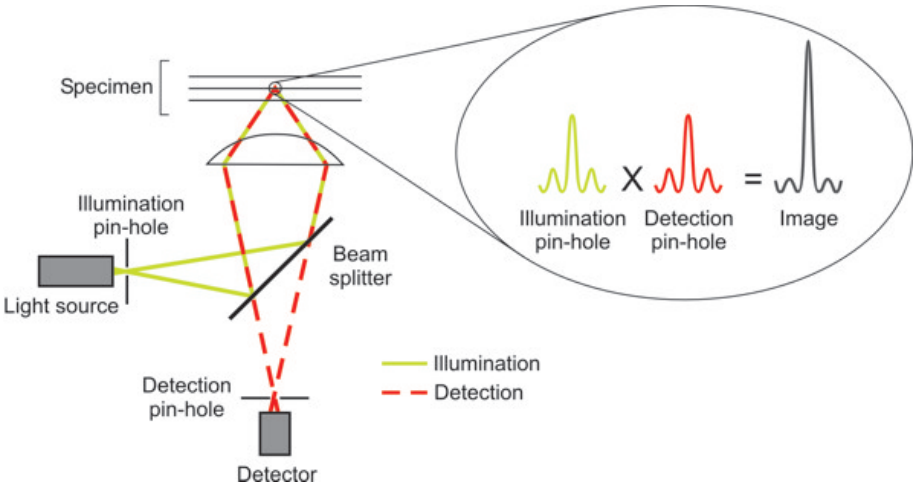


**Figure 2.2:** Confocal image formation. The diffraction patterns of both illumination and detection aperture pinholes are multiplied to form the image of a point of the specimen.

A confocal microscope behaves as a coherent optical system in which the diffraction patterns of both (illumination and detection) pinhole apertures are multiplied to form the image of a point of the specimen [9]. This gives rise to a sharpened central peak and weak outer rings with the consequent increase in resolution (see figure 2.2). Even though the improvement in resolution may at first sight seem to contravene the basic limits of optics, it can be explained by a principle described by Lukosz [10, 11], which states that resolution may be improved at the expense of field of view. In the case of a confocal microscope, the field of view is reduced by means of the back projected image of a point detector in conjunction with the focused point light source. Nevertheless, the field of view can be increased by scanning. There are basically two different ways of scanning which have been achieved by various methods in practical instruments. The alternatives are either to scan a focused light beam across a stationary sample, or to scan the sample mechanically across a stationary focused light spot. In the first case, scanning can be very fast and many images per second can be acquired. In the second case, scanning is much slower but as the optical path remains stationary, undistorted images of very high quality are produced.

## 2.2 Description of the home built confocal microscope

Figure 2.3 shows schematically the different components of the home-built SCOM set-up and helps as a guide for the detailed descriptions presented in the next sections of this chapter.

A number of light sources can be employed to obtain either monochromatic or white light illumination. In every case, the light provided by the source is coupled into a single-mode optical fiber to obtain a point-like light source equivalent to the illumination pin-hole described in the previous section. Light coming out of the fiber is collimated to form the illumination beam. With the help of a dichroic mirror or a beam splitter, the illumination beam is directed to a high numerical aperture microscope objective that focuses it onto the sample. Light coming from the sample is collected by the same objective and directed by a mirror to the single photon detectors and/or the spectrograph. In order to acquire an image or to study different regions, the sample can be mechanically scanned over the focused beam by means of a piezoelectric xyz stage. Furthermore, although not included in figure 2.3, the microscope is equipped with a second single mode fiber aligned in the confocal system that can be coupled to any of the light sources. This allows to perform simultaneous illumination with two wavelengths. In the following, for simplicity and because both fibers are equivalent, only one fiber is considered.

The set-up is very flexible. Different modes of illumination and detection can be implemented to perform a variety of studies, such as fluorescence, Raman[2] and light scattering measurements.

Following, all the components of the set-up and their functions are described in detail. Section 2.2.1 describes the illumination, section 2.2.2 the scanning and section 2.2.3 the detection. The time correlated single photon counting unit is described in section 2.2.4, and the computer control in section 2.2.5.

### 2.2.1 Light sources and illumination

A variety of light sources can be adapted to the microscope. Table 2.1 lists the principal characteristics of the light sources used in the experiments presented in this dissertation.

Light provided by any of these sources is focused with a suitable microscope objective and coupled into a single-mode optical fiber. For this, the fiber is mounted on a positioning xyz$\theta\phi$ stage (*New Focus Inc.*) with sub-micrometer precision. When using laser light, a $\lambda/2$ and a $\lambda/4$ plates (*OWIS GmbH*) are placed before the light is coupled into the fiber and adjusted to compensate its polarization effects. Two

[2]Although no Raman scattering measurements were performed in this work, the changes in set-up configuration required to allow such measurements are straight forward

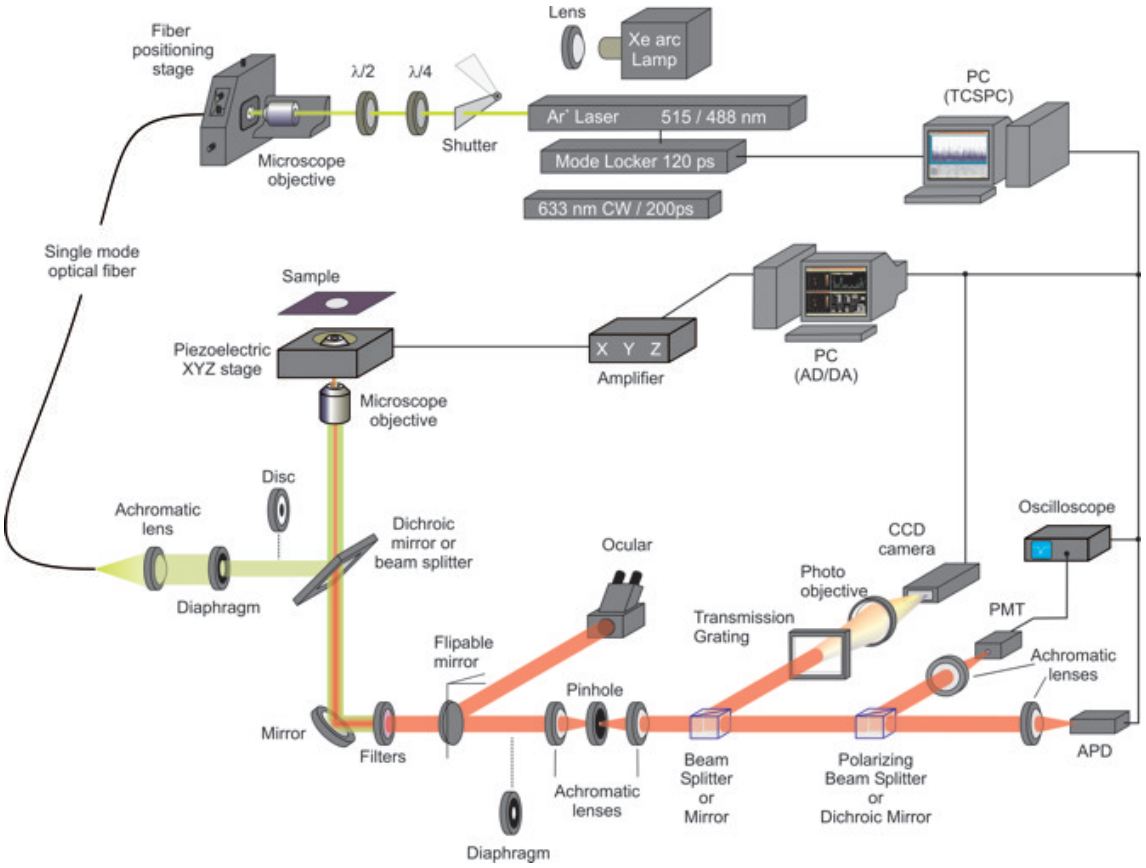


**Figure 2.3:** Schematic of the home-built confocal microscope

types of fibers were used: standard single-mode fibers for 635 or 515 nm (*Thor Labs Inc.*) or photonic crystal fibers (*Endless Single Mode, Blaze Photonics Ltd.*); the latter has the characteristic of acting as a single mode fiber in a wide range of wavelengths [12, 13]. The pure-Gaussian-mode (TEM00) light coming out of the fiber is collimated with a 150 mm focal length achromatic lens (*OWIS GmbH*) to form the illumination beam.

The illumination beam is aligned with the main optical axis of the microscope (for alignment details please refer to section 2.3), and its diameter is adjusted with a diaphragm. If the experiment requires annular illumination, a blocking disc can be introduced in the axis of the illumination beam. The diaphragm and the blocking disc should be placed as close as possible to the microscope objective in order to minimize the optical path to the focus and therefore the diffraction effects from the borders of the pin-hole or the disc. Furthermore, it is advisable to minimize the number of optical elements between the fiber tip and the microscope objective because small distortions of the illumination beam can produce important effects in the focus.

A 100×, 1.4 NA, oil immersed microscope objective (*Plan-Apo, Nikon GmbH*) is

| Light source | Wavelength [nm] | CW | Pulses | | Power [mW] | Manufacturer / model |
|---|---|---|---|---|---|---|
| | | | FWHM [ns] | Repetition [Mhz] | | |
| **Argon-ion laser** | 460<br>488<br>515 | Yes | 0.2 | 68 | 2500<br>(at 515 nm) | *Coherent inc., Innova 90C. Mode Locker: PulseDrive, APE GmbH* |
| **Helium-Neon laser** | 633 | Yes | – | – | 10 | *Uniphase inc.* |
| **Laser diode** | 633 | No | 0.2 - 0.8 | 50 | 0.1 - 2.5 | *Becker und Hickl GmbH, BHL -150* |
| **Xenon-arc lamp** | ~ 300 - 800 (with water IR filter) | Yes | – | – | 150000 | *OSRAM, XBO150* |

**Table 2.1:** Light sources. CW stands for continuous wave and FWHM for full width at half maximum.

used to focus the illumination beam onto the samples. The microscope objective is mounted on a xyz stage with micrometer precision.

### Fluorescence measurements

For fluorescence measurements laser light is used. Line pass filters (*Omega Optics Inc.*) are used to refine the illumination wavelength and a dichroic mirror (*AHF AG*) is used to direct the illumination beam to the microscope objective and to separate the excitation from the fluorescence light.

### Light scattering measurements

For light scattering measurements, annular illumination (see next subsection) is combined with a reduced detection beam. Instead of a dichroic mirror, a 50/50 beam splitter (*OWIS GmbH*) is used to direct the illumination beam to the microscope objective and to separate the excitation from the fluorescence light.

### Focusing angles and annular illumination

The TEM00 light provided by the single mode fiber is collimated with an achromatic lens with minimized spherical aberration. Therefore, the illumination beam

can be considered as being formed by plane waves. A microscope objective is an optical system that produces aplanatic images; i.e. axially stigmatic and obeying the sine condition [14] (null spherical aberration). Hence, the plane waves of the illumination beam are transformed by the objective in spherical waves with the center at the Gaussian focus. The maximum focusing angle ($\theta_{NA}$) is determined by the numerical aperture (NA) of the objective and the refractive index of the focusing medium ($n_{glass}$) according to:

$$\theta_{NA} = \arcsin\left(\frac{NA}{n_{glass}}\right) \tag{2.1}$$

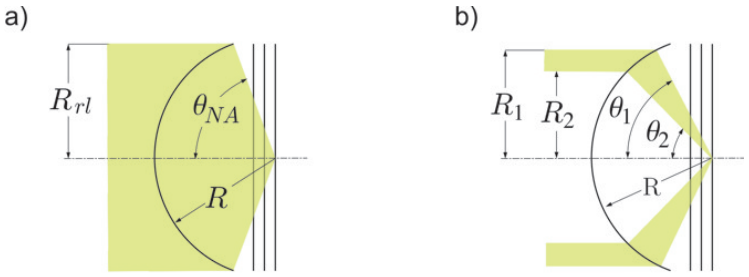


**Figure 2.4:** Focusing angles. Geometric representation of the focal sphere of the microscope objective and the focusing angles for the cases of: a) Complete illumination of the rear lens of the objective, b) Annular illumination.

The radius of the focal sphere $R$ (see figure 2.4.a) is determined by the radius of the rear lens of the objective $R_{rl}$, and the refractive index of the focusing medium ($n_{glass}$):

$$R = \frac{R_{rl}}{\sin\theta_{NA}} = \frac{R_{rl}\ n_{glass}}{NA} \tag{2.2}$$

Thus, if the rear lens of the objective is illuminated with an annular beam of outer radius $R_1$ and inner radius $R_2$, the maximum and minimum focusing angles, $\theta_1$ and $\theta_2$ respectively (see figure 2.4.b), are given by:

$$\theta_{1,2} = \arcsin\left(\frac{R_{1,2}}{R}\right) = \arcsin\left(\frac{R_{1,2}\ NA}{R_{rl}\ n_{glass}}\right) \tag{2.3}$$

The microscope objective used in all the experiments presented in this dissertation has a NA=1.4 and the refractive index of the glass slides (and the matching oil) is $n_{glass}$=1.503, which leads to a maximum focusing angle of 68.6°. The rear lens of the objective has a radius of 4.45 mm, therefore the radius of the effective focal sphere is 4.78 mm.

### 2.2.2 Scanning

To form an image with the home-built confocal system, the sample is stepwise mechanically scanned over the focus of the microscope objective, as the detected photons are counted at each step (pixel of the image). In comparison to optical scanning, mechanical scanning offers quality at the expense of speed [15][3]. Furthermore, having no moving optical elements makes it easier to adapt new elements in the optical path, and also makes the alignment more stable.

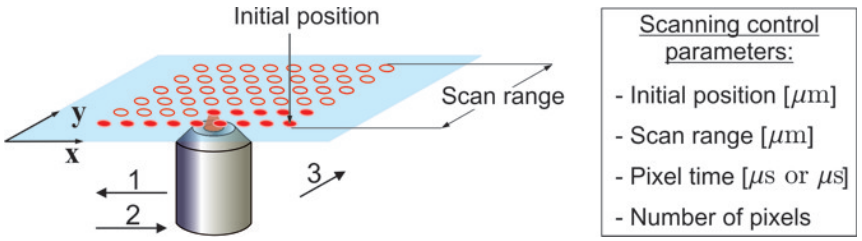


**Figure 2.5:** Scanning process. The parameters used to control the scanning are listed on the right.

Four parameters are used to control the scanning: the *initial position*, the *scanning range*, the *number of pixels* (the same for both dimensions), and the *pixel time* (counting time at each pixel). The scanning process, depicted in figure 2.5, is as follows. The sample is first moved to the *initial position*. Then, it is moved stepwise, forward and backward, along the (arbitrarily called) **x** direction (arrows 1 and 2 in figure 2.5), to a definite extent set by the *scanning range*, and with a definite number of steps set by the *number of pixels*. The sample remains a certain time, set by *pixel time*, at each position, while it is illuminated and fluorescence or scattered light photons are counted to give the intensity of one pixel of the image. Next, the sample is moved one step in the **y** direction in order to start the next **x**-line (arrow 3 in figure 2.5). The process is repeated until the scanning of a squared area of the sample is completed.

The scanning is accomplished by a computer controlled xyz-piezoelectric stage (*TRITOR 101 CAP, Jena Piezosystems GmbH*), operated with a capacitive closed loop feedback to correct the drift of the piezoelectric drivers. The piezoelectric stage can be driven (via a driving signal with a voltage from 0 to 10 V) through a range from 0 to 80 $\mu$m in each direction with a resolution of 0.5 nm. The driving signal for the stage is generated with a computer controlled 15-bit Analog to Digital / Digital to Analog (AD/DA) converter (*ADWin-light-16, Jäger GmbH*), and then amplified with 3 (one for each of the x, y, and z channels) independent low-noise amplifiers (*ENV40CAP, Jena Piezosystems GmbH*). The minimum scanning step is limited by the 15-bit resolution of the AD/DA converter to 2.4 nm. The AD/DA converter is

[3]For details about the different scanning methods, see the book by T. Wilson [16]

equipped with a local processor and local memory that enable to perform real-time measurements with a resolution of 25 ns, regardless of the speed of the controlling computer.

The data acquisition also is accomplished by the same AD/DA converter. For each pixel of an x-scanned line (forward and backward), the position, the counts, and the starting and final counting times, are stored in the local memory of the AD/DA converter. Then, the sample is moved in the y direction, and before starting the next x-line, all the information is transferred to the controlling computer. Like this, the counting times are measured with a resolution of 25 ns. The so collected data has the information corresponding to two images of the same region: one forward-scanned and the other backward-scanned. The individual images need to be extracted from the complete data.

### Forward and backward images from the collected data

While scanning at a reasonable speed[4]($\sim 0.5 - 2$ lines/s), the piezoelectric stage response in the **x** direction is delayed with respect to the driving signal. In the **y** direction, due to the time necessary for the data transfer, the piezoelectric stage has sufficient time to reach the set position.

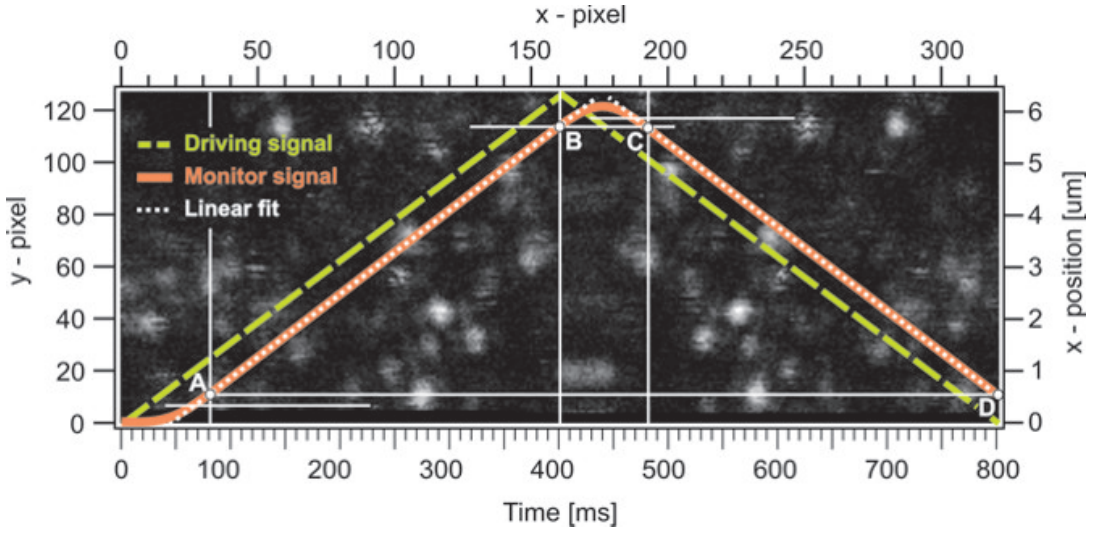


**Figure 2.6:** Scanning delay. Complete data collected to construct backward and forward images of $5 \times 5\,\mu m^2$, $128 \times 128$ pixels each. Extra pixels were scanned in the x-direction in order to discard the pixels corresponding to the delay near the direction inversion points.

[4]The scanning speed here mentioned is an actual speed in $\mu$m/s, then it relates the scanning range, the pixel-time and the number of pixels. A reasonable value for the scanning rate is for example 40 $\mu$m/s, corresponding to an image of $10 \times 10\,\mu m^2$, with $250 \times 250$ pixels and a collection time of 1 ms

Figure 2.6, shows a complete ($320 \times 128$ pixels) fluorescence image obtained with the confocal microscope. The image has a mirror symmetry because it is formed by scanning forward and backward the same region of the sample. The left and top axis show the pixels of the image. The left axis shows the x-position of the stage in $\mu$m, and the bottom axis the time necessary to scan forward and backward an x-line. The dashed-line curve is the driving signal (i.e. the desired x position) sent to the piezoelectric stage to perform a forward and backward scan along the **x** direction. The solid-line curve is the corresponding monitor signal provided by the capacitive closed loop, which is meant to report the actual position of the piezoelectric stage. The delay between the driving signal and the position of the stage reported by the capacitive loop can be clearly seen by comparing the driving to the monitor signals.

If the individual forward and backward images are constructed by taking into account the driving signal (i.e. dividing the image in figure 2.6 in two through the center), the images present two artifacts. First, due to the inertia of the piezoelectric drivers at the direction inversion points, the images appear blurred at one edge (the forward image on the left and the backward image on the rigt side). Second, due to the total delay, the forward and backward images are shifted with respect to each other.

Correction of these artifacts is extremely important because they directly affect the accuracy in the determination of the position of fluorescent dyes or any other measurable feature on the sample. For this reason, in order to construct consistent forward and backward images that permit proper position determination, the data acquisition software has to take into account the behavior of the piezoelectric stage. The software code can be found in appendix A.3. In principle, a complete correction could be accomplished by taking into account the capacitive monitor signal which is supposed to report the actual position of the stage at any time. Such correction consists of three steps. First, a number of lines are scanned with the set parameters, and the forward and backward linear regions of the monitor signal are determined, as well as the number of *invalid pixels* at the inversion points. Second, a new scan is performed with an additional number of pixels, equal to the *invalid pixels*, in the x direction, in order to be able to discard them and still keep the desired scan range. Third, the new linear regions of the monitor signal are found, and the forward and backward images are constructed only with those pixels. Like this, the forward images are constructed with the pixels between the points A and B in figure 2.6, and the backward images similarly with the pixels between the points C and D. The so made images, delimited in figure 2.6 by the vertical white lines, would not be blurred anymore at one edge. Yet, they are still shifted with respect to each other. The explanation for this extra shift is that the capacitive monitor signal is electronically delayed. The only way to account for this, is via an empirical calibration parameter. It is observed that faster scanning leads to a larger shift between forward and backward images. To quantify the shift, several images of the same region of a sample, produced at different scanning speeds, are necessary. Then, the

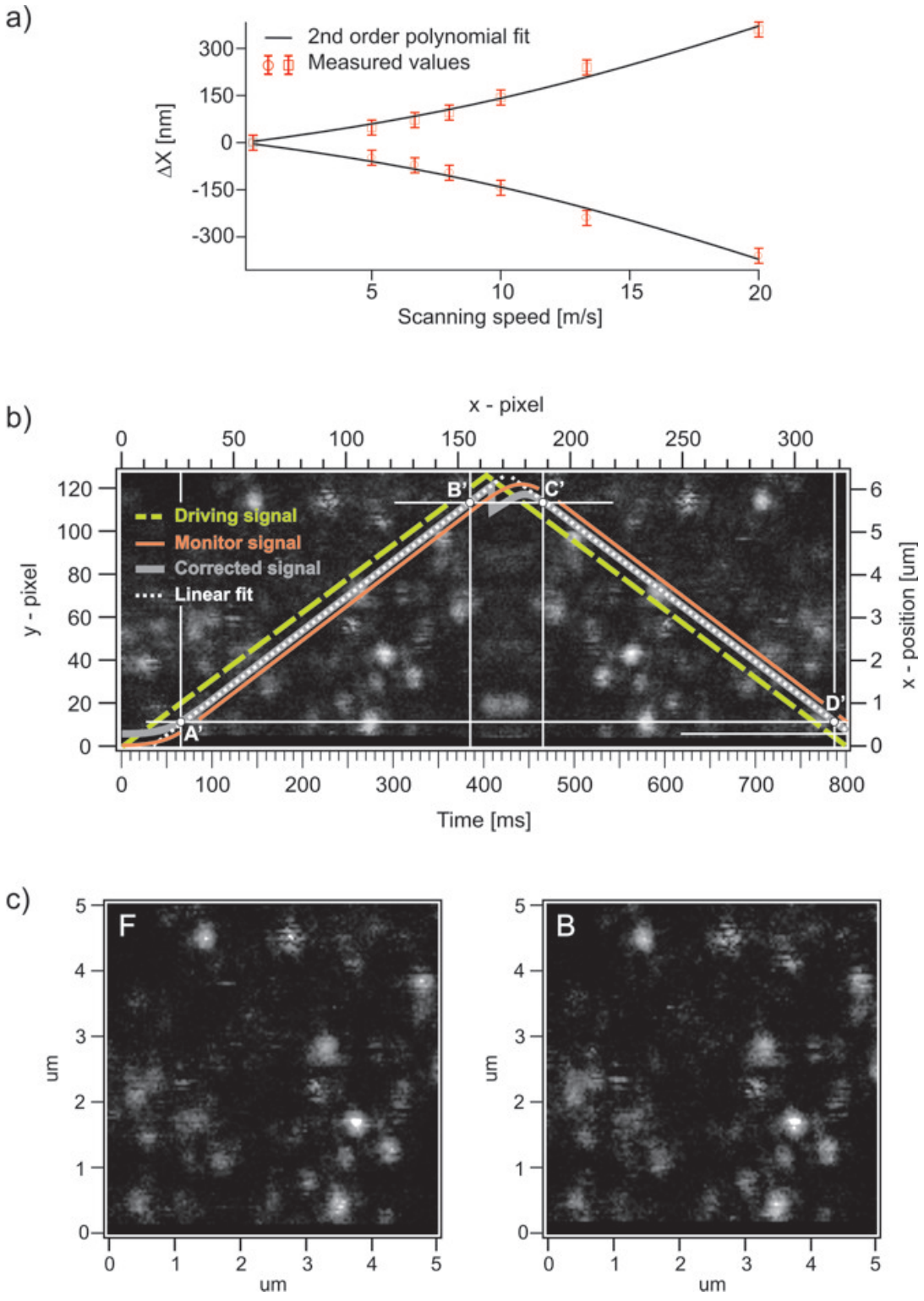


**Figure 2.7:** Scanning correction. a) Position shift of an arbitrary feature as a function of the scanning speed. b) the corrected monitor signal was added to figure 2.6. c) forward (F) and backward (B) images after the corrections.

position of one feature can be followed, on both forward and backward images, as a function of the scanning speed. In this manner, as shown in figure 2.7.a, the position shift vs. scanning speed can be fitted with a polynomial function and the empirical correction parameters are obtained. Using the correction parameters, the monitor signal can be corrected to give the actual position of the sample. In figure 2.7.b the same data of figure 2.6 is shown, but this time the empirically corrected monitor signal is shown. Then, the pixels corresponding to the forward and backward linear regions of the corrected monitor signal are found (following the algorithm detailed in the appendix A.3), and the forward and backward images are constructed. These images, delimited in figure 2.7.b by the vertical white lines and shown in more detail in figure 2.7.c, are consistent; the average shift between forward and backward images is smaller than one pixel size.

### 2.2.3 Detection

The detection channel can be adapted to different experimental designs. In the experiments presented in this dissertation, fluorescence and light scattering measurements were performed and the corresponding detection schemes are described below.

Common to all the detection schemes is that light collected from the sample is directed to the detection channel via a silvered mirror (*OWIS GmbH*; figure 2.3). Then, the light is focused with a 100 mm focal length achromatic lens (*OWIS GmbH*) into a 150 $\mu$m confocal (to the microscope objective) pinhole (*New Focus Inc.*), and collimated again with a second 100 mm focal length achromatic lens (*OWIS GmbH*). For imaging, this collimated beam is directed and focused with another 100 mm focal length achromatic lens (*OWIS GmbH*) to one of the single photon counting detectors. For spectrally resolved measurements, the detected collimated beam is directed to the transmission grating spectrograph. Further information about the single photon detectors and the transmission grating spectrograph is given below.

In addition, the microscope is equipped with an ocular (*Axiomat Plan W* $10\times25$*, Carl Zeiss Germany*) that can be used for focusing (see section 2.3.4) and visual inspection of the samples.

Other optical elements such as polarizing beam splitters, or dichroic mirrors can be installed in the detection channel according to the requirements of a particular experiment.

The photon counting for imaging is accomplished by a digital counter of the same AD/DA converter that controls the scanning. This counter only requires TTL (Transistor-Transistor Logic) input pulses. Therefore, any detector can be adapted to the set-up as long as its output signal is (or is transformed to) a TTL pulse.

### Fluorescence measurements

For fluorescence measurements, in order to remove residual excitation light not filtered by the dichroic mirror, suitable long-pass (*Omega Optics Inc.*) and notch (*Notch Plus, Kaiser Optical Systems Inc.*) filters are placed in the detection channel.

### Light scattering measurements

For light scattering measurements, no filters are used. Instead, annular illumination is employed and the outer part of the detected beam (which under ring illumination conditions contains mainly reflected light) is blocked by a diaphragm so that only scattered light can reach the detectors (see figure 2.8).

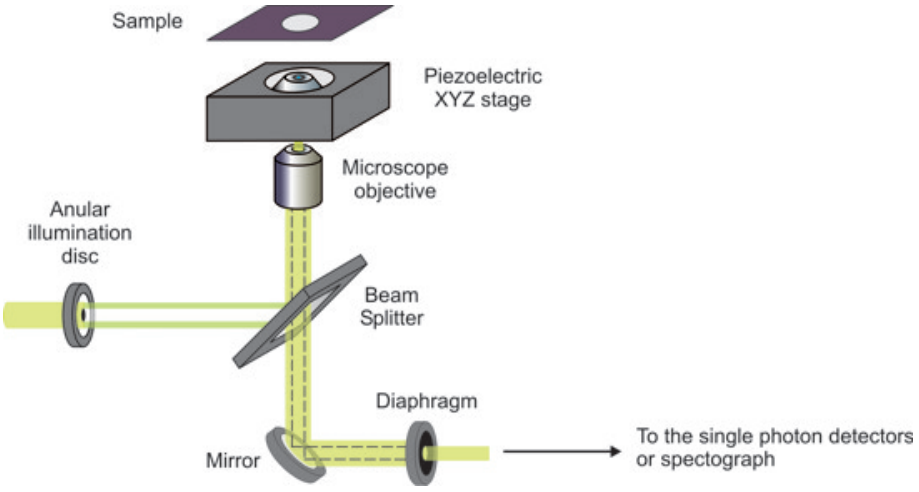


**Figure 2.8:** Light scattering set-up configuration. The dashed line shows the path followed by the reflected light.

It is also possible to work with the inverse configuration; i.e. illuminate with a reduced beam and block the inner part of the detection channel with an appropriate disc.

### The single photon detectors

The set-up counts with two different single photon detectors: an Avalanche Photo Diode (APD) and a Photo-Multiplier Tube (PMT). Both detectors can be used for imaging and time correlated measurements. Table 2.2 shows the principal technical characteristics of each detector.

The APD provides TTL pulses that can be directly counted by the AD/DA converter. The PMT instead provides very weak, fast and negative pulses. The easiest way to transform this signal into a TTL pulse is by means of an Oscilloscope.

| Single photon detector | Dark counts [CPS] | Active area diameter [mm] | Quantum efficiency * [%] $\lambda$ [nm] | Output pulses | Linear response up to * [x10$^6$ cps] | Manufacturer / model |
|---|---|---|---|---|---|---|
| APD | < 100 | 0.18 | 400 10<br>500 48<br>600 66<br>700 73<br>800 61 | Positive TTL<br>2.5 V (50 Ω)<br>FWHM 30 ns | 5 | *Perkin Elmer Optoelectronics inc, SPCM-AQR13* |
| PMT | < 50 | 5 | 400 22<br>500 40<br>600 40<br>700 13<br>800 0 | -3 mV (50 Ω)<br>FWHM 2 ns | 1.5 | *Hamamatsu Photonics KK, H7422-40* |

**Table 2.2:** Single photon counting detectors. APD: avalanche photo diode. PMT: photo multiplier tube. CPS: counts per second. $\lambda$: wavelength. FWHM: full width at half maximum. All the quantities were corroborated in the laboratory, except the ones marked with * which are taken from the manufacturer specifications.

The 50 Ω input channel of a 300 MHz oscilloscope (*Tektronix 2465*) is supplied with the PMT signal. Once the triggering is adjusted, the monitor output of the oscilloscope provides one TTL for each PMT pulse. The power supply, the Peltier cooling, and the gain of the PMT are computer controlled with a controller and a software specifically designed for this detector (*DCC-100, Becker und Hickl GmbH*).

### The transmission grating spectrograph

In order to measure single molecule fluorescence and light scattering spectra, a transmission grating spectrograph was adapted to the set-up. The spectrograph consists of a volume phase holographic (VPH) transmission grating (*HVG-590 and HVG-690, Kaiser Optical Systems Inc.*), a photo objective (*35 mm, f1.4, Nikon Inc.*) and a high quantum efficiency, charge-coupled device (CCD) camera (*SensiCam QE, PCO Imaging GmbH*). Table 2.3 presents the relevant technical information for these components.

The collimated detected beam is directed to the VPH grating either by a silvered mirror or by a beam splitter. Light is diffracted by the VPH grating at angles according to classical diffraction and the energy distribution is governed by the Bragg condition. The photo objective focuses the spectrally dispersed light into a line of the CCD sensor of the camera.

The spectral ranges covered by the *HVG-590* and *HVG-690* gratings are from 390 to 790 nm and from 500 to 800 nm, respectively. The size of the detectable spectral range depends on the angular dispersion of the grating, the focal length

| VPH grating<br>*Kaiser Optical Systems inc.* | Photo Objective<br>*Nikon inc. ,* | CCD camera<br>*PCO Imaging GmbH, SensiCam QE* |
|---|---|---|
| Angular dispersion [°/nm]<br>HVG-590.... 0.0657<br>HVG-650.... 0.0496 | Focal distance... 35 mm<br>Maximum diaphragm apperture..... 25 mm | Sensor..... 1376x1040 pixels<br>pixel size..... 6.45x6.45 $um^2$<br>dynamic range.... 12 bit<br>non linearity..... <1%<br>$\lambda$ [nm] QE [%]<br>400 43<br>500 60<br>600 55<br>700 40<br>800 21 |

**Table 2.3:** Spectrograph components. The angular dispersion of the gratings were measured in the laboratory. The other information is presented as provided by the manufacturer.

and the diaphragm aperture of the photo objective, the diameter of the detected beam (8.9 mm), and the size of the CCD sensor. The spectral resolution is directly determined as the ratio of the spectral range and the number of pixels of the CCD sensor[5]. For the mentioned objective and CCD camera, the maximum detectable spectral range is 260 nm with a resolution of 0.19 nm with the *HVG-650* grating, and 340 nm with a resolution of 0.25 nm with the *HVG-590* grating. The position of the detectable spectral range can be shifted simply by moving the CCD camera.

### 2.2.4 Time Correlated Single Photon Counting

Time Correlated Single Photon Counting (TCSPC) [17] has been one of the best ways of measuring fluorescence decay times since the method was conceived in 1961 by Bollinger and Thomas [18].

TCSPC is based on the detection of single photons and the computation of their individual detection times. Figure 2.9 helps to explain the TCSPC working principle. The excitation light should be pulsed at such frequency that the fluorescence is allowed to decay completely in between pulses. In addition, the detected fluorescence intensity should be low enough so that the probability of detecting two photons in between pulses is negligible. The latter condition is naturally fulfilled in the case of single molecule fluorescence measurements. Under these conditions, every time a photon is detected, the time elapsed from the last excitation pulse is computed (mic-t in figure 2.9.a). Then, if the laser pulses are narrow enough in comparison to the typical fluorescence decay time, the fluorescence decay curve is directly obtained

[5]The photo objective focuses the monochromatic beams dispersed by the grating into diffraction limited spots with a size ranging from 1.9 to 3.5 $\mu$m, depending on the wavelength. The pixel size of the CCD sensor is 6.75 $\mu$m.

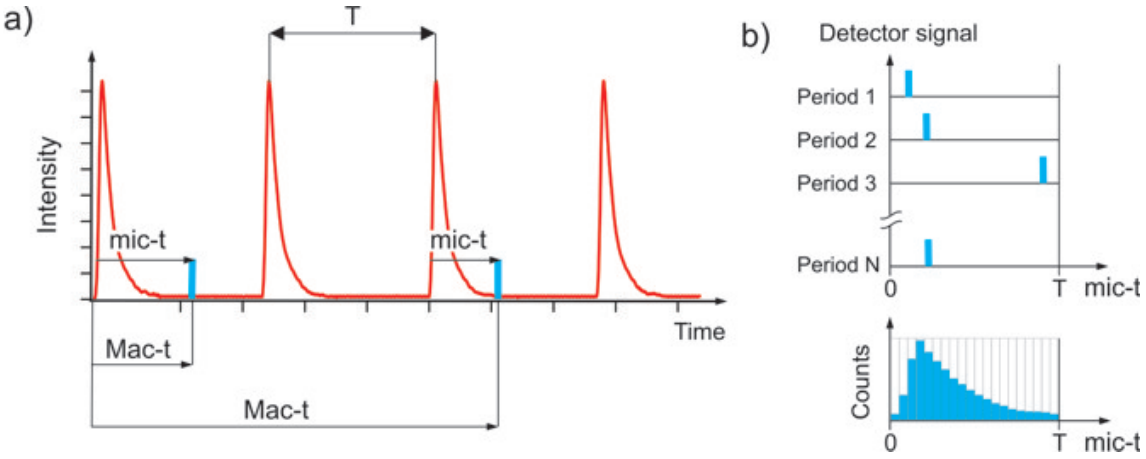


**Figure 2.9:** Time correlated single photon counting principle. a) The curve represents the excitation light pulses, and the short vertical lines represent detected fluorescence photons. For each detected photon, the time from the beginning of the experiment (Mac-t) and the time from the last excitation pulse (mic-t) are determined. b) The fluorescence decay curve is obtained by computing a histogram of the mic-t times.

by making a histogram of the detected mic-t times, as shown schematically in figure 2.9.b.

The microscope is equipped with an independent TCSPC module (*SPCM-630, Becker und Hickl GmbH*). The device can measure the mic-t times with a resolution of 12 ps, up to a rate of 8 MHz [6]. Furthermore, the TCSPC unit also records, for every detected photon, the detection time from the beginning of the experiment (Mac-t in figure 2.9) with a resolution of 50 ns.

The TCSPC module needs only two input signals. The pulse-train signal from the laser, which is typically a sinusoidal signal with a frequency equal to the repetition rate of the laser pulses, and the single photon detector signal. In both cases the signals need to have an amplitude in between -50 mV and -1 V. Therefore, both the APD and the PMT signals need to be treated with specific electronics before feeding the TCSPC. The APD signal is processed by a router (*HRT-82, Becker und Hickl GmbH*) that transforms the positive TTL pulses provided by the APD into the required negative pulses. The PMT signal is already negative but too weak for the TCSPC, therefore it needs to be amplified with a 26 dB, broadband (5 kHz - 1.6 GHz) amplifier (*HFAC-26, Becker und Hickl GmbH*).

The ultimate time resolution for the determination of fluorescence lifetimes is usually limited by one of the following two factors. First, the width of the laser

[6] In fact, the TCSPC unit takes advantage of the low intensity conditions. It determines the time from the photon detection until the next excitation pulse, and calculates the mic-t time later by difference. In this manner, the TCSPC unit performs the time calculation only when a photon is detected and not for all the pulses. This is justified by the fact that for usual laser pulses repetition rates ($\sim$ 50 MHz), the probability of detecting photons in consecutive pulses is negligible (detection rates for a single molecule are $\sim$ 0.05 MHz).

pulses which is around 300 ps for both pulsed lasers. Second, the reproducibility of the rising cant of the detector pulses. The latter is important due to the zero crossing method used by the TCSPC unit to determine the temporal position of the signals; further details can be found in the TCSPC operation manual [19].

### 2.2.5 Computer control

Several functions of the microscope are computer controlled, either via commercially available software or by home made programs developed during the work for the present dissertation. This section describes how the computer control of the different functions is organized. Details about the operation can be found in section 2.4.

#### Scanning and confocal data acquisition control

The operation of the piezoelectric stage, as well as the data acquisition for all types of imaging, is accomplished with the AD/DA converter. The AD/DA is computer controlled with a home made software that consists of three parts. The first part consists of routines that operate at the lowest level, directly on the local CPU and memory of the AD/DA converter and perform the basic operations, such as scanning a line or counting photons at one pixel. These routines were programmed in a specific computer language (ADBasic [20]) provided by the AD/DA manufacturer. The second part is the PC user interface. With this software, the user can set the scanning parameters, as well as observe on-line the collected data and save it in an appropriate format. The PC user interface was programmed in Igor [21] in order to take advantage of Igor's built-in capabilities for data treatment. Finally, the third part consists of a set of routines required for the communication between the PC user interface and the local CPU of the AD/DA converter. These routines were programmed in C++. The code of all these programs is presented and described in the appendix A.3.

#### CCD camera and spectra acquisition control

The CCD camera can be controlled with specific software provided by the manufacturer, and details about the operation can be found in the operation manual of the camera [22]. All the relevant parameters for the operation of the CCD camera can be controlled, such as the active region of the CCD sensor and the collection time. It is also possible to record up to 9999 frames as a function of time with a minimum collection time of 1 ms (maximum repetition rate of 1000 spectra per second).

#### TCSPC unit control

The TCSPC unit has its control software control provided by the manufacturer; details about the operation can be found in the user manual of the TCSPC module [19].

## 2.3 Alignment

The complete alignment of the set-up can be separated in four parts. The first one is the in-coupling of light (provided by any of the light sources) to the single mode fiber. The second is the collimation of the light provided by the fiber and the alignment of the illumination beam. The third one is the alignment of the dichroic mirror or beam splitter and the microscope objective. Finally, the fourth part is the alignment of the detection optics and detectors. In the present section, the four alignment procedures are explained.

### 2.3.1 Light coupling into the single mode fiber

A fundamental pre-requisite for an effective coupling of light into the single mode fiber is that both tips of the fiber have to be be sharply cut. For this, it is first necessary to remove the polymer cladding[7], and then cut the tips with a diamond fiber cutter (*RXS Kabelgarnituren GmbH*).

The process of in-coupling light into the single mode optical fiber consists of two steps. First, light provided by any of the sources has to be focused onto the fiber tip. Second, the fiber position needs to be adjusted in order to maximize the in-coupled light. The different light sources have different focusing requirements as explained below. To couple the focused light into the fiber one should first position the fiber tip approximately in the focus by moving the tip in x, y and z directions, until light scattered by the fiber tip is observed. Then, iterative adjustments of the fiber tip position in x, y, and z directions, should be done as the light intensity coming out of the fiber is monitored. Once the x, y and z positions are optimized, further fine adjustments of the tilting ($\theta$ and $\phi$) of the fiber can be done.

When using laser light, in order to control the polarization of the illumination beam, a $\lambda/2$ and a $\lambda/4$ plates are placed between the laser and the fiber. The angular position of the plates have to be adjusted in order to produce a polarization state in the laser beam such that, after the polarization effects of the fiber, the light exiting the fiber has the desired polarization.

[7]Removing of the polymer cladding is facilitated by immersing the fiber tips in acetone for 2-5 minutes

The microscope is equipped with polarization filter films (*OWIS GmbH*) to control the linear or circular polarization state of the illumination beam. The polarization of the Xe-arc lamp white light cannot be controlled before the fiber. However, a certain polarization state can be filtered from the illumination beam at the exit of the fiber by means of a polarizing film.

#### Focusing the gas phase laser light

The gas-phase lasers (He-Ne and Ar-ion) provide gaussian beams with long coherence distances. In this case, a standard microscope objective is sufficient to focus the beam and to obtain highly efficient coupling into the fiber. In particular, a 16×, 0.3 NA microscope objective (*Wetzlar Germany GmbH*) was used.

#### Focusing the diode laser light

The pulsed diode laser provides a multi-mode, non-gaussian beam, with very short collimation distance (< 1 mm). This divergent beam can be collimated with a standard 10×, 0.2 NA microscope objective to an approximately 8:1 aspect ratio beam. This beam is then focused by a 16×, 0.3 NA objective on the tip of the single mode fiber. The light coupling is very inefficient in this case.

#### Focusing the white light

Light provided by the Xe-arc lamp is highly divergent and cannot be efficiently coupled into the single mode fiber. The best results were obtained by successively focusing the light with a 28 mm f2.8 photo objective (*Nikon Japan*) and a 20×, 0.4 NA microscope objective, into the single mode fiber.

Although the photonic crystal fiber would be, in principle, ideal to obtain single mode white light, spectral instabilities were observed. The white light exiting the photonic crystal fiber showed spectral fluctuations in the sub ms range that prohibited the use of this fiber to guide white light in any of the experiments.

### 2.3.2 Collimation of the illumination beam

The optical fiber acts as a point-like light source providing a divergent beam which needs to be collimated in order to form the illumination beam.

The first step to collimate and align the illumination beam is to precisely define an optical axis by means of a reference laser beam and two aperture diaphragms[8]

[8] One diaphragm is sufficient if one works with a rail that allows for translation along the optical axis

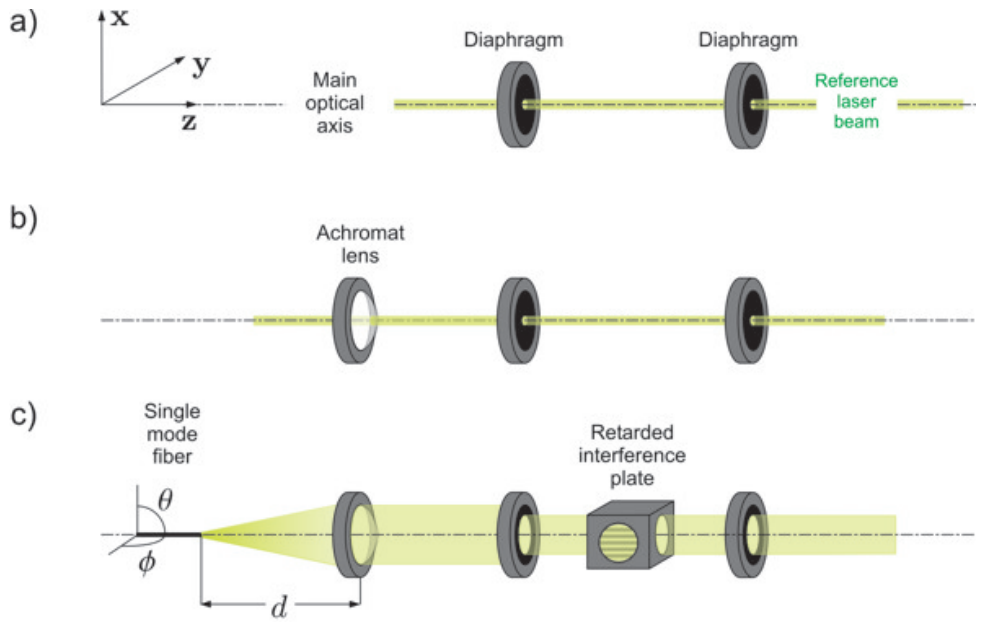


**Figure 2.10:** Collimation and alignment of the illumination beam. a) Definition of an optical axis. b) Introduction of the collimation lens, centered and perpendicularly in the optical axis. c) Positioning of the optical fiber.

(figure 2.10.a). Then, the collimating achromatic lens is introduced centered and perpendicular to the optical axis (i.e. the reference laser beam should not deviate, see figure 2.10.b). From now on, the collimating lens should not be moved in any direction but along the optical axis (z). Next, the reference laser beam can be removed and the optical fiber should be placed near the optical axis (figure 2.10.c). The distance $d$ along the optical axis (z) between the fiber tip and the lens should be adjusted in order to collimate the light. Collimation can be easily checked with the help of the retarded interference shear plate (*09SPM001, Melles Griot GmbH*), which produces interference fringes parallel to the beam when it is collimated [23]. Then, the position in the plane perpendicular to the optical axis (x,y) and the direction $(\theta, \phi)$ of the fiber should be adjusted. The direction of the collimated beam is determined by the (x,y)-position of the fiber tip. Modifying the direction of the fiber (*theta* and *phi*) changes the intensity profile of the beam because the illumination over the surface of the collimating lens changes. The aim is to illuminate the collimating lens as uniformly as possible. The (x,y)-position and the direction $(\theta, \phi)$ have to be adjusted iteratively until the beam is directed along the optical axis with a uniform intensity distribution. At the end of this procedure the collimation should be checked again with the retarded interference plate, and, if necessary, the distance $d$ should be corrected.

#### Alignment for annular illumination

Annular illumination requires the positioning of a blocking disc in the center of the illumination beam. There are two ways to do this. The blocking disc can be glued onto a glass slide, or it can be held with very thin cords[9]. The disc is mounted in a positioning stage that allows it to be moved it in three dimensions. The position of the disc can be controlled by closing the diaphragms that define the optical axis. If the disc is in the center of the illumination beam, the diaphragms should close concentrically with the disc.

### 2.3.3 Alignment of the dichroic mirror and the microscope objective

In fluorescence measurements, the illumination beam is directed to the microscope objective by a dichroic mirror that also separates the illumination from fluorescence light. In light scattering measurements, instead of a dichroic mirror, a 50/50 beam splitter is used. The alignment procedure is the same in both cases, so the following explanation for the dichroic mirror, is also valid for the 50/50 beam splitter.

The aim of this procedure is to direct the collimated illumination beam centered and parallel to the high NA microscope objective that focuses the excitation light onto the sample. To achieve this, the positions of the dichroic mirror and the microscope objective should be adjusted. First arrangement of the positions of both the objective and mirror can be done by eye. For further fine adjustment of the positions, the objective can be moved in the plane parallel to the sample, and the dichroic mirror can be moved in all three coordinates and can also be tilted. All movement are accomplished with micrometer precision.

The fine correction of the relative position of the illumination beam and microscope objective can be done with the help of the reflections of the illumination beam in the internal lenses of the microscope objective (see figure 2.11). Relatively high laser intensity is required to easily see the reflections, and the collimation lens should be displaced further from the fiber tip in order to make the beam slightly convergent. A screen, placed just before the objective, and with a small aperture ($\sim 6\,\mathrm{mm}$) to let the convergent beam pass through, allows the visualization of the beam reflections in the internal lenses of the microscope objective. If the beam and objective are to be concentric and parallel, all the reflections should be concentric as well, and their images should coincide on the screen aperture (which should be concentric with the convergent illumination beam). To attain this, the position of the objective should be adjusted iteratively with tilting of the dichroic mirror.

[9] In the experiments presented in this dissertation human hairs were used.

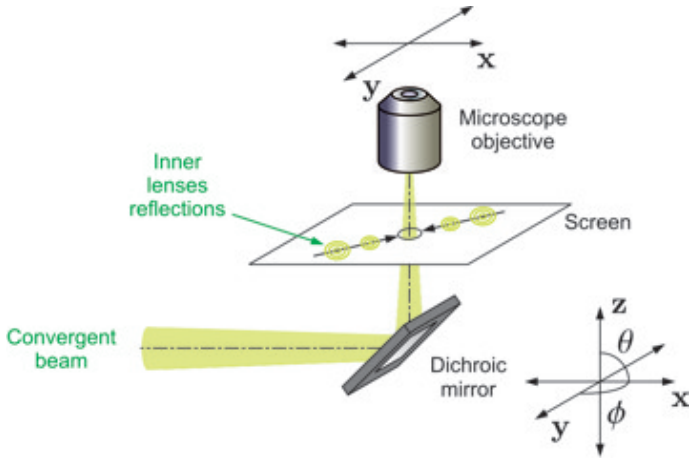


**Figure 2.11:** Alignment of the dichroic mirror and microscope objective. The objective can be moved in the **xy** plane. The mirror can be moved and tilted in all directions (**x**, **y**, **z**, $\theta$ and $\phi$). When the illumination beam and the microscope objective are centered and parallel all the reflections of the beam on the inner lenses of the objective coincide in the center.

### 2.3.4 Alignments in the detection

The aim of these alignment procedures is to assure the selective detection of light coming only from the focal spot with the different detectors.

To proceed with the alignment, it is necessary to have a visible beam of light collected by the objective from its focus. To achieve this, a microscope coverslip should be placed in the sample holder (see section 2.4.1 for details about how to place the microscope coverslip), laser illumination with sufficiently high intensity should be used and all filters should be removed. Like this, the light reflected at the glass/air interface can be easily seen. By moving the objective up and down, the focus of the objective should be placed at the glass/air interface so that the reflected beam consists of light from the focal spot. At this point, as the reflected light comes from the focus, it is collected and collimated by the microscope objective. Therefore, it is possible to control that the focus of the objective is at the glass/air interface by controlling the collimation of the reflected beam. There are two ways of controlling the collimation of the reflected beam. One is, by using the collimation tester shear plate [23], as described in section 2.3.2. The other, more practical method, is to direct the reflected beam to the microscope Huygenian ocular (there is a flippable mirror installed for this purpose) and then project it onto a screen[10]. The ocular amplifies any deviation from the collimation and the adjustment can be accomplished by eye (see figure 2.12).

The collimated reflected beam should be directed to the detection path with a silvered mirror. There, it is focused with an achromatic lens into the confocal pin-hole, and collimated again with a second achromatic lens. The positions of both lenses

[10]IMPORTANT: do not look into the eyepiece if no filter is blocking the laser light

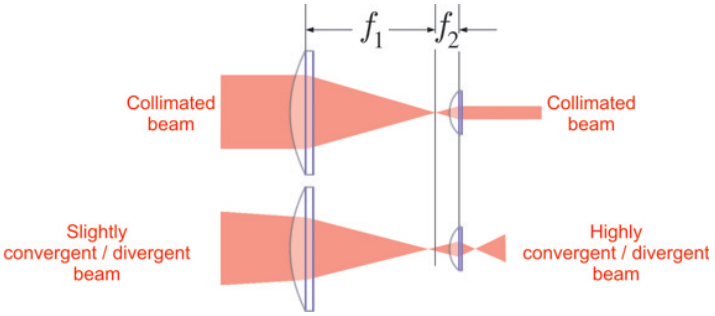


**Figure 2.12:** Huygenian ocular. The system consists of two conjugated lenses, one has a much shorter focal distance than the other ($f_1 > f_2$). a) A collimated beam is focused by the first lens into the focal point of the second lens, therefore producing a collimated beam of small size. b) If the incoming beam is slightly convergent (divergent), the first lens focuses it further from (closer to) the second lens, which due to its short focal distance produces a highly convergent (divergent) beam.

and pinhole can be adjusted with micrometer precision in x, y, and z directions. The adjustment should be done in sequential order. Then, by means of mirrors, (if necessary polarizing) beam splitters, or dichroic mirrors, the reflected beam can be directed to the combination of detectors (APD, PMT, spectrograph) required by the experiment.

### Alignment of the avalanche photo diode

The reflected beam should be focused into the small active area of the APD with an (100 mm focal length) achromatic lens. For this purpose, the APD is mounted on an xyz stage with micrometer precision. The first alignment can be accomplished by eye but fine adjustments can only be done when a real (fluorescent or scattering) sample is measured by optimizing the APD position in order to maximize the signal.

### Alignment of the photomultiplier tube

Due to the big active area of the PMT, the alignment is considerably simple. The reflected beam should be focused onto the active area of the PMT with an achromatic (100 mm focal length) lens. This can be accomplished by eye and no further adjustments are needed.

Illumination of the active area of the PMT with high intensities (even when it is switched off) can increase the dark-count rate of the PMT. Eventually, it can take several days until the nominal dark-count rate is recovered. For this reason, the active area of the PMT should be covered during the alignment procedure.

### Alignment of the spectrograph

The collimated reflected beam should be directed first to the VPH grating. Light dispersed by the grating is collected by the photo objective and focused on the CCD sensor. Both the photo objective and the CCD sensor should be centered in the spectral range of interest. The latter can be accomplished with the help of two different laser light sources, for example the 460 nm line of the Ar-ion laser and the 633 nm of the HeNe laser, as shown schematically in figure 2.13.

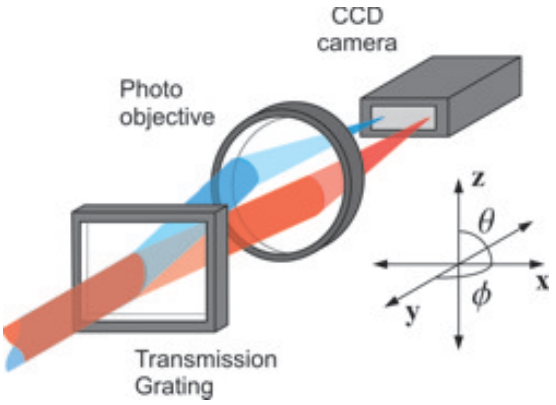


**Figure 2.13:** Alignment of the spectrograph. Both the photo objective and the CCD camera can be moved in x, y and z directions, as well as tilted in $\phi$ and $\theta$. Using a two-color beam helps to center the photo objective in the spectral range of interest, and to place the CCD camera in the right position.

The photo objective and the CCD camera can be moved and tilted in all directions. To maximize the detectable spectral range the photo objective needs to be as close as possible to the grating, and its diaphragm has to be completely open. Then, the position of the camera and the focus of the photo objective need to be adjusted in order to produce a sharp image of the spectra in the desired position of the CCD sensor. For this, it is convenient to use white light illumination and set the camera on *live mode* [24] because this allows to monitor on-line how light of different wavelengths is focused on the CCD sensor. The light dispersed by the VPH grating should be focused by the photo objective to a straight line on the CCD sensor. It is advisable to accommodate the camera position in such a way that the light is focused on a horizontal pixel line of the CCD sensor because in that case the data analysis is simpler.

### Alignment of the detection for light scattering measurements

In this case, annular illumination is used and the diameter of the detected beam should be reduced with a diaphragm in order to block the reflected light (see figure 2.8). Because of the annular illumination, the reflected light beam used for the

alignment looks like an annulus. The diaphragm should be placed centered to this annulus and closed to a point in which no light can pass through. The size of the diaphragm can be at first adjusted by eye. Once a scattering sample is placed on the microscope, the size of the diaphragm can be optimized in order to get the best signal to background.

## 2.4 Operation

In this section, instructions about how to perform the basic operations with the microscope are given. First, it is explained what the sample requirements are and how the sample should be mounted. Second, all the operations related to imaging are explained. Finally, the instructions to perform time correlated measurements and to record spectra are given.

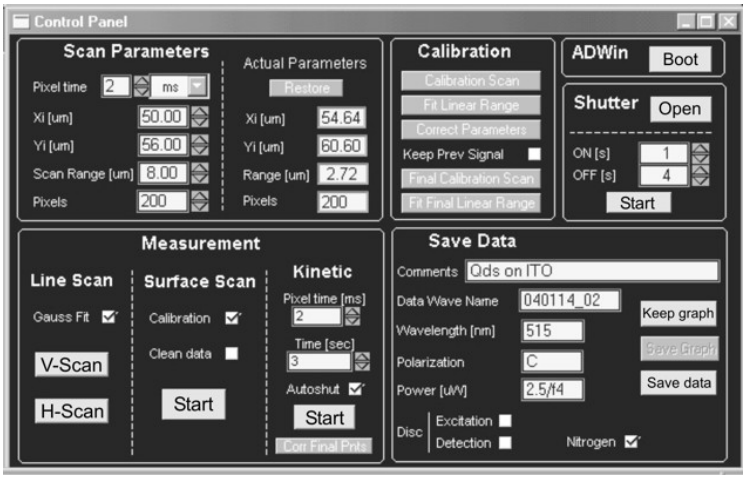


**Figure 2.14:** Control panel of the PC user interface used to operate the home-built confocal microscope.

Many of the computer controlled functions of the microscope explained below can be managed from the PC user interface[11]. The *control panel* for this interface is shown in figure 2.14. For further details about the microscope control and data acquisition software please refer to appendix A.3.

Before performing any operation from the PC user interface software, it is necessary to boot the local processor of the AD/DA converter by pressing the button called *Boot* in the *ADWin* division of the *control panel*. This action, in addition to resetting the local processor of the AD/DA converter, clears up the local memory of the AD/DA converter and loads all necessary routines.

[11]The PC-user interface file is called SAC_v7.pxp

### 2.4.1 Sample requirements and mounting

Due to the short working distance of the high NA microscope objective, the samples should be prepared on thin microscope coverslips (0.13 - 0.16 mm). The sample should be placed on the sample holder (see figure 2.15), fixed with the magnetic film, and then moved with care to the piezoelectric stage. The region of interest of the sample should be positioned on top of the front lens of the microscope objective, with sufficient immersion oil between the objective and the sample.

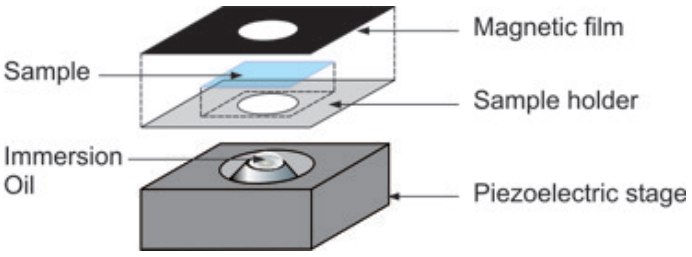


**Figure 2.15:** Sample holder. The sample holder consists of a thin square plate ($\sim 75\times75\,\mathrm{mm}^2$) of steel with a perforation (Ø 20 mm) in the center. The sample should be placed on top of the sample holder and fixed with a magnetic film. Then, the complete set should be positioned on the piezoelectric stage.

After placing a new sample on the microscope, the focus should be adjusted. It is advisable to start by placing the focus of the objective on the glass/air (or sample/surrounding medium) interface as described in section 2.3.4).

### 2.4.2 Imaging

The first step to make an image is to mount a sample and to focus the microscope. Then, from the control panel (figure 2.14) the parameters for scanning an image can be set: the initial position (*Xi* and *Yi*) in $\mu$m, the scanning range (*Scan Range*) in $\mu$m, the number of pixels per line (*Pixels*), and the counting time per pixel (*Pixeltime*) in ms or $\mu$s. The process of acquiring an image is initiated by pressing the button *Start*, in the division called *Surface Scan* of the control panel (figure 2.14).

If the *Calibration* check-box is checked, a calibration procedure is performed before the image scanning in order to account for the delayed response of the piezoelectric stage; i.e. a number of lines is scanned with the set parameters and the corrections parameters, necessary to construct consistent forward- and backward-scanned images from the collected data, are determined. An overview of this calibration procedure is given in section 2.2.2. The code of the algorithm used is presented and commented in the appendix A.3.

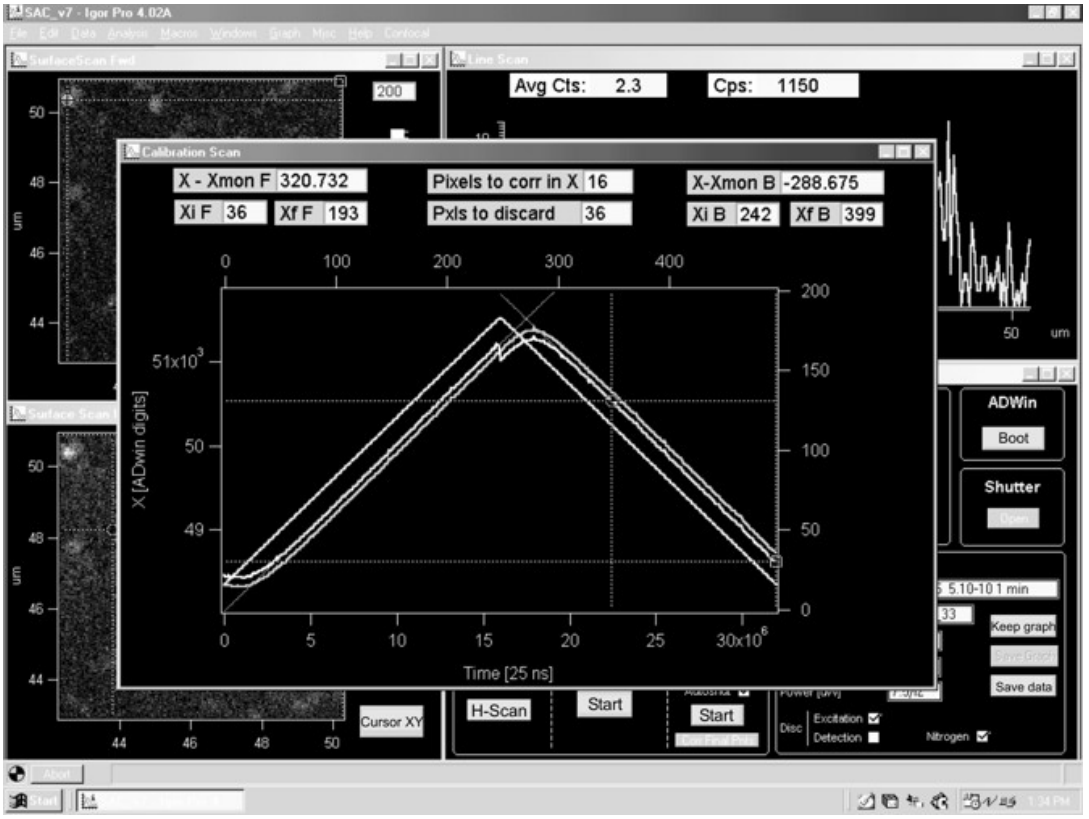


**Figure 2.16:** Calibration screen. Screen shot of the user interface software during the calibration procedure before the start of the scanning to acquire an image. The software displays the parameters of the calibration procedure that corrects the effects of the inertia of the piezoelectric drivers and electronic delays. The curves are the driving signal to scan the x-direction, the capacitive monitor signal of the piezo stage and the actual x-position of the piezoelectric stage after correction (see section 2.2.2). The thin lines are linear fits used to determine the linear range of the x-position. Further information can be found in the appendix A.3.

While the test lines for calibration are being scanned, the screen of the user interface looks like in figure 2.16. The driving and monitor signals of the piezo stage are displayed together with the corrected x-position (see section 2.2.2)[12].

Once the scanning to acquire an image starts, the screen of the user interface looks like in figure 2.17. On the left, the forward- and backward-scanned images are displayed and updated line by line as the acquired data is transferred to the PC[13]. In addition, the profile of the last scanned line is also displayed on the upper right corner of the screen.

[12]It is possible that the monitor signal suddenly appears extremely noisy. This is due to instabilities in the monitor output of the amplifier. If this happens, the BNC connector from the monitor output of the amplifier should be unplugged for some seconds and the scanning should be restarted.

[13]The images displayed on the user interface software are rotated 90° counter-clockwise with respect to the sample, as seen from the front of the microscope.

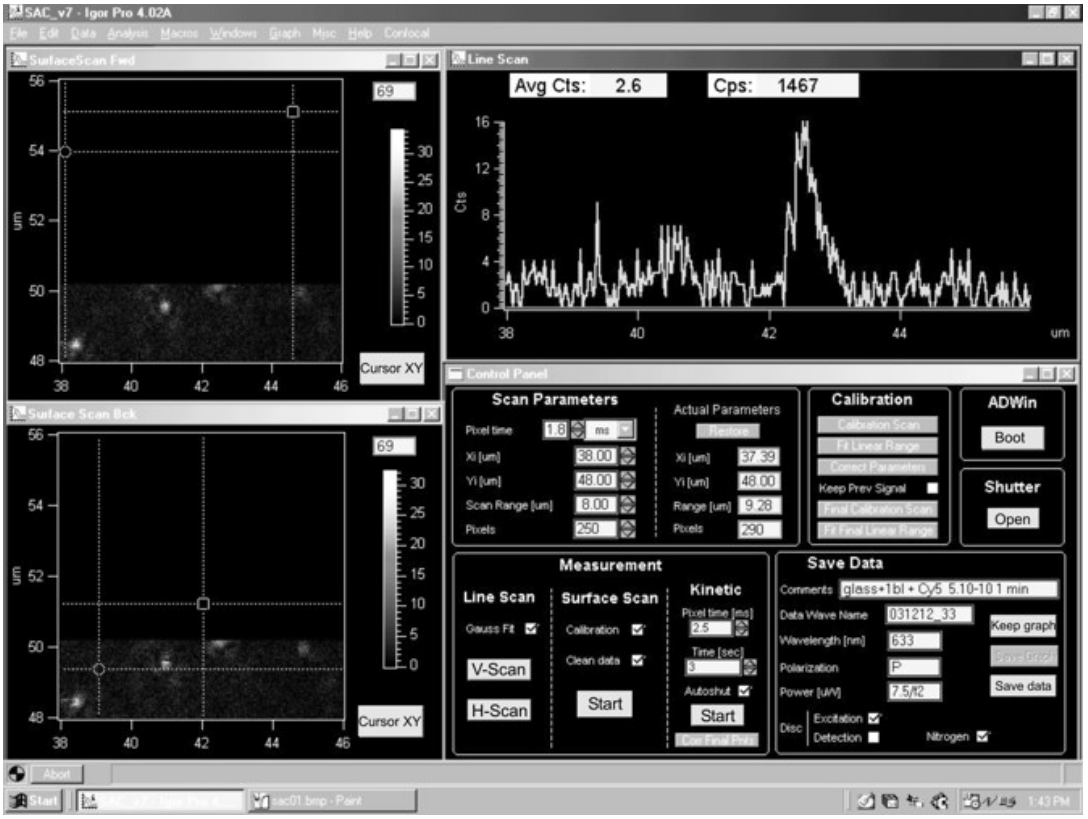


**Figure 2.17:** Scanning screen. Screen shot of the user interface software during the scanning to acquire an image.

### Line scanning

The computer control also allows to perform vertical and horizontal line scans. The lines are scanned repeatedly until the user stops the process. The procedure for the scanning of a vertical or horizontal line is initiated by pressing the buttons *V-Scan* or *H-Scan* of the division *Measurement/Line Scan* of the *control panel*. The range of the line scan is set by the position of the cursors in any of the images. The round cursor (A) sets the starting point and the squared cursor (B) sets the final point for the line scan. Figure 2.18 shows a screen shot while a horizontal line is being scanned. The limits were set by the cursors in the upper image (forward-scanned).

Line scanning is very helpful to optimize the focus of an image of single molecules as well as to adjust the APD position. One way to optimize the focus of a single molecule fluorescence image is to make a line scan through the center of a detected fluorescence spot and adjust the z-position of the sample in order to make the profile narrowest[14]. For extra help, it is possible to check the *Gauss Fit* check-box, and a Gaussian curve is fitted after every scanned line and the full width at half maximum

[14]Care should be taken to scan through the center of a feature because otherwise the signal might seem to become narrow only because a part of a higher order Airy disc is being detected.

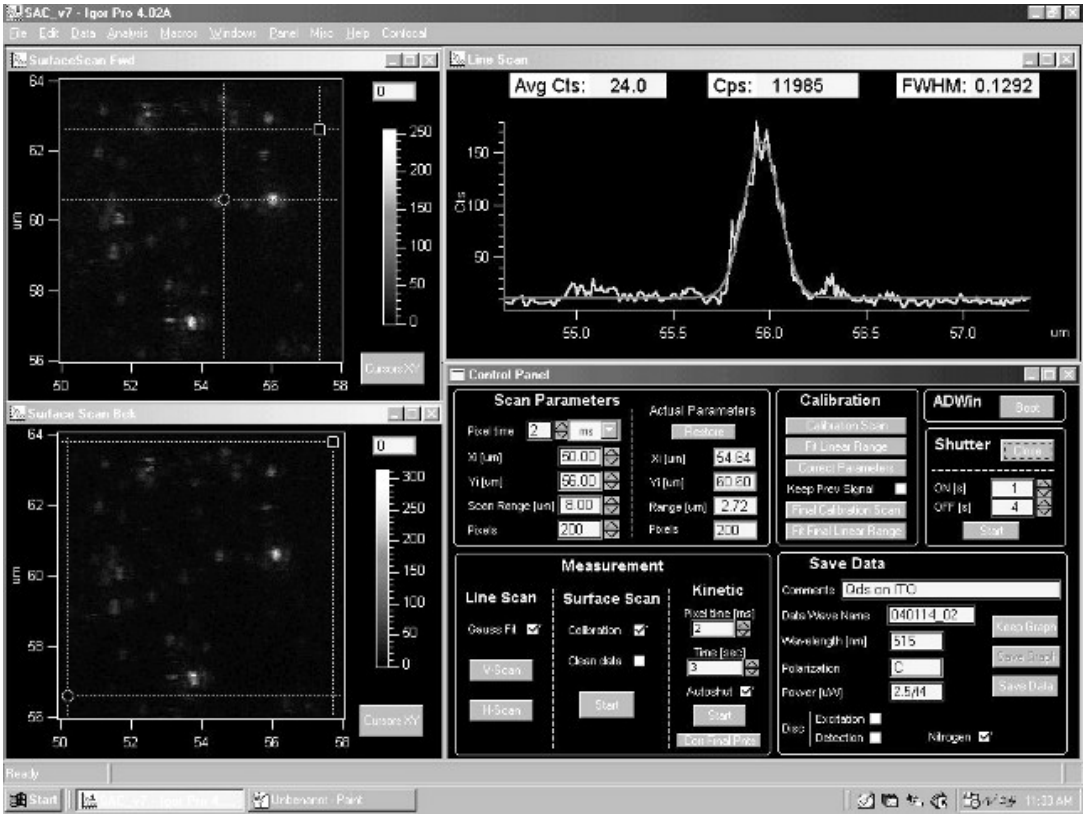


**Figure 2.18:** Line scan screen. Screen shot of the user interface software during a line scan.

(FWHM) is displayed. A line scan is also useful to adjust the position of the APD in order to maximize the signal.

### Data format

The obtained data is stored in the form of a third order tensor. The rows and columns are determined by the number of pixels of the complete image (forward and backward). Then, each layer (third dimension of the data tensor) has different information stored for every pixel. The first and second layers store the x and y position, respectively, of each pixel in units of the AD/DA digits ($AD$), which can be translated into $\mu$m by:

$$X[\mu m] = \frac{80\ X[AD]}{32768} \tag{2.4}$$

The third layer stores the counts (i.e. the number of photons detected in the pixel). The fourth and fifth layers store the initial and final time, respectively, of each pixel in ns, with a resolution of 25 ns. The sixth layer contains the capacitive monitor signal for the x-position of each pixel, again in AD/DA digits.

#### Saving Data

To save the complete data, the buttons *Save Data* in the division *Save Data* of the *control panel* should be used. The data is saved in Igor binary format [25] together with the adjacent information entered in the other fields of the *Save Data* division of the control panel (*Comments, Wavelength, Power*, etc.). In addition, the scanning parameters (*Pixeltime, Xi, Yi, Scan Range, Pixels*) are stored, as well as the necessary information to reconstruct the forward and backward images from the data[15]. Software to extract the information from this type of data was programmed as well but it is not discussed in this dissertation[16].

### 2.4.3 Time correlated measurements

Two kinds of time correlated measurements are described in this section. Lifetime imaging and fluorescence vs. time traces. Both are performed with the help of the TCSPC module (see 2.2.3). Details about the operation of the TCSPC module can be found in its user manual [19]. In these kinds of measurement, data needs to be collected simultaneously by the AD/DA converter and the TCSPC unit. Therefore, it is necessary to divide the detector signal (simply by a BNC T-connector), and send it to both the AD/DA converter and TCSPC unit (see sections 2.2.3 and 2.2.4 for the input signal requirements of the AD/DA and TCSPC).

#### Lifetime imaging

Lifetime imaging consists of recording a fluorescence image in which also the fluorescence excited state lifetime is stored. That means that each pixel of the image should contain information about the position, the number of photons counted at that position, and the time after the excitation pulse at which those photons were detected (mic-t in section 2.2.4).

Once an interesting region of the sample has been identified, the TCSPC module should be started first in mode FIFO. Then, the confocal image scanning should begin, so that in both the TCSPC and confocal data the complete information is stored. In this manner, every photon seen by the detector is doubly detected, by the AD/DA counter and the TCSPC, and two sets of data are obtained. The data from the confocal image, recorded in Igor as described above, contains for every pixel, besides the position, the time at which the counter was started and the time at which it was stopped (with 25 ns resolution). The data obtained with the TCSPC consists of two values for every detected photon, recorded in chronological order:

[15] All this information is saved together with the data in the Igor binary file as the *note* associated to the saved *wave*, and one can get access to it with the Igor command note(wavename).

[16] The file is called ConfocalAnalyis.pxp and is attached in a CD-ROM to the copy of this dissertation at the MPI-P library.

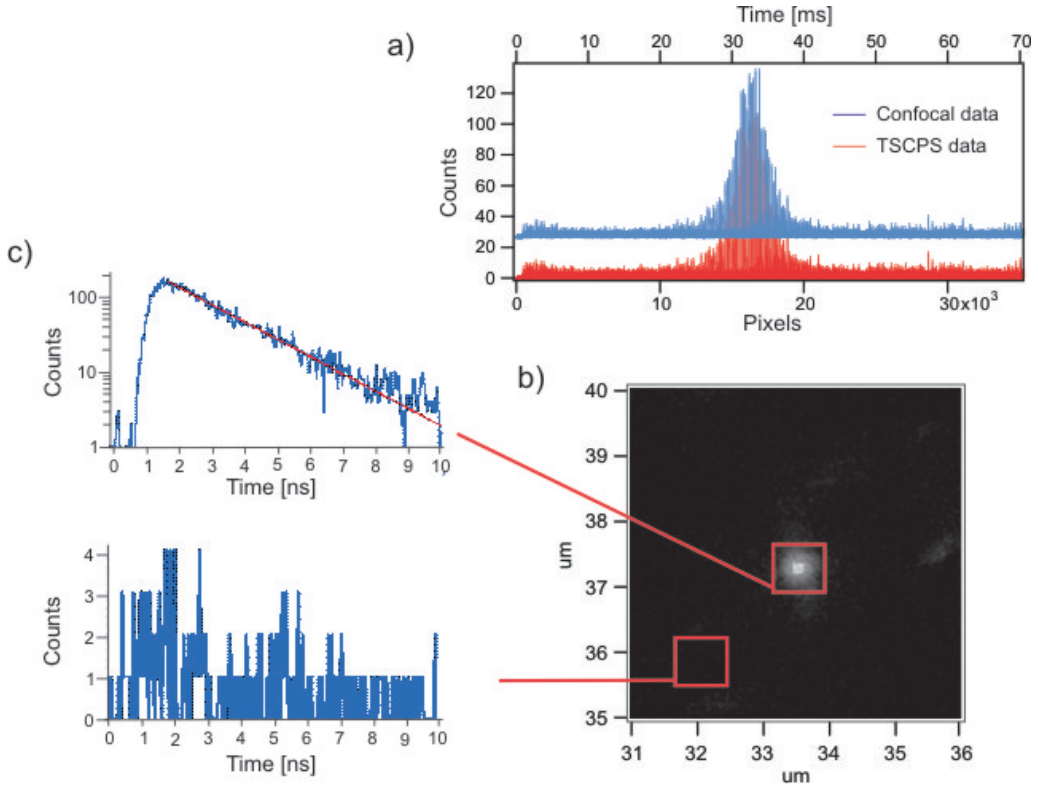


**Figure 2.19:** Fluorescence lifetime imaging. a) To produce a fluorescence lifetime image, the confocal data and the TCSPC data need to be linearized in time and synchronized. b) Fluorescence lifetime image constructed from the data shown in a). c) Fluorescence decay curves of a single fluorescent dye and of the background are shown for comparison.

the detection time after the excitation pulse mic-t, with 12 ps resolution, and the detection time from the beginning of the measurement mac-t, with 50 ns resolution (see section 2.2.4). Then, to obtain a fluorescence lifetime image, it is necessary to combine these two sets of data in order to assign a position (a pixel) to each detected photon in the TCSPC.

Another piece of software was developed to synchronize the two sets of data and construct the lifetime image. To perform the synchronization, both data sets are linearized in time with an arbitrary origin. A histogram of the TCSPC mac-t data is done with a bin width equal to the pixel time of the confocal data and then compared to the latter (figure 2.19.a). If both data sets do not match in time, the origin of the TCSPC data is shifted to later times (and a small part of the TCSPC discarded[17]), a new histogram is computed and compared to the confocal data. The process is repeated until an optimum match is achieved (Figure 2.19.a). Once the TCSPC and confocal data are synchronized, the detection time (TCSPC mac-t time) of every TCSPC-detected photon is compared to the initial and final collection times of each

[17]Recall that the TCSPC module is started before the confocal image, therefore the first part of the TCSPC data does not correspond to the confocal data.

pixel of the confocal image, in order to find the pixel to which the photon corresponds. At the end, an image is constructed in which for every photon of each pixel the TCSPC mic-t time is known; i.e. a fluorescence lifetime image. Then, as shown in figures 2.19.b and 2.19.c, from the fluorescence lifetime image, the fluorescence excited state lifetime of different molecules or regions of the sample can be studied.

### Fluorescence vs. time measurements

Fluorescence vs. time measurements, also called kinetic traces, consist of recording the fluorescence emission of a certain molecule or region of the sample as a function of time. The procedure to carry out a fluorescence vs. time measurement is as follows. First, an image of the region of interest of the sample is acquired and the TCSPC must be ready to start in FIFO mode (see [19] for details). Next, the round (A) cursor, on any of the confocal images, is positioned on the point of the sample that is going to be studied. Then, pressing the *Start* button in the *Kinetic* division of the *control panel* moves the sample to the position marked by the cursor A[18], opens the shutter of the excitation light, starts recording the photons detected by the AD/DA counter as a function of time, and displays the kinetic trace on the top-right graph. Figure 2.20 shows a screen shot of the PC user interface during a fluorescence vs. time measurement of the feature marked by the cursor A on the bottom-left (backward) image.

The stage needs around 10 seconds to move to the selected position and reach stability. This time can be used to start the TCSPC module in FIFO mode to record the kinetic trace. If this time is not sufficient, the TCSPC module can also be started earlier. Like this, the fluorescence vs. time trace is recorded independently by the AD/DA counter and the TCSPC unit. However, these two data sets are different. The data collected by the AD/DA counter and displayed on the PC user interface is intrinsically binned; i.e. it is not the detection time of each photon what is recorded, but the number of photons detected within a time interval of a size determined by the *Pixel time* parameter in the *Kinetic* division of the *control panel*. This is not convenient because the interesting time scale of the processes involved in the fluorescence fluctuations need to be known a priori in order to choose the appropriate bin width. In addition, the data presents gaps due to the fact that the AD/DA card cannot store and deliver data at the same time. So the photons detected during the time necessary to transfer the data to the computer memory are not recorded. The *Time* parameter in the *Kinetic* division of the *control panel* determines how often this data transfer is performed. In contrast, the TCSPC data is not inherently binned because the TCSPC unit records the detection time of each photon. The data employed for further analysis is therefore the TCSPC one. The

[18]The sample is moved to the position marked by the cursor A in the last active image (also called *top image* because the operating system Windows places the last active window on top of the others).

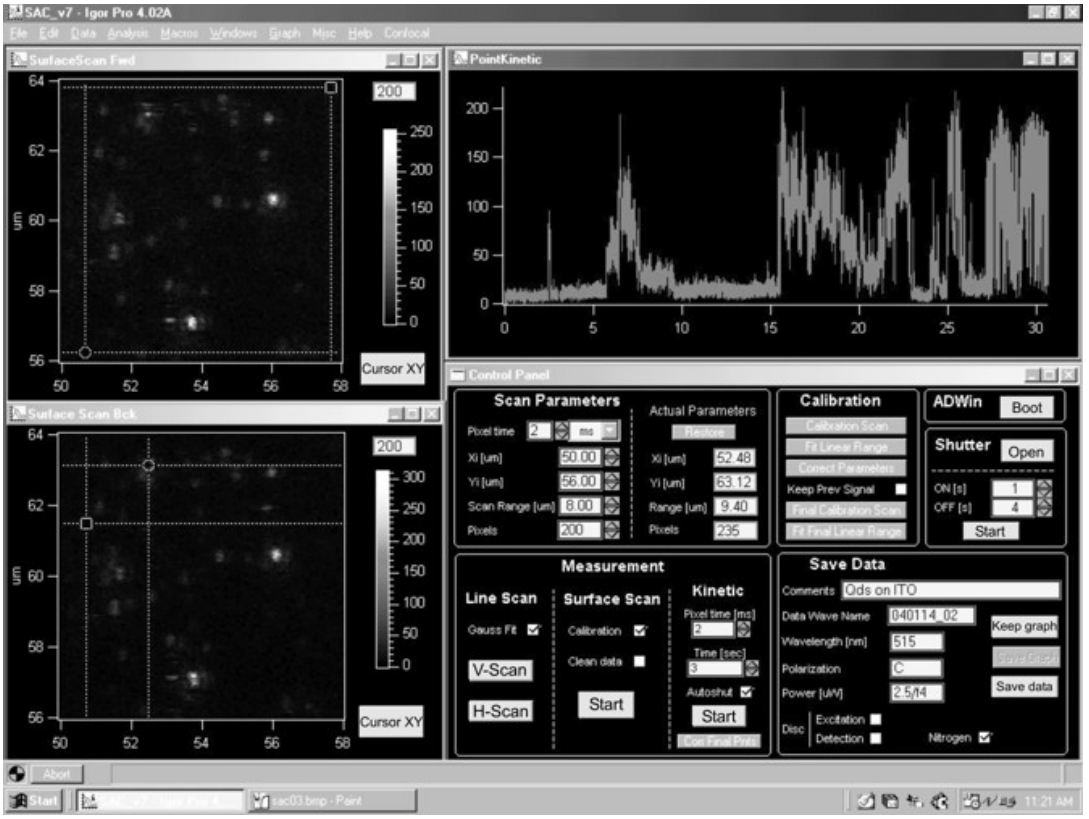


**Figure 2.20:** Kinetic trace screen. Screen shot of the user interface software during the recording of a fluorescence vs. time trace. The software records the data and updates the display periodically at a frequency defined by the *Time* parameter in the *Kinetic* division of the *control panel*.

data recorded for the PC user interface is discarded after each measurement but is of practical importance because it allows to visualize on-line the kinetic trace.

### 2.4.4 Spectra measurements

The procedure to measure the spectrum of light from a specific point of the sample is basically the same as that to measure a kinetic traces. Once a feature of interest is identified in a confocal image, its position should be marked with the round (A) cursor and the *Start* button of the *Kinetic* division of the control panel should be pressed. The sample is then moved to the desired position, the shutter of the excitation light is opened and data is collected as explained in the previous section. However, in this case, the detected light should be directed to the VPH grating either by a mirror or a beam splitter, depending on the experimental requirements. The detected light is spectrally dispersed by the grating and detected by the CCD camera, which has its own control and data acquisition software provided by the manufacturer [22]. The images acquired with the CCD camera contain the spectral

information and can be analyzed with another home made software which is not discussed in this text[19].

If the VPH grating and the CCD camera are properly aligned and focused (see section 2.3.4), the spectral response is linear through the whole range of the grating. After every realignment of the instrument, it is necessary to check the calibration of the spectrograph. This can be accomplished simply by directing monochromatic light of different wavelengths to the spectrograph, measuring the position of those wavelengths on the CCD sensor and obtaining a calibration curve. After a sample change or small alignment corrections, it is recommended to verify the calibration curve with one wavelength. This can be easily done by measuring the position of one laser line on the CCD sensor.

[19]The file is called CCDAnalysis.pxp and is attached in a CD-ROM to the copy of this dissertation in the MPI-P library.

# Chapter 3

# Modelling the fluorescence signal of a single molecule through a layered system

A theoretical method is set-up to model the scanning confocal microscopy fluorescence signal of single molecules through a general (non-magnetic) layered system. The method considers the fluorescent dye molecule as a point oscillating dipole of fixed orientation interacting classically with the electromagnetic field. First in this chapter, the problem is described and the relevant parameters are introduced. Then, expressions for the de-excitation rates and for the spatial distribution of the excitation field and are derived for single molecules of arbitrary orientation. Finally, the results obtained for the excitation and the emission are combined to give an expression for the single molecule fluorescence signal.

## 3.1 Description of the problem.

The fluorescence signal of a single molecule positioned at the first interface of a layered system is to be modelled. Excitation and detection of fluorescence is considered to be accomplished with the high numerical aperture microscope objective of an episcopic illumination scanning confocal optical microscope as the one described in chapter 2.

The detectable fluorescence intensity emitted by a single molecule, in the absence of triplet blinking[1], is given by:

$$I_{SM} = \Gamma_{exc}\ \eta\ \frac{\Gamma_r}{\Gamma_r + \Gamma_{nr}} \tag{3.1}$$

where $\Gamma_{exc}$ is the fluorescence excitation rate, $\Gamma_r$ and $\Gamma_{nr}$ are, respectively, the total

[1]The concept of triplet blinking is explained in section 5.1

radiative and non-radiative de-excitation rates of the molecule, and $\eta$ is the overall detection efficiency including the collection efficiency of the optical system and the quantum efficiency of the detectors. The ratio $\frac{\Gamma_r}{\Gamma_r+\Gamma_{nr}}$ represents the radiative, thus detectable, fraction of the de-excitation.

It is important to note that for the problem considered here $\Gamma_{nr}$ has two different components. First, every fluorophore has an intrinsic non-radiative de-excitation rate $\Gamma_{nr}^{i}$ due to the internal relaxation pathways of the molecule which might depend on experimental conditions such as the surrounding medium (for example solvent and pH) and the temperature. Second, the nearby layered system can introduce additional non-radiative decay channels such as excitation of evanescent modes or direct energy transfer. This leads to an electromagnetic non-radiative de-excitation rate $\Gamma_{nr}^{em}$. With these considerations equation 3.1 writes:

$$I_{SM} = \Gamma_{exc}\ \eta\ \frac{\Gamma_r}{\Gamma_r + \Gamma_{nr}^{i} + \Gamma_{nr}^{em}} \tag{3.2}$$

The intrinsic non-radiative decay rate does not depend on the interactions of the fluorophore with the electromagnetic field. Therefore, the model presented here can only account for it by introducing an intrinsic fluorescence quantum efficiency as an additional parameter. The electromagnetic non-radiative decay rate can be calculated with the model as presented in the next section.

Accurate determination of $\eta$ is difficult and can even depend on the alignment of the detection system. For this reason, the method presented here is set-up for the calculation of a theoretical single molecule fluorescence signal proportional to the experimental one.

The influence of the environment on the fluorescence behavior of a molecule can be theoretically studied in different ways. In the approach presented in this chapter, the molecule is considered as a point oscillating dipole defined by its transition dipole moment $\boldsymbol{\mu}$. It is thought to be placed in either side of one of the outer interfaces of a plane (non-magnetic) layered system and interacting classically with the electromagnetic field. Figure 3.1 depicts the situation and introduces some of the coordinates relevant for the calculations.

The present chapter is dedicated to derive expressions for the rates $\Gamma_{exc}$, $\Gamma_r$ and $\Gamma_{nr}$ of equation 3.1 that permit the calculation of a theoretical single molecule fluorescence signal. Expressions for the electromagnetic de-excitation rates $\Gamma_r$ and $\Gamma_{nr}$ are derived in section 3.2. The excitation rate $\Gamma_{exc}$ is considered in section 3.3.

### Interface boundary conditions

The model presented here considers a fluorophore in the outermost interface of a plane, non magnetic (unitary permeability), layered system. Depending on the

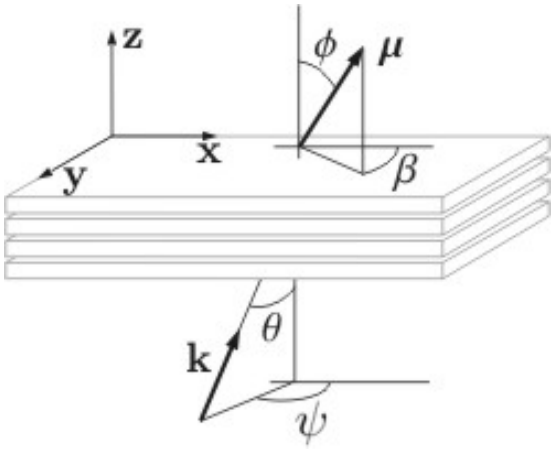


**Figure 3.1:** Coordinate system. The orientation of the transition dipole $\boldsymbol{\mu}$ of the fluorescent dye-molecules is defined by $\beta$ and $\phi$. The direction of the incident or emitted radiation of wavevector $\mathbf{k}$ is defined by $\psi$ and $\theta$.

dielectric contrast, the results on either side of the interface can be very different due to the electromagnetic boundary conditions for the electric field. For a plane interface between media $A$ and $B$, those boundary conditions write:

$$\begin{aligned} E_{\parallel,A} &= E_{\parallel,B} \\ \epsilon_A\, E_{\perp,A} &= \epsilon_B\, E_{\perp,B}, \end{aligned} \tag{3.3}$$

where $\epsilon_A$ and $\epsilon_B$ are the dielectric constants of the respective mediums. The symbols $\parallel$ and $\perp$ stand for the components of the electric field parallel and perpendicular to the interface plane.

## 3.2 The emission

The influence of the surroundings, particularly a nearby conducting surface, on the spontaneous emission of an oscillating point dipole was first discussed by Sommerfeld [26] and later extended by Chance et al. [27]. Analytical solutions to this problem have been obtained by introducing the Hertz vector potential or dyadic Green's functions [27]. In this chapter, an alternative approach, originally due to Weyl [28] and used by a number of authors [29, 30], is generalized to be applied to any non-magnetic layered system. The dipolar field is considered as a superposition of s- and p-polarized plane waves, and the influence of the layered system is described by its plane-wave reflection coefficients.

It is convenient to normalize all the rates to the total emission of a free dipole in a given homogenous reference medium:

$$\Gamma_R = \frac{\mu^2 \omega \mathrm{k}_R}{12\pi\epsilon_0\epsilon_R} \tag{3.4}$$

because the normalized rates do not depend on the actual value of the transition dipole moment. $\omega$ is the frequency and $\mathrm{k}_R$ is the wavevector (in the reference medium of refractive index $n_R$) of the emitted radiation. $\epsilon_0$ and $\epsilon_R$ are the dielectric constants of vacuum and the reference medium respectively.

First, the radiative de-excitation rates to different regions of the space are calculated via the application of the *Lorentz reciprocity theorem*. Then, following the *back-reacted field* approach, the total electromagnetic de-excitation rate is calculated.

### 3.2.1 Radiative decay rate to different regions of space

By application of the *Lorentz reciprocity theorem* [31, 32], the radiation emitted by an oscillating dipole in a certain direction can be calculated as the local electric field, at the dipole position, generated by a plane wave incident from that direction. Therefore, the calculation of the radiative decay rate to a given region of space is analogous to the determination of the electric field intensity generated at the dipole position by plane waves incident from all possible directions in the region of interest.

The electric field produced by a plane wave in any point of a layered system can be calculated by solving Maxwell's equations via a *transfer matrix algorithm* (TMA) [33]. In the TMA, the layers (see figure 3.2) are defined by their thicknesses ($d_i$) and complex dielectric constants ($\epsilon_i$). The uppermost and lowermost layers ($d_0$ and $d_N$) are considered to be semi-infinite and all the interfaces are assumed to be plane and parallel. The total thickness of the layered system is assumed to be small in comparison to the size of the incident plane wave front.

A plane electromagnetic wave defined by its wavevector $\mathbf{k}$, the parallel (to the incidence plane) component of its electric field $E^p$, and the perpendicular component $E^s$, is considered to strike one of the outermost interfaces with an angle of incidence $\theta_0$. The angle of incidence ($\theta_0$) determines the component of the wavevector parallel to the interfaces, $\mathbf{k}_\rho$, which due to the electromagnetic boundary conditions, remains constant through the whole multi-layer system. The electric field (amplitude and phase) in a given z-position of the layered system, which can be thought as the interference result of the waves successively reflected and refracted at the interfaces, can be calculated via the TMA as a function of $\mathbf{k}_\rho$ or equivalently as a function of $\theta_i$ ($= \arcsin \mathrm{k}_\rho/\mathrm{k}_i$).

By considering the symmetry of the dipole field in front of a plane interface, it is found that the emission rate of a molecule with an arbitrary out of plane orientation $\Gamma(\phi)$ (see figure 3.1), can be calculated from the emission rates of the two limiting cases of dipoles parallel $\Gamma_\parallel$ and perpendicular $\Gamma_\perp$ to the interface [34][2]:

$$\Gamma(\phi) = \sin^2(\phi)\ \Gamma_\parallel\ +\ \cos^2(\phi)\ \Gamma_\perp \tag{3.5}$$

[2]Equation 3.5 is valid after $2\pi$-integration over the azimuth angle ($\beta$ in figure 3.1).

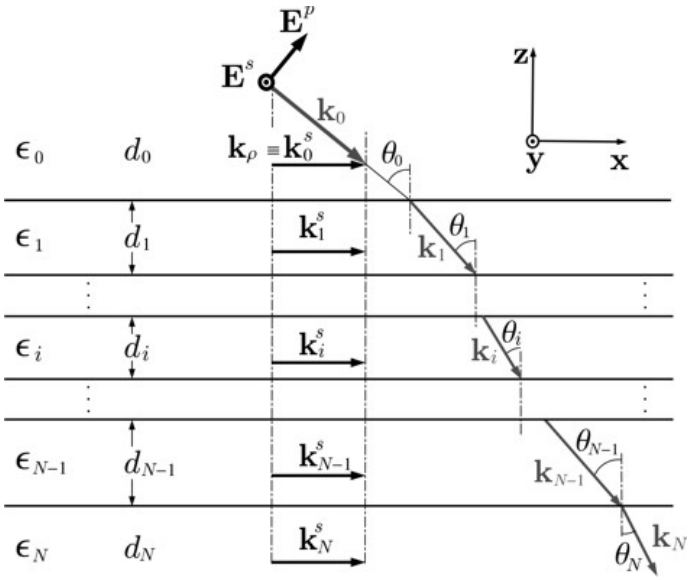


**Figure 3.2:** General multi-layer system showing the relevant parameters for the *transfer matrix algorithm* (TMA) and the coordinate system.

It is therefore sufficient to calculate the two particular cases.

After the introduction of the normalization factors (equation 3.4) and $2\pi$-integration around the azimuthal angle, the emission rates to a region of space in medium $m$ for a parallel and perpendicular dipole can be calculated by the following integrals:

$$\Gamma_{m,\parallel} = \frac{3\ \mathrm{k}_0}{4\, n_R} \int_0^{\mathrm{k}_{max}} \frac{\mathrm{k}_\rho}{\sqrt{\mathrm{k}_m - \mathrm{k}_\rho}} \left(|E_x(\mathrm{k}_\rho)|^2 + |E_y(\mathrm{k}_\rho)|^2\right) \mathrm{dk}_\rho$$

$$\Gamma_{m,\perp} = \frac{3\ \mathrm{k}_0}{2\, n_R} \int_0^{\mathrm{k}_{max}} \frac{\mathrm{k}_\rho}{\sqrt{\mathrm{k}_m - \mathrm{k}_\rho}} |E_z(\mathrm{k}_\rho)|^2 \mathrm{dk}_\rho \tag{3.6}$$

where $\mathrm{k}_0$ ($= 2\pi/\lambda$) and $\mathrm{k}_m$ ($= n_m\ \mathrm{k}_0$) are the wave vectors of the emitted radiation in vacuum and in medium $m$, respectively. $n_R$ is the refractive index of the reference medium; i.e. the rates are normalized to the total emission of a dipole in a medium of refractive index $n_R$. $E_i(\mathrm{k}_\rho)$ are expressions for the Cartesian components of the electric field at the dipole position as a function of $\mathrm{k}_\rho$. They are obtained via the TMA for plane waves incident from medium $m$ and depend on the thicknesses and dielectric constants of the layers and the wavelength of the emitted radiation.

The integration limits define the region of space of interest. To compute the far-field emission to a complete semi-space, the integration should be accomplished between zero and the wavevector of the emitted radiation in medium $m$ ($\mathrm{k}_{max} = \mathrm{k}_m$). Further integration between $\mathrm{k}_m$ and infinity accounts for the contribution of high wavevector, evanescent components of the dipole field, which can eventually propagate as waveguide modes in some of the layers but do not contribute to the detectable

far field emission. Taking into account that $\mathrm{k}_\rho = \mathrm{k}_m \sin\theta_m$, it is possible to calculate the emission rate in a given angular range by integrating between the appropriate limits of $\mathrm{k}_\rho$. To calculate the theoretical fluorescence signal, the radiation emitted into the collection solid angle of the microscope objective needs to be computed.

### 3.2.2 Total electromagnetic decay rate

The normalized total electromagnetic decay rate for a dipole with dipole moment $\boldsymbol{\mu}$, located in a reference medium of dielectric constant $\epsilon_R$ and in front of a plane layered system, can be calculated by application of Poynting's Theorem as follows [30, 34]:

$$\Gamma^{em}_{total} = 1 + \frac{6\pi\epsilon_0\epsilon_R}{\mu^2\ \mathrm{k}_R^3}\ \mathrm{Im}[\mathbf{E}_{br}\cdot\boldsymbol{\mu}^*] \tag{3.7}$$

where $\epsilon_0$ is the permittivity of vacuum, $\epsilon_R$ is the dielectric constant of reference medium, and $\mathbf{k}_R$ is the wavevector of the emitted radiation in the reference medium. $\mathbf{E}_{br}$ is the *back-reacted* electric field, which is defined as the difference, at the dipole position, between the field in the presence of the interface and the field in the free dielectric reference medium. A detailed description of the calculation of $\mathbf{E}_{br}$ can be found in [34, 35].

In the case of a plane interface, due to symmetry reasons, the parallel (to the interface) component of the back reacted field generated by a perpendicular dipole vanishes, and viceversa. Therefore, the total back-reacted field generated by a dipole of arbitrary orientation can be written as a composition of the back-reacted fields generated by the parallel and perpendicular components of the dipole ($E_{br\parallel}$ and $E_{br\perp}$ respectively):

$$\mathbf{E}_{br} = \begin{bmatrix} E_{br\parallel}\sin\phi\cos\beta \\ E_{br\parallel}\sin\phi\sin\beta \\ E_{br\perp}\cos\phi \end{bmatrix} \tag{3.8}$$

where $\phi$ and $\beta$ are the azimuth and polar angles that define an arbitrary direction for the transition dipole as shown in figure 3.1. Then, the product $\mathbf{E}_{br}\cdot\boldsymbol{\mu}^*$ for a dipole with arbitrary orientation writes:

$$\begin{aligned}\mathbf{E}_{br}\cdot\boldsymbol{\mu}^* &= \begin{bmatrix} E_{br\parallel}\sin\phi\cos\beta \\ E_{br\parallel}\sin\phi\sin\beta \\ E_{br\perp}\cos\phi \end{bmatrix}\cdot\mu^*\begin{bmatrix} \sin\phi\cos\beta \\ \sin\phi\sin\beta \\ \cos\phi \end{bmatrix} \\ &= \mu^*\ (\sin^2(\phi)\ E_{br\parallel}\ +\ \cos^2(\phi)\ E_{br\perp})\end{aligned} \tag{3.9}$$

The back reacted fields generated by a parallel and a perpendicular dipole can

be calculated by the following integrals [34]:

$$E_{br\parallel} = \frac{i\,\mu}{4\pi\epsilon_0\epsilon_R} \int_0^\infty \left[ -\frac{\mathrm{k}_\rho\ \mathrm{k}_{R,z}\ r_P(\mathrm{k}_\rho)}{2} \ +\ \frac{\mathrm{k}_\rho\ \mathrm{k}_R^2\ r_S(\mathrm{k}_\rho)}{2\ \mathrm{k}_{R,z}} \right] \mathrm{dk}_\rho$$

$$E_{br\perp} = \frac{i\,\mu}{4\pi\epsilon_0\epsilon_R} \int_0^\infty \frac{(\mathrm{k}_\rho)^3}{\mathrm{k}_{R,z}}\ r_P(\mathrm{k}_\rho)\ \mathrm{dk}_\rho \tag{3.10}$$

where $\mathbf{k}_R$ is the wave vector of the emitted radiation in the reference medium, and $\mathrm{k}_{R,z}$ its projection on the **z**-direction. $r_P$ and $r_S$ are the reflectivity coefficients of the layered system (from the reference medium), for a p- and s-polarized plane wave, respectively. They are functions of $\mathrm{k}_\rho$ and can be calculated with the TMA. Then, the term in brackets in equation 3.7 does not depend on $\mu$, and the normalized total electromagnetic decay rates for the parallel and perpendicular dipoles can be calculated as:

$$\Gamma^{em}_{total,\parallel} = \ 1 + \frac{3}{2\ \mathrm{k}_R^3}\ \mathrm{Im}\left[ i \int_0^\infty \left[ -\frac{\mathrm{k}_\rho\ \mathrm{k}_{R,z}\ r_P(\mathrm{k}_\rho)}{2} \ +\ \frac{\mathrm{k}_\rho\ \mathrm{k}_R^2\ r_S(\mathrm{k}_\rho)}{2\ \mathrm{k}_{R,z}} \right] \mathrm{dk}_\rho \right]$$

$$\Gamma^{em}_{total,\perp} = \ 1 + \frac{3}{2\ \mathrm{k}_R^3}\ \mathrm{Im}\left[ i \int_0^\infty \frac{(\mathrm{k}_\rho)^3}{\mathrm{k}_{R,z}}\ r_P(\mathrm{k}_\rho)\ \mathrm{dk}_\rho \right] \tag{3.11}$$

Finally, from equations 3.7 and 3.9, the total electromagnetic decay rate of a molecule with and arbitrary out-of-plane orientation $\phi$ is calculated as:

$$\Gamma^{em}_{total}(\phi) = \sin^2(\phi)\ \Gamma^{em}_{total,\parallel} \ +\ \cos^2(\phi)\ \Gamma^{em}_{total,\perp} \tag{3.12}$$

### The case of a dipole on the inner side of the first interface

So far, the total electromagnetic decay rate was calculated for a dipole in front of the layered system. It is simple to extend this result to the case of a dipole infinitely close to the interface from the inner side of the first layer. Due to the fact that the materials are non-magnetic, the only change to the Poynting computation of the power flux arises from the discontinuity of the perpendicular component of the electric field. Then, $\Gamma^{em}_{total,\parallel}$ takes the same value on both sides of the interface and $\Gamma^{em}_{total,\perp}$ needs to be scaled by a factor $(\epsilon_R/\epsilon_1)^2$, where $\epsilon_1$ is the dielectric constant of the first layer.

### 3.2.3 Non-radiative electromagnetic de-excitation rate

The non-radiative electromagnetic decay rate $\Gamma_{nr}^{em}$ can be calculated as the difference of the total electromagnetic de-excitation rate $\Gamma_{total}^{em}$ and the total radiative decay rates to the complete space. According to figure 3.2:

$$\Gamma_{nr}^{em}(\phi) = \Gamma_{total}^{em}(\phi) - \Gamma_0(\phi) - \Gamma_N(\phi) \tag{3.13}$$

where $\Gamma_0$ and $\Gamma_N$ are the radiative decay rates to the semi-spaces above and below the thin layered system.

### 3.2.4 Detectable fraction of the de-excitation rate

The detectable fraction of the de-excitation rate is the fraction corresponding to radiation emitted into the collection solid angle of the objective. For an ideal fluorophore with a $\Gamma_{nr}^{i} = 0$ and a transition dipole with an out-of-plane orientation according to $\phi$, this fraction writes:

$$\Gamma_{det}(\phi) = \frac{\Gamma_{obj}(\phi)}{\Gamma_{total}^{em}(\phi)} = \frac{\sin^2(\phi)\,\Gamma_{obj,\parallel} + \cos^2(\phi)\,\Gamma_{obj,\perp}}{\sin^2(\phi)\,\Gamma_{total,\parallel}^{em} + \cos^2(\phi)\,\Gamma_{total,\perp}^{em}} \tag{3.14}$$

$\Gamma_{obj}$ is the radiative de-excitation rate emitted into the collection solid angle of the microscope objective calculated by the integrals 3.6 between the appropriate limits. $\Gamma_{total}^{em}$ is the total de-excitation rate calculated by equations 3.11. Both $\Gamma_{obj}$ and $\Gamma_{total}^{em}$ are normalized to the total emission of a dipole in the same reference medium.

#### Modifications for the case of a fluorophore with $\Gamma_{nr}^{i} \neq 0$

The intrinsic quantum efficiency $QE$ of a fluorophore in a given medium is defined as a function of its intrinsic radiative and non radiative de-excitation rates in that medium:

$$QE = \frac{\Gamma_r^i}{\Gamma_r^i + \Gamma_{nr}^i} \tag{3.15}$$

So far, an ideal fluorophore with $\Gamma_{nr}^{i} = 0$, or equivalently with $QE = 1$, was considered. If a fluorophore has $\Gamma_{nr}^{i} \neq 0$, its quantum efficiency is smaller than 1, and the amount of radiation emitted in a time unit is reduced.

$\Gamma_{det}$ is composed of rates which are normalized to the total emission of a free dipole in a reference medium ($\Gamma_r^i$). Therefore, in order to account for a $QE < 1$, an intrinsic non-radiative decay rate, normalized as well to the total radiative de-excitation rate, needs to be added to $\Gamma_{total}^{em}$ in the denominator of $\Gamma_{det}$ (as shown in

equation 3.2). It is easy to express this intrinsic normalized non-radiative decay rate $\overline{\Gamma^i_{nr}}$ as a function of the QE:

$$\overline{\Gamma^i_{nr}} = \frac{\Gamma^i_{nr}}{\Gamma^i_r} = \frac{1-QE}{QE} \tag{3.16}$$

$\overline{\Gamma^i_{nr}}$ is a function exclusively of $QE$ and is therefore not expected to depend on external parameters such as the properties of the layered system or the position and orientation of the fluorophore with respect to the interfaces. Then, the detectable fraction of the emitted radiation for an arbitrarily oriented fluorophore with $\Gamma^i_{nr} \neq 0$ writes:

$$\Gamma_{det}(\phi) = \frac{\Gamma_{obj}(\phi)}{\Gamma^{em}_{total}(\phi) + \overline{\Gamma^i_{nr}}} = \frac{\sin^2(\phi)\,\Gamma_{obj,\parallel} + \cos^2(\phi)\,\Gamma_{obj,\perp}}{\sin^2(\phi)\,\Gamma^{em}_{total,\parallel} + \cos^2(\phi)\,\Gamma^{em}_{total,\perp} + \frac{1-QE}{QE}} \tag{3.17}$$

## 3.3 The excitation

Far from saturation, the excitation rate of a fluorophore positioned at $\mathbf{r}$ and with a transition dipole moment $\boldsymbol{\mu}$, is proportional to the square modulus of the projection of the electric field at that position $\mathbf{E}(\mathbf{r})$ along the dipole direction:

$$\Gamma_{exc}(\mathbf{r}) \propto |\boldsymbol{\mu} \cdot \mathbf{E}(\mathbf{r})|^2 \tag{3.18}$$

As a consequence, in scanning confocal optical microscopy (SCOM), the spatial distribution of the fluorescence signal of a single molecule reflects the spatial distribution of the electric field intensity along the direction of the molecule transition dipole. In the experimental conditions, this electric field is produced by the excitation light when it is focused by the microscope objective through the layered system of the samples. In this section, a theoretical method to calculate this field is presented.

### 3.3.1 Electric field distribution near a geometric focus in a layered system

The time independent part of the electric field $\mathbf{E}$ in a point $\mathbf{r}$ near the geometric focus of an aplanatic optical system, such as the microscope objective, can be calculated by adding the contributions of an angular distribution of electromagnetic

plane waves traveling to the focus as [36]:

$$\mathbf{E}(\mathbf{r}) = C \iint_{\Omega} f\, \mathbf{E}_0 e^{i\mathbf{k}\cdot\mathbf{r}} \mathrm{d}\Omega \tag{3.19}$$

where $C$ is a constant, $\mathbf{E}_0$ is the complex amplitude of the plane waves at an origin (normally the Gaussian focal point) from which the position of the point of interest $\mathbf{r}$ is measured, $\mathbf{k}$ is the wavevector of the radiation, and $\Omega$ is the solid angle defining the angular distribution of plane waves. $f$ is a scalar function called *strength function*, it depends on the properties of the focusing system and accounts for the different intensities of rays focused in different directions. Equation 3.19 is valid for an aberration free optical system and under geometric optics approximation; i.e. the distance between the exit pupil plane and the image region ($d_f$ in figure 3.3), and the linear dimensions of the exit pupil (front lens of the microscope objective), are assumed to be large in comparison to the wavelength. This approach was first proposed by Richards and Wolf [36, 37] and used by a number of authors to tailor the focus geometry [38] or to determine the three-dimensional orientation of single molecules [39, 40]. Those works considered the focus of light to occur through an homogeneous medium or in the presence of a single interface. In contrast, in the model presented here, the focusing of light occurs through a layered system. The mentioned approach needs therefore to be generalized to consider the focusing of a plane wave front through a multilayer system.

The next paragraphs are dedicated to the calculation of the electric field at the Gaussian focus $\mathbf{E}_0$, the product $\mathbf{k}\cdot\mathbf{r}$, and the introduction of the strength function $f$, in order to write the integral 3.19 for the focusing of light through a layered system. Figure 3.3 shows the geometry of the problem and introduces some of the variables and the coordinates used in the following calculations.

A monochromatic, linearly polarized plane-wave front is considered as the source field $\mathbf{E}_{src}$ which is focused through a layered system with a microscope objective. In order to account for the amplitude of the plane waves at the focus ($\mathbf{E}_0$), it is first necessary to find an expression for the electric field generated by a focused wave in any point of the layered system. A Cartesian coordinate system is considered with the **x**-axis along the polarization direction of $\mathbf{E}_{src}$ and the **z**-axis along the optical axis, as shown in figure 3.3.a. For simplicity, a source field with unitary intensity is considered: $\mathbf{E}_{src} = (1; 0; 0)$.

Plane waves that are focused by a certain point of the rear lens of the objective, strike the layered system with a given incidence angle and defined p- and s-polarized components (see figure 3.3). The radial position of the focusing point $R$ defines the incidence angle $\theta$ of the focused wave as explained in section 2.2.1. The angular position of the focusing point $\psi$ defines the p- and s-polarized components of the focused wave.

The local electric field in any point of the layered system, produced by a plane

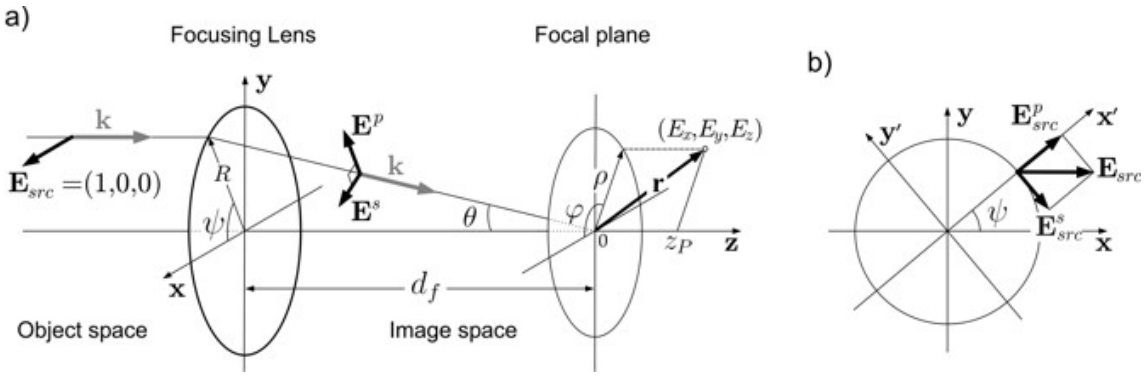


**Figure 3.3:** Electric field near a geometric focus. a) Geometry of the problem of the calculation of the electric field near a geometric focus. The source field ($\mathbf{E}_{src}$) is a linearly polarized, monochromatic plane wave front (k = $2\pi/\lambda$). A Cartesian coordinate system is taken such that the source field lies along the **x** axis, and the optical axis along the **z** direction. Focusing is accomplished by an aplanatic system. Rays focused at different radial positions $R$ of the focusing lens are focused with a different angle $\theta$. b) Rays focused at different angular positions of the lens ($\psi$) are focused with different p- and s- polarized components ($\mathbf{E}^p_{src}$ and $\mathbf{E}^s_{src}$ respectively).

wave incident with angle $\theta$ with respect to **z** and with given p- and s-components of its electric field, can be calculated with the *transfer matrix algorithm* (TMA, see section 3.2). The TMA calculates the fields in a primed coordinate system rotated around the **z**-axis in order to place the **y'**-axis along the s-polarized component, as shown in figure 3.3.b (and 3.2). In this rotated coordinate system, the p- and s-polarized components of the source field are:

$$E^p_{src} = \cos\psi \qquad\qquad E^s_{src} = -\sin\psi \tag{3.20}$$

It is convenient first to use the TMA to obtain expressions for the electric field components at the point of interest generated by an incident plane wave with both p- and s-components of unitary intensity. Let those field components in the rotated coordinate system be $E^p_{z'}$, $E^p_{x'}$, and $E^s_{y'}$. For a given wavelength, the expressions of these normalized field components are a function exclusively of the layered system properties (thickness $d_i$ and dielectric constant $\epsilon_i$ of each layer, and the z-position in the layered system $z_{ls}$) and the angle of incidence $\theta$:

$$\begin{aligned} E^p_{x'} &= E^p_{x'}(\theta, d_i, \epsilon_i, z_{ls}) \\ E^s_{y'} &= E^s_{y'}(\theta, d_i, \epsilon_i, z_{ls}) \\ E^p_{z'} &= E^p_{z'}(\theta, d_i, \epsilon_i, z_{ls}) \end{aligned} \tag{3.21}$$

A wave of $\mathbf{E}_{src}$ focused by a given point of the rear lens at an angular position defined by $\psi$, has a p- and an s-polarized components given by equations 3.20. Then, to obtain the components of the electric field at the point of interest generated by

a such a wave, it is necessary to multiply the normalized expressions 3.21 by the corresponding p- or s-component of the source wave:

$$\mathbf{E}'_0 = \begin{bmatrix} E_{0\,x'} \\ E_{0\,y'} \\ E_{0\,z'} \end{bmatrix} = \begin{bmatrix} E^p_{x'}(\theta, d_i, \epsilon_i, z_{ls}) E^p_{src} \\ -E^s_{y'}(\theta, d_i, \epsilon_i, z_{ls}) E^s_{src} \\ E^p_{z'}(\theta, d_i, \epsilon_i, z_{ls}) E^p_{src} \end{bmatrix} = \begin{bmatrix} E^p_{x'}(\theta, d_i, \epsilon_i, z_{ls}) \cos\psi \\ -E^s_{y'}(\theta, d_i, \epsilon_i, z_{ls}) \sin\psi \\ E^p_{z'}(\theta, d_i, \epsilon_i, z_{ls}) \cos\psi \end{bmatrix} \tag{3.22}$$

This is the electric field, written in the primed coordinates system, generated at the point of interest of the layered system by a source plane wave focused by a point of the rear lens of the objective defined by $\psi$ and $\theta$[3]. Thus, in order to obtain $\mathbf{E}_0$, $\mathbf{E}_{0'}$ has to be rotated to the original **xyz** coordinates system:

$$\mathbf{E}_0 = \mathbf{E}_{0'} \begin{bmatrix} \cos\psi & \sin\psi & 0 \\ -\sin\psi & \cos\psi & 0 \\ 0 & 0 & 1 \end{bmatrix} = \begin{bmatrix} E_{0\,x'}\cos\psi - E_{0\,y'}\sin\psi \\ E_{0\,x'}\sin\psi + E_{0\,y'}\cos\psi \\ E_{0\,z'} \end{bmatrix} \tag{3.23}$$

Finally, the x-, y-, and z-components of $\mathbf{E}_0$ can be written as a function of $\theta$ and $\psi$ as:

$$\begin{aligned} E_{0\,x} &= E^p_{x'}(\theta)\cos^2\psi + E^s_{y'}(\theta)\sin^2\psi \\ E_{0\,y} &= \left[E^p_{x'}(\theta) - E^s_{y'}(\theta)\right]\cos\psi\sin\psi \\ E_{0\,z} &= E^p_{z'}(\theta)\cos\psi \end{aligned} \tag{3.24}$$

where the dependencies on $d_i$, $\epsilon_i$ and $z_{ls}$ were not explicitly written.

Next, to calculate the integral 3.19 in an arbitrary point near the geometric focus, an expression for $\mathbf{k}\cdot\mathbf{r}$ is necessary. According to figure 3.3, one can write:

$$\mathbf{r} = \begin{pmatrix} \rho\cos\varphi \\ \rho\sin\varphi \\ z_P \end{pmatrix} \qquad \mathbf{k} = \mathrm{k}\begin{pmatrix} \cos\psi\sin\theta \\ \sin\psi\sin\theta \\ \cos\theta \end{pmatrix} \tag{3.25}$$

and the scalar product leads to:

$$\mathbf{k}\cdot\mathbf{r} = \mathrm{k}(\rho\sin\theta(\cos(\psi-\varphi)) + z_P\cos\theta) \tag{3.26}$$

The microscope objective is an aplanatic system of revolution; i.e. axially stigmatic and obeying the sine condition all around the **z** axis. Hence, the plane wave front of the source field in the object space is transformed into a spherical wave front in the image space without aberrations. The *strength function* $f$ is in this case

[3] As shown in section 2.2.1, a point of the objective rear lens can be equivalently defined in polar coordinates $(R, \psi)$ or by a set $(\theta, \psi)$, because $R = \sin\theta\, R_{rl}\, n_{glass}/NA$.

found to be [37]:

$$f(\theta) = \sqrt{\cos\theta} \tag{3.27}$$

Introducing in integral 3.19 the electric field components 3.24, the path difference exponent 3.26, and the strength function 3.27:

$$E_j(\mathbf{r}) = C \int_0^{2\pi} \int_{\theta_{min}}^{\theta_{max}} \sqrt{\cos\theta}\, E_{0\,j}(\theta,\psi)\; e^{i\mathrm{k}(\rho\sin\theta(\cos(\psi-\varphi))+z_P\cos\theta)}\; \sin\theta\,\mathrm{d}\theta\,\mathrm{d}\psi \tag{3.28}$$

where $j$ stands for x, y, or z, and the solid angle $\Omega$ is integrated in spherical coordinates. The azimuth angle $\psi$ is integrated all around the **z**-axis, and the focusing angle range ($\theta_{min}$ and $\theta_{max}$) depends on parameters such as the NA of the objective, the diameter of the illumination beam and the blocking disc in annular illumination (see section 2.2.1).

The integral 3.28 permits the calculation (up to a constant) of the electric field in any point near the focus of the microscope objective, when the latter is illuminated with a linearly polarized plane wave front. The electric field distribution over a region near the focus can be calculated by performing the integration for each point **r** of the region. Nevertheless, if the illumination beam has rotational symmetry around the **z**-axis, and for points **r** in a plane parallel to the focal plane, it is only necessary to calculate one in-plane (**xy**) component of the electric field along two directions, and the **z**-component along one direction. In particular:

$$E_x(\mathbf{r}=(x,0,z_P)) = E_x(\rho,\varphi=0,z_P) \;\equiv E_x^x \tag{3.29}$$

$$E_x(\mathbf{r}=(0,y,z_P)) = E_x(\rho,\varphi=\frac{\pi}{2},z_P) \equiv E_x^y \tag{3.30}$$

$$E_z(\mathbf{r}=(x,0,z_P)) = E_z(\rho,\varphi=0,z_P) \;\equiv E_z^x \tag{3.31}$$

From these components, the total field along any radial direction, defined by $\varphi = \alpha$, in the plane of interest can be calculated. To understand this point, it is necessary to make some symmetry considerations; first for the in-plane components $E_x$ and $E_y$, and then for the $E_z$ component.

Due to the mirror symmetry of the problem with respect to the **x**-axis, any y-component of the fields along the **x**-axis vanishes. One way to see this, is to imagine that the waves focused through the positive-y semi-plane of the objective rear lens generate a non-zero y-component along the **x**-axis. Then, the plane waves focused through the negative-y semi-plane would generate a y-component, along the **x**-axis, of equal magnitude and opposite sign. Figure 3.4.a shows this effect schematically.

Due to the inversion symmetry with respect to the **y**-axis imposed by the direction of the source field, any y-component of the fields along the **y**-axis vanishes. One way to see this, is to imagine the source field generates a non-zero y-component in a

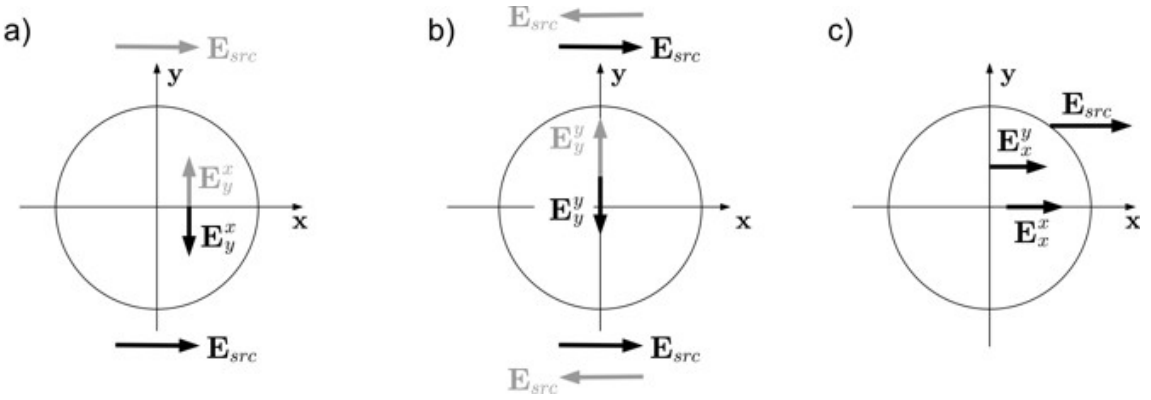


**Figure 3.4:** Symmetry considerations in the focal plane. a) Due to the mirror symmetry of the problem with respect to the **x**-axis, no y-components of the fields are generated along the **x**-axis. b) Due to the inversion symmetry with respect to the **y**-axis imposed by the source field direction, no y-components are generated along the **y**-axis. c) Then, the fields generated along the **x**- or **y**-axis, have only x in-plane component.

given point of the **y**-axis. Then, as shown in figure 3.4.b, half a period later both the source field and the generated y-component have the same amplitude and point in the opposite direction. On the other hand, it is possible to choose an **x**-axis pointing in the opposite direction. This would invert the direction of the source field but not the generated y-component. Then, there are two valid solutions for the generated y-component produced by the same source field but pointing in opposite directions. Therefore, the y-component of the electric field along the **y**-axis needs to be null.

As a consequence, a source field polarized along the **x**-axis generates in-plane ($z = z_P$) fields along the **x**- and **y**-axis that only have x-components, as depicted in figure 3.4.c. To describe the in-plane field distribution it is then sufficient to know $E_x^x$ and $E_x^y$:

$$\begin{aligned} \mathbf{E}(\mathbf{r} = (x, 0, z_P)) &= (E_x^x, 0, E_z^x) \qquad E_y^x = 0 \\ \mathbf{E}(\mathbf{r} = (0, y, z_P)) &= (E_x^y, 0, E_z^y) \qquad E_y^y = 0 \end{aligned} \tag{3.32}$$

To obtain the field along an arbitrary in-plane direction $\alpha$ it is convenient to consider a primed coordinate system rotated an angle $\alpha$ around **z**, in order to place the direction of interest along the **x'**-axis. The source field ($\mathbf{E}_{src} = (1, 0, 0)$) can be decomposed in two components along the rotated axis as shown in figure 3.5.a:

$$\begin{aligned} \mathbf{E}_{src} &= \mathbf{E}_{src,x'} + \mathbf{E}_{src,y'} \\ E_{src,x'} &= \cos\alpha \\ E_{src,y'} &= -\sin\alpha \end{aligned} \tag{3.33}$$

Taking into account that no field components perpendicular to the source field are

generated (equations 3.32), $E_{src,x'}$ and $E_{src,y'}$ generate the fields depicted in figure 3.5.b, which can be calculated by scaling the components $E_x^x$ and $E_x^y$ (equations 3.29 and 3.30) with the corresponding components of the source field. Then, the fields generated along the **x'**-axis are:

$$\begin{aligned} E_{x'}^{x'} &= E_x^x E_{src,x'} = E_x^x \cos\alpha \\ E_{y'}^{x'} &= -E_x^y E_{src,x'} = E_x^y \sin\alpha \end{aligned} \tag{3.34}$$

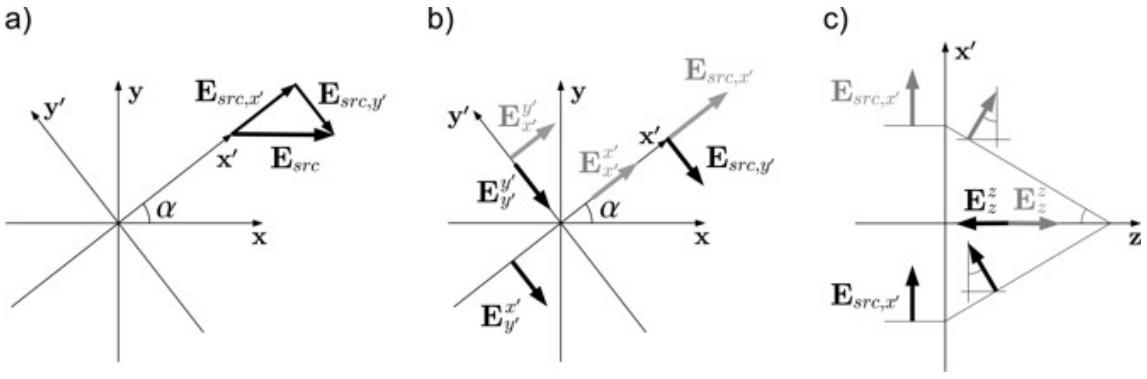


**Figure 3.5:** Electric fields along an arbitrary direction. a) In-plane fields generated by the source field in a coordinate system **x'y'** rotated $\alpha$ around **z**-axis with respect to the original coordinates system **xy**. b) Electric fields generated by the x'- and y'-components of the source field. c) Due to the inversion symmetry of the z-component of the source field with respect to the **z**-axis in any incidence plane, the field generated along the **z**-axis have zero z-component.

To write the field along the arbitrary in plane direction $\varphi = \alpha$ on the original **xy** coordinates system, the contributions of $E_{x'}^{x'}$ and $E_{y'}^{x'}$ on the **x**- and **y**-axis of the original coordinates system have to be added[4]:

$$\begin{aligned} E_x(\rho, \varphi = \alpha, z_P) &= E_{x'}^{x'} \cos\alpha + E_{y'}^{x'} \sin\alpha = E_x^x \cos^2\alpha + E_x^y \sin^2\alpha \\ E_y(\rho, \varphi = \alpha, z_P) &= E_{x'}^{x'} \sin\alpha - E_{y'}^{x'} \cos\alpha = (E_x^x - E_x^y) \sin\alpha \cos\alpha \end{aligned} \tag{3.35}$$

Next, it necessary to show that $E_z$ is zero both along the **y**- and **z**-axis. First, following the same reasoning that lead to the nullity of $E_y^x$ and $E_y^y$, it can be seen that $E_z^y$ has to be zero as well. Second, in a similar way, as depicted in figure 3.5.c, for any plane of incidence, the p-component of the source field focused through the one half of the objective lens generates a field along the z-axis opposite to the one generated by the p-component of the source field focused through the other half of the objective. Then, $E_z^z$ is zero and as a consequence, it is possible to obtain the

[4]This is basically the same projection that was done to obtain $\mathbf{E}_0$ from $\mathbf{E}_{0'}$ in equation 3.23.

projection on any other radial direction by:

$$E_z(\rho, \varphi = \alpha, z_P) = E_z^x \cos\alpha \tag{3.36}$$

Summarizing, the field in any point $(\rho, \varphi)$ of a plane parallel to the focal plane $(z = z_P)$ can be calculated by means of the x- and z-components of the electric field along the **x**-axis and the x-component along the **y**-axis ($E_x^x$, $E_z^x$ and $E_x^y$; equations 3.29, 3.31 and 3.30 respectively) by:

$$\mathbf{E}(\mathbf{r} = (\rho, \varphi, z_P)) = \begin{bmatrix} E_x(\rho, \varphi, z_P) \\ E_y(\rho, \varphi, z_P) \\ E_z(\rho, \varphi, z_P) \end{bmatrix} = \begin{bmatrix} E_x^x(\rho)\cos^2\varphi + E_x^y(\rho)\sin^2\varphi \\ (E_x^x(\rho) - E_x^y(\rho))\sin\varphi\cos\varphi \\ E_z^x(\rho)\cos\varphi \end{bmatrix} \tag{3.37}$$

In order to calculate the fluorescence excitation rate of a single molecule, it is necessary to write an expression for the projection of this electric field on the direction of the transition dipole of the molecule $\boldsymbol{\mu}$ (equation 3.18). If the orientation of $\boldsymbol{\mu}$ is defined by an azimuth angle $\phi$ and a polar angle $\beta$, as shown in figure 3.1, the projection of the excitation field on the dipole direction is:

$$\mathbf{E}(\mathbf{r}) \cdot \boldsymbol{\mu} = E_x(\mathbf{r})\sin\phi\cos\beta + E_y(\mathbf{r})\sin\phi\sin\beta + E_z(\mathbf{r})\cos\phi \tag{3.38}$$

Finally, recalling equation 3.18 the fluorescence excitation rate for a molecule positioned at $\mathbf{r}$, and with a transition dipole oriented according to $\phi$ and $\beta$ is:

$$\Gamma_{exc}(\mathbf{r}, \phi, \beta) \propto \left|E_x(\mathbf{r})\sin\phi\cos\beta + E_y(\mathbf{r})\sin\phi\sin\beta + E_z(\mathbf{r})\cos\phi\right|^2 \tag{3.39}$$

## 3.4 Single molecule fluorescence signal

At this point, it is possible to recall equation 3.1 and combine the results obtained for the excitation and the emission in order to write an expression for the theoretical fluorescence signal of a fluorophore in the outermost interface of a layered system:

$$I_{SM}^{theo}(\mathbf{r}, \phi, \beta) = \Gamma_{exc}(\mathbf{r}, \phi, \beta)\,\Gamma_{det}(\phi) \tag{3.40}$$

where $\Gamma_{exc}$ is calculated by equation 3.39 and $\Gamma_{det}$ by equation 3.17.

Because of the uncertainty in the detection efficiency ($\eta$ in equation 3.1) and that the electric field in $\Gamma_{exc}$ is calculated up to a constant, this theoretical signal is proportional to the experimental one. For a given orientation of the transition

dipole of the fluorophore, $\Gamma_{exc}$ defines the spatial distribution of the fluorescence signal intensity and $\Gamma_{det}$ scales the signals according to the detectable radiation emitted from a molecule with the given out-of-plane orientation.

## 3.5 Conclusions

A method to model the fluorescence signal of single molecules was set up by considering the chromophores as oscillating dipoles interacting classically with the electromagnetic field, placed at the outer interface of a layered system and with arbitrary orientations.

The method is of general applicability to any non-magnetic plane layered system and considers the excitation and the emission separately. Calculations performed with this model can be useful to design and compare experimental configurations (i.e. different illumination modes, materials and thicknesses of the layered system and detection schemes) and to determine the three-dimensional orientation of single chromophores under different conditions.

# Chapter 4

# Excitation and detection of single molecule fluorescence through a thin gold film

In this chapter, it is demonstrated that fluorescence of single molecules in the nanometric vicinity of a thin gold film can be detected and studied through the gold film with an epi-illumination scanning confocal microscope. The influence of the separation distance to the gold film is experimentally studied, as well as different illumination modes to discriminate the contributions of transmitted and forbidden[1] light for excitation. The theoretical model presented in chapter 3 is applied for the calculation of theoretical single molecule fluorescence signals in the experimental conditions. Theoretical and experimental signals are compared in order to interpret the observations.

## 4.1 Introduction

A number of processes of great technological and scientific importance involve a fluorophore working near a metallic layer. Among the most important certainly are sensitized solar cells, organic light emitting diodes and a variety of sensors.

The problem of spontaneous emission near a conducting surface has been already studied, both experimentally and theoretically, for several decades. The first theoretical approach to the problem was reported by Sommerfeld in 1909 [26], and after the pioneering experiments by Drexhage et al. [41–43], a considerable number of experimental and theoretical investigations were dedicated to study the influence of a nearby metallic layer on the fluorescence emission [27, 29, 44–47].

More recently, room-temperature optical spectroscopy of single fluorescent molecules

[1] By forbidden light it is meant light incident at angles higher than the angle of total internal reflection.

became possible [48,49], and since then, an increasing number of scientific questions are being addressed on a single molecule level. Surprisingly, only one experimental work was reported of single molecule fluorescence near a metal surface. Yokota et al. imaged single fluorescently labelled proteins with a surface plasmon fluorescence microscopy set-up in 1998 [50]. In those experiments, excitation was accomplished by the surface plasmon field at the metal/solution interface via a Kretschmann prism coupling configuration, and fluorescence collection was done with a high numerical aperture objective from the other side of the sample. The same geometry was later modelled by Enderlein [51].

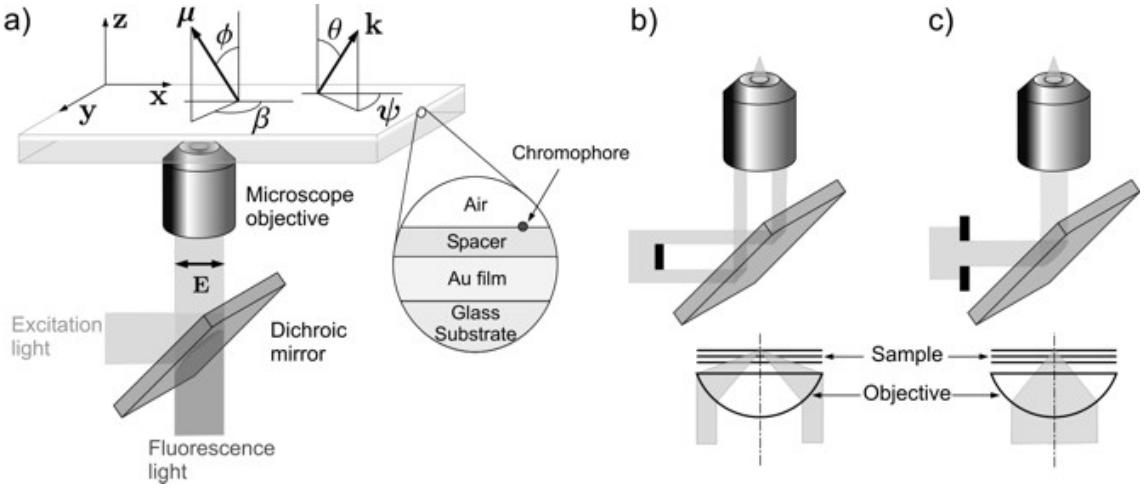


**Figure 4.1:** Experimental configuration. a) The Cartesian coordinate system adopted takes the polarization direction of the illumination beam as reference for the **x**-axis and the **z**-axis is perpendicular to the interfaces. The orientation of the transition dipoles of the chromophores ($\boldsymbol{\mu}$) is defined by $\boldsymbol{\phi}$ and $\boldsymbol{\beta}$. The direction of emitted or incident radiation (of wavevector **k**) is defined by $\boldsymbol{\theta}$ and $\boldsymbol{\psi}$. b) High angle of incidence illumination (forbidden light, FL). c) Low angle of incidence illumination (transmitted light, TL).

The experimental scheme presented here differs from the one of Yokota et al. A sample scanning confocal microscope was used in an episcopic illumination (epi-illumination) arrangement from the gold side (see figure 4.1.a). The fluorescence of single molecules is excited and detected from the same side of the sample, through the gold film. In comparison to the experimental scheme of Yokota et al., this scheme presents two important advantages. First, the sample is not constantly illuminated because the confocal scanning technique allows to excite and detect fluorescence on one (diffraction limited) spot of the sample at a time. This considerably reduces irreversible photo-bleaching of the samples, which is of major importance in single molecule experiments. Second, the chromophores side of the sample remains free, therefore allowing the application of a complementary technique. At this point, it is worth remarking that due to its metallic properties in the visible range, its chemical stability, and the possibility of obtaining atomically flat terraces, gold has

became one of the most widely used substrates for a number of techniques, such as scanning tunnelling microscopy (STM, [52]), atomic force microscopy (AFM, [53]) and electrochemistry (EC, [54]).

In this chapter, experimental and theoretical investigations are combined to address the following questions. Is it at all possible to detect the fluorescence of single molecules through a thin metallic film? If that is the case, how close to the gold film can the molecules be before their emission becomes undetectable? How does this experimental scheme compare to the detection from the air side and to the case without the gold film?

## 4.2 Experimental

The sample geometry is depicted in figure 4.1 together with the illumination modes employed in the experiments. In this section, details about the sample preparation and the measurement procedures are given.

### 4.2.1 Sample preparation

The sample preparation consists of five steps: cleaning of the glass substrates, deposition of the gold film, functionalization of the gold surface, layer by layer deposition of the polyelectrolyte spacer, and finally deposition of the fluorescent dye-molecules.

Thin ($0.13 - 0.16$ mm) glass coverslips (*N° 1, Menzel-Gläser*) were cleaned successively with Hellmanex 2%, Milli-Q water and ethanol ($\geq 98\%$, *Riedel - de Haën*). In addition, to remove any rest of organic material, the coverslips were heated in air for two hours at 500 °C. Next, a 44 nm gold (*Agar Scientific Ltd.*) film was thermally evaporated onto the substrates (thermal evaporator: *Edwards FL400*). The freshly prepared gold surfaces were functionalized with a self-assembled monolayer (SAM) of 3-mercaptopropionic acid (MPA, *Aldrich*) as the substrates were immersed in a 0.03 M Milli-Q water solution of MPA for one hour. After that, the substrates were thoroughly rinsed with Milli-Q water in order to remove all unbound MPA. The so prepared surfaces contain free carboxylic groups, which hydrolyze in water to render the surface negatively charged. The next step is the layer by layer deposition of the polyelectrolyte spacer which was accomplished based on the procedure published by Decher [55]. Successive polyelectrolyte layers of positively charged poly(allylamine hydrochloride) (PAH; MW 70 000, *Aldrich*), and negatively charged poly(styrene sulfonate) (PSS; MW 70000, *Aldrich*) were deposited onto the functionalized gold. Both polyelectrolytes were deposited from 0.02 monomol/l water solutions. Salts were added to the solutions to adjust the ionic strength; $MnCl_2$ (99%, *Merck*) 0.5 M was used for the PSS solution and NaBr (99+%, *Aldrich*) 2 M for the PAH [56].

The acidity of both polyelectrolyte solutions was adjusted to pH=2 by adding HCl. To perform the deposition, the samples were alternatively immersed in the polyelectrolyte solutions for 20 minutes, starting with PAH. In between immersions, the samples were thoroughly rinsed with water and dried with nitrogen. Samples with 1, 2, 3 and 4 PAH-PSS bilayers were prepared, corresponding to spacer thicknesses of 4.5, 10, 15, 24 nm, respectively, as determined in earlier studies [46, 57]. Before use, both polyelectrolytes were purified in order to minimize the fluorescence background. PAH was purified by dialysis with a membrane tube with a cut-off molecular weight of 3500 (*Spectra/por-6, Spectrum Laboratories Inc.*). The dialysis was conducted for six days as the water was exchanged twice a day. PSS was purified by a controlled precipitation method. The polymer was dissolved in water and then the solution was transferred slowly (drop by drop) into ethanol ($\geq 98\%$, *Riedel - de Haën*) close to its freezing temperature (-50 to -60 °C). The precipitated polymer was then filtered and dried in vacuum. After this treatment the fluorescence background was reduced considerably and reached a level low enough to allow for single molecule measurements. Namely, a typical sample with four PAH-PSS bilayers presented between none and two diffraction limited impurities with fluorescence signals comparable to the one of a single dye-molecule within an area of $10 \times 10\,\mu\text{m}^2$.

Single fluorescent dye-molecules 1,1',3,3,3',3'-hexamethylindicarbocyanine iodide [DiIC1(5), *Molecular probes*, maximum excitation at $\lambda_{exc} = 638$ nm, maximum emission at $\lambda_{em} = 670$ nm] were deposited electrostatically on a negatively charged surface terminated with PSS, by immersing the samples for one minute in a $10^{-10}$ M, Milli-Q water solution of the dye. Then, the samples were rinsed with Milli-Q water and dried with a stream of nitrogen.

### 4.2.2 Measurement

The samples were studied in the SCOM set-up described in chapter 2. Fluorescence of single molecules was excited and detected through the gold film with an epi-illumination scheme as shown in figure 4.1.a. He-Ne laser light, with a wavelength $\lambda = 633$ nm, was used for excitation. The illumination beam was linearly polarized and the intensities used ranged from 3 to 12 kW/cm$^2$ [2]. Suitable dichroic mirror, Notch and long-pass filters were used to separate fluorescence from reflected excitation light. Fluorescence micrographs were recorded by scanning the samples with three different modes of illumination, as depicted in figure 4.1. First, images were acquired under full beam (FB) illumination. Second, by using a blocking disc, images were acquired under annular illumination, corresponding to large angles of incidence; in the following, this scheme is called forbidden light (FL) illumination.

[2] These intensity values are not the actual intensities at the focus. They are calculated simply by dividing the full beam intensity by the area of the focal spot ($A$) given by the theoretical diffraction limit: $A = \pi R^2; R = 0.61\ \lambda/NA$). Therefore, they would only represent the actual intensity at the focus of a transparent non-absorbing sample.

Finally, images were also recorded by illuminating with a reduced beam diameter, corresponding to small angles of incidence; in the following, this scheme is called transmitted light (TL) illumination.

The range of angles of incidence corresponding to each illumination mode depends on the numerical aperture of the microscope objective (NA= 1.4), the refractive index of the focusing medium ($n_{glass} = 1.503$), and on the beam and blocking disc diameter, as explained in section 2.2.1. For FB and FL illumination modes, the beam diameter was adjusted to completely illuminate the rear lens of the objective, which has a diameter of 8.9 mm. In the case of TL illumination, the beam diameter was reduced to 5 mm. The blocking disc used in the FL illumination mode had a diameter of 5 mm. Then, the ranges of angles of incidence $\theta$ corresponding to each illumination mode are:

- Full beam (FB) illumination: $0° < \theta < 68.6°$
- Forbidden light (FL) illumination: $31.6° < \theta < 68.6°$
- Transmitted light (TL) illumination: $0° < \theta < 31.6°$

As their name indicate, the aim of the different modes of illumination is to discriminate the contributions of transmitted and forbidden light for the excitation of the dye-molecules. Figure 4.2 aids to explain this point. The curves are the theoretical reflectivity coefficient of the sample system, with a spacer thickness of 0 nm (bare gold) and 24 nm (4 PAH-PSS bilayers), for a $\lambda = 633$ nm, p-polarized plane wave, as a function of the angle of incidence from the glass side[3]. Below the $\theta$-axis, the angular ranges corresponding to the different modes of illumination are indicated.

For low incidence angles the reflectivity of the samples is relatively high because the gold film acts as a good mirror. Above the critical angle of total internal reflection of the glass substrates, $\theta_c = 41.7°$, the reflectivity increases even more and approaches unity; it does not reach unity due to losses produced by the evanescent field at the glass/gold interface in the absorbing gold. Then, the names chosen for the illumination modes are justified. The TL illumination mode corresponds to angles of incidence below $\theta_c$, and the FL illumination mode corresponds to angles of incidence mainly above $\theta_c$.

At even higher angles of incidence, the component parallel to the interfaces of the wavevector of the incident radiation increases and eventually matches the resonance condition to couple to surface plasmons [58]. This resonant coupling to surface plasmons (surface plasmon resonance, SPR) translates in a minimum in the reflectivity, and has associated an enhanced evanescent electric field at the metal/spacer interface that decays exponentially into the dielectric medium. For the bare gold sample the SPR occurs at an incidence angle of 44.1°, and for a sample with a 4-bilayer spacer (24 nm) at 48.3°. Then, by comparing these angles to the ranges of incidence

[3]The curves were calculated by solving Maxwell equations for the layered system with a *transfer matrix algorithm* (see section 3.2). The dielectric constants of the materials for a wavelength of 633 nm are listed in table 4.1.

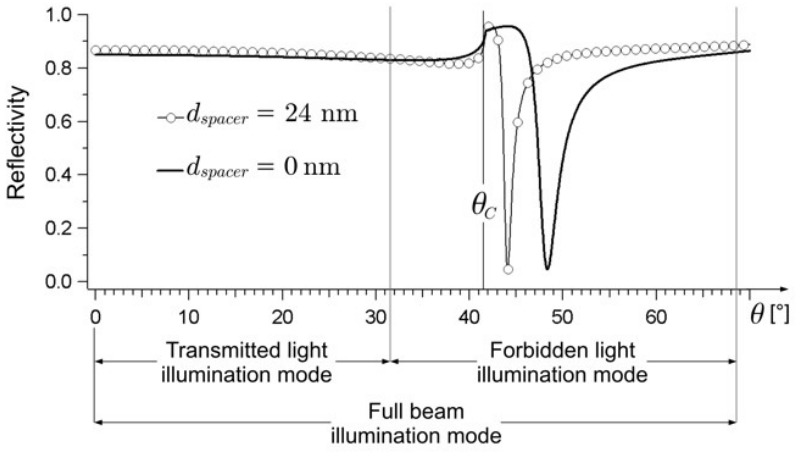


**Figure 4.2:** Reflectivity of the sample system. P-polarization reflectivity coefficient of the samples with spacer thicknesses of 0 (bare gold) and 24 nm, as a function of the angle of incidence from the glass side. The critical angle of total internal reflection (41.7°) is marked as $\theta_c$. The minima in reflectivity corresponds to the excitation of the surface plasmon resonance [58].

angle of each illumination mode, it is seen that the full beam (FB) and the forbidden light (FL) illumination modes can excite the SPR. The TL illumination mode cannot.

## 4.3 Single molecule fluorescence images through a thin gold film

In this section, it is demonstrated experimentally that it is indeed possible to excite and detect fluorescence of single molecules through the gold film and three aspects of the present configuration are investigated. First, the characteristics of the fluorescence images obtained. Second, images are acquired with different illumination modes in order to find out what are the most effective pathways for the propagation of light imposed by the layered sample. Third, samples with different thicknesses of the polyelectrolyte spacer are studied in order to establish the minimum separation distance between the dye-molecules and the gold film, before the fluorescence becomes undetectable.

### 4.3.1 Full beam images

The experiments presented here show that single molecule fluorescence can in fact be excited and detected through the gold film. Figure 4.3 shows a typical full beam illumination image of single fluorescent dye-molecules on a sample with a 4-bilayer spacer (24 nm thickness).

The great majority of the detected fluorescence signals have the same characteristic spatial distribution, which is clearly different from the typical diffraction limited spot that would be observed in the absence of the gold film (figure 4.4.a). Similar patterns were already observed in single molecule fluorescence images obtained with annular [39, 40] (figure 4.4.b) and radially polarized illumination [59]. They are due to the fact that the chromophores have a fixed transition dipole, and therefore, their fluorescence images reflect the spatial distribution of the electric field intensity along the dipole direction (see section 3.3). If the chromophores are randomly oriented, and the electric field has similar intensity in all directions, but different spatial distribution, a variety of patterns is observed (see figure 4.4.b) that provide information about the three-dimensional orientation of the transition dipole of the molecules.

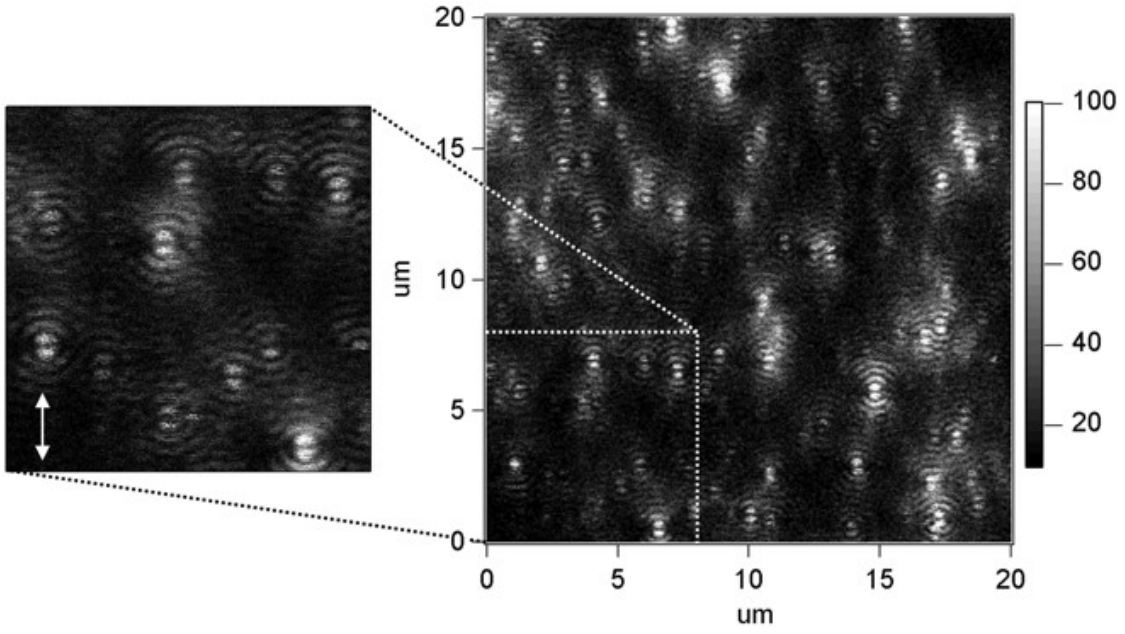


**Figure 4.3:** Full beam illumination images. Typical fluorescence micrograph of single dye-molecules separated by a 24 nm spacer from the 44 nm gold film obtained with FB illumination. Intensity: 3.2 kW/cm$^2$, scanned area: $20 \times 20\,\mu$m$^2$ ($350 \times 350$ pixels), counting time per pixel: 1.5 ms. The small image is a detail ($250 \times 250$ pixels) of the region marked with the white dashed line. The double arrow in the small image shows the polarization direction.

The patterns observed through the gold film present different intensities but have all the same geometry: two center bright lobes are separated by a dark gap perpendicular to the polarization direction, and are accompanied by weaker bright and dark fringes at the sides. This is in fact the symmetry that corresponds to the spatial distribution of the intensity of the longitudinal (along the optical axis of the objective) component of the electric field generated at the focus of a microscope objective [39, 59]. The observed patterns are in great contrast to what is expected for light focused through an non-metallic medium (no gold film), because in that case, and under the same illumination conditions (linearly polarized light and full beam

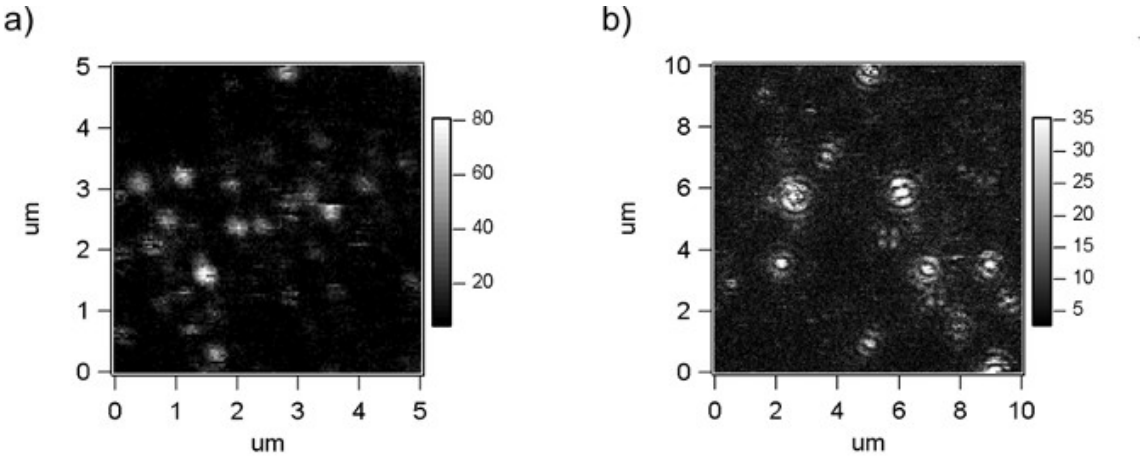


**Figure 4.4:** Typical fluorescence micrographs of single dye-molecules on a glass substrate (without gold film). a) FB illumination: round diffraction limited signals are observed. b) Annular illumination: a variety of patterns is observed due to the different orientations of the chromophores.

illumination), this longitudinal component of the electric field would be considerably weaker than the in plane component along the polarization direction.

### 4.3.2 Different illumination modes

In order to discriminate the contributions of transmitted light and forbidden light for the excitation of the chromophores, the samples with 4-bilayer spacers were studied with the three different modes of illumination described in section 4.2. In figure 4.5, the images on the left column were recorded with full beam (FB) illumination, the ones in the center with transmitted light (TL), and the ones on the right with forbidden light (FL) illumination.

The images obtained with FL illumination are very similar to the ones obtained with FB illumination described above in section 4.3.1. In general, the background in FL illumination is reduced approximately to one half, due to the considerable smaller amount of reflected light (see figure 1.2). The images obtained with TL illumination are strikingly different. The characteristic patterns are no longer observed. Instead, very weak, round signals are detected, with a size larger than the diffraction limit ($\sim 500\,\mathrm{nm}$).

By comparing the images obtained with the different illumination modes, it can be seen that these round signals obtained with TL illumination do not always overlap with the characteristic patterns obtained with the FB or FL illumination modes. The figures in the lower row are intended to further clarify this effect. The scanned region is smaller and five dash-line circles were placed on top of each image, on the same position, corresponding to five detected signals with TL illumination. By comparing the FB to the TL images, it can be seen that very weak signals in the FB image

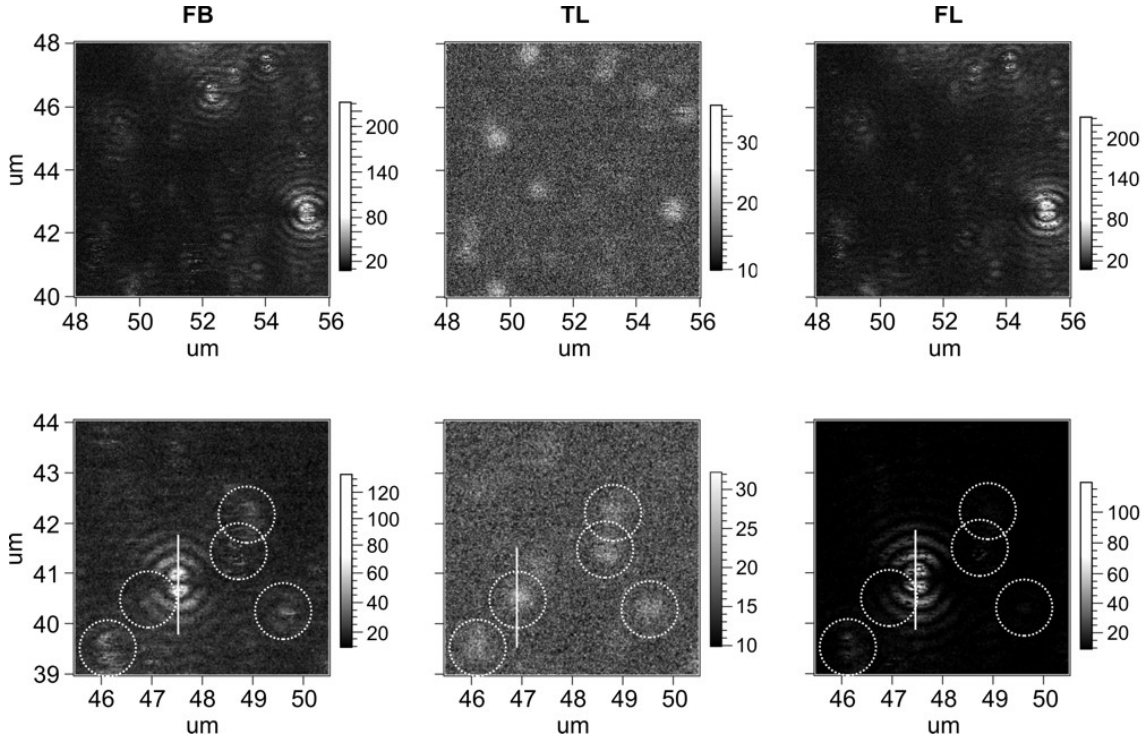


**Figure 4.5:** Different modes of illumination. Typical images (upper row $8 \times 8\mu m^2$ and lower row $5 \times 5\mu m^2$) of the samples with a spacer of 4-bilayers (24 nm), obtained with full beam (FB, left), transmitted light (TL, center) and forbidden light (FL, right) illumination. Profiles along the white vertical lines are compared to the theoretical signals in figure 4.18.

correspond to the round TL signals. Those FB signals are so weak that can be easily covered by the much stronger characteristic patterns, and very careful observation is necessary not to confuse them with the background. Even though the background is reduced, they become weaker under FL illumination. The strongest signal in both the FB and FL images has a very clear pattern and shows almost no signal in the TL image.

The facts that the images obtained with FB and FL illumination are so similar, and the images obtained with TL illumination present so weak signals, indicate that light propagates most effectively through the layered system via surface plasmons (the TL illumination mode cannot excite surface plasmon; see figure 4.2). Excitation of the dye-molecules is therefore accomplished principally by the evanescent field of the surface plasmon which decays exponentially from the gold surface with a 1/e decay-length of approximately 240 nm [4]. This axial field localization is approximately two times higher than the one obtained in a confocal system when $\lambda = 633$ nm light is focused in a dielectric medium by a 1.4 NA microscope objective.

[4]The electric field in the layered system, from which the decay-length was calculated, was obtained via the TMA.

### 4.3.3 Influence of the separation distance to the gold film

Molecular fluorescence can be strongly suppressed by a close nearby metallic surface. This effect, frequently called quenching, was observed in a number of ensemble investigations of fluorescence near metals [42, 45, 46, 60]. The quenching is due the fact that energy transfer to the metal provides additional electromagnetic non-radiative decay channels for an excited molecule that predominate at very short distances (the emission rates of a fluorophore in a layered system is further treated in 3.2). Therefore, for the practical use of the present detection scheme, it is of great importance to know the minimum separation distance at which the single dye-molecules can be placed from the gold film before their fluorescence becomes undetectable. To address this question, samples with polyelectrolyte spacers of four different thicknesses were studied.

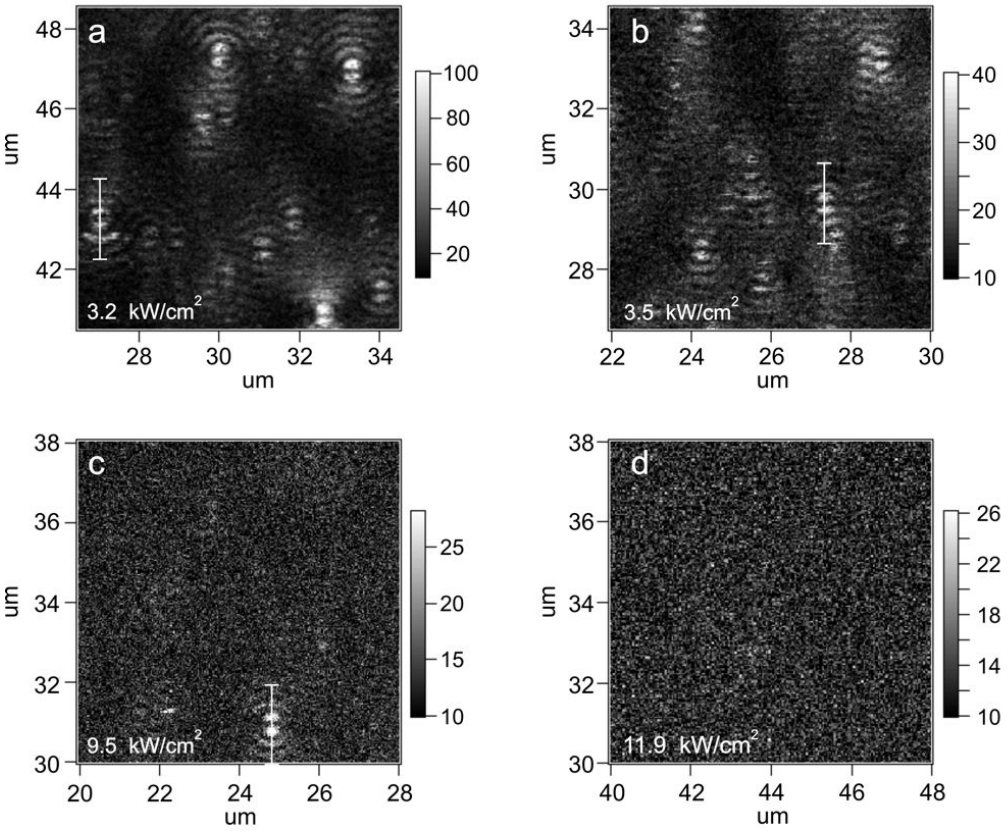


**Figure 4.6:** Influence of the separation distance to the gold film. Images ($8\times8\,\mu m^2$; 2 ms per pixel) of the samples with different spacer thicknesses. a) 4 bilayers (24 nm). b) 3 bilayers (15 nm). c) 2 bilayers (10 nm). d) 1 bilayer (4.5 nm). The excitation power used is shown in each image.

Figure 4.6 shows FL images of the samples with 4-, 3-, 2-, and 1-bilayer spacers, corresponding to separation distances of the chromophores from the gold film of 24, 15, 10, and 4.5 nm, respectively. In all the samples, the great majority of

the detected signals present the same characteristic pattern discussed above. These images correspond to samples from the same batch produced under the same conditions. Therefore, the same surface density of dye-molecules is expected for all of them. The detection of single molecule fluorescence becomes more difficult as the spacer thickness decreases; note on the bottom-left of each image the increasing excitation intensity used as the spacer thickness decreases. The average signal to background ratio reduces together with the number of detected molecules. For the 4-bilayer spacer samples, the average[5] signal to background ratio is found to be 6, for the 3-bilayer spacer samples it is 3.5 and for the 2-bilayer spacer samples it is 1.3. Fluorescence signals were much rarer in the samples with 2-bilayer spacers, and no fluorescence signals were detected in the samples with 1-bilayer spacer.

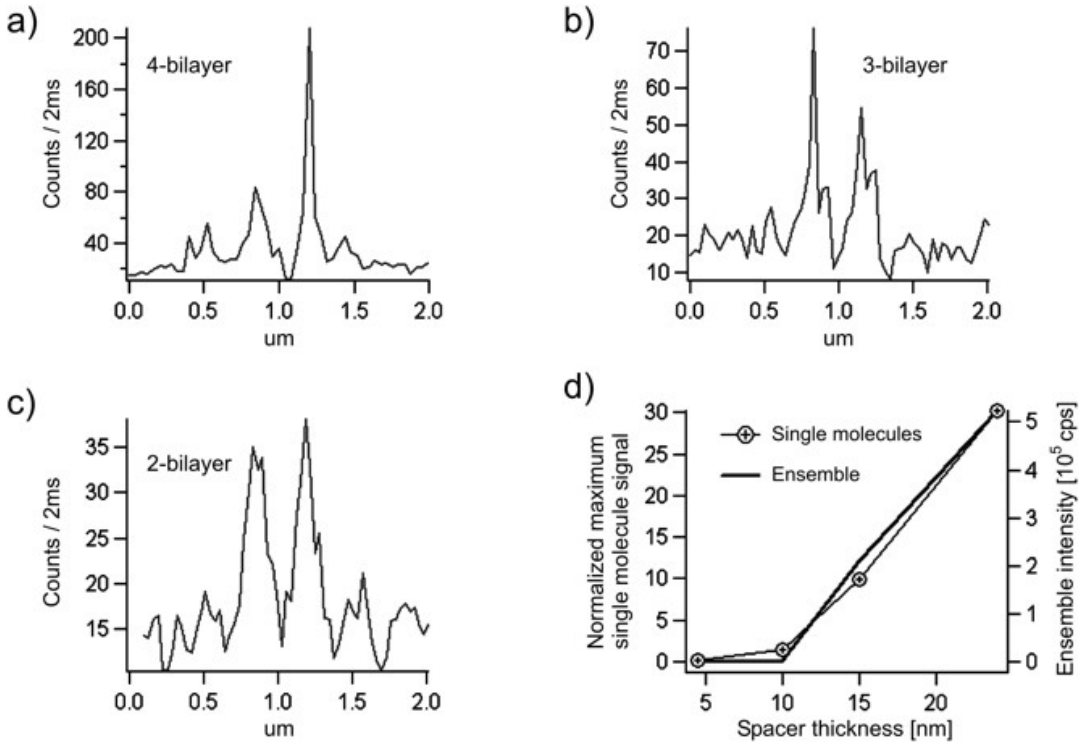


**Figure 4.7:** Quenching behavior. a), b) and c) Profiles corresponding to the vertical white lines on the images of the samples with a 4-, 3- and 2-bilayer spacer of figure 4.6. These are representative maximum signals for each kind of sample. d) Normalized maximum single molecule fluorescence signals ($\overline{I_M}$, equation 4.1) from a), b) and c), and the ensemble fluorescence intensity [46] as a function of the spacer thickness.

The present results on a single molecule level present the same quenching behavior observed on an ensemble of fluorophores on the same sample system carried out by Vasilev et al. [46]. Vasilev et al. measured the fluorescence intensity emitted by an ensemble of molecules to the glass side of the samples as a function of the spacer

[5]Average taken over 20 randomly chosen signals for the 4- and 3-bilayer spacer samples, and over 5 signals for the 2-bilayer spacer samples.

thickness. The excitation was in that case performed by a surface plasmon field at the gold/spacer interface generated by a laser beam of constant intensity, incident at the angle of surface plasmon resonance. Then, in order to compare the single molecule quenching behavior observed in the present experiments to the ensemble one measured by Vasilev et al., the maximum single molecule signals detected on each type of sample ($I_M$) were identified and normalized by:

$$\overline{I_M} = \frac{I_M - I_{bg}}{t_p \; P} \tag{4.1}$$

where $I_{bg}$ is the average background intensity, $t_p$ is the counting time per pixel and $P$ is the excitation power. Figures 4.7.a, b, and c show the profiles of representative maximum signals detected on the samples with 4-, 3- and 2-bilayer spacers, marked with a white line on the corresponding images of figure 4.6. These maximum values were normalized as explained above (equation 4.1), and plotted as a function of the spacer thickness[6], together with ensemble results of Vasilev et al.[7], in figure 4.7.d. Both quenching trends are in excellent agreement, providing further evidence that the excitation of the single dye-molecules is accomplished via surface plasmons at the metal-polyelectrolyte interface.

## 4.4 Modelling the experimental scheme

In order to properly interpret the single molecule fluorescence signals, and to understand the advantages and limitations of the present scheme, the fluorescence excitation and emission of a single molecule under the experimental conditions is modelled following the approach described in chapter 3. The first part of this chapter introduces the concepts necessary to understand the theoretical results presented next. Section 4.4.2, considers the de-excitation rates and section 4.4.3 the excitation rate. In section 4.4.4, the theoretical results obtained for the excitation and for the emission are brought together to calculate the theoretical fluorescence signals of a fluorophore under the experimental conditions.

### 4.4.1 Fundamental concepts

The excitation and emission properties of a fluorophore are greatly affected by the properties of the surrounding media. In particular, a nearby metallic surface can

[6]No single molecule fluorescence signal was detected on the samples with 1-bilayer spacer. Therefore the signals must be smaller than the background intensity. The value of $\overline{I_M}$ for the 1-bilayer spacer sample shown in figure 4.7.d was calculated assuming a signal equal to half the background intensity.

[7]Reproduced with permission of the authors

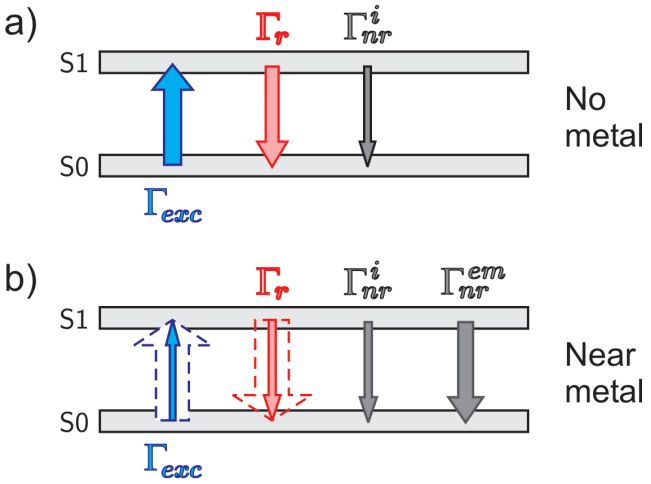


**Figure 4.8:** Schematic representation of the excitation and de-excitation rates of a fluorophore. a) In free-space. b) Interacting with a metal. $\Gamma_{exc}$ is the excitation rate from the singlet ground state S0 to the singlet excited state S1. $\Gamma_r$ is the radiative decay rate, $\Gamma^i_{nr}$ the intrinsic non-radiative decay rate, and $\Gamma^{em}_{nr}$ represents the electromagnetic non-radiative decay channels introduced by the metal.

affect both the excitation and the de-excitation rates, as schematically represented in figure 4.8.

The excitation rate is modified via changes (increase or reduction) in the local strength of the electric field. For example, under surface plasmon resonance conditions [58], the electric field intensity at the metal/dielectric interface can reach enhancements of several orders of magnitude. This enhancement strongly depends on the experimental geometry, the dielectric constants of the materials, and the frequency of the radiation [61].

The emission of a molecule can be characterized by its radiative and non-radiative decay rates. The presence of a nearby metallic surface can influence both. The radiative decay rate $\Gamma_r$ can be enhanced or suppressed depending on the separation distance to the metal and on the orientation of the transition dipole of the molecule. An enhancement of the radiative decay rate can lead to an increase of the observed quantum yield and shortening of the observed lifetime [62]. The non-radiative decay rate is modified because the metal introduces additional electromagnetic non-radiative decay channels, which involve both excitation of evanescent modes in the metal and direct energy transfer from the excited state of the molecule to the metal [63, 64]. These electromagnetic non-radiative de-excitation channels join the intrinsic ones to further reduce the fluorescence quantum yield of the molecule, and at short distances ($< \lambda/30$) are so dominant that they can quench the emission completely [41].

The excitation and the emission of a single molecule in the experimental conditions are modelled in the next two sections with the method presented in chapter 3. Table 4.1 lists the parameters used for the sample layers in the calculations. The emission wavelength of the DiIC1(5) and the dielectric constants of the layers were experimentally determined [46]. The fluorescent dye-molecules are considered to be in the interface between the polyelectrolyte spacer and air.

| | $d$ [nm] | $\epsilon$ ($\lambda$=633 nm) | $\epsilon$ ($\lambda$=670 nm) |
|---|---|---|---|
| *glass* | | 2.26 | 2.25 |
| *Au* | 44 | $-12.65 + i\,1.01$ | $-14.94 + i\,1.1$ |
| *spacer* | 0–1000 | 2.38 | 2.32 |
| *air* | | 1 | 1 |

**Table 4.1:** Properties of the sample layers. Thicknesses $d$ and dielectric constants $\epsilon$ (for the excitation and emission wavelengths $\lambda$) of the sample layers. The glass substrates and the air are considered semi-infinite.

### Photo-bleaching

Fluorescent dye-molecules undergo irreversible photo-bleaching. The reaction mechanism of photo-bleaching is yet unclear but it is found experimentally that for the DiIC1(5) dye it occurs at a constant rate from the excited state [47]. Therefore, an enhancement of the total de-excitation rate is accompanied by an increase in the average number of cycles ($nc$) that a molecule can perform between the ground and excited states before it photo-bleaches. Then, it is possible to write:

$$nc \propto \Gamma^{em}_{total} + \Gamma^{i}_{nr} \tag{4.2}$$

For a given set of excitation and de-excitation rates, a higher number of excitation/de-excitation cycles $nc$ yields a higher number of photons emitted by a single molecule.

### Spacer/air interface: spacer or air side?

The fluorescent dye-molecules are placed by the electrostatic deposition method on the spacer/air interface of the samples, but it remains a priori uncertain on which side of the interface. As it will be shown in the next two sections, because of the electromagnetic boundary conditions for the electric field, both the excitation and emission rates are considerably different for molecules on either side of the interface. Equations 3.3 write for the present case:

$$\begin{aligned} E_{\parallel,air} &= E_{\parallel,spacer} \\ \epsilon_{air}\, E_{\perp,air} &= \epsilon_{spacer}\, E_{\perp,spacer} \end{aligned} \tag{4.3}$$

In the modelling, both possibilities are considered and all calculations are performed for the cases of molecules on the air and on the spacer side of the interface. Later, by comparing the theoretical results to the experiments, it will be possible to conclude how the molecules optically behave, as being on the air or on the spacer side.

### 4.4.2 Detectable fraction of the emitted fluorescence

Following the approach presented in section 3.2, the electromagnetic decay rates of a fluorophore at the air/spacer interface of the samples were calculated. The parameters were set in order to represent the experimental conditions. The wavelength was set to 670 nm, the emission wavelength of the DiIC1(5). The dielectric constants of the materials for this wavelength are listed in table 4.1. A gold film thickness of 44 nm was considered and the spacer thickness was varied from 0 to 1000 nm, in order to observe the influence on the rates of the separation distance between the molecules and the gold film.

Figure 4.9 shows the normalized decay rates of a parallel (top) and a perpendicular (bottom) dipole on the air side of the spacer/air interface, as a function of the spacer thickness. The total decay rate ($\Gamma^{em}_{total}$), the decay rate to the air ($\Gamma_{air}$) and the glass semi-space ($\Gamma_{glass}$), and the electromagnetic non-radiative decay rate ($\Gamma^{em}_{nr} = \Gamma^{em}_{total} - \Gamma_{air} - \Gamma_{glass}$) are plotted; all normalized to the total emission of a free dipole in air. For very thick spacers, as the influence of the gold film vanishes, all the rates tend to a constant value. At very short distances from the metal film, the excited molecule can very effectively transfer its excess energy to the metal. Due to this dominant non-radiative decay channels, for separation distances in the order of $\lambda/30$, the total decay rate diverges to extremely high values. For intermediate spacer thickness ($\lesssim \lambda$) all the rates present damped oscillations.

In addition, the emission rate into the collection solid angle of the objective $\Gamma_{obj}$ was calculated and it is shown in the small graphs on the left of figure 4.9 . Fluorescence detection is accomplished with a 1.4 NA microscope objective from the glass substrates, which have a refractive index $n_{glass} = 1.503$. The collected radiation is therefore the fraction emitted to the glass side, up to an angle $\theta = 68.6°$ from the normal to the interfaces. Then, $\Gamma_{obj}$ is obtained by integrating equations 3.6 between zero and $\mathrm{k}_{max} = n_{glass}\,\mathrm{k}_0\,\sin(68.6°)$, where $\mathrm{k}_0$ is the wavevector of the emitted radiation ($\lambda = 670\,\mathrm{nm}$) in vacuum.

From these calculated rates, it is possible to obtain the fraction of the electromagnetic de-excitation rate corresponding to radiation collected in a time unit by the microscope objective: $\Gamma_{det} = \Gamma_{obj}\,/\Gamma^{em}_{total}$ (equation 3.14). This ratio represents, for an ideal molecule with a null intrinsic non-radiative decay rate ($\Gamma^{i}_{nr} = 0$), the detectable fluorescence emission. In figure 4.10, $\Gamma_{det}$ is plotted as a function of the spacer thickness for dipoles parallel and perpendicular to the sample plane.

In both cases, $\Gamma_{det}$ oscillates as a function of the separation distance to the gold film. However, in the range of spacer thicknesses used in the experiments, $\Gamma_{det}$ increases monotonically with the spacer thickness and is always higher for the perpendicular dipole (small graph and table in figure 4.10).

From the boundary conditions of the electric field (equations 4.3) the electromagnetic decay rates for the parallel dipole are the same on both sides of the interface. Instead, for a perpendicular dipole, all the electromagnetic decay rates on the spacer

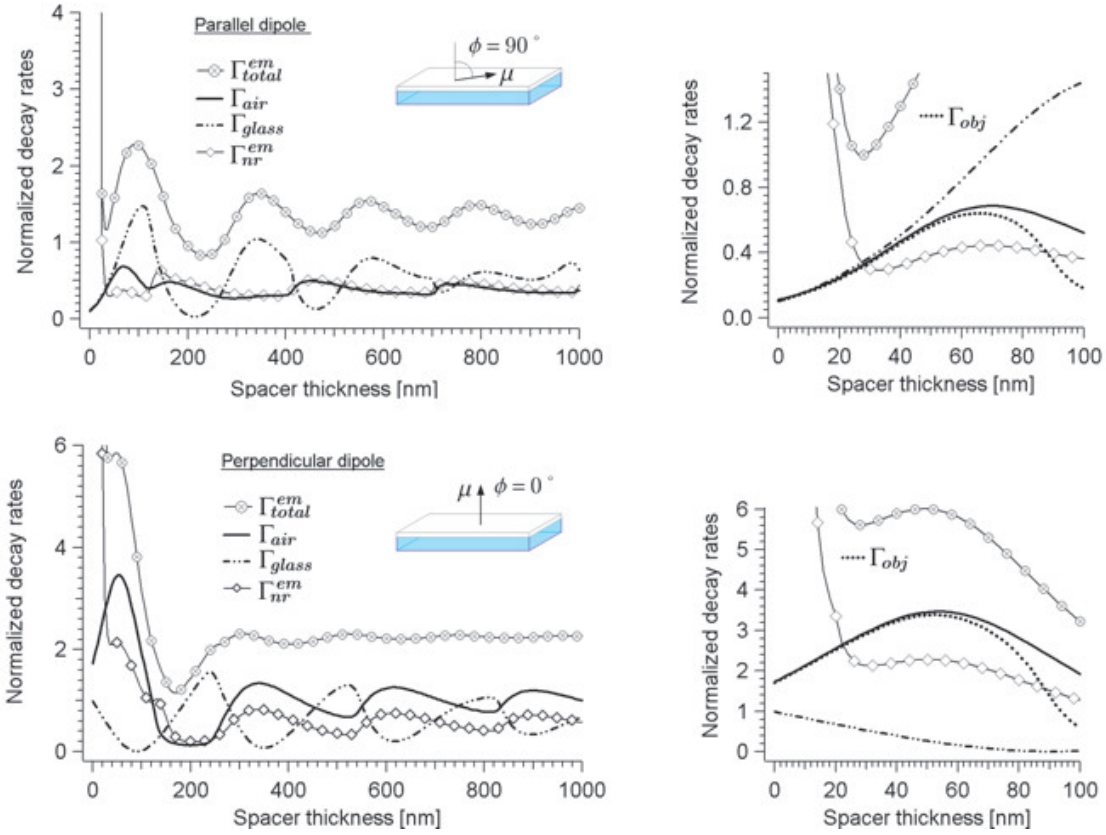


**Figure 4.9:** Electromagnetic decay rates. Electromagnetic decay rates normalized to the total emission of a free dipole in air, for a parallel (top) and for a perpendicular (bottom) dipole on the air side of the air/spacer interface of the samples, emitting at $\lambda = 670\,\text{nm}$. On the right (detail of the region of spacer thickness between 0 and 100 nm), the detectable fraction of the radiative decay $\Gamma_{obj}$ is plotted as well.

side are decreased by a factor $(\epsilon_{spacer}/\epsilon_{air})^2$.

The value of $\Gamma_{det}$ for a molecule with arbitrary orientation of its transition dipole is given by equation 3.14. For parallel and perpendicular dipoles, the fraction takes the same value on any side of the interface, but for intermediate orientations it does not. As an example, figure 4.11.a shows $\Gamma_{det}$ as a function of the out of plane orientation of the transition dipole for molecules on either side of the spacer(24 nm)/air interface. It can be seen that, in general, the fluorescence emission collected by the objective is higher for molecules on the air side of the interface. In the experimental scheme, for a 4-bilayer (24 nm) spacer, almost 50% of the de-excitation rate of a perpendicular dipole on the air side of the interface corresponds to detectable fluorescence. For the case of a parallel dipole, this fraction is slightly higher than 25%. And for molecules which transition dipoles are oriented with an angle above 30° with respect to the interface plane, $\Gamma_{det} > 40\%$.

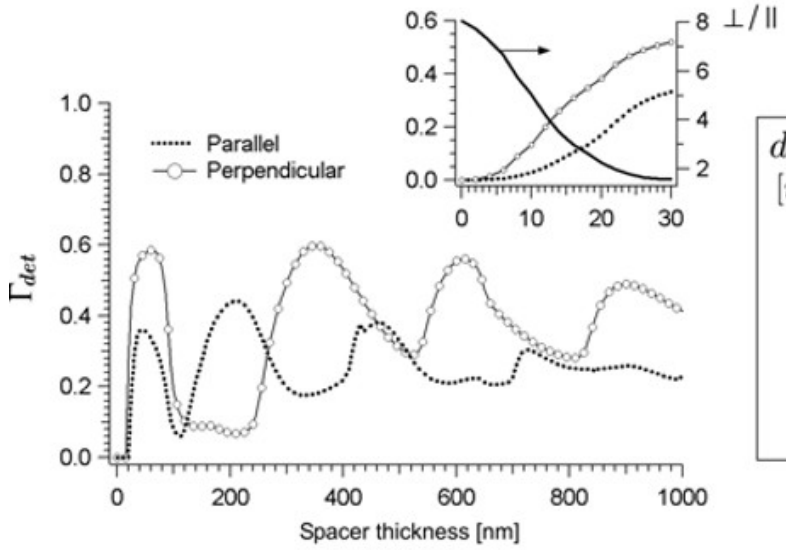


| $d_{spacer}$ $[nm]$ | ⊥ | ∥ | ⊥/∥ |
|---|---|---|---|
| 4 | 0.014 | 0.002 | 7.2 |
| 8 | 0.091 | 0.016 | 5.7 |
| 12 | 0.199 | 0.047 | 4.2 |
| 16 | 0.310 | 0.104 | 3.0 |
| 20 | 0.383 | 0.170 | 2.3 |
| 24 | 0.467 | 0.262 | 1.8 |

**Figure 4.10:** Detectable fraction of the fluorescence emission as function of the spacer thickness. $\Gamma_{det}$ for a parallel and a perpendicular dipole, on the air side of the spacer/air interface, as a function of the spacer thickness. The small graph shows a close up of the region of spacer thicknesses used in the experiments. The list displays the values of $\Gamma_{det}$ for the parallel and for the perpendicular dipole for spacers from 4 to 24 nm, and their ratio (black solid curve, right axis in the small graph).

### Comparison to the detection from the air side

It is interesting to compare the present detection scheme to the detection from the air side with a high NA microscope objective. For this reason the ratio $\Gamma_{air,0<\theta<64.2^\circ}/\Gamma^{em}_{total}$ was also calculated. This ratio represents the fraction of the de-excitation rate of a fluorophore (on the air side of the spacer/air interface) that corresponds to fluorescence emitted to the air side into the collection solid angle of an 0.9 NA objective. $\Gamma_{air,0<\theta<64.2^\circ}/\Gamma^{em}_{total}$ is 0.25 for a parallel dipole and 0.07 for a perpendicular one. Then, in comparison to the detection from the air side, the present detection scheme through the gold film is equivalent for a parallel dipole but is almost 7 times more effective for a perpendicular dipole.

### The case of a fluorophore with $\Gamma^{i}_{nr} \neq 0$

Figure 4.11.b. shows the detectable fluorescence fraction of the emission ($\Gamma_{det}$) of a fluorophore on the air side of the spacer(24 nm)/air interface of the samples, as a function of its out of plane orientation, for different intrinsic quantum efficiencies (equation 3.17). It can be seen that, since the total electromagnetic decay rate of a parallel dipole at 24 nm distance from the gold film is close to unity (unaffected by the gold film; see figure 4.9), the $QE$ reduces their detectable emission fraction almost linearly. In contrast, the reduction for a perpendicular dipole is damped

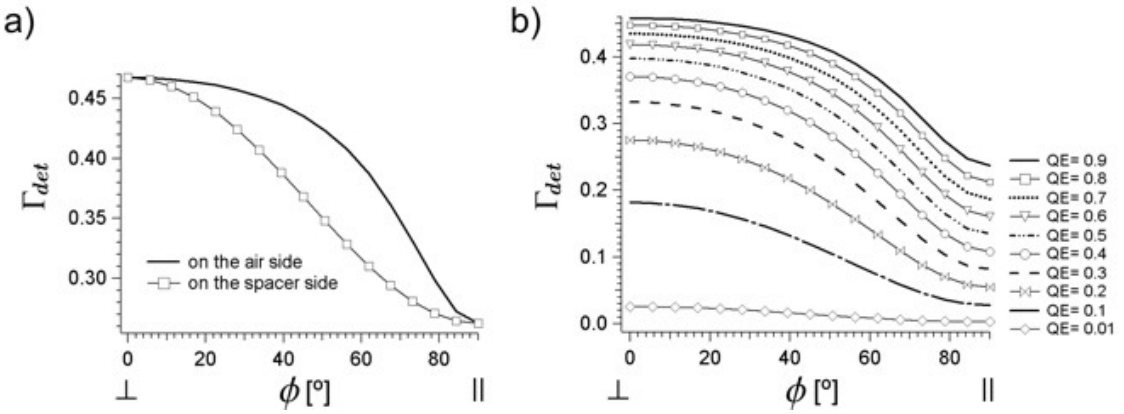


**Figure 4.11:** Detectable fraction of the fluorescence emission as function of the orientation. a) $\Gamma_{det}$ for an ideal fluorophore ($QE = 1$), on either side of the spacer(24 nm)/air interface, as a function of out of plane orientation of the transition dipole. b) Effect of a smaller $QE$ for the fluorophore on the air side.

due to the strongest enhancement of their total electromagnetic decay rate. As an example, it can be seen from figure 4.11.b that a $QE$=0.5 reduces the detectable fraction of a parallel dipole by 48% and the one of a perpendicular dipole by less than 15%.

### Comparison to the detection in a sample without the gold film

The de-excitation rates were calculated as well for molecules on the air side of the spacer/air interface of samples without the gold film. Table 4.2 presents the results for the samples with and without the gold film.

By comparing the rates to the complete glass semi-space ($\Gamma_{glass}$) and to the collection solid angle of the objective ($\Gamma_{obj}$), it can be seen that in all cases practically the complete emission to the glass side is collected by the objective. For the sample with gold film, 99% of the radiation emitted by a perpendicular dipole to the glass side is collected. For the parallel dipole 96%. This collection efficiencies are slightly higher than the ones corresponding to the case of a sample without the gold film (93% and 91% for the perpendicular and parallel dipoles respectively). The explanation for this stronger orientation of the emission is that, analogously to the case of the excitation light, fluorescence light emitted by the fluorophores propagates through the gold film via surface plasmon back coupling.

In order to compare the detection efficiency of the two cases it is necessary to compute the number of detectable photons emitted by a single molecule with and without the gold film. Two factors need to be considered. First, the fraction of the de-excitation rates corresponding to radiation collected by the objective (equation 3.17). Second, the number of excitation/de-excitation cycles that the molecule can

| | ∥ With Au | Without Au | ⊥ With Au | Without Au |
|---|---|---|---|---|
| $\Gamma^{em}_{total}$ | 1.05 | 1.34 | 5.75 | 2.21 |
| $\Gamma_{glass}$ | 0.29 | 1.18 | 2.72 | 2.00 |
| $\Gamma_{obj}$ | 0.28 | 1.08 | 2.67 | 1.87 |

**Table 4.2:** Influence of the gold film on the decay rates. De-excitation rates of a molecule on the air side of the spacer(24 nm)/air interface of a sample with and without the 44 nm gold film.

perform before undergoing irreversible photo-bleaching (equation 4.2). Then, the number of detectable photons $n_{h\nu}$ emitted by a single molecule which transition dipole has an out-of-plane orientation defined by $\phi$ is:

$$n_{h\nu} = nc\,\frac{\Gamma_{obj}}{\Gamma_{total}}(\phi) \propto \Gamma_{obj}(\phi) \tag{4.4}$$

From the values displayed in table 4.2 it can be seen that the present detection scheme through the gold film is less effective for molecules with its transition dipole parallel to the interface but it is more effective in the case of molecules with its transition dipole perpendicular to the interface. The number of detectable photons emitted by a parallel molecule in the sample with the gold film is 26% of the photons that the same molecule would emit in the sample without the gold film. For the case of a perpendicular molecule this percentage rises to 140%.

### 4.4.3 Excitation field at the chromophores position

Following the method presented in section 3.3, the electric field distribution at the molecules position was calculated for the different modes of illumination. The calculation parameters were set in order to represent the experimental conditions. A linearly polarized ($\lambda = 633$ nm) plane wave front was considered to be focused at the spacer/air interface of the samples, with a gold film thickness of 44 nm and a spacer thickness of 24 nm. The dielectric constants of the materials for a wavelength of 633 nm are listed in table 4.1. In order to calculate the fields produced by the different illumination modes, the integration limits for $\theta$, in equation 3.28, were set in accordance to the range of angles of incidence of each illumination mode (see section 4.2.2).

Figure 4.12 shows the intensity distribution of the x-, y- and z-components of the electric field generated on the air side of the spacer/air interface of the samples. In order to compare the relative intensities of the components, all the fields were normalized with the same factor in order to produce a FB z-component with a maximum intensity of 100. The maximum intensity of each component is shown on the upper left of the each image and a line profile is shown to the right of the corresponding image.

The symmetry characteristics of the patterns is the same for the three modes

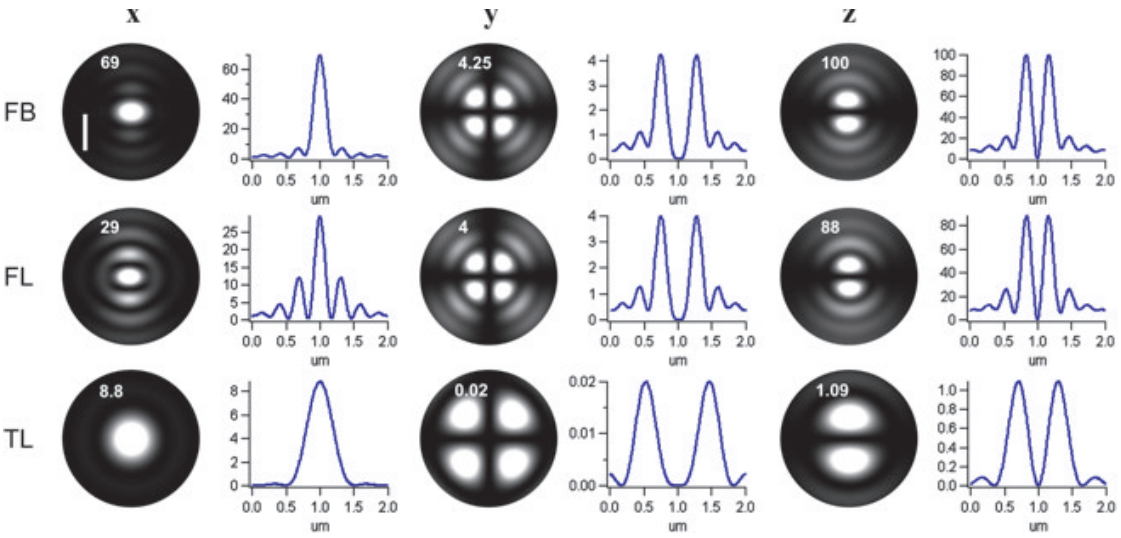


**Figure 4.12:** Electric field distribution in the samples. Theoretical calculations of the square modulus of the x-, y-, and z-components of the electric field on the air side of the spacer/air interface of the samples. From top to bottom, the results corresponding to full beam (FB), forbidden light (FL), and transmitted light (TL) illumination are shown. The white bar in the upper left image, shows the polarization direction and is a scale bar of 500 nm. The images are plotted with grey scales in which zero is black and one half of the maximum intensity is white so that the white color saturation in the images show the size at half maximum. The maximum intensity value of each component is written in the upper left corner the image. To the right of each pattern, a line profile is shown. For the x- and z-components, the profile corresponds to a vertical centered line. For the y-components corresponds to a line at 45° passing trough the center.

of illumination. The x-components have a central dominant peak and concentric side lobes of lower intensity. The intensity of the side lobes is maximum along the polarization direction. The y-components present two nodal lines, one along the polarization direction and the other along the perpendicular direction. The maximum intensities lie on directions at 45° with respect to the nodal lines, with four main peaks and weaker side lobes. The z-components present one nodal line perpendicular to the polarization direction, and has two main peaks and weaker side lobes at the sides of the nodal line.

Under FB illumination conditions, the strongest component of the electric field is the z one. The x-component follows, and the y-component is practically negligible in comparison to the other two. Under FL illumination conditions, the main peaks of all components are slightly sharpened, their intensity is reduced and the intensity of the side lobes increased. Because the y- and z-components are mainly generated by waves focused with great angles of incidence, the intensity of the x-component is the most reduced. This effect of the annular illumination is well known and was used to equalize the intensities of the in-plane and out-of-plane components of the fields, in order to facilitate the determination of the three dimensional orientation of single molecules [39]. Under TL illumination conditions, the results are, naturally,

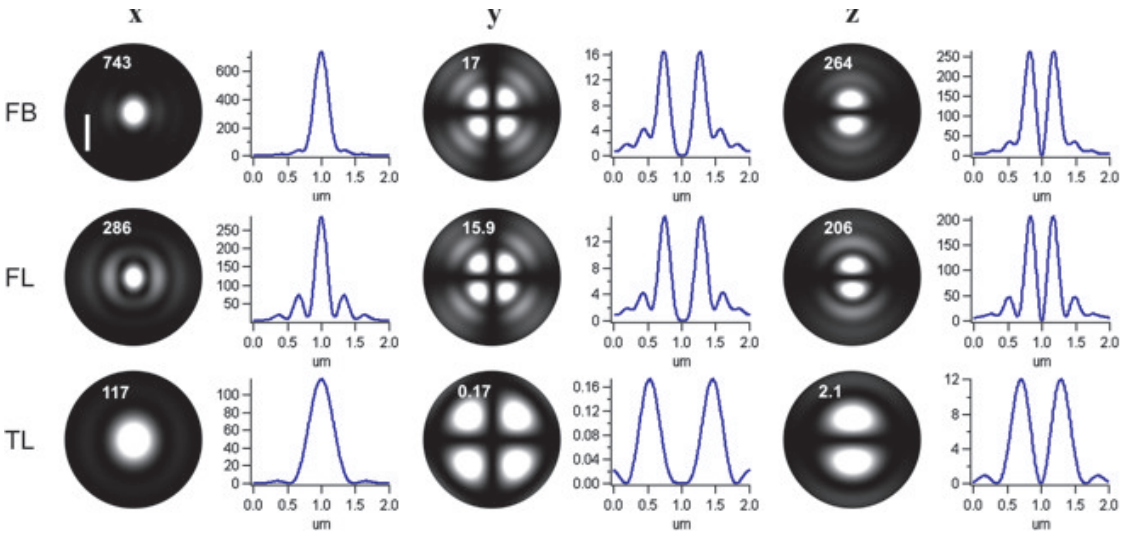


**Figure 4.13:** Electric field distribution in a sample without the gold film. Theoretical calculations of the square modulus of the x-, y-, and z-component of the electric field, on the air side of the spacer/air interface of a layered system like the one of the samples but without the gold film. The results are presented in the same fashion as in figure 4.12 with the difference that the profiles of the x-components correspond here to a horizontal centered line.

complementary to the ones obtained FL illumination. The intensity of all peaks is decreased but this time the y- and z-components are the most affected. The size of all patterns is increased due to the smaller effective NA corresponding to TL illumination.

As inferred from the experimental results, the calculated electric fields show that light propagates most effectively through the layered samples via surface plasmon excitation. The FB and FL illumination modes, as they can excite the surface plasmon resonance (SPR), generate strong fields of similar intensities. In contrast, the TL illumination mode cannot excite the SPR and generates therefore a very weak field at the spacer/air interface.

The electric field distribution on the polymer side of the spacer/air interface was calculated too but they are not shown. The only difference to the results on the air side is the reduction of the z-component due to the boundary conditions for the electric field (equations 4.3). Thus, the results for the x- and y-components are the same as those shown figure 4.12, and the results for the z-components show the same spatial distribution but their intensities are a factor $\epsilon^2_{spacer} = 5.67$ weaker.

In order to examine the influence of the gold film, the electric field distribution was also calculated on the air side, of the spacer/air interface of a sample without the gold film. The results are presented in figure 4.13. The same normalization factor as in the case with gold was used so that the intensities can be compared. The field distribution of all components present the same symmetry as in the case of the sample with the gold film, and the differences between FB, FL, and TL illumination

are basically the same described for the case with the gold film. The only change observed is that the maximum intensities of the x-component lie in this case in a direction perpendicular to the polarization direction.

With respect to the relative intensities, it can be seen that the gold film reduces the intensity of the three components, but to different extents. The intensity of the x-component is the most drastically affected; the gold film reduces it approximately one order of magnitude. The y- and the z-components are less affected; the gold film reduces their intensities by a factor of approximately 4 and 2.5, respectively.

### 4.4.4 Theoretical fluorescence signal

The theoretical fluorescence signal corresponding to the three modes of illumination was calculated for an ideal fluorophore on both sides of the spacer/air interface, and with different orientations of its transition dipole by means of equation 3.40. The procedure consists of scaling the calculated fields shown in the previous section by the fraction of the de-excitation corresponding to detected fluorescence $\Gamma_{det}$.

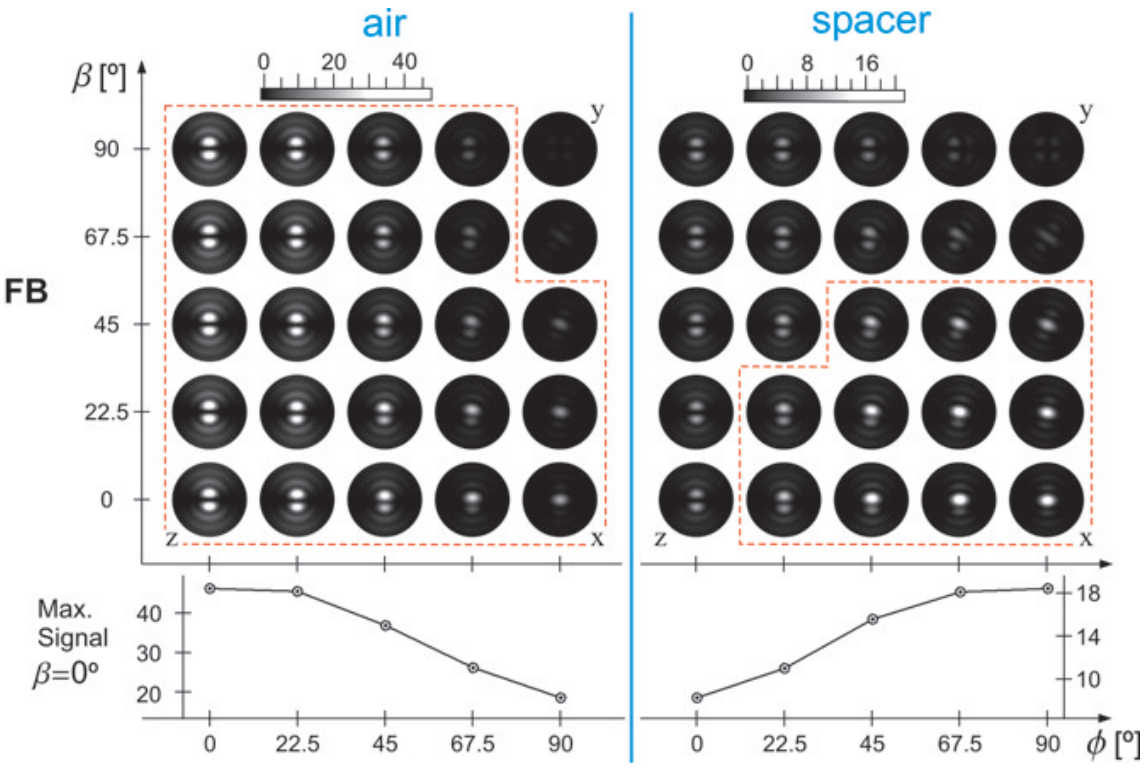


**Figure 4.14:** Modelled FB illumination fluorescence signals. Calculated fluorescence signal of an ideal ($QE = 1$) fluorophore under FB illumination on the air (left) and on the spacer (right) sides of the air/spacer interface. The orientation of the transition dipole of the fluorophore is defined by $\phi$ and $\beta$ according to figure 4.1. At the bottom, the maxima of the signals for $\beta = 0$ as a function of $\phi$.

The so modelled signals, calculated with the method explained in chapter 3, are proportional to the experimental ones[8]. Furthermore, as the actual value of the non-radiative decay rate of the chromophore is unknown, an ideal fluorophore with $\Gamma_{nr}^{i} = 0$ was considered in the determination of the detectable fraction of the fluorescence emission. This is at first a good approximation because the fluorophores used in the experiments are supposed to have intrinsic quantum yields near unity. The changes introduced by a $\Gamma_{nr}^{i} \neq 0$ are discussed later in this section.

Figure 4.14 shows the modelled FB-illumination fluorescence signals. The results on either side of the interface are noticeable different. On the air side, the molecules with a greater out of plane (z-) component of their transition dipole present the stronger signals, and the majority of the signals present the spatial distribution characteristic of the intensity of the z-component of the electric field. On the contrary, on the spacer side of the interface, the molecules with a greater in-plane component parallel to the polarization direction present the strongest signals, with a spatial distribution that is the one characteristic of the intensity of the x-component of the electric field.

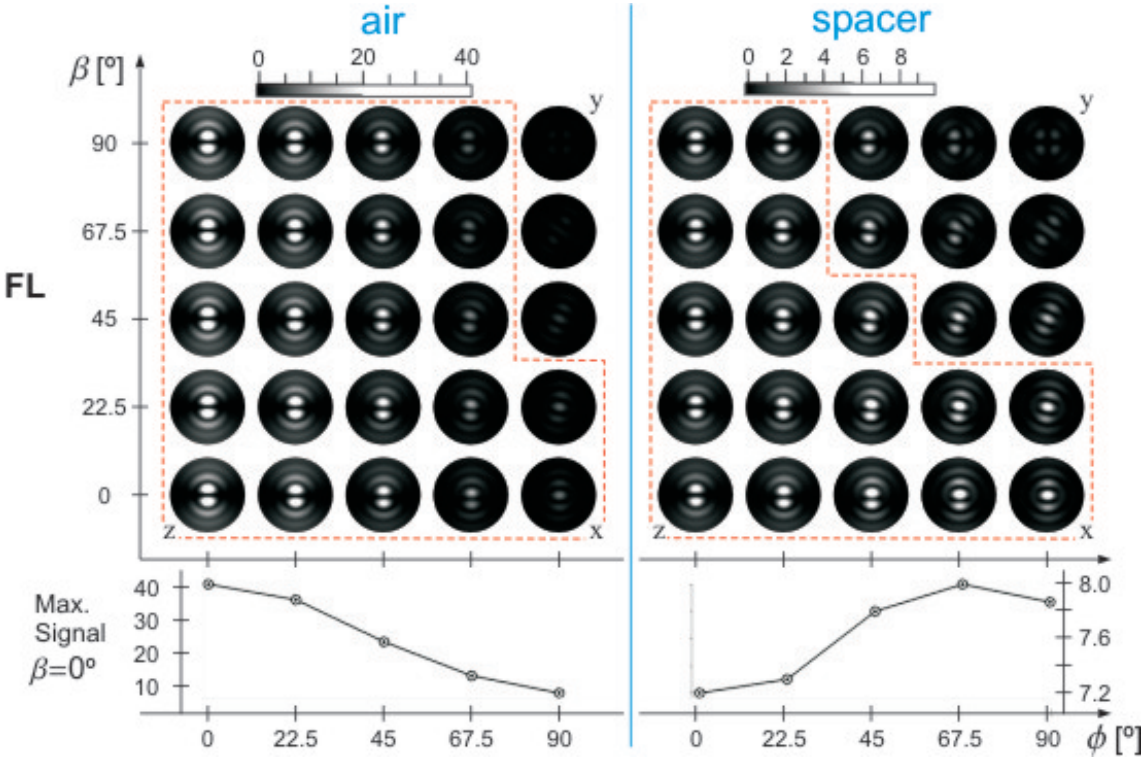


**Figure 4.15:** Modelled FL illumination fluorescence signals. Calculated fluorescence signal of an ideal ($QE = 1$) fluorophore under FL illumination on the air (left) and on the spacer (right) sides of the air/spacer interface. The orientation of the transition dipole of the fluorophore is defined by $\phi$ and $\beta$ according to figure 4.1. At the bottom, the maxima of the signals for $\beta = 0$ as a function of $\phi$.

[8]Up to the small polarization dependence of the transmission coefficient of the dichroic mirror and the filters.

The modelled fluorescence signals corresponding to forbidden light illumination are presented in figure 4.15. The differences with the results for FB illumination are due to the fact that, under FL illumination, the x-component of the electric field is reduced markedly more than the other two (see section 4.4.3). On the air side the molecules with greater out of plane component of their transition dipole present comparatively even stronger signals than in the case of FB illumination. On the spacer side, the signals of the in plane (along **x**) and out of plane molecules become comparable, but much weaker.

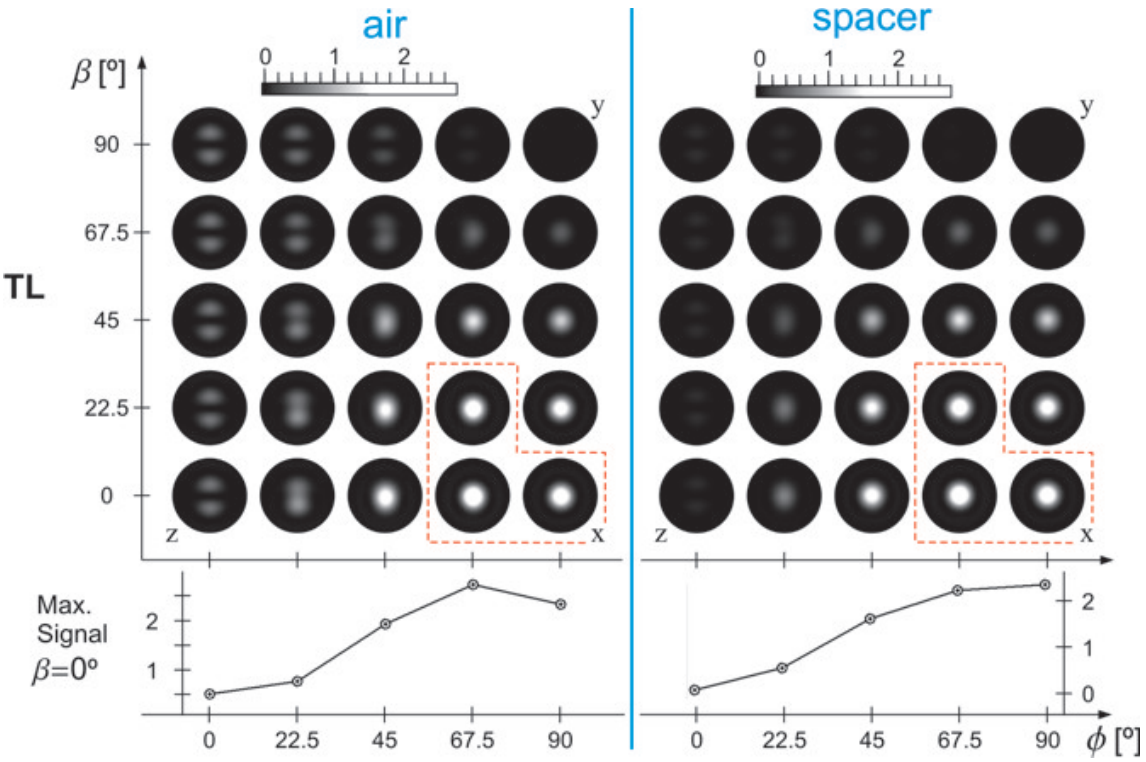


**Figure 4.16:** Modelled TL illumination fluorescence signals. Calculated fluorescence signal of an ideal ($QE = 1$) fluorophore under TL illumination on the air (left) and on the spacer (right) sides of the air/spacer interface. The orientation of the transition dipole of the fluorophore is defined by $\phi$ and $\beta$ according to figure 4.1. At the bottom, the maxima of the signals for $\beta = 0$ as a function of $\phi$.

Finally, the modelled fluorescence signals for transmitted light illumination are shown in figure 4.16. As expected from the electric field calculations, the signals on both sides of the interface are very weak in comparison to the FB and FL signals. The stronger signals are the ones corresponding to molecules with an important component of their transition dipole along the polarization direction (**x**). In fact, in comparison to the signal of an **x**-oriented dipole, the signals of **z**- and **y**-oriented dipoles are negligible.

**Fluorescence signal of a fluorophore with $\Gamma_{nr}^{i} \neq 0$**

Until now, an ideal fluorophore with null $\Gamma_{nr}^{i}$ ($QE = 1$), was considered because the actual value of $QE$ is uncertain but expected to be close to unity. Nevertheless, it is possible as well to calculate the theoretical fluorescence signal of a fluorophore with non-zero $\Gamma_{nr}^{i}$ ($QE < 1$). The effects on the detectable fraction of emitted fluorescence produced by quantum efficiencies smaller than one, discussed in section 4.4.2, reflect directly in the theoretical fluorescence signals. As the $QE$ reduces, the relative intensity of molecules with great out of plane components of their transition dipoles increases in comparison to the signals of in-plane molecules.

## 4.5 Conclusions

The first conclusion to be drawn from the experimental observations shown in figures 4.3 and 4.6 is that single molecule fluorescence in the nanometric vicinity of a thin gold film can be excited and detected, with a confocal epi-illumination scheme, through a thin gold film down to a separation distance of 15 nm from the gold surface.

Second, from the comparison of the images obtained with the different illumination modes and the theoretical calculations, it can be concluded that the surface plasmon resonance in the gold thin film plays a fundamental role. Surface plasmons provide the most effective propagation path for the excitation and fluorescence light. In excitation, if the surface plasmon resonance is not excited, almost no excitation field is generated at the chromophores position. In detection, if the NA of the objective is not large enough to collect the highly oriented surface plasmon back-coupled fluorescence light, almost no fluorescence emission is detected.

The excitation field generated by the surface plasmons decays exponentially from the gold surface with a typical length shorter than the axial field localization obtained in a 1.4 NA confocal system. For the geometry of the samples, the electric field decays in air with a 1/e distance of 240 nm, which is approximately 2 times smaller than the confocal z-resolution for 633 nm.

Another evident observation is that the great majority of the experimentally detected fluorescence signals present the spatial distribution corresponding to the intensity of the z-component of the electric field generated at the spacer/air interface. Figure 4.17 shows an example. In fact, in all the images recorded (containing around 500 fluorescence signals of single molecules) no fluorescence signal was detected with a clear x-pattern. Thus, a direct comparison of the calculated fluorescence signals for FB and FL illumination to the experimental images allows to conclude that the single fluorophores behave optically as being placed on the air side of the spacer/air interface. Furthermore, the theoretically calculated fluorescence signals for an ideal ($QE = 1$) fluorophore on the air side of the interface are in quantitative agreement

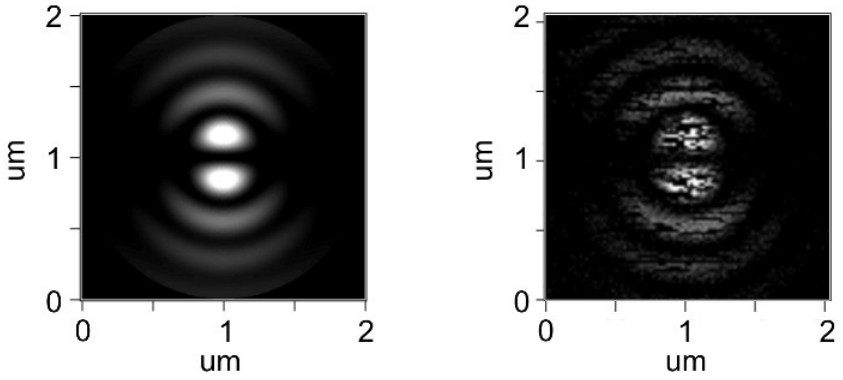


**Figure 4.17:** Modelled and experimental fluorescence signals. Comparison of the experimentally observed fluorescence signals (right; note the dynamic blinking during the scanning) and the theoretical fluorescence signal of an ideal fluorophore which transition dipole is parallel to the **z** direction (left).

with the experiments. The grey filled curves in figure 4.18 shows the profiles of three experimental fluorescence signals of single molecules obtained with the three illumination modes. The images of those signals are shown in figure 4.5 and the points from which the profiles were taken are marked with white lines. The FB and FL profiles correspond to the same molecule which is, to be judged from spatial distribution of the fluorescence signal and the fact that presents one of the most intense signals, oriented almost perfectly along the **z**-direction. The TL profile corresponds to a molecule that gave one of the strongest TL signals, therefore it should be oriented parallel to the interface and close to the **x**-direction. Plotted (in black) together with the FB and FL experimental profiles, are the profiles of the modelled signals corresponding to a fluorophore oriented along the **z**-axis, calculated for FB and FL illumination conditions respectively. Together with the experimental TL profile, the profile of the TL modelled signal of a fluorophore oriented along the **x**-axis is plotted (also in black). The theoretical profiles were not fitted to the experiment. They were all scaled by the same factor given by:

$$sf = \frac{FB_{max}^{exp} - BG_{FB}}{FB_{max}^{theo}} \tag{4.5}$$

where $FB_{max}^{exp}$ is the maximum of the experimental FB signal, $BG_{FB}$ is the average experimental FB background intensity and $FB_{max}^{theo}$ is the maximum of the modelled FB signal. After normalization, the experimental average background was added to the corresponding profile.

By applying the same scaling factor to the theoretical fluorescence signals shown in figures 4.14, 4.15 and 4.16, and comparing them to the experimental background, it is possible to identify the experimentally detectable signals. The signals surrounded by the dashed lines are the ones that present a peak value equal or higher

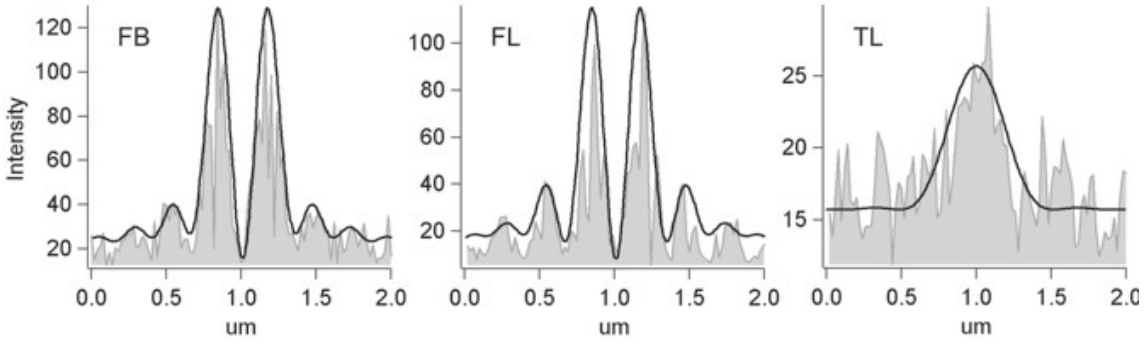


**Figure 4.18:** Experimental and theoretical fluorescence signals for the different illumination modes. Comparison of the profiles of the experimentally observed (grey filled) and the theoretical (black) fluorescence signals for the different illumination modes. The experimental profiles correspond to the white lines in the images of figure 4.5.

than 50% of the corresponding experimental background (this represents a signal to background ratio equal or higher than the TL signals shown in figure 4.18). Those signals are in principle detectable. With the same procedure it is possible to predict very low signal-to-background ratios for the fluorescence signals of single molecules on the spacer side of the interface.

The calculated fluorescence signals provide the explanation to the fact that the TL signals do not coincide with the FB or FL. As can be noted by comparing the theoretical fluorescence signals for FB or FL, to the ones for TL, the reason is that those signals correspond to different molecules with different orientations. Then, a FB/FL signal would coincide with a TL signal in only two cases. First, when the orientation of a molecule has an optimum compromise between x- and z-components, and even in this case, the detected signal would be very weak in comparison to the dominant signals of molecules oriented closer to the interface normal. Second, when more than one molecule lie close (on the same diffraction limited spot) to each other.

Due to the changes in the total de-excitation rate introduced by the gold presence, it is found that the number of detectable photons emitted by a parallel molecule in the sample with the gold film is 26% of the photons the same molecule would emit in a sample without the gold film. For the case of a perpendicular molecule, due to the surface plasmon enhancement, this percentage rises to 140%.

For the same sample geometry, the detection through the gold film was compared to the detection from the air side with an 0.9 NA objective. The surface plasmon mediated detection through the gold film is more effective for all dipole orientations and almost 7 times more effective for the perpendicular case.

# Chapter 5

# Influence of a nearby gold film on single molecule fluorescence dynamics

The fluorescence emission of a single molecule is a dynamic process that presents *bright* and *dark* periods due to temporary excursions of the excited molecule to the triplet states. The international scientific community baptized this phenomenon as fluorescence (*on-off*) *blinking*, and the traces of fluorescence emission vs. time as *kinetic traces*.

First in this chapter, the accepted theoretical model of molecular fluorescence blinking is presented. Then, two methods for the analysis of kinetic traces are presented and compared via Monte-Carlo simulations. Finally, the influence of a nearby metallic film on the fluorescence blinking of single dye molecules is experimentally investigated.

## 5.1 Single molecule fluorescence. Electronic transition rates

The simplest quantum mechanical picture that one can think of to represent the processes involved in molecular fluorescence and that can explain a dark state is a three-level system as depicted in figure 5.1: a ground singlet state S0, an excited singlet state S1, and a triplet state T1. The excited triplet and singlet states share the same common molecular geometry for some energy in order to allow inter-system crossing.

Upon absorption of a photon, an electron originally in S0 can be excited to S1 with a rate $\Gamma_{exc} = \Gamma_{12}$. Then, several processes can occur. The excited molecule can decay directly to the singlet ground state both radiatively and non-radiatively, with rates $\Gamma_{21,r}$ and $\Gamma_{21,nr}$, respectively. The molecule can perform many cycles like this

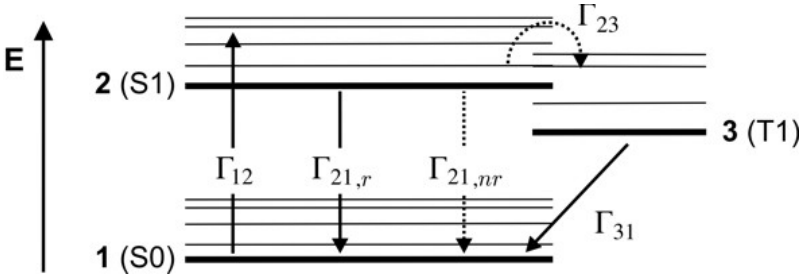


**Figure 5.1:** Three-level description of molecular fluorescence. S0 and S1 are the ground and excited singlet states, respectively, and T1 is the triplet. The levels are located vertically in a schematic energy (E) axis. The thin lines represent the vibrational states of each electronic state.

in the *singlet subspace* and emit a number of photons; i.e. the molecule is *bright*.

In addition, if there is a mechanism to unpair two electron spins (such as spin-orbit coupling) and the excited singlet state S0 shares for some energy the same molecular geometry with the triplet T1, the excited molecule may, with a probability given by $\Gamma_{23}$, undergo inter-system crossing (ISC) to the lower energy triplet state T1. Due to spin selection rules, the singlet-triplet transitions are radiative-forbidden [65]. The molecule is then trapped in the triplet state until ISC occurs again. During this time in the *triplet subspace*, the molecule remains *dark*.

If the triplet lifetime is long enough (slow $\Gamma_{31}$), these *bright* and *dark* periods can be observed when the fluorescence of a single molecule is followed in time. This effect is known as fluorescence or triplet *blinking* or *photon bunching*.

Based on this model, under constant excitation and far from optical saturation ($\Gamma_{21,r} \gg \Gamma_{12}$), the fluorescence intensity $I$ emitted by a single molecule, while it cycles in the singlet subspace, is given by the product of the radiative decay rate and the fractional instant population of the singlet excited state:

$$I = \Gamma_{21,r} \frac{\Gamma_{12}}{\Gamma_{21,r} + \Gamma_{21,nr} + \Gamma_{23}} \tag{5.1}$$

And the fluorescence intensity while the molecule resides in the triplet subspace is zero. However, in a real experiment, only a fraction of the emitted photons are detected and there is always a background intensity $I_{bg}$. Then the experimental intensities while the molecule cycles in the singlet or the triplet subspace, called $I_{on}$ and $I_{off}$, respectively, are:

$$I_{on} = \Gamma_{21,r}^{det} \frac{\Gamma_{12}}{\Gamma_{21,r} + \Gamma_{21,nr} + \Gamma_{23}} + I_{bg} \tag{5.2}$$

$$I_{off} = I_{bg} \tag{5.3}$$

where $\Gamma_{21,r}^{det}$ is the fraction of the radiative decay rate emitted into the detector.

It is also possible to derive the transitions rates from the on-state to the off-state, and viceversa. Following the nomenclature proposed in [66], the rate for the transition from the off- to the on-state will be called $k_{on}$, the transition rate from the on- to the off-state will be called $k_{off}$. Then, $k_{on}$ is simply the relaxation rate of the triplet state $\Gamma_{31}$, and $k_{off}$ is the product of the fraction of time that the molecule spends in the singlet excited state S1, and the probability to jump to the triplet state T1:

$$k_{on} = \Gamma_{31} \tag{5.4}$$

$$k_{off} = \Gamma_{23} \frac{\Gamma_{12}}{\Gamma_{21,r} + \Gamma_{21,nr} + \Gamma_{23}} \tag{5.5}$$

As the on→off and on←off transitions are single rate processes, the length of the on- and off-periods ($t_{on}$ and $t_{off}$) are exponentially distributed:

$$\begin{aligned} P(t_{on} = t) &= \tfrac{1}{\tau_{on}} e^{-t/\tau_{on}} \\ P(t_{off} = t) &= \tfrac{1}{\tau_{off}} e^{-t/\tau_{off}} \end{aligned} \tag{5.6}$$

with average times for each state given by:

$$\begin{aligned} \tau_{on} &= \frac{1}{k_{off}} = \frac{\Gamma_{21,r} + \Gamma_{21,nr} + \Gamma_{23}}{\Gamma_{12}\Gamma_{23}} \\ \tau_{off} &= \frac{1}{k_{on}} = \frac{1}{k_{31}} \end{aligned} \tag{5.7}$$

Then, the time averaged intensity of a single molecule is given by:

$$\langle I \rangle = \frac{I_{on}\tau_{on} + I_{off}\tau_{off}}{\tau_{on} + \tau_{off}} = \frac{I_{on}k_{off} + I_{off}k_{on}}{k_{on} + k_{off}} \tag{5.8}$$

From equations 5.8, 5.4 and 5.5, it can be seen that for the case of $k_{off} \gg k_{on}$, the fluorescence emission is limited to a value independent of the excitation rate given by:

$$I_{triplet} = \frac{\Gamma_{21,r}\Gamma_{31}}{\Gamma_{23}} + I_{bg} \tag{5.9}$$

This effect is called triplet saturation or triplet bottleneck.

## 5.2 Kinetic traces analysis methods

Kinetic traces are recorded with the TCSPC module as explained in section 2.4.3. In order to extract the desired information about triplet blinking dynamics from the recorded photon detection times, it is necessary to analyze carefully the raw data obtained with the TCSPC module (see section 2.2.4). Figure 5.2 shows as an example the TCSPC mac-t times corresponding to 239980 photons detected during 18 seconds from a single DiIC1(5) molecule. The intensity fluctuations can be observed as changes in the slope of the curve, as shown in the small inset of figure 5.2. When the molecule is emitting, more photons are detected in a unit time, and therefore the slope is lower. The opposite occurs when the molecule is not emitting. For an ideal on⥋off system, only two slopes would be observed.

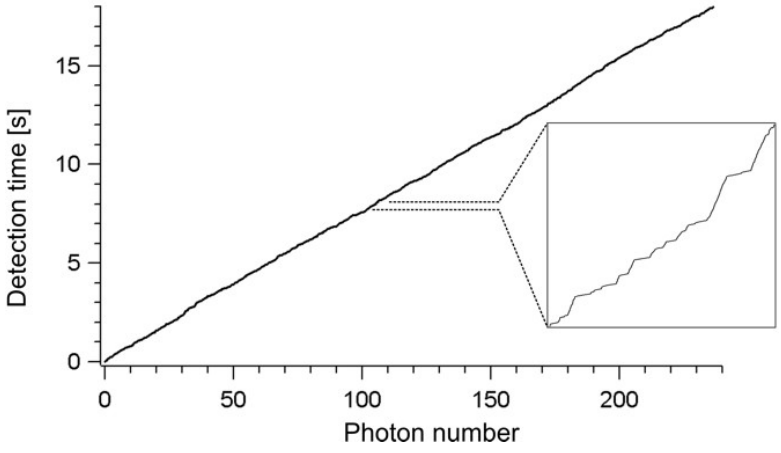


**Figure 5.2:** Photon detection times. Arrival times (TCSPC mac-t times) of each detected fluorescence photon in chronological order. Fluorescence on- and off-periods are observed as fluctuations in the slope of the curve.

Two methods were used to extract the on⥋off transition rates from the TCSPC data. The first one, is based on a widely used method for the analysis of the intensity autocorrelation and is explained in section 5.2.1. The second method, described in section 5.2.2, consists of finding the optimum bin-width to make a histogram of the data and then distinguishing the on- and the off-periods with a suitable threshold.

### 5.2.1 Autocorrelation analysis

The autocorrelation method was first developed for the study of triplet intensity fluctuations of single molecules in solution [67] and then applied to the study of immobilized single molecules at cryogenic [68, 69] and room temperatures [70, 71].

The normalized intensity autocorrelation is defined as the rate of detection of two photons in a time interval $\tau$ relative to that rate if the photon detection would

be uncorrelated and can be expressed as:

$$C^{(2)}(\tau) = \frac{\langle I(t)I(t+\tau)\rangle}{\langle I(t)\rangle^2} \tag{5.10}$$

where $I(t)$ is the intensity as a function of time and the angle brackets denote time average. In practice, the TCSPC data is divided in time intervals of a given size $bw$ and the autocorrelation is calculated as:

$$C^{(2)}(\tau) = \frac{\langle N(t)N(t+\tau)\rangle}{\langle N(t)\rangle^2} \tag{5.11}$$

where $N(t)$ are the photons detected in a given interval (of length $bw$) centered at a time $t$ and the angle brackets denote time average. As an example, the autocorrelation of the data shown in figure 5.2 is shown in figure 5.3.

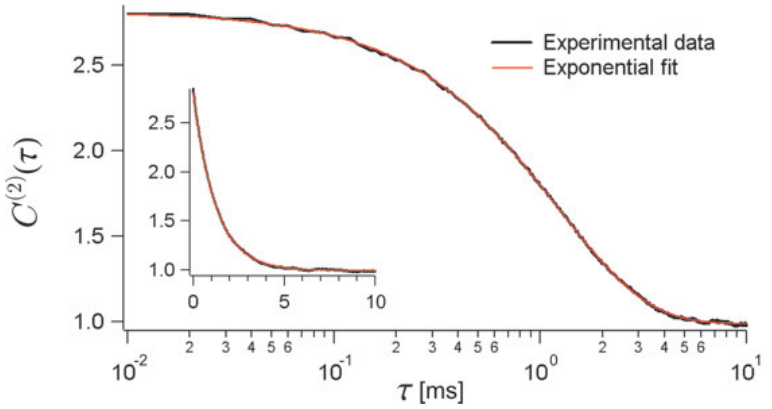


**Figure 5.3:** Autocorrelation of the data shown figure 5.2. The horizontal axis has a logarithmic scale to easily identify the inflexion point which abscissa corresponds to the characteristic time of the process observed. In the inset, the same data is plotted with linear scales. The experimental data can be satisfactorily fitted with a single exponential decay.

For uncorrelated events $C^{(2)}(\tau) = 1$ and for correlated events $C^{(2)}(\tau) > 1$. If $C^{(2)}(\tau)$ is computed in the right time window for a certain process, a decay of $C^{(2)}(\tau)$ to unity is observed as $\tau$ increases. From this decay it is possible to extract information about the characteristic time of the process dynamics. For the fluctuations of the fluorescence emission of a single molecule due to excursions from the excited singlet state to the triplet state, the autocorrelation decay is a single exponential (see figure 5.3). Based on the 3-level model introduced in section 5.1 it is possible to obtain an analytical expression for this exponential decay [72, 73]:

$$C^{(2)}(\tau) = 1 + A\ e^{-\kappa\ \tau}$$

$$\kappa = k_{on} + k_{off} \tag{5.12}$$

$$A = \frac{k_{on}\ k_{off}\ \left(I_{on} - I_{off}\right)^2}{\left(k_{on} I_{on} + k_{off} I_{off}\right)^2}$$

$I_{on}$ and $I_{off}$ are the intensities of the on- and off-states respectively. $k_{on}$ and $k_{off}$ the rate constants of the on⇆off transitions as defined in section 5.1 (equations 5.4 and 5.5). The equations 5.12 are valid under two conditions [68]. First the times probed by $C^{(2)}(\tau)$ are long in comparison to the total radiative decay time, which means that photon anti-bunching and Rabi oscillations are not visible. Second, the assumption is made that the inter-system crossing rate $\Gamma_{23}$ (see figure 5.1) and the triplet relaxation rate $\Gamma_{31}$ are much smaller than the total decay of the excited singlet $\Gamma_{21,r} + \Gamma_{21,nr} + \Gamma_{23}$. Single molecule triplet blinking normally fulfils the two conditions.

Values for $A$ and $\kappa$ can be obtained from an exponential fit to the experimental autocorrelation (see figure 5.3). Then, by combining equations 5.8 and 5.12 it can be found that:

$$k_{off} = \frac{\kappa\, A\, \langle I \rangle^2}{A\, \langle I \rangle^2 + \left(\langle I \rangle - I_{off}\right)^2} \tag{5.13}$$

All the parameters in equation 5.13 can be determined experimentally: $I_{off}$ is the average experimental background intensity and $\langle I \rangle$ is the overall average intensity; i.e. the total number of detected photons divided by the total collection time. Finally, $k_{on}$ can be obtained from equation 5.12.

### 5.2.2 Trace-histogram analysis

If one makes a time histogram of the raw data shown in figure 5.2, one finds some bins with a high number of photons corresponding to the on state, and some bins with a low number of photons corresponding to the off state of the molecule (figure 5.4.a). Then, it possible to choose a threshold $T$, a number of photons marked by the horizontal line in figure 5.4.a, and classify all the bins with less than $T$ photons as off-bins, and all the bins with $T$ photons or more as on-bins. From this histogram analysis it is possible to calculate the average length of the on- and off-periods that lead to the values of $k_{on}$ and $k_{off}$.

However, choosing arbitrary bin-widths and thresholds can yield misleading information. As can be seen in figure 5.4.b, a broad bin-width can help to distinguish better between the two states, but the price to pay is that many short on- and

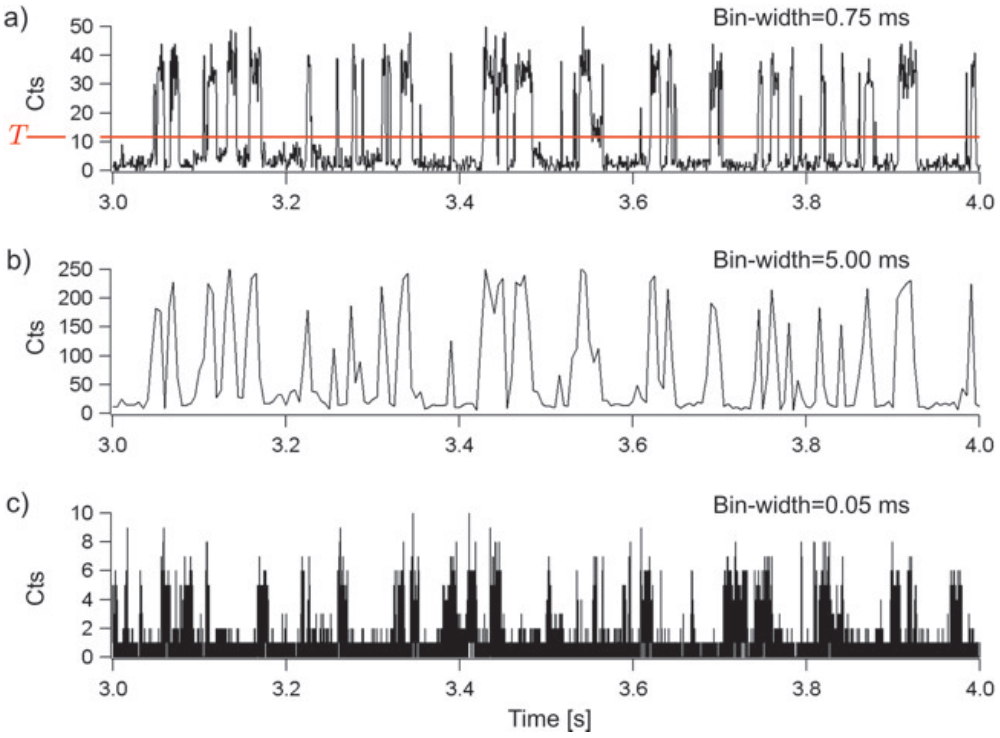


**Figure 5.4:** Effect of the bin-width on the kinetic trace histogram analysis. Time histograms of the kinetic trace data shown in figure 5.2 computed with different bin-widths: a) 0.75 ms. b) 5 ms. c) 0.05 ms. To distinguish the on- from the off-bins it is necessary to set a threshold, for example the horizontal line shown in a).

off-periods remain hidden inside the big bins. The opposite occurs if one takes very narrow bins (figure 5.4.c), the increase in time resolution is paid by higher uncertainty in distinguishing which bin is on and which is off. Then, there is a bin-width (range) that makes the optimum compromise between time resolution and accuracy in distinguishing the on from the off state. The procedure presented here is dedicated to find this bin-width, place a suitable threshold and extract the information from the data histogram.

This method is based on the fact the on-state and the off-state have a characteristic intensity $I_j$, $j$ standing for on or off. Then, the number of detected photons $N$ in a unit time in any of the two (on or off) states is a Poisson random variable with an average rate $I_j$ and the probability of detecting $k$ photons in a time unit is:

$$P_{(N=k)} = \frac{{I_j}^k \, e^{-I_j}}{k!} \tag{5.14}$$

The number of photons $N_t$ detected not in a time unit but in a time interval

$t > 0$ is then:

$$P_{(N_t=k)} = \frac{(I_j t)^k \; e^{-I_j\, t}}{k!} \tag{5.15}$$

Calling $X$ the waiting time until the next photon, the probability that $X$ is larger than a time $t$ can be calculated as:

$$P_{(X>t)} = P_{(N_t=0)} = e^{-I_j\, t} \tag{5.16}$$
$$\Rightarrow P_{(X<t)} = 1 - e^{-I_j\, t} \tag{5.17}$$
$$\Rightarrow P_{(X=t)} = I_j \; e^{-I_j \; t} \tag{5.18}$$

This has the consequence that the probability of detecting a photon at a given time is independent of when the last photon was detected; i.e. the process of detecting photons is memoryless (which can be seen by verifying that for $0 < s < t$, $P_{(X>t\,/\,X>s)} = P_{(X>t-s)} P_{(X>s)} = P_{(X>t)}$).

The time elapsed between two consecutive detected photons (inter-photon times) is a probe of $P_{(X>t)}$. As there are two populations, the on and the off, with two different average intensities, $I_{on}$ and $I_{off}$, a double exponential (equation 5.16) curve is found in a histogram of the inter-photon times:

$$P_{(X>t)} = A_{on}\, e^{-I_{on}\, t} + A_{off}\, e^{-I_{off}\, t} \tag{5.19}$$

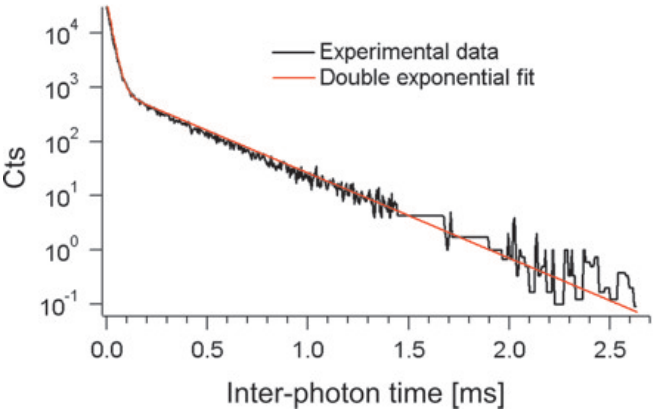


**Figure 5.5:** Inter-photon times histogram. Histogram of inter-photon times of the data shown in figure 5.2. For the double exponential fit one of the exponents is fixed to the value of the experimental average background intensity $I_{off}$.

Figure 5.5 shows the inter-photon times histogram of the data shown in figure 5.2. A double exponential fit allows to obtain the experimental values for $I_{on}$ and $I_{off}$ from the exponents. In fact, there is no need to extract $I_{off}$ from the fit, it is possible to obtain it directly from the data as the average background intensity, and use this value as a constraint in the fit to obtain $I_{on}$. But there is more information to be extracted from the two pre-factors, $A_{on}$ and $A_{off}$. The normalized exponential probability distribution of equation 5.16, is continuous in time and considers the

detection time of one photon. Then, it has a pre-factor equal to one ($\lim_{\Delta t \to 0} P_{(X>\Delta t)} = 1$). Instead, the histogram of figure 5.5 is discrete in time and considers the detection times of a number of photons; $N_{on} + N_{off}$ photons of the on and off state respectively are grouped in bins of bin-width $bw$. In this case, the pre-factors $A_{on}$ and $A_{off}$ for the discrete probability distributions are the number of photons to be found in a certain bin. From equation 5.18:

$$A_j = \frac{N_j \int_t^{t+bw} I_j \, e^{-I_j \, t} \, dt}{e^{-I_j \, t}} = N_j \left(1 - e^{-I_j \, bw}\right) \tag{5.20}$$

where $j$ stands for on or off, depending on the population. Then, the total number of photons detected in each state can be directly calculated from the double-exponential pre-factors $A_{on}$ and $A_{off}$ as:

$$N_j = \frac{A_j}{(1 - e^{-I_j \, bw})} \tag{5.21}$$

Finally, considering that the average intensity of each of the states is simply the ratio between the total number of photons and the total time in that state ($I_J = N_j/T_j$), the total time that the molecule spends on the on- or off-state can be calculated as:

$$T_j = \frac{A_j}{I_j \, (1 - e^{-I_j \, bw})} \tag{5.22}$$

Next, with the information obtained from the inter-photon time histogram, an iterative process is carried out in order to find the optimum bin-width and threshold that allow to distinguish between the on and off states with the highest accuracy and time resolution from a histogram of the kinetic trace.

For a given bin-width $bw$, the number of photons per bin of the on- or off-population is given by equation 5.15 with $t = bw$. Then, in the histogram of the kinetic trace, there are two populations of photons per bin, the on- and the off-populations which have $n$ photons per bin with a probability given by:

$$P_j(n) \; = \; \frac{(I_j \, bw)^n \; e^{-I_j \, bw}}{n!} \tag{5.23}$$

The iterative process starts with a very small bin-width (25 ns), and calculates the number of bins corresponding to each state $bins_{\,j} = T_j/bw$. Then, the total number of bins that are wrongly classified when a threshold $T$ is used to distinguish the on- from the off-bins can be calculated by:

$$Wrong \; bins = bins_{\,on} \sum_{n=0}^{T} P_{on}(n) + bins_{\,off} \left(1 - \sum_{n=0}^{T} P_{off}(n)\right) \tag{5.24}$$

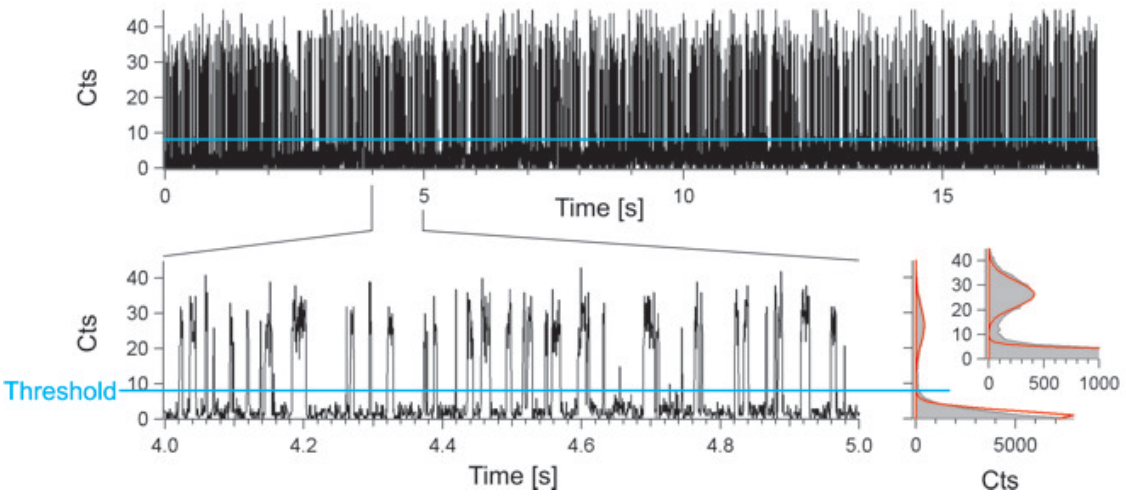


**Figure 5.6:** Kinetic trace histogram. Top, optimum bin-width (0.61 ms) histogram of the data shown in figure 5.2. The horizontal line shows the optimum threshold (9 photons) to distinguish the on- from the off-bins. Bottom-right, the intensity histogram (photons per bin, solid grey) and Poisson distributions. The vertical scale is the same as in the histogram. In the small graph the intensity histogram and the Poisson distributions are plotted up to 1000 counts.

For a given bin-width, the total number of wrongly classified bins is calculated for different values of the threshold sweeping from zero to the average of the on-population ($I_{on}\, bw$). The optimum threshold (for the given bin-width) is found if less than 1 bin is wrongly classified. In case no threshold fulfils that condition, the bin-width is increased and the procedure is repeated successively. In this manner, the minimum bin-width that allows to place a threshold between the (Poisson-distributed) on- and off-populations that fulfils the condition $Wrong\ bins < 1$ is found. Then, a time histogram of the data is constructed with the optimum bin-width and the on- and off-periods are identified via the optimum threshold with the highest reliability and time resolution possible.

Figure 5.6 shows the optimum bin-width histogram of the data shown in figure 5.2 and the optimum threshold (horizontal line). On the bottom of figure 5.6 a smaller region of the histogram is shown corresponding to the photons detected between the fourth and fifth second. The on$\leftrightarrows$off fluorescence fluctuations can be clearly seen. On the bottom-right of figure 5.6 the histogram of the photons per bin (intensity) obtained in the kinetic trace histogram (solid grey) is shown. The on-intensity and the off-intensity can be clearly distinguished. The curves are Poisson distributions defined by equation 5.23 scaled to the corresponding maximum of the on- or off-intensity. In the small graph, only the region from 0 to 1000 counts in the horizontal scale is plotted, in order to observe better the on-intensity distribution and the region between the on- and off-intensities. It can be seen that in the region between the on- and off-intensities, the experimental intensity deviates from the Poisson distributions to higher values. This corresponds to *mixed* bins in which a

part of an on-time and a part of an off-time occurred. This can be due to on-times shorter than the bin-width or to bins computed at the beginning or the end of an on-time. The latter being the most probable because the average on-time $\tau_{on}$ is much larger than the bin-width (see below).

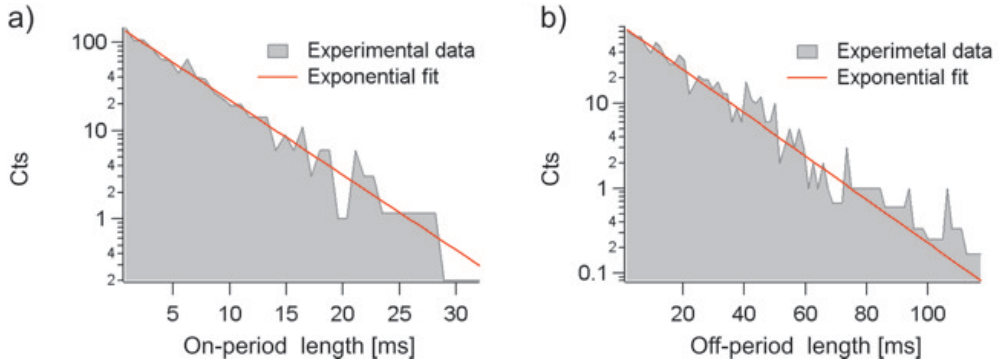


**Figure 5.7:** Histograms of the length of the on-periods (a) and of the off-periods (b) obtained from the analysis of the kinetic trace histogram of figure 5.6.

The optimized kinetic trace histogram can be analyzed to find the on- and off-bins and determine the length of the on- and off-periods. Histograms of the length of the on- and off-periods show exponential decays with exponents equal to $k_{on}$ and $k_{off}$ respectively (equations 5.6). Figure 5.7 shows the histograms of the length of the on- (a) and off-periods (b) obtained from the analysis of the kinetic trace histogram shown in figure 5.6. The values of $k_{on}$ and $k_{off}$ are obtained from the exponential fits.

### 5.2.3 Comparison

Table 5.1 presents the results obtained from the analysis of the data of shown in figure 5.2 via the autocorrelation and trace-histogram methods. Both methods provide similar but not equal results.

The trace-histogram method retrieves a value of $I_{on}$ slightly lower than the real one and a value of $I_{off}$ slightly higher than the real one. This is a consequence of the *mixed bins* explained above: some of the on-photons are computed in *mixed bins* that do not reach the threshold to be counted as on-bins.

#### Monte-Carlo simulated data

In order to know which analysis is more reliable, both methods were tested with Monte-Carlo simulations. A three-level system like the one described in section 5.1 was programmed in Igor [21]. The input parameters are the transition rates ($\Gamma_{12}$, $\Gamma_{21}$, $\Gamma_{23}$, $\Gamma_{31}$), the background count-rate ($I_{off}$), and the total time. The Monte-Carlo simulation generates a set of TCSPC mac-t (photon detection) times

| Parameter \ Method | Interphoton times | Trace Histogram | Auto-correlation |
|---|---|---|---|
| Ion [1/s] | 46600 | 43600 | 46200 |
| Ioff [1/s] | 3610 | 4010 | 3610 |
| ton [s] | 3.9 | 4.1 | 4.0 |
| toff [s] | 15.1 | 13.8 | 14.0 |
| $k$on [1/s] | | 75.1 | 72.8 |
| $k$off [1/s] | | 250 | 252 |
| $\tau$off [ms] | | 13.3 | 13.7 |
| $\tau$on [ms] | | 4.0 | 4.0 |

**Table 5.1:** Results of the analysis of the TCSPC data shown in figure 5.2. The autocorrelation and trace-histogram methods provide similar but not exactly the same results.

that can be then analyzed with the autocorrelation and trace-histogram methods and the reliability with which both methods retrieve the original rates can be tested.

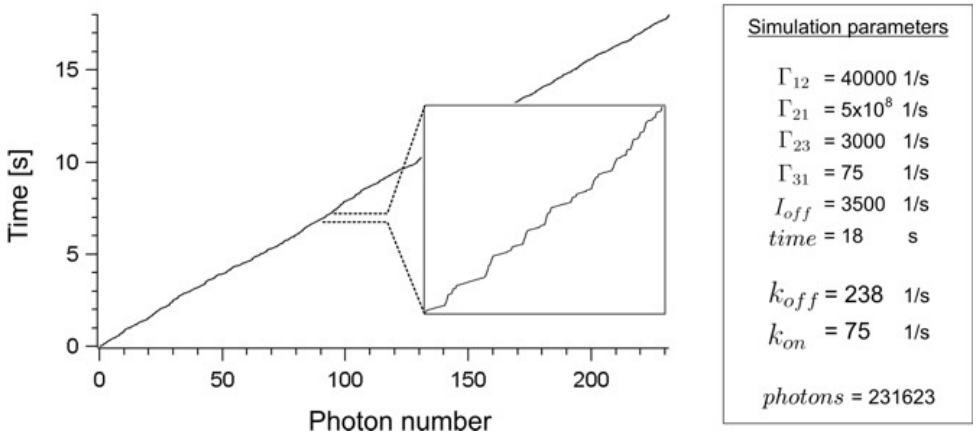


**Figure 5.8:** Monte-Carlo simulated detection times of photons emitted by a single molecule based on a 3-level system (section 5.1. The transition rates used for the simulation are listed on the right together with values of $k_{on}$ and $k_{off}$.

A simulated TCSPC (mac-t times) trace with a length of 18 seconds is shown in figure 5.8. The input parameters are listed on the right of figure 5.8 and were chosen to generate simulated data similar to the experimental one (figure 5.2) that was analyzed in the previous two sections.

Figure 5.9.a shows the autocorrelation of the photon detection times and figure 5.9.b the inter-photon times histogram. Figure 5.9.c presents a histogram of the simulated kinetic trace with the optimum bin-width. The optimum bin-width for the simulated data is very similar to the one determined for the experimental data and the threshold is the same. The *mixed bins* are observed in the simulated data as well; they represent an intrinsic limitation of the trace-histogram method. Figure

| Parameter \ Method | Simulation | Interphoton times | Trace Histogram | Auto-correlation |
|---|---|---|---|---|
| Ion [1/s] | 43261 | 43907 | 40700 | 42700 |
| Ioff [1/s] | 3500 | 3500 | 3650 | 3500 |
| ton [s] | 4.3 | 4.29 | 4.6 | 4.4 |
| toff [s] | 13.7 | 13.7 | 13.4 | 13.6 |
| $k_{on}$ [1/s] | 75 | | 75.8 | 74.5 |
| $k_{off}$ [1/s] | 238 | | 236 | 232 |
| $\tau_{off}$ [ms] | 13.3 | | 13.2 | 13.4 |
| $\tau_{on}$ [ms] | 4.2 | | 4.2 | 4.3 |

**Table 5.2:** Comparison of the analysis results of the simulated data obtained by the autocorrelation and the trace-histogram methods.

5.9.d presents the histogram of the length of the simulated on- and off-periods.

The results obtained from the analysis of the simulated data with the autocorrelation and trace-histogram methods are presented in table 5.2. Again, both methods provide values for $k_{on}$ and $k_{off}$ similar to the real ones but still different.

To test the reliability of the two methods to retrieve the values of $k_{on}$ and $k_{off}$, kinetic traces of different total times (10 for each time) were simulated with the input parameters shown in figure 5.8 and analyzed with both methods. The average values obtained for $k_{on}$ and $k_{off}$ are plotted in figure 5.10; the error bars denote plus minus one standard deviation.

The longer the kinetic traces, the higher the number of on-off cycles and therefore the results become more accurate with both methods. The trace-histogram method retrieves systematically slightly lower values of $k_{off}$. Even though the statistical errors are similar for both methods, the average values of $k_{on}$ and $k_{off}$ provided by the autocorrelation method are closer to the actual values (note that the first point of $k_{off}$ obtained by the TH method is out of the range of the plot).

The application of the autocorrelation method as presented here is limited to 3-level single molecule fluorescence blinking. In contrast, the trace histogram method is more versatile and can be applied to a other kinds of blinking process.

## 5.3 Experimental

The experimental scheme is shown in figure 5.11. Single fluorescent dye molecules (DiIC1(5), *Molecular probes*) are deposited at the interface between a layer by layer polyelectrolyte film and air.

Two kinds of samples were prepared. In the ones, the polyelectrolyte film was deposited directly on a glass substrate (sample A in figure 5.11). In the others, the polyelectrolyte film was used to place the chromophores at a controlled distance from a thin gold film (sample B in figure 5.11), exactly as described in chapter 4.

Like this, the chromophores environment is the same in both samples and the

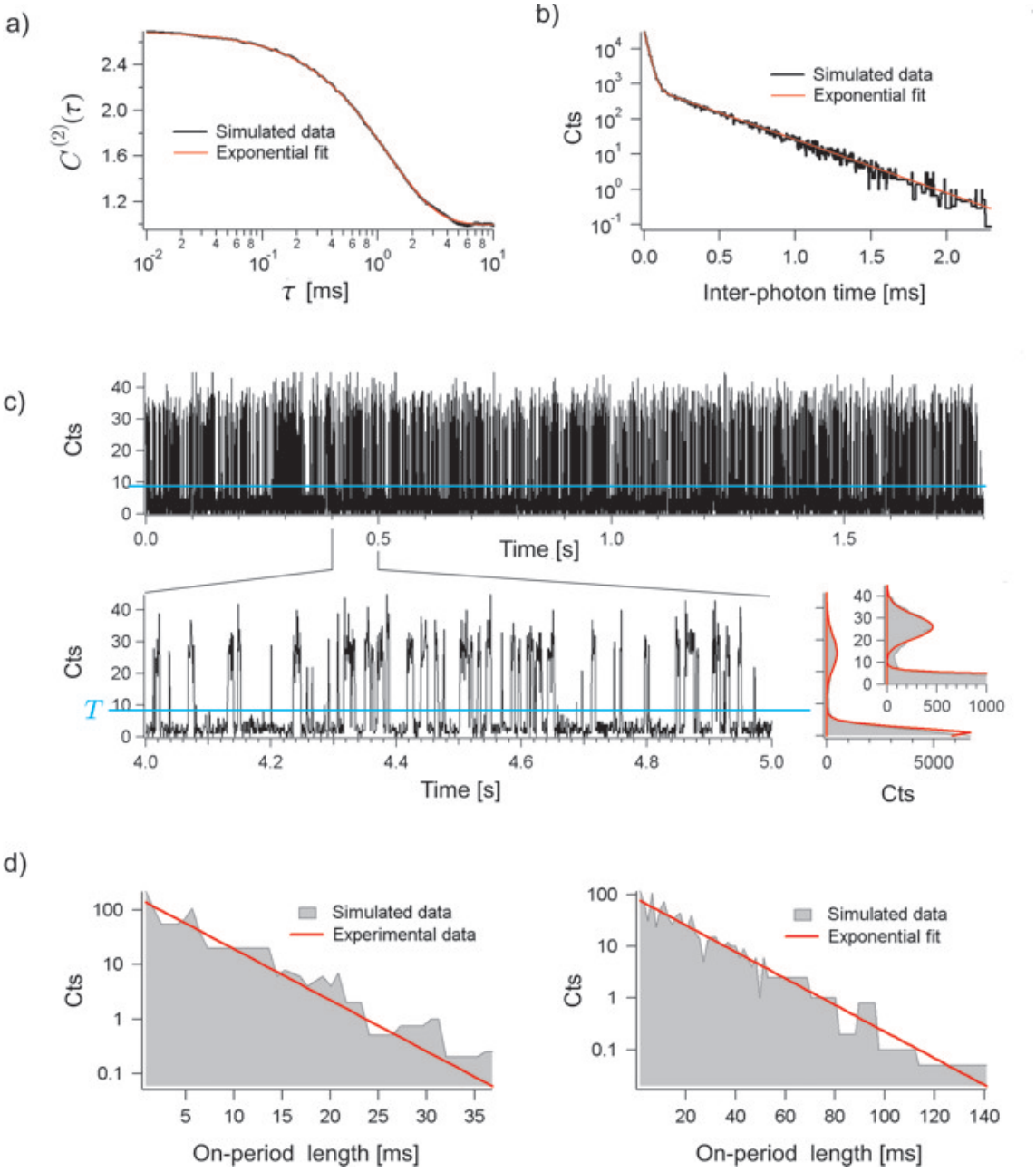


**Figure 5.9:** Analysis of the simulated data. Autocorrelation and trace-histogram analysis of the simulated data shown in figure 5.8. a) Autocorrelation. b) Inter-photon times histogram, c) histogram of the kinetic trace with optimum bin-width (0.66 ms) and poisson on- and off-population of number of photons per bin. The optimum threshold (9 photons) is marked by the horizontal line. d) Histograms of the length of the on- and off-periods of the simulated kinetic trace.

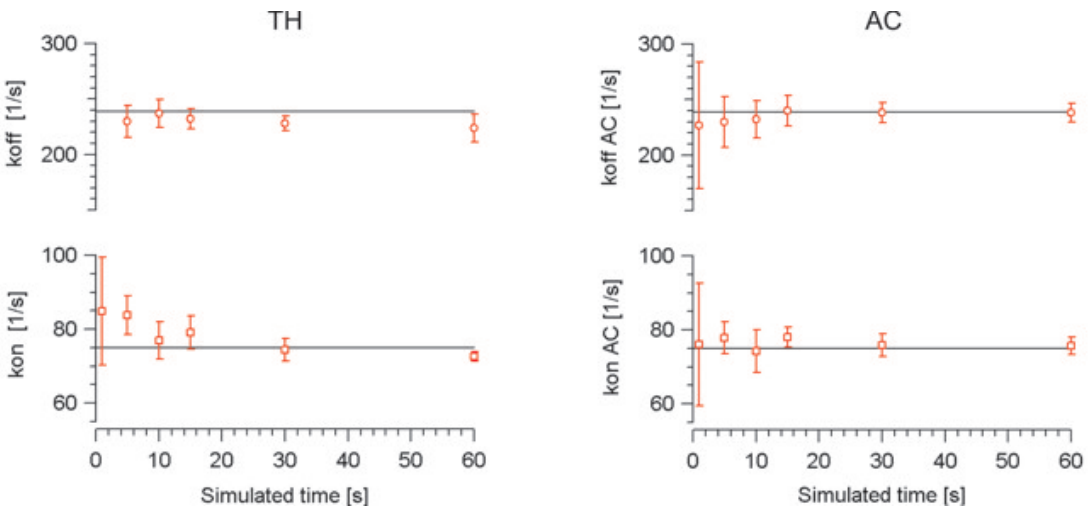


**Figure 5.10:** Average values of $k_{on}$ and $k_{off}$ retrieved by the trace-histogram (TH) and autocorrelation (AC) methods from the analysis of simulated kinetic traces of different length (simulated time).

only difference between the samples is the presence or the absence of the nearby gold film.

In both cases, the fluorescence emission as a function of time, as well as the excited state lifetime were recorded from single molecules, in order to gain information about the influence of the nearby gold film on the electronic transitions rates.

### 5.3.1 Sample preparation

The samples with gold film were prepared with a 4-bilayer polyelectrolyte spacer following the method described in 4.2.1.

The samples without gold, were prepared with a 2.5-bilayer polyelectrolyte film deposited onto 3-aminopropyltriethoxy-silane (3-APTES, *Aldrich*) functionalized glass substrates. The functionalization of the glass substrates was accomplished by the following steps:

- Cleaning with surfactant (*Hellmanex-II, Hellma GmbH*) and water.
- Treatment with a 1:1:5 mixture of $H_2O_2$:$NH_3$:$H_2O$ at 80 °C for 30 minutes.
- Silanes self assembly by immersing the substrates for one hour in a 0.1 M Milli-Q water solution of 3-APTES.
- Rinsing with Milli-Q water and drying with nitrogen.
- Annealing for one hour at 120 °C.

The so prepared substrates contain free amino groups which in water render

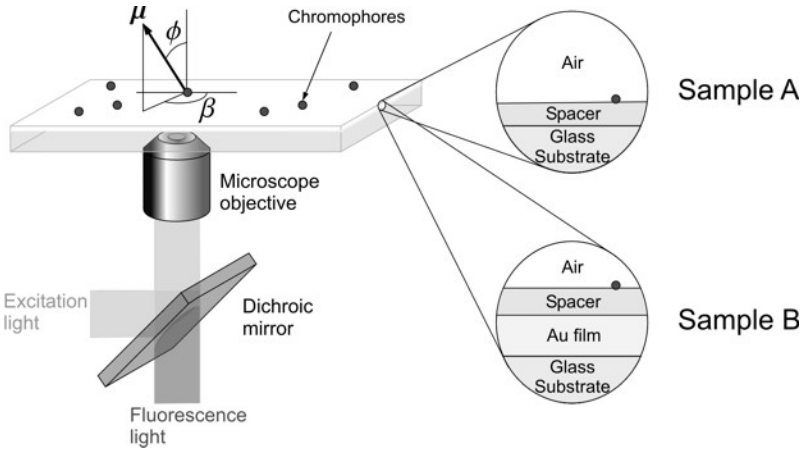


**Figure 5.11:** Schematic of the experimental configuration. Fluorescent dye molecules with arbitrary orientations (defined by $\beta$ and $\phi$) of their transition dipoles $\boldsymbol{\mu}$ are placed at the interface between a polyelectrolyte film and air. In sample A, the polyelectrolyte film is deposited directly on a glass substrate. In sample B, the polyelectrolyte film acts as a dielectric spacer between the chromophores and a 44 nm gold film.

the surface positively charged. Then, a 2.5-bilayer polyelectrolyte film was deposited by the layer by layer method starting with PSS, as described in the previous chapter (section 4.2.1). Finally, single fluorescent dye molecules 1,1',3,3,3',3'-hexamethylindicarbocyanine iodide [DiIC1(5), *Molecular probes*, maximum excitation at $\lambda_{exc} = 638\,\text{nm}$, maximum emission at $\lambda_{em} = 670\,\text{nm}$] were deposited electrostatically on a negatively charged surface terminated with PSS, by immersing the samples for one minute in a $10^{-10}$ M, Milli-Q water solution of the dyes. Then, the samples were rinsed with Milli-Q water and dried with a stream of nitrogen.

### 5.3.2 Measurement

The measurements were performed with the SCOM set-up described in chapter 2 and consisted of imaging a region of the samples, identifying a single molecule and recording the fluorescence emission of that molecule as a function of time. The avalanche photo diode (APD) was used as single photon detector and the red pulsed diode laser was used for excitation at 633 nm with a repetition rate of 50 MHz. The total instrumental response was limited by the APD response to 1 ns. The fluorescence emission was recorded as a function of time with the TCSPC module (see section 2.2.4). The mac-t times contain information about fluorescence fluctuations in a time-scale longer than several hundreds of $\mu$s, such as the triplet blinking. The mic-t times allow to obtain the excited state lifetime with a resolution limited by the APD response.

Kinetic traces from around 35 molecules in each of the samples were recorded

and analyzed with the trace-histogram and autocorrelation methods. Since the autocorrelation method is more accurate, only the results obtained with this method were taken into account. Nevertheless, only the kinetic traces that showed a three-level behavior with both methods were considered; i.e. the autocorrelation and the histograms of the length of the on- and of-periods were satisfactorily fitted by a single exponential.

## 5.4 Influence of a nearby thin Au film on the electronic transition rates

Figure 5.12 shows the distributions of the singlet decay rate $\Gamma_{21}$ (inverse of the excited state lifetime), $k_{on}$ and $k_{off}$ obtained from 33 molecules in the sample without the gold film and 42 molecules in the sample with the gold film. The influence of the gold presence on each rate is analyzed next.

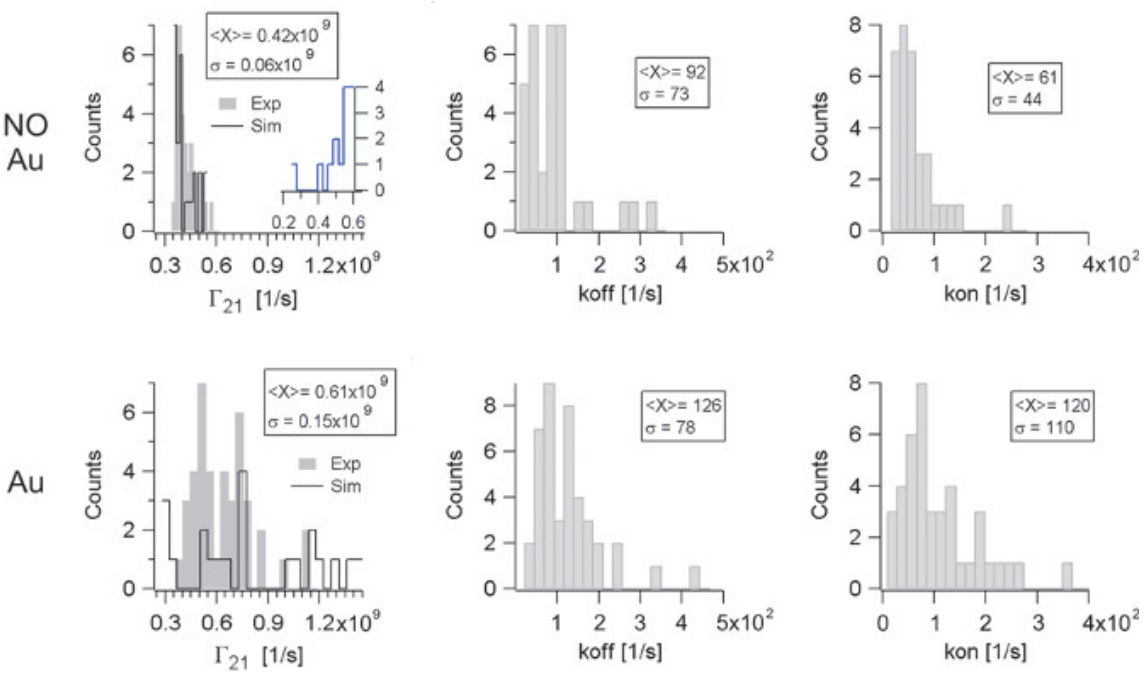


**Figure 5.12:** Distributions of values of $\Gamma_{21}$, $k_{on}$ and $k_{off}$ obtained via the autocorrelation analysis of the kinetic traces from molecules in the samples with (bottom) and without (top) the gold film. The averages and standard deviations are shown in the graphs. In the case of $\Gamma_{21}$, together with the experimental distributions (Exp), Monte-Carlo simulated (Sim) distributions considering the chromophores on the air side are plotted. The inset in the graph of $\Gamma_{21}$ for the case without gold is a Monte-Carlo simulated distribution considering the chromophores on the spacer side of the interface.

| | $\Gamma^{em}_{total}$ $\parallel$ | $\Gamma^{em}_{total}$ $\perp$ |
|---|---|---|
| without Au | 1.34 | 2.21 |
| with Au | 1.05 | 5.75 |

**Table 5.3:** Calculated normalized total electromagnetic de-excitation rate of a parallel and a perpendicular dipole in the samples with and without gold (on the air side of the spacer/air interface).

### 5.4.1 Influence on $\Gamma_{21}$

The influence of the gold can be clearly seen by comparing in the distributions of $\Gamma_{21}$ for the molecules in the samples with and without gold.

The molecules in the sample without the gold film present a narrow distribution with an average value of $0.42 \times 10^9$ 1/s which width and asymmetry can be explained by the different orientations of the molecules. The total electromagnetic decay rate of a chromophore in the samples with gold was calculated in section 4.4.2 by means of the method described in section 3.2. The same method can be used to calculate the decay rate of molecules in the samples without the gold film. In chapter 4, it was concluded that the chromophores electrostatically deposited on the surface of the polyelectrolyte spacer behave optically as being on the air side of the spacer/air interface. Nevertheless, it is worth to consider the two possibilities again and see whether that statement is confirmed or not. The calculated total electromagnetic decay rates of molecules on the air side of the spacer/air interface which transition dipole lie parallel and perpendicular to the polyelectrolyte surface are listed in table 5.3. Since these rates are normalized to the total emission of a dipole in air, they are proportional to the actual rates.

The parallel and perpendicular dipoles are the limiting cases and molecules with orientations in between have intermediate decay rates. In the absence of the gold film, the ratio $\Gamma^{em}_{total,\perp}/\Gamma^{em}_{total,\parallel}$ is 1.65 and can quantitatively account for the observed range of $\Gamma_{21}$ values. The asymmetry of the distribution in favor of lower values of $\Gamma_{21}$ arises from the facts that the molecules are randomly oriented in the sample and that they were randomly selected to be studied. Then, as there are more molecules oriented parallel to the surface, the distribution is richer in lower values of $\Gamma_{21}$. To illustrate this effect, a Monte-Carlo simulated distribution of $\Gamma_{21}$ values is shown in figure 5.12 together with the experimental data[1]. This result supports

[1]The simulations consider molecules randomly oriented in three dimensions and that are randomly selected. The simulated distributions, as the experimental ones, are made up of 33 and 42 values for the cases without and with Au, respectively. The $\Gamma_{21}$ of an arbitrarily oriented molecule was calculated by equation 3.5. For the case of chromophores on the AIR side of the interface, the values of $\Gamma_{21,\parallel}$ and $\Gamma_{21,\perp}$ were obtained by multiplying the theoretical values (shown in table 5.3) by a factor equal to the ratio of the MINIMUM detected $\Gamma_{21}$ in the sample without gold and the theoretical value for the parallel dipole $\Gamma_{21,\parallel}$ (0.35/1.34=0.26). For the case of chromophores in the spacer side of the interface, the theoretical values were multiplied by a factor equal to the ratio of the MAXIMUM detected $\Gamma_{21}$ in the sample without gold and the theoretical value for the parallel dipole $\Gamma_{21,\perp}$ (0.63/1.34=0.47).

the conclusion made in chapter 4 that the chromophores behave optically as being in the air side of the spacer/air interface. If the chromophores were in the polymer side, due to the electromagnetic boundary conditions at the interface (see section 3.1), the parallel molecules would have the same $\Gamma^{em}_{total,\parallel}$ and the perpendicular ones would have a $\Gamma^{em}_{total,\perp} = 0.41$. This predicts a range of $\Gamma_{21}$ two times broader than the observed experimentally and a distribution with the opposite asymmetry (i.e. richer in higher values of $\Gamma_{21}$). A simulated distribution of this situation[1] is shown in figure 5.12 (inset in the graph of $\Gamma_{21}$ for the case without gold).

The molecules in the sample with the gold film present a much broader distribution of $\Gamma_{21}$ with an average of $0.61 \times 10^9$ 1/s. In this case, the range of $\Gamma_{21}$ values observed is narrower than the theoretically predicted. In the presence of the gold film, the ratio $\Gamma^{em}_{total,\parallel}/\Gamma^{em}_{total,\perp}$ is approximately 5.5 and the experimentally observed ratio of maximum to minimum $\Gamma_{21}$ is approximately 3. To illustrate this, a simulated distribution is shown together with the experimental data[2]. The experiments do not probe the extremes of the $\Gamma_{21}$ distribution because of two reasons. The low-$\Gamma_{21}$ end is not probed because it corresponds to molecules which transition dipole lies parallel to interface and, as demonstrated in chapter 4, those molecules are practically undetectable through the gold film. This is supported by the fact that, even though the calculations predict for the parallel molecules near gold a minimum $\Gamma_{21}$ around 25% smaller than in the case without gold, the observed minimum values of $\Gamma_{21}$ are practically equal in both cases. The high-$\Gamma_{21}$ end of the distribution is not probed because they cannot be measured due to the limiting time resolution of the APD ($\sim 1$ ns).

### 5.4.2 Influence on $k_{off}$

The distributions of $k_{off}$ for the molecules in the samples with and without gold present different average values and similar broadness. However, before drawing any conclusion from this results, it is necessary to take into account that $k_{off}$ depends on the excitation rate $\Gamma_{12}$ (equation 5.5); and the excitation rate depends on many parameters such as the illumination intensity, the sample geometry, the molecules absorption cross section and absorption dipole orientation. From equations 5.5 and 5.2 it can be seen that:

$$\frac{k_{off}}{I_{on} - I_{off}} = \frac{\Gamma_{23}}{\Gamma^{det}_{21,r}} \tag{5.25}$$

and since $\Gamma^{det}_{21,r}$ can be calculated (up to a constant value) via the method presented in 3.2, it is possible to obtain information about $\Gamma_{23}$ from the distributions of the ratio $k_{off}/(I_{on} - I_{off})$.

[2]The simulation was performed with the theoretical values of $\Gamma^{em}_{total,\parallel}$ and $\Gamma^{em}_{total,\perp}$ multiplied by the proportionality factor obtained for the data without gold (0.26; see previous footnote).

Figure 5.13 shows the experimental distributions of $k_{off}/(I_{on}-I_{off})$ for the cases with and without gold. Table 5.4 lists the calculated detectable decay rate $\Gamma_{21,r}^{det}$ [3] of parallel and perpendicular dipoles on the air side of the air/spacer interface, as well as the average for an ensemble of arbitrarily oriented molecules.

The distribution of $k_{off}/(I_{on}-I_{off})$ is broader for the molecules near gold. The reason for this is that the molecules near gold with arbitrary out-of-plane orientations span a larger range of $\Gamma_{21}^{det}$ than the molecules in the sample without gold. As a consequence, the range of $I_{on}$ (equation 5.2) is also larger for the molecules near gold.

By means of equation 5.25, it is possible to calculate a quantity proportional to $\Gamma_{23}$ as:

$$\langle\Gamma_{23}\rangle \propto \frac{k_{off}}{I_{on}-I_{off}}\Gamma_{21,r\ avg}^{det} \tag{5.26}$$

Then, taking the experimental average value of $k_{off}/(I_{on}-I_{off})$ and the calculated average value of $\Gamma_{21,r}^{det}$, it can be calculated that the chromophores have in the sample without gold an average $\langle\Gamma_{23}\rangle \propto 0.043\times 1.34 = 0.058$ and in the sample with gold $\langle\Gamma_{23}\rangle \propto 0.052\times 1.09 = 0.057$. Here it should be noted that the average value of $\Gamma_{21,r}^{det}$ used in this calculation is an isotropic average that considers all orientations equally probable. As explained above, this is not the case in the experiments with gold because the molecules parallel to the interface are hardly detectable. Nevertheless, under this conditions, no effect of the gold film on the ISC rate $\Gamma_{23}$ is observed.

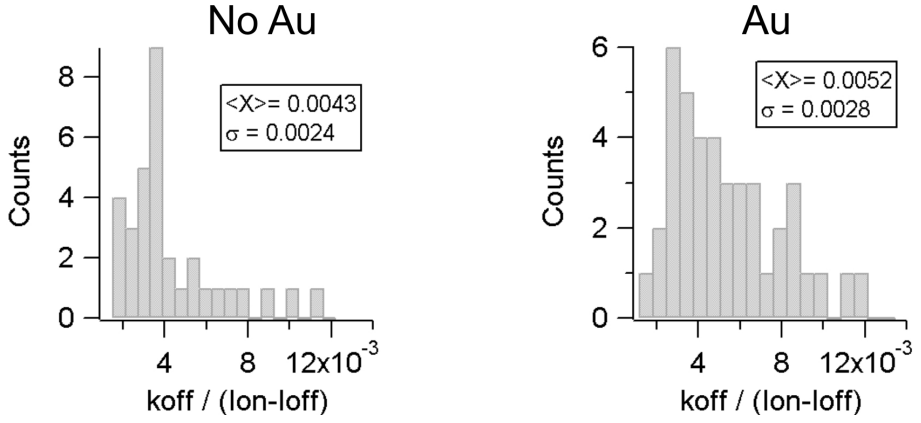


**Figure 5.13:** Distribution of $k_{off}/(I_{on}-I_{off})$ obtained via the autocorrelation analysis of the kinetic traces from molecules in the samples with and without the gold film. The average and standard deviation of each distribution are shown in the graphs.

[3] This rate was called $\Gamma_{obj}$ in chapters 3 and 4

| | $\Gamma_{21,r}^{det}$ $\parallel$ | $\Gamma_{21,r}^{det}$ $\perp$ | $avg$ |
|---|---|---|---|
| without Au | 1.08 | 1.87 | 1.34 |
| with Au | 0.29 | 2.72 | 1.09 |

**Table 5.4:** Calculated normalized radiative de-excitation rate of a parallel and perpendicular dipole emitted into the collection solid angle of the microscope objective in the samples with and without gold. The average ($avg$) value is calculated as $1/3\times\Gamma_{\perp}+2/3\times\Gamma_{\parallel}$.

### 5.4.3 Influence on $k_{on}$

In the case of $k_{on}$, the gold film produces a noticeable effect. The distribution of $k_{on}$ for the case with gold is more than two times broader and presents an average value two times higher than the case without gold. It should be noted that the experiments with gold have, in average, a lower signal to background ratio. This can produce a slight broadening of the distribution due to a higher uncertainty in the autocorrelation analysis. However, a statistical analysis with simulated data shows that this is not enough to account for the experimental broadness. Another effect of the lower signal to background ratio, is to make the detection of short on-periods more difficult. This leads to the fact that the measured average length of the off-periods is higher than the real one, leading to a smaller values of $k_{on}$. The experiments show however higher values of $k_{on}$ so that the real effect could be stronger than observed.

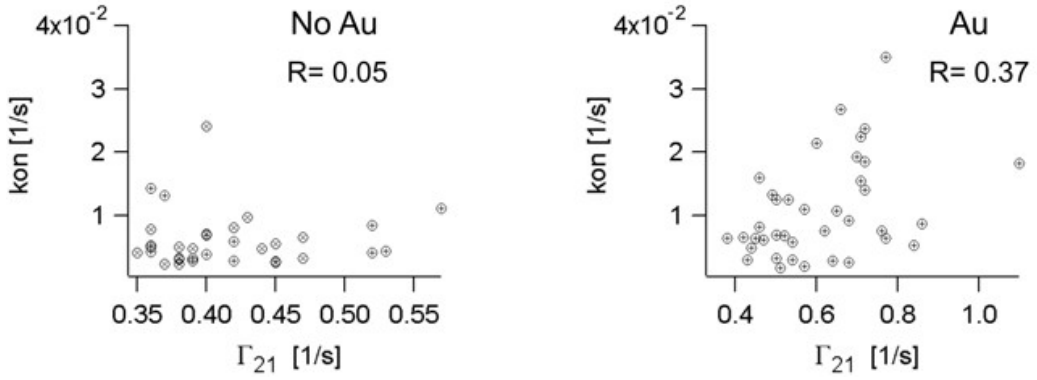


**Figure 5.14:** $k_{on}$ as a function of $\Gamma_{21}$ for the chromophores in the sample with and without gold. The corresponding linear (Pearson) correlation coefficient is shown in the graphs.

Further evidence of the influence of the nearby gold film on $k_{on}$ is found in the correlation between $k_{on}$ and $\Gamma_{21}$. Figure 5.14 shows the scatter plots of $k_{on}$ vs. $\Gamma_{21}$ for the molecules in the samples with and without gold. The linear correlation coefficient shown in the corresponding graphs indicate that $k_{on}$ and $\Gamma_{21}$ are positively correlated in the case with gold while they are not in the case without gold. The

wider range of $\Gamma_{21}$ spanned by the chromophores in the sample with gold is purely an effect of the gold influence. Therefore, the correlation between $k_{on}$ and $\Gamma_{21}$ in the complete range of $\Gamma_{21}$ is a manifestation of the gold film influence on $k_{on}$.

This indicates that $k_{on}$ ($= \Gamma_{31}$) can be enhanced in the same way as $\Gamma_{21}$ by the gold film. To understand this, it is important to recall that the transition 3→1 involves two different processes. First, a process that is able to pair back the electron spins should occur (possibly spin-orbit coupling) in order to provide the additional angular momentum to break the selection rule. Then, the molecule can decay to the singlet ground state via the emission of a photon. The gold film is able to accelerate the transition 3→1 by influencing the radiative part of the process. In addition, the positive correlation of $\Gamma_{21}$ and $k_{on}$ implies that the orientation of the transition dipole associated to the 3→1 radiative decay must be oriented close to the singlet transition dipole. The latter is not surprising because in order for ISC to occur, the excited singlet and triplet states should share a common molecular geometry.

## 5.5 Conclusions

The autocorrelation and the trace-histogram methods for the analysis of single molecule fluorescence blinking were introduced and their performance was compared via the analysis of Monte-Carlo simulated data. The trace-histogram method was improved with respect to reported versions in order to systematically find the best compromise between time resolution and accuracy in distinguishing between on- and off-states.

The autocorrelation method is more demanding in terms of computing effort and reliable, specially for the analysis of short traces. However, can be applied only to a three-level blinking system. The trace-histogram method on the other hand is more versatile and can be employed to investigate other kinds of blinking.

The influence of a nearby metallic surface on the electronic transition rates was investigated via studies of single molecule fluorescence blinking and excited state lifetime. The $\Gamma_{21}$, $k_{off}$ and $k_{on}$ of individual dye molecules in the presence and in the absence of a nearby thin gold film were compared.

The gold film provides additional de-excitation channels for the excited molecules which strongly depend on the chromophores orientation. This is clearly observed as a broadening of the distribution of $\Gamma_{21}$. Comparison to theoretical calculations can explain the observed effect quantitatively in the case without gold and indicates that the distribution of chromophores near gold was not completely probed. The latter is due to two reasons: the fact that parallel molecules are practically undetectable through the gold film and the limiting time resolution of the APD. Furthermore, the number of studied molecules might have been insufficient to probe such a broad distribution.

No influence of the gold presence was observed on the ISC rate $\Gamma_{23}$. This is

expected because the effect of the gold film is to introduce additional available electromagnetic modes that should not influence the spin-unpairing process responsible of the non-radiative transition 2→ 3.

A noticeable (2-fold in average) increase of $k_{on}$ (= $\Gamma_{31}$) due the gold film was observed. The gold film is able to accelerate the transition 3→1. A positive correlation is found between $\Gamma_{21}$ and $k_{on}$ indicating that the gold influences the radiative part of the 3→1 transition and that the transition dipole associated must have an orientation similar to the singlet transition dipole.

Further investigations are necessary to complete the results obtained in this chapter. It would be beneficial to study a larger number molecules; especially in the case with gold. A faster photo-detector needs to be employed in order to probe the complete $\Gamma_{21}$ distribution of the molecules near gold. Additional information could be obtained by correlating the transition rates to the three-dimensional orientation of the individual molecules.

# Chapter 6

# Photoluminescence blinking of $Zn_{0.42}Cd_{0.58}Se$ nano-crystals

Colloidal semiconductor nano-crystals, also known as quantum dots (QDs) are attractive fluorophores for a variety of growing applications in spectroscopy of single biological molecules [74,75] and quantum information processing using single-photon sources [76]. However, severe intermittence in emission (also known as blinking) has been universally observed and represents an intrinsic limitation for the practical use of QDs.

The fluorescence behavior of single QDs was reported to change dramatically when they are adsorbed on a rough metal film [6]. The observed changes include a fivefold increase in the observed fluorescence intensity and a striking reduction of the blinking, showing that it is indeed possible to enhance the performance of the QDs by electromagnetic interactions with metallic objects. Nevertheless, since processes behind the photoluminescence blinking of QDs are not yet understood, the enhancing effect cannot be exploited in a controlled manner.

The most commonly mechanism suggested for the blinking of QDs relates the switching between dark and bright states to ionization and neutralization events in the QD. If that is the case, the electric transport properties of the surrounding media is expected to influence the blinking behavior. To investigate this, the emission of $Zn_{0.42}Cd_{0.58}Se$ QDs deposited on glass and on ITO-coated glass substrates is studied as a function of time under different excitation intensities.

The blinking of QDs is simulated via a general model in order to identify the influence of the most important experimental parameters. The photo-induced effects of the blinking are taken into account in the simulations via an independent single-rate transition from the on- to the off-state.

## 6.1 Brief Introduction and current status

Colloidal semiconducting nano-crystals, also known as quantum dots (QDs), are of tremendous interest due to their applications as light-emitting devices [77, 78], lasers [79,80] and biological labels [81–83]. In comparison to organic fluorescent dye molecules, QDs have a number of comparative advantages: they are much brighter, they are more photostable and they have a broad band-edge absorption and a narrow emission band [81, 82, 84].

The first studied II-VI semiconducting crystallites were CdS QDs in the context of photo-electrochemical reactions at interfaces [85, 86]. CdS QDs with a size in the order of 50 Å show quantum confinement effects that lead to a size dependent lowest excited electronic state. The earliest studies on colloidal semiconducting particles were focused on the size dependence of the photoluminescence and the redox potential [87–91]. Later on, owing to their size-dependent tunable emission across the complete visible spectrum, CdSe nano-crystals have become the most extensively investigated QDs [92–96].

Although the large number of investigations dedicated to these colloidal QDs, the nature of the emitting state is still controversial. In comparison to CdSe and CdS bulk exciton (electron-hole pair) recombination, the emission from colloidal QDs is much red-shifted and has an extremely long radiative lifetime ($\sim 1\,\mu$s at 10 K, compared to 1 ns for bulk [91, 97]). Parabolic band theory cannot explain this data in terms of recombination of internal states and it was proposed that band edge emission of II-VI semiconducting colloidal QDs arises from the recombination of weakly overlapping surface- or defect-localized carriers [91, 97, 98]. Nevertheless, more careful band structure calculations for II-VI semiconducting nano-particles of different shapes show that the exciton ground state is not optically active (it has angular momentum projection $\pm 2$). This can explain the experimental observations without introducing surface or defects states. Higher energy states of the exciton are produced upon absorption of one photon, which then thermalize to the optically forbidden ground state from which radiative recombination has a long decay time [99]. Experiments supporting the existence of the optically passive exciton state have been reported [100, 101].

With the advent of photoluminescence studies on a single QD level, severe fluctuations in the photoluminescence emission were found [102]. This luminescence fluctuations, also called (on-off) blinking, depend on experimental parameters such as temperature and excitation intensity. The on- and off-periods present non-trivial (power-law) statistics and can render the QD dot dark for periods of hundreds of seconds. Surface passivation by a suitable inorganic or organic layer was reported to improve the quantum efficiency and photo-bleaching stability of QDs [103–106] but the same blinking behavior was universally observed in capped and uncapped QDs of different kinds [107–110]. This blinking represents an intrinsic limitation for the QDs applications because it limits their quantum efficiency and brightness and

makes their use in molecular tracking very complicated.

Several models have been suggested to account for the dynamics of the blinking but most of them fail to explain the power-law statistics such as the quantum jump model, the activated kinetics model, the static barrier tunnelling model (all reviewed in [110]). Two models can account for the on- and off-times statistics. First, Shimizu et al. suggested a trap state that randomly wanders in the energy space and eventually shifts into resonance with the excited state [109]. At each crossing of the trap and excited states the QD can switch from on to off or viceversa. Second, Kuno et al. suggested a model in which an excited electron or hole can tunnel to a trap state rendering the QD dark until tunnelling back to the excited state allows the radiative recombination. To explain the power-law probabilities of the on- and off-times it is necessary to introduce tunnelling barriers that fluctuate in the time scale of the blinking [111]. Both Shimizu and Kuno can explain the power-law probability densities for the on- and off-periods but they differ in the following. The model of Kuno, since the tunnelling barriers fluctuate in the same time-scale of the blinking, predicts some residual memory effect; i.e. short (long) periods should preferably be followed by short (long) periods. The model of Shimitzu does not predict any residual memory effect because after each on-off transition the random-walk of the trap state starts from the same point. This residual memory effect was not observed in the experiments [111].

With respect to the physical processes involved in the blinking, one of the first proposed models involves Auger ionization of the excited QD. In this model, a charged QD is a dark QD and therefore the average neutralization time corresponds to the average off-time [102]. Electrostatic force microscopy experiments showed that QDs can be charged both by thermal and photo-induced processes [112]. Still, single rate charging and neutralization processes cannot explain the power-law probability densities of the on- and off-periods [101].

Two important contributions to the discussion of QD blinking have been reported more recently. First, Schlegel et al. [113] introduced the concept and experimental evidence, that the QD photoluminescence blinking does not occur between an off- and an on-state but between an off-state and a distribution of on-states. They showed that the different emission intensities correspond to different excited state lifetimes. To explain the observations, they proposed the presence of fluctuating non-radiative pathways. Those results were confirmed by Fisher et al. [114]. Second, Hohng and Ha reported an almost complete suppression of the photoluminescence blinking of QDs in the presence of $\beta$-mercaptoethanol [115]. However, despite all the experimental and theoretical efforts dedicated to understand the QDs emission process, the mechanism of the blinking remains uncertain and none of the proposed models provides a complete physical picture of the process.

In the experiments presented here, the photoluminescence blinking of a new kind of QDs is studied: monocrystalline alloyed $Zn_{0.42}Cd_{0.58}Se$ QDs [116]. Naturally, the first question addressed in this chapter is therefore whether the blinking of this new

kind of QDs also present the universally observed power-law. Next, if the ionization model is correct, a different blinking behavior is expected for QDs deposited on isolating and on semiconducting substrates. In order to investigate this, the luminescence blinking of $Zn_{0.42}Cd_{0.58}Se$ QDs is studied on glass and Indium-Tin-Oxide (ITO) coated glass substrates as a function of the excitation intensity. Finally, the blinking of QDs is modelled via a Monte-Carlo method. In the modelling, an single-rate transition from the on- to the off-state is proposed to account for the photo-induced effects observed in the blinking. The dependence of this transition rate on the excitation intensity is analyzed.

## 6.2 Experimental

### 6.2.1 Sample preparation

Monocrystalline $Zn_{0.42}Cd_{0.58}Se$ nano-particles were provided by the Department of Materials Science of the National University of Singapore. The preparation method and the ensemble photoluminescence characteristics of the $Zn_{0.42}Cd_{0.58}Se$ QDs are described in [116]. The nano-crystals studied here have an average size of 6.2 nm. As shown in figure 6.1, the QDs present an ensemble band-edge absorption peaking at 515 nm and an ensemble emission maximum at 550 nm with a full-width at half maximum (FWHM) of 40 nm. Figure 6.1.b also shows the emission spectra of four individual $Zn_{0.42}Cd_{0.58}Se$ QDs on a glass substrate; the FWHM of single dot emission spectra ranges from 13 to 24 nm.

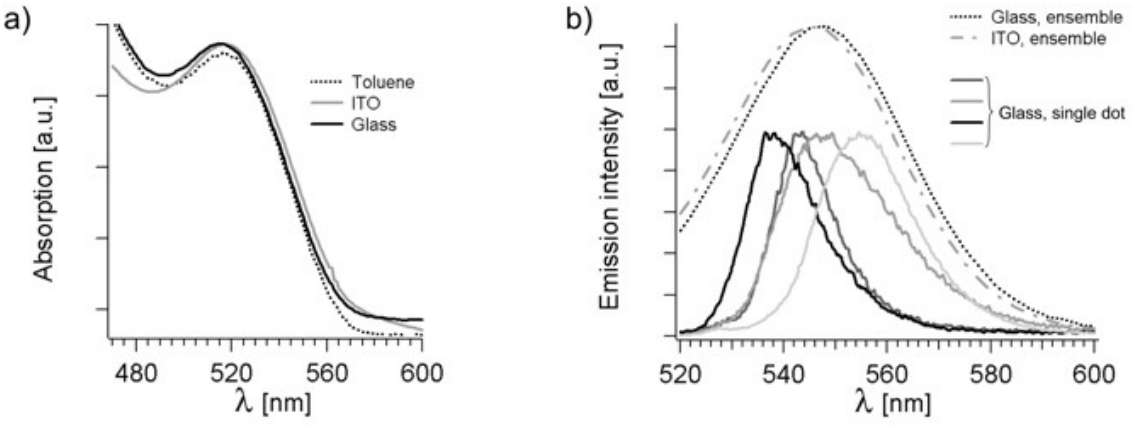


**Figure 6.1:** a) Absorption of $Zn_{0.42}Cd_{0.58}Se$ QDs in toluene, on glass and on ITO-coated glass substrates. b) Ensemble (on glass and ITO) and 4 individual (on glass) photoluminescence spectra of $Zn_{0.42}Cd_{0.58}Se$ QDs excited at 514.5 nm.

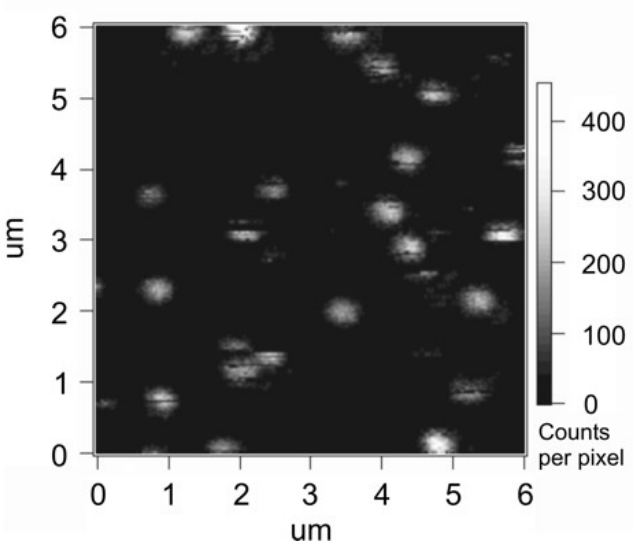


**Figure 6.2:** Typical photoluminescence image of the samples with individual QDs excited at 514.5 nm. Blinking is observed during the scanning for the image acquisition.

$Zn_{0.42}Cd_{0.58}Se$ QDs were diluted in toluene ($\geq$ 99.7%, *Riedel - de Haën*) and spin casted onto glass (*N° 1, Menzel-Gläser*) or Indium-Tin-Oxide(ITO)-coated glass substrates (50 nm, *Fraunhofer-Institut IST, Braunschweig*). The concentration was adjusted in order to obtain a surface density of approximately one QD per $\mu m^2$, as shown in the micrograph of figure 6.2.

### 6.2.2 Measurement

The measurements were performed with the SCOM set-up described in chapter 2 and consisted of imaging a region of the samples, identifying a single QD and recording the photoluminescence emission of that QD as a function of time. The avalanche photo diode (APD) was used as single photon detector and the Ar-ion laser was used for circularly polarized excitation at 514.5 nm. The repetition rate of the Ar-ion laser (60 MHz) was too high to allow measurements of the relatively long photoluminescence excited state lifetime of the QDs. Therefore, continuous wave illumination was used. Suitable dichroic and notch filters were used to separate the QDs emission from the excitation light.

The photoluminescence emission of around 350 individual $Zn_{0.42}Cd_{0.58}Se$ QDs was recorded as a function of time with the TCSPC module of the set-up. The photon detection mac-t times contain the information about photoluminescence fluctuations (see section 2.2.4). Kinetic traces were recorded under different excitation powers, which were measured before the recording of each kinetic trace with a photo power meter (*S120, Thor Labs Inc.*).

## 6.3 QD kinetic traces

Photoluminescence vs. time traces (kinetic traces) of single $Zn_{0.42}Cd_{0.58}Se$ QDs were analyzed with the trace-histogram method described in section 5.2.2.

### 6.3.1 General characteristics

Although at first sight they might seem similar to the kinetic traces of single dye-molecules (see chapter 5), the kinetic traces obtained from QDs, on both glass and ITO-coated glass substrates, hide a much more complex process. Five representative kinetic traces from QDs are plotted in figure 6.3 (left), together with the histograms of the photons per bin, i.e. intensity (center) and the distributions of the length of the on- and off-periods (right).

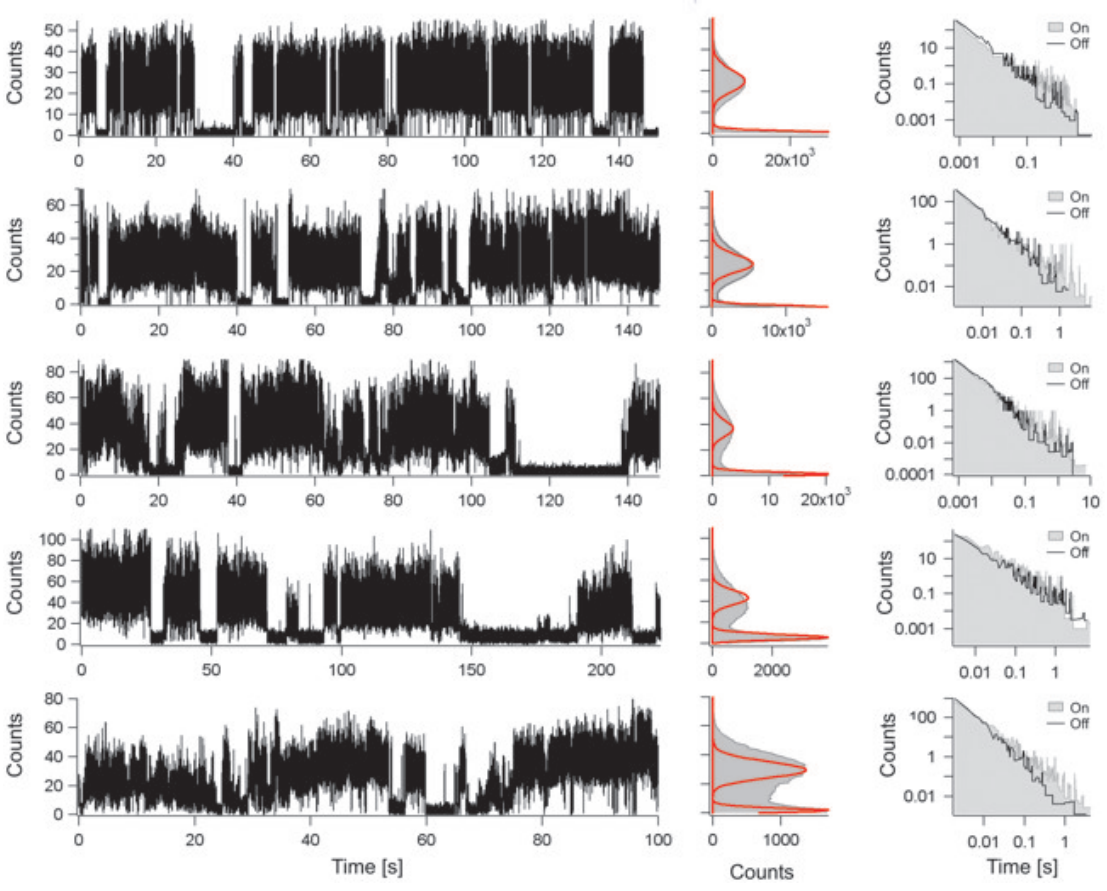


**Figure 6.3:** QDs kinetic traces. Left: Photoluminescence emission vs. time traces of different QDs. Center: histogram of the photons per bin of each trace (intensity; solid grey) and Poisson distributions (lines) with average equal to the experimental intensities. Right: histograms of the length of the on- and off-periods.

In comparison to molecular fluorescence kinetic traces, there are two evident differences. First, the QDs are able to remain on and off for much longer time periods than the fluorescent dyes. Second, the QD traces are more chaotic, in the sense that a variety of blinking rates is found even on a single QD.

Some observations can be made from a direct inspection of the intensity distributions (figure 6.3, center). As in the case of molecular fluorescence, the blinking of QDs present a Poisson distributed off-intensity with an average value equal to the background intensity. This indicates that the QDs indeed stop emitting during the dark periods. In contrast, the on-intensity is not Poisson distributed. The traces shown in figure 6.3 present on-populations with different degrees of deviation from a Poisson distribution. At this point it is important to mention that even though the algorithm of the trace-histogram analysis was designed to find an optimum threshold between two Poisson-distributed states (section 5.2.2), it also works in this case and finds reasonable thresholds. The thresholds found in the case of the QDs do not always separate the two states but they do exclude the off-state.

The histograms of the length of the on- and off-periods (on- and off-times; figure 6.3, right) show the power-law probability density that was already observed in QDs of different compositions [109, 111]. It is remarkable that similar power-law probability densities are found for on- and off- period lengths regardless the distribution of the on-intensity. Even the on- and off-periods of the first trace in figure 6.3, which shows an on-intensity only slightly broader than a Poisson distribution, have clear power-law probability densities.

The deviation of the on-intensity from a Poisson distribution has been attributed to very short on-periods (very probable given the power-law probability density) which are partly detected because of the finite time resolution of the experimental methods [110]. The Monte-Carlo simulations presented later in this chapter will show that this is in fact not true.

### 6.3.2 Effect of the excitation intensity

Kinetic traces of QDs were recorded at different excitation intensities from QDs on both glass and ITO-coated glass substrates. In figure 6.4 the on- and off-periods recorded from many ($\sim 12$ for each intensity) QDs on glass substrates are computed together in a common histogram for each excitation intensity P.

For every excitation power, the same time $T$ (shown in each graph) of each individual trace was computed. A power-law ($y = A\,x^{-m}$) was fitted to each off-time length histogram, and the obtained exponent is written in the legend of the corresponding graph.

The probability of a certain length of an off-period shows a clear power-law over more than 4 decades in time and more than 6 (and in some cases even 8) decades in probability density with no clear dependence on the excitation intensity. The

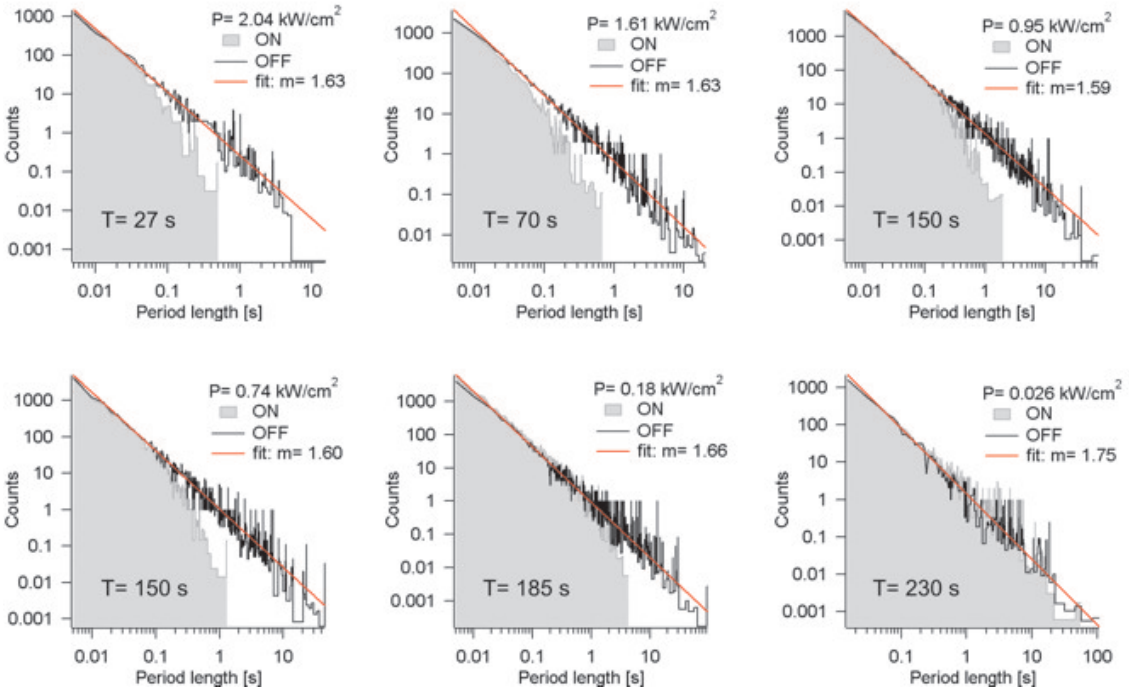


**Figure 6.4:** Histograms of the length of the on- and off-periods obtained from the common computation of several individual kinetic traces of different $Zn_{0.42}Cd_{0.58}Se$ QDs on glass under various excitation intensities (P). The same total time (T) from each kinetic trace was computed. The off-time length histograms are fitted with a power-law which exponent ($m$) is shown in each graph.

probability of a certain length of an on-period shows the same power-law behavior for short times but as the excitation intensity increases, the probability of a long on-period takes smaller values than the power-law. This gradual deviation from the power-law arises from the common computation of the on-times of different kinetic traces and is not observed in the on-times of individual traces. The individual traces are simply truncated at a maximum on-time shorter than the maximum off-time [109]. Figure 6.5 shows an example.

The same experiment was conducted with the $Zn_{0.42}Cd_{0.58}Se$ QDs deposited on ITO-coated glass substrates. The on- and off-time length histograms are shown in figure 6.6 in the same fashion as the results for glass substrates. In this case, the behavior is similar but the deviations of the on-time length histogram from the power-law are less pronounced, indicating that the dependence on excitation intensity is weaker.

The probability of the length of an off-period seems to be independent of the excitation intensity and the nature of the substrate. This suggests, at least for the long periods, the presence of two distinct processes. One responsible for the length of an on-period and the other ruling the length of an off-period.

Since the kinetic traces are composed of tens of millions of photon detection

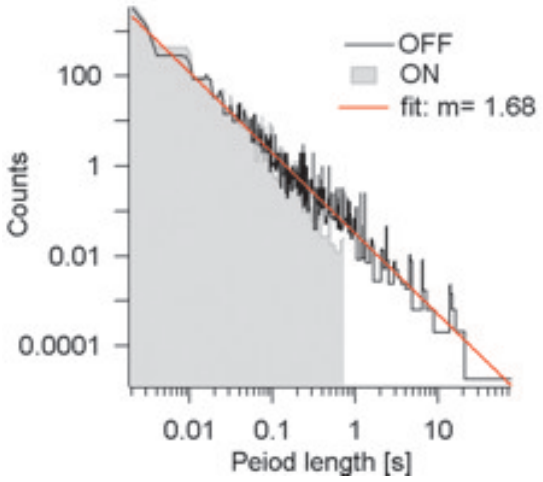


**Figure 6.5:** Histogram of the on- and off-times of a single kinetic trace. Both the on- and off-periods follow the power-law but with different maximum times.

times, it is in practice impossible to compare them directly. Therefore. it is necessary to find a few characteristic parameters that can describe the blinking. From the analysis of the kinetic traces, several parameters can be obtained to characterize the blinking behavior. In this case, on and off intensities, the exponent of the off-time length histogram power-law, the number of detected on-off cycles per second and the on-time fraction were chosen and are analyzed below.

Later in this chapter, a Monte-carlo procedure is employed to simulate the blinking of QDs and to reproduce the experimental data. Some of the characteristic quantities obtained from the trace-histogram analysis will be used as input for the Monte-Carlo simulations and some others as measure for comparison between the simulated and experimental traces.

Since there is no established mechanism for the photoluminescence blinking of QDs, it is meaningful to try to frame the experimental results within the most commonly suggested ionization mechanism because that could lead to the design of new experiments of theoretical calculations to confirm or refute the hypothesis. In this model, a positively charged QD is a dark QD and a neutral QD is a bright QD, and blinking occurs due to ionization and neutralization events. Whenever possible, the following results will be discussed in the context of this model.

### Off-intensity and on-intensity.

From the histogram analysis of the kinetic traces, it is possible to count the photons corresponding to on- and to off-periods ($N_{on}$ and $N_{off}$) and to calculate the off and on intensities ($I_{on}$ and $I_{off}$).

Figure 6.7.a shows, as a function of the excitation intensity $P$, the off-intensity

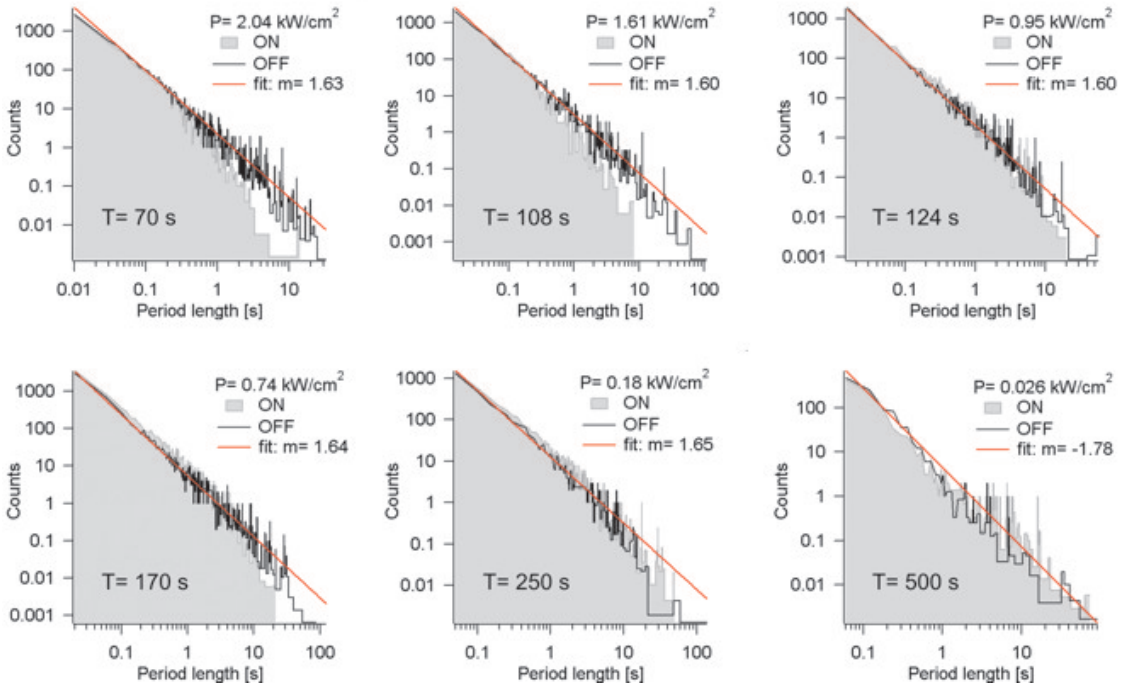


**Figure 6.6:** Histograms of the length of the on- and off-periods obtained from the common computation of several individual kinetic traces of different $Zn_{0.42}Cd_{0.58}Se$ QDs on ITO under various excitation intensities (P). The same total time (T) from each kinetic trace was computed. The off-time length histograms are fitted with a power-law which exponent ($m$) is shown in each graph.

for QDs on glass and on ITO-coated glass substrates calculated as:

$$I_{off} = \frac{N_{off}}{T_{off}} \tag{6.1}$$

where $T_{off}$ is the total off-time.

Two different on-intensities, shown in figure 6.7.b as a function of the excitation intensity, were calculated as:

$$I_{on,net} = \frac{N_{on}}{T_{on}} - I_{off} \qquad I_{on,avg} = \frac{N_{on}}{(T_{on} + T_{off})} - I_{off} \tag{6.2}$$

where $T_{on}$ is the total on-time.

$I_{on,net}$[1] represents the intrinsic emission capacity of the QDs and it is observed to increase with the excitation intensity. $I_{on,avg}$ is the time-averaged on-intensity. It represents the time average photoluminescence emission of one QD (or the average emission of an ensemble of QDs) and remains almost constant over the whole studied excitation intensity range. This shows how the blinking process limits the ultimate

[1]Note that $I_{on,net}$ differs from the $I_{on}$ defined in chapter 5 in that $I_{on,net}$ does not include the background intensity $I_{off}$.

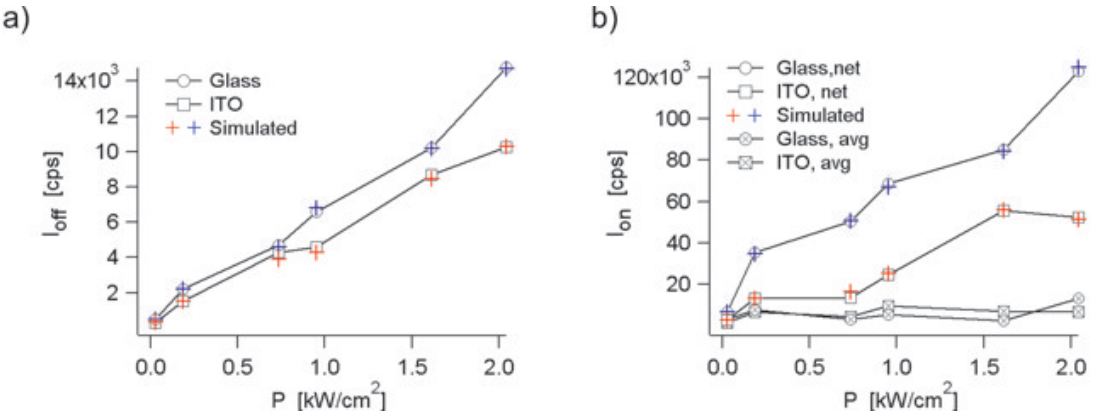


**Figure 6.7:** a) Experimental and simulated off-intensity. b) Experimental and simulated net on-intensity and experimental overall on-intensity. All as a function of the excitation intensity P for $Zn_{0.42}Cd_{0.58}Se$ QDs on glass and ITO-coated glass substrates.

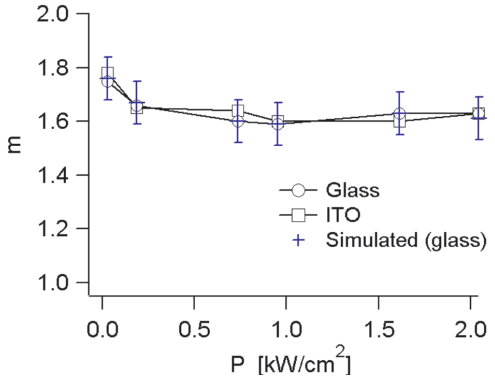


**Figure 6.8:** Exponent of the power-law fit to the experimental and simulated (glass only) off-period length histograms of the QDs on glass and ITO-coated glass substrates, as a function of the excitation intensity P.

performance of the QDs.

The increase of $I_{on}$ and $I_{off}$ is not perfectly linear with the excitation power. This is due principally to the fact that the measured values of intensity are very sensitive to the alignment of the detector. Since, the active area of the APD has a diameter of 180 $\mu$m, a misalignment of some tens of micrometers can produce a considerable drop in the measured intensity. As the off-intensity is composed mainly of background intensity its dependence on the detector alignment is less pronounced.

### Power-law exponent

All the histograms of the off-periods length can be satisfactorily fitted with a power-law ($y = A\,x^{-m}$) with an exponent $m$ between 1 and 2, and close to 1.6.

As shown in figure 6.8, the power-law exponent does not show any evident dependence on the excitation power. The weak tendency to higher values as the power

increases is an artefact of the trace-histogram analysis method. All the simulated points shown in figure 6.8 (and the error bars) were obtained from Monte-Carlo simulated data (see next section) with exponents between of 1.72 and 1.74.

### Detected cycles per second

Another relevant parameter for the characterization of the blinking process is the frequency with which a QD jumps from the on- to the off-state and viceversa. The number of on-off cycles per second was computed and is shown in figure 6.9.a for the QDs on glass and ITO-coated glass substrates as a function of the excitation intensity.

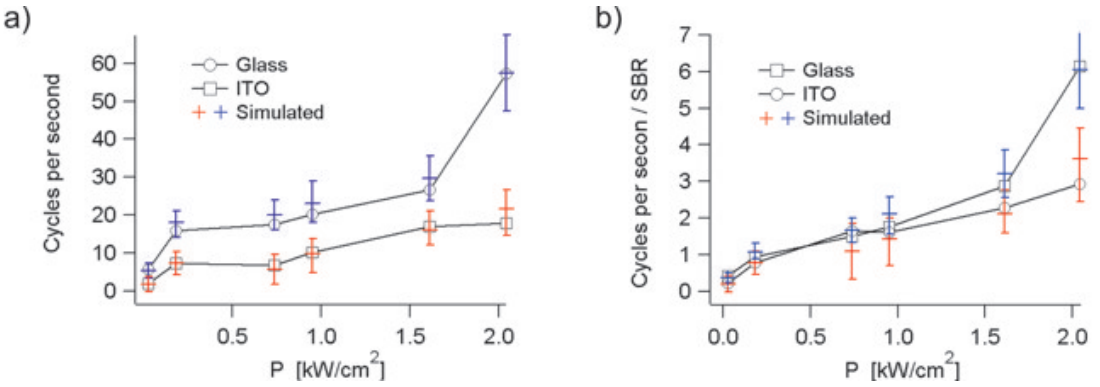


**Figure 6.9:** a) Experimental and simulated on/off cycles per second for the QDs on glass and ITO-coated glass substrates, as a function of the excitation intensity P. b) Experimental cycles per second normalized by the signal to background ratio (SBR).

It can be observed that the number of cycles per second follows a trend similar to the net on-intensity $I_{on,net}$. This is due to the fact that as the signal to background ratio (SBR) increases, shorter on-periods become detectable. To account for this and try to detect a real effect, the number of cycles per second were divided by the SBR (6.9.b). The number of cycles per second shows a practically linear increase with the SBR except for last (or the last two) points for the QDs on glass which deviates to higher values.

### On-time fraction

The fraction of time that the QDs spend in the on-state was computed as $T_{on}/(T_{on}+T_{off})$ and is shown in figure 6.10 as a function of the excitation intensity $P$.

At very low intensities, the QDs spend approximately half of the time in the on-state and as the excitation intensity increases, the on-time fraction reduces. The reduction is much stronger for the QDs on glass substrates.

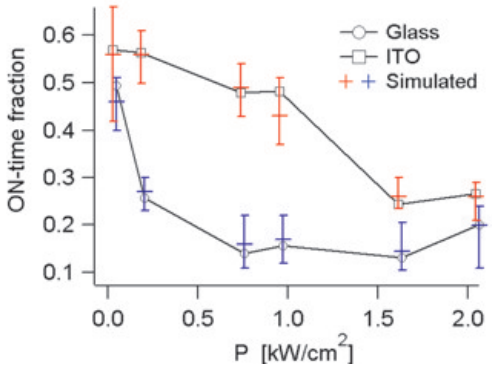


**Figure 6.10:** Experimental and simulated on-time fraction for the QDs on glass and ITO-coated glass substrates, as a function of the excitation intensity P.

This results are in qualitative agreement with the ionization model that states that a positively charged QD is a dark QD and a neutral QD is a bright QD. Krauss et al. [112] carried out electrostatic measurements on single QDs and showed that, at room temperature and in dry air, approximately 50% of the QDs were positively charged and 50% were neutral, and that the percentage of positively charged dots increased upon illumination with light of energy above the absorption band edge of the QDs.

Following this line, the different on-time fraction behavior observed for QDs on glass and on ITO-coated glass substrates could be explained by taking into account that glass is an insulator and ITO is a semiconductor of relatively low work function ($\phi = 4.4 - 4.7\,\text{eV}$ [117]). Then, on ITO, the electrons have a relatively high mobility and given the fact that the QDs are either positively charged or neutral, they can rapidly build up a negative charge density around a QD. As a consequence, ejection of an electron from the QD to the substrate is less viable leading to longer on-times for the QDs on ITO.

However, it should be noted that the physical picture described above is contradictory to the observation that even at very low excitation intensities the QDs on ITO seem to be half the time in the off-state; i.e. ionized.

### Correlations between adjacent on- and off-times

Additional information about the physical nature of the fluctuations involved in the blinking process may be obtained via correlations of adjacent on- and off-times.

Figure 6.11 shows, as an example, the scatter plots of the on-times vs. the successive on-times, the off-times vs. the successive off-times and the on-times vs. the successive off-times, of the on- and off-periods detected from QDs on glass under an excitation power $P = 0.74\,\text{kW/cm}^2$. A similar behavior is found for the other excitation intensities, both for QDs on glass and on ITO substrates. No evident correlation is observed when the graphs are plotted on a linear scale (upper two rows in figure 6.11). Nevertheless, when the graphs are plotted in a logarithmic

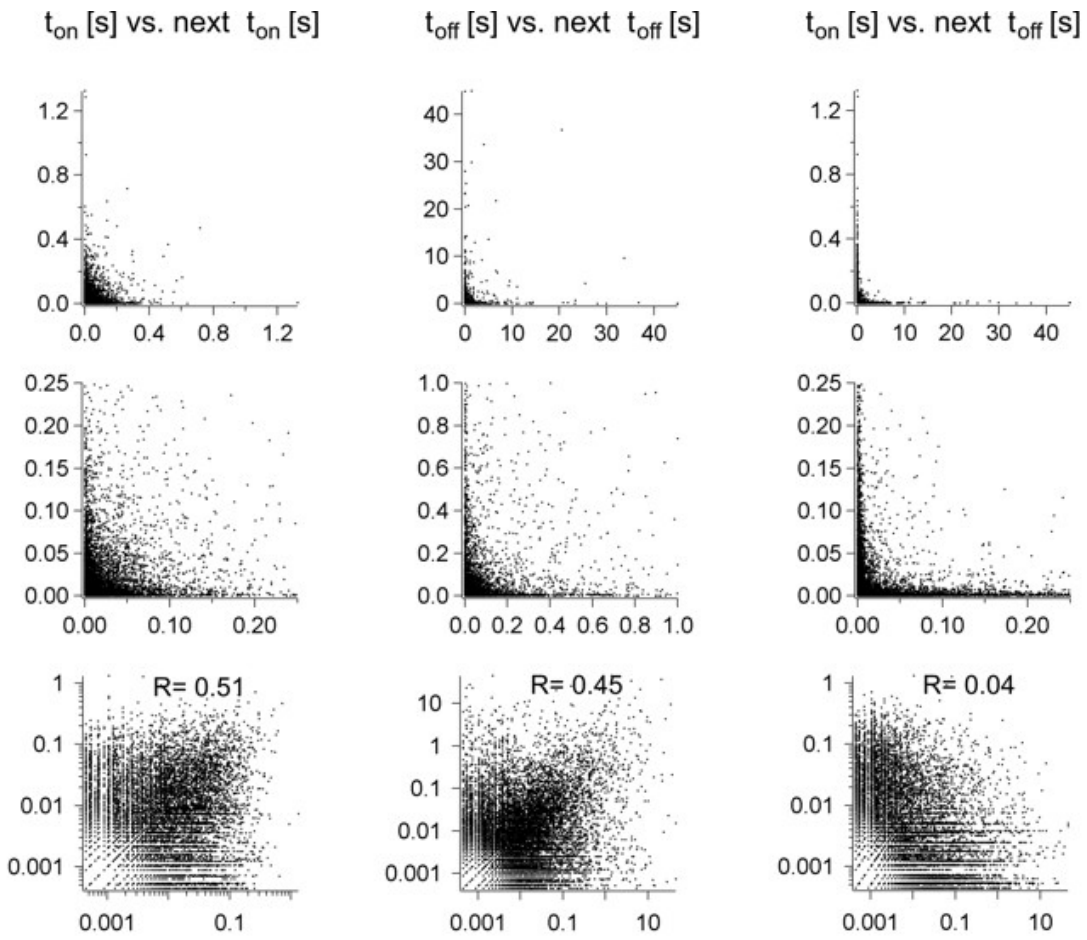


**Figure 6.11:** Correlations of adjacent on- and off-times plotted on linear (first and second rows) and logarithmic scales. The linear correlation coefficient of the logarithm of the times is shown in the corresponding graphs. The scatter plot of $t_{off}$ vs. the next $t_{on}$ (not shown) is similar to the one of $t_{on}$ vs. the next $t_{off}$; also in that case no correlation was found.

scale, a noticeable correlation is observed between consecutive on-times and between consecutive off-times. Remarkably no correlation is observed between adjacent on- and off-times.

In order to quantify the linear correlation between the logarithm of adjacent times, the (Pearson) correlation coefficient $R$ was calculated as [118] [2]:

$$R = \frac{\sum_n (X_n - \overline{X})(Y_n - \overline{Y})}{\sqrt{\sum_n (X_n - \overline{X})^2} \sqrt{\sum_n (Y_n - \overline{Y})^2}} \tag{6.3}$$

[2] $R$ measures the strength of the linear relationship between two variables by taking values between -1 and 1 inclusive. This limiting cases indicate that all the $(x, y)$ points of a scatter plot can be connected by a straight line which slope is -1 or 1, respectively. $R = 0$ indicates no evidence of a linear relationship between $X$ and $Y$.

where $X$ and $Y$ stand for the logarithm of the corresponding time-period plotted along the x- or y-axis in the scatter plots of figure 6.11. $\overline{X}$ and $\overline{Y}$ are the averages of $X$ and $Y$, respectively, and the sums are performed for all the $n$ points of each scatter plot.

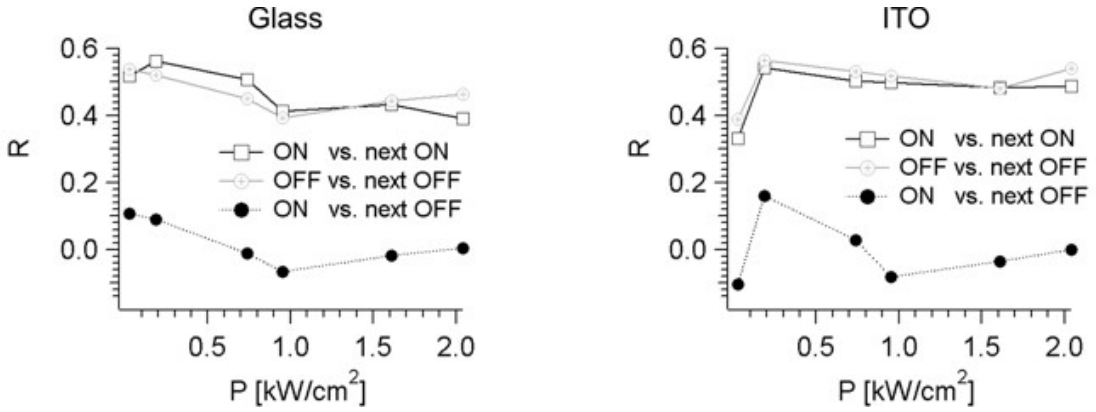


**Figure 6.12:** Correlation coefficient of adjacent on- and off-times as a function of the excitation intensity $P$.

Figure 6.12 shows the correlation coefficients obtained from the on- and off-periods of QDs on glass and on ITO for the different excitation intensities. No evident dependence of the correlation behavior on the excitation power was found. The correlation coefficient $R$ between successive on-times and between successive off-times oscillates around 0.5 and the correlation coefficient between adjacent on- and off-times oscillates around zero.

This results support the idea that the processes responsible of turning a QD bright is distinct from the process that turns a QD dark. In addition it indicates that both processes have certain residual memory. This residual memory effect was predicted by the model of ionization through fluctuating tunnelling barriers proposed by Kuno et al. [110, 111] but it was not observed experimentally.

## 6.4 Modelling the QDs blinking

The modelling of the QDs blinking is performed to address the following questions. Are the on-intensities deviated from a Poisson behavior really due to partly detected short on-times produced by the power-law probability density? Can the photo-induced shortening of the on-time fraction be explained by the presence of an additional independent pathway which introduces a characteristic lifetime for the on-state? If that is the case, how does this characteristic lifetime depend on the excitation intensity?

### 6.4.1 Blinking model

Since there is no analytical description of the QD blinking, the simulations were performed via a Monte-Carlo method that takes into account the experimentally observed characteristics of the blinking.

The emission of a QD is considered to switch between an on- and an off-state, each of them with a characteristic intensity $I_{on}$ and $I_{off}$. Two processes are responsible for the blinking: one spontaneous on↔off switching and one photo-induced transition from the on-state to the off-state.

Under no illumination, the probability of a certain length of an on- or an off-period, $P(t_{on})$ and $P(t_{off})$ respectively, follows a power-law with an exponent between -1 and -2 (figures 6.4 and 6.6). In order to make the power-law probability density normalizable, it is necessary to restrict its domain by means of an arbitrary minimum time $t_{min}$. Given that, for very low excitation intensities, the on-time fraction is close to 0.5 (figure 6.10) and that $P(t_{on})$ and $P(t_{off})$ become practically indistinguishable, the same $t_{min}$ was used for the $t_{on}$ and the $t_{off}$ probabilities. Then, the time $t_j$ spent by the QD in state $j$ (on or off) has a probability density $P(t_j)$ given by:

$$P(t_j) = \frac{m-1}{t_{min}^{1-m}}\ t_j^{-m} \qquad\qquad t_{min} < t_j < \infty \tag{6.4}$$

In addition to the random power-law distributed on-off blinking, an extra independent pathway from the on- to the off-state is included in the simulations to explain the experimentally observed photo-induced ($PI$) reduction of the on-time fraction. This transition is considered to occur at a constant rate and is therefore exponentially distributed with a characteristic time $\tau_{PI}$:

$$P_{PI}(t_{on}) = \frac{1}{\tau_{PI}}\ e^{-t_{on}/\tau_{PI}} \tag{6.5}$$

It is important to note that although it is not possible to assign an average on-time because of the power-law distribution (which normalization depends on the arbitrary $t_{min}$), the extra, exponentially distributed pathway allows to assign an average photo-induced on-time $\tau_{PI}$.

### 6.4.2 Monte-Carlo procedure

Based on the general assumptions described above, a Monte-Carlo procedure was set-up to simulate a blinking QD with the following input parameters:

- $T$: total simulated time.
- $m$: exponent of the power-law probability density.
- $I_{off}$: background intensity (figure 6.7.a).

- $I_{on}$: net fluorescence intensity (figure 6.7.b).
- $t_{min}$: minimum allowed on- or off- time (equation 6.4).
- $\tau_{PI}$: photo-induced on-state lifetime.

From equations 6.4 and 6.5, the times that the simulated QD spends on the off- and on-state are calculated as:

$$\begin{aligned} t_{off} &= t_{min}\, R_{dm}^{\,1/(1-m)} \\ t_{on} &= Min\left[t_{min}\, R_{dm}^{\,1/(1-m)}, -\tau_{PI}\, \ln(R_{dm})\right] \end{aligned} \tag{6.6}$$

where Min[a,b] takes the minimum of a and b, and $R_{dm} \in (0, 1]$ is a random number.

The total simulated time $T$ is filled with background photons (photon detection times). The background photons are separated by times $t_{h\nu,off}$, calculated according to equation 5.16 as:

$$t_{h\nu,off} = -\frac{1}{I_{off}}\, \ln(R_{dm}) \tag{6.7}$$

Within the on-periods, extra photons are added with detection times separated by $t_{h\nu,on}$ calculated as:

$$t_{h\nu,on} = -\frac{1}{I_{on}}\, \ln(R_{dm}) \tag{6.8}$$

The Monte-Carlo procedure generates photon detection times in the same fashion as the TCSPC module. The simulated data was then analyzed via the trace-histogram method (see section 5.2.2) in the same way as the experimental data.

Because $T$, $m$, $I_{on}$ and $I_{off}$ are obtained from the experiments, the only parameters left free to reproduce the experimental data are $t_{min}$ and $\tau_{PI}$. The influence of each simulation input parameter on the simulated kinetic traces is explained below.

### $T$: total simulated time.

The finite length of the experimental kinetic traces sets a higher limit for the detectable on- or off-period and makes the detection of periods of length comparable to the length of the kinetic trace less probable. For this reason, for all other parameters fixed, a short kinetic trace has with higher probability a larger number of cycles per second.

In order to permit a proper comparison of the experimental data to the simulations, $T$ was set to the length of the experimental traces for each excitation power (shown in the graphs of figures 6.4 and 6.6).

### $m$: exponent of the power-law probability density

The histogram analysis method retrieves systematically values of $m$ which are slightly smaller than the actual value. All simulations were performed with $m$ between 1.72 and 1.74. The values obtained from the simulations are shown in figure 6.8; the error bars indicate the range of values of $m$ obtained from approximately 10 simulations with the other input parameters fixed.

### $I_{on}$ and $I_{off}$: background and net fluorescence intensity

The trace-histogram method retrieves systematically values slightly higher for $I_{off}$ and lower for $I_{on}$ due to the *mixed bins* explained in section 5.2.2 (see also section 5.2.3). In the simulations, the experimental values of $I_{off}$ and $I_{on,net}$ (figure 6.7) were used as starting values. Then, the inputs were adjusted in order to obtain from the analysis values more similar to the experimental ones (see figure 6.7).

### $t_{min}$: minimum allowed on- or off- time

The influence of an arbitrary $t_{min}$ was tested by varying it from $10^{-6}$ to 1 ms. In general, a smaller $t_{min}$ produces shorter on and off times with higher probability and a consequent higher number of cycles per second. Several ($\sim 7$) kinetic traces were simulated with different values of $t_{min}$ (and all the other input parameters fixed) and then analyzed with the trace histogram method. No changes in the detected number of cycles per second were noticed for $t_{min}$ below $10^{-4}$ ms.

The reason is that as $t_{min}$ becomes smaller, the generated shorter on- and off-times become undetectable and their influence vanishes. Figure 6.13 illustrates this effect. The simulated on- and off-periods are shown together with the on- and off-periods observed in the kinetic trace histogram.

The $t_{min}$ input was set to $10^{-5}$ ms in all simulations. This value is small enough and no noticeable influence on the number of cycles per second is expected. Lower values were not used because they increased greatly the computational time.

### $\tau_{PI}$: photo-induced on-state lifetime

$\tau_{PI}$ is the only parameter that can introduce a difference between the on- and off-times distributions. A shorter $\tau_{PI}$ makes long on-times less probable with a consequent higher number of cycles per second and shorter total on-time fraction.

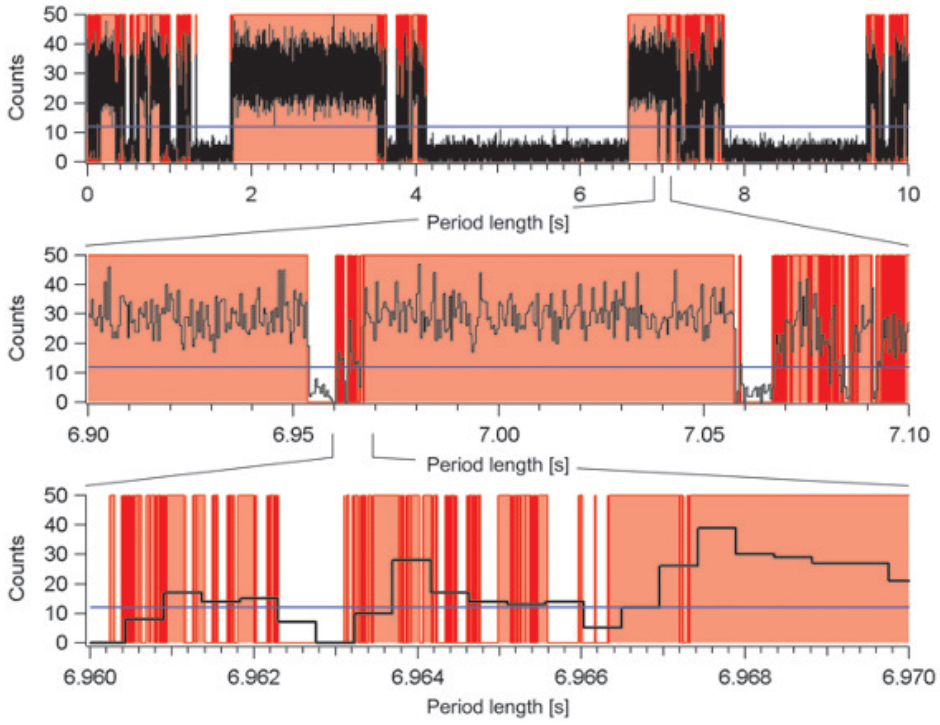


**Figure 6.13:** Simulated and detected on- and off-periods. The filled curve shows the simulated on- and off-periods (time resolution 1$\mu$s), the black curve is the kinetic trace histogram (bin-width 0.46 ms) and the horizontal line marks the threshold found via the trace histogram method to distinguish the on- from the off-bins.

### 6.4.3 Simulated blinking

Figure 6.14 shows a simulated kinetic trace (left), the photons per bin histogram (center) and the histogram of the length of the on- and off-periods.

The simulated kinetic trace and its on- and off-period distributions look very similar to the experimental ones. However, the intensity distribution does not. In contrast to the experiments, the simulated on-intensity is Poisson distributed. This was corroborated by simulations using input parameters spanning the complete experimental range and no deviation from the Poisson behavior was observed. The hypothesis that the deviations of the on-intensity distribution from a Poisson behavior are due to partly detected short on-times produced in great quantity by the power-law probability [119] can be refuted.

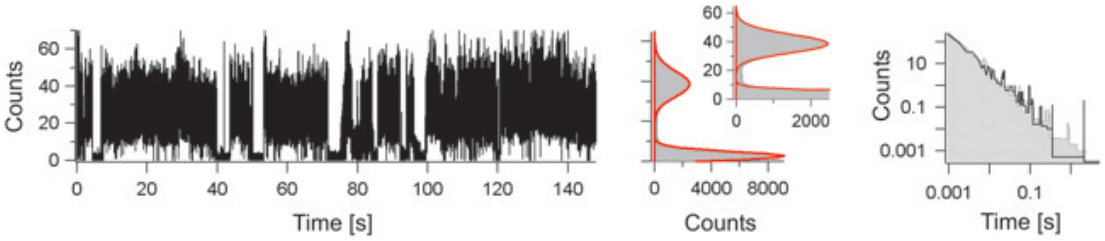


**Figure 6.14:** Simulated QD kinetic trace. Left: Photoluminescence emission vs. time traces. Center: histogram of the photons per bin (intensity; solid grey) and Poisson distributions (lines) with average equal to the experimental on and off intensities. Right: histograms of the length of the on- and off-periods.

### Reproduction of the experimental data

Simulations were carried out to try to reproduce the experimental results. To simulate the data obtained with the different excitation intensities, the corresponding experimental parameters ($T$, $I_{on}$, $I_{off}$) were used as input for the Monte-Carlo algorithm. For each excitation intensity, a number of traces equal to the number of experimental traces was simulated and then analyzed with the trace-histogram method. All the traces were simulated with exponents $m$ between 1.72 and 1.74.

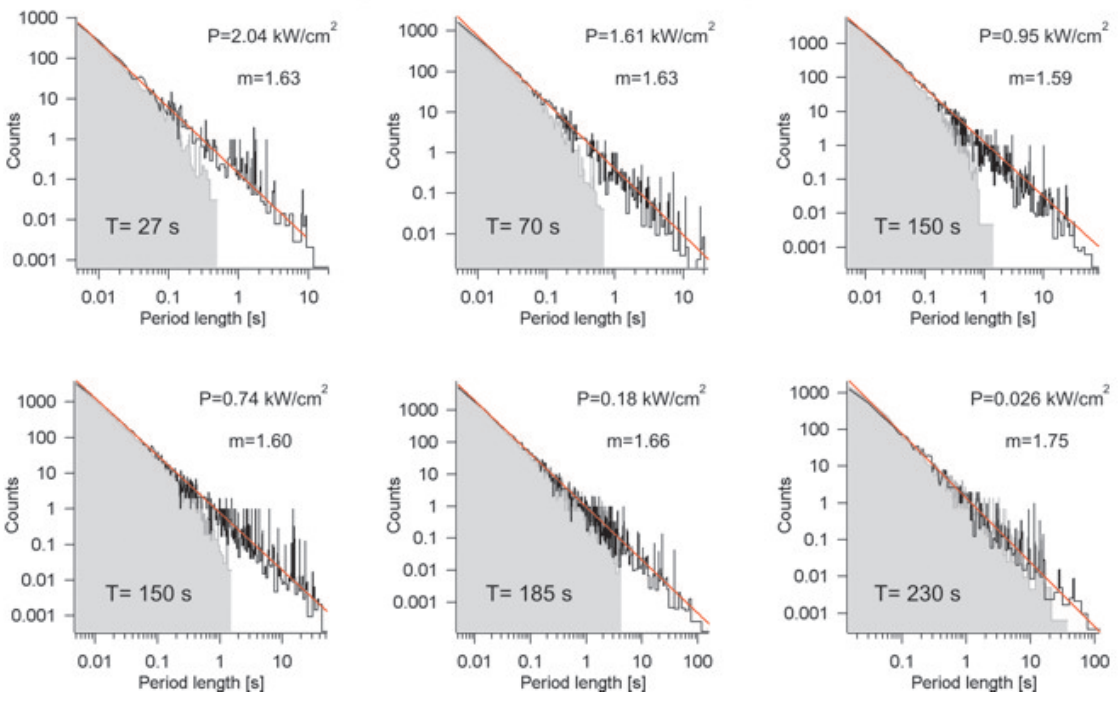


**Figure 6.15:** Histograms of the length of the on- and off-periods of the simulated kinetic traces. The simulations were performed to reproduce the experimental data of the QDs on glass for the different excitation intensities $P$. The results are presented in the same fashion as figure 6.4.

Like this, the only parameter left to introduce a difference between the on- and off-times and reproduce the experimental photo-induced effects is $\tau_P I$. The value of $\tau_{PI}$ was varied in order to find an optimum agreement between simulation and experimental data (on-time fraction and cycles per second) was reached.

Figure 6.15 shows the histograms of the on- and off-period lengths simulated for the QDs on glass and figure 6.16 for the QDs on ITO-coated glass. To compare better to the experimental data, a power-law was fitted to the off-time histograms with a fixed exponent equal to the experimental one.

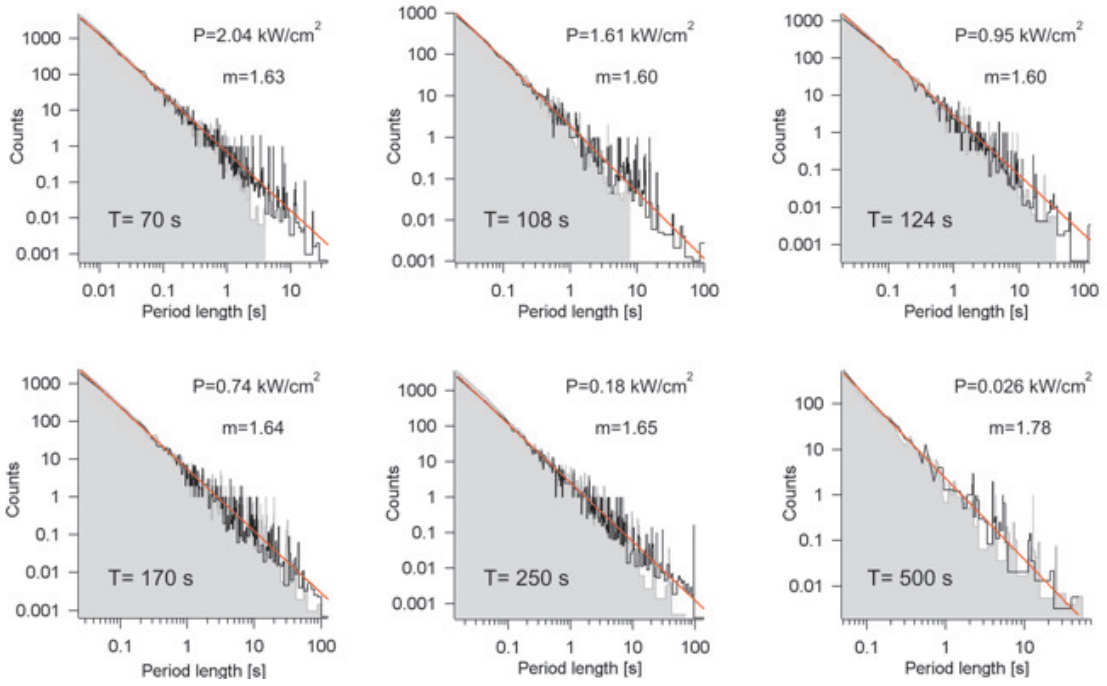


**Figure 6.16:** Histograms of the length of the on- and off-periods of the simulated kinetic traces. The simulations were performed to reproduce the experimental data of the QDs on ITO for the different excitation intensities $P$. The results are presented in the same fashion as figure 6.4.

All the characteristic parameters of the QDs blinking can be reproduced with the model (see figures 6.7 to 6.10) except for the non-Poissonian on-intensity distribution (figure 6.14) and the residual memory effect of the consecutive on-times and consecutive off-times. Figure 6.17 shows exemplary plots of the on-times vs. the successive on-times, the off-times vs. the successive off-times and the on-times vs. the successive off-times obtained from the simulated kinetic traces. As expected from the random generated on- and off-time periods, no correlation is observed in this case.

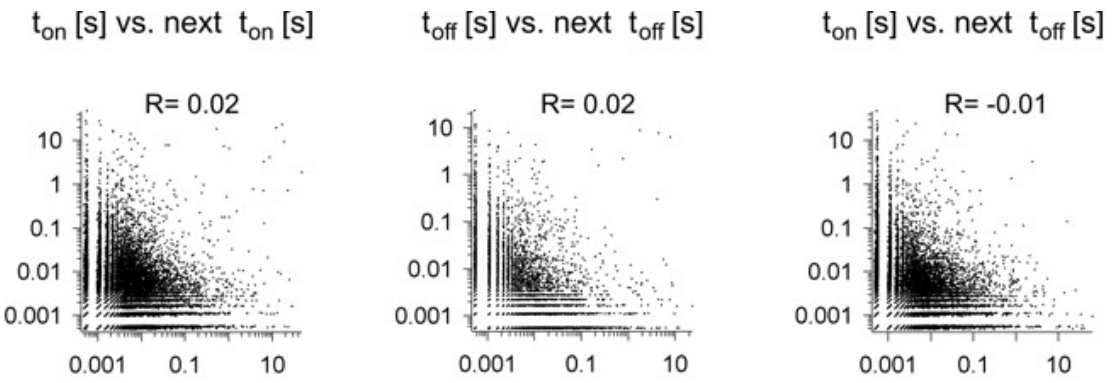


**Figure 6.17:** Correlations between adjacent on- and off-times (on logarithmic scales) obtained from the trace-histogram analysis of simulated traces.

### The photo-induced on-time lifetime

By means of the photo-induced lifetime $\tau_{PI}$ it was possible to reproduce quantitatively all the photo-induced characteristics of the QD blinking observed in the experiments: decrease of the on-time fraction, increase of the cycles per second and decrease of the maximum on-time. So, three characteristic parameters of the blinking can be accounted for by a single parameter in the simulations.

The photo-induced lifetime of the on-state $\tau_{PI}$ that best reproduced the experimental data for each excitation power ($P$) is plotted in figure 6.18 as a function of $P$ on linear, log-linear and log-log scales.

The excitation intensity dependence of $\tau_{PI,glass}$ and $\tau_{PI,ITO}$ are noticeable different. While the dependence of $\tau_{PI,ITO}$ on $P$ can be satisfactorily fitted by a single exponential, the dependence of $\tau_{PI,glass}$ cannot. Instead, $\tau_{PI,glass}$ as a function of $P$ can be represented by either a double-exponential or a power-law with exponent close to -1. The error bars in figure 6.18 were obtained by searching the extreme values of $\tau_{PI}$ that could still reproduce the experimental data within the statistical errors of the cycles per second and the on-time fraction. The photo-induced lifetime of the on-state $\tau_{PI}$ can be interpreted as the inverse of a photo-induced rate from the on to the off state $k_{off,PI}$:

$$k_{off,PI} = \frac{1}{\tau_{PI}} \tag{6.9}$$

In the case of QDs on glass, it is observed that the dependence of $\tau_{PI}$ with $P$ roughly follows a power-law with exponent -1. In this case:

$$k_{off,PI} \propto P \tag{6.10}$$

This indicates the presence of a one-photon photo-induced process responsible for the shortening of the on-times. Within the frame of the ionization model, this

would mean that on glass, a one-photon photo-ionization process dominates the shortening of the on-periods.

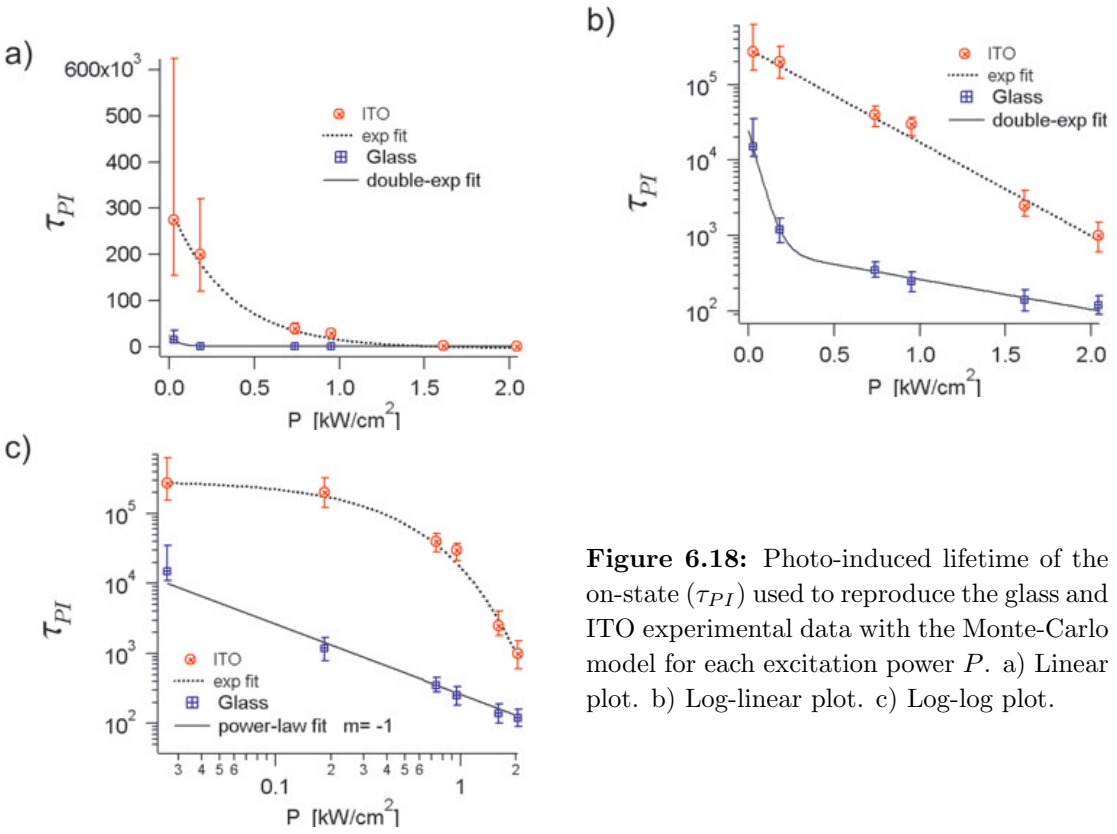


**Figure 6.18:** Photo-induced lifetime of the on-state ($\tau_{PI}$) used to reproduce the glass and ITO experimental data with the Monte-Carlo model for each excitation power $P$. a) Linear plot. b) Log-linear plot. c) Log-log plot.

No trace of a $P^{-1}$ dependence of $\tau_{PI}$ is found for the QDs on ITO, indicating that a completely different mechanism is ruling the photo-induced shortening of the on-times. The approximately exponential behavior of $\tau_{PI}$ with $P$ leads to a photo-induced rate:

$$\mathrm{k}_{off,PI} \propto \ e^{cP} \qquad\qquad c = constant \qquad\qquad (6.11)$$

No physical picture was found for this dependence. For example a thermally activated process cannot account for it: assuming that $\mathrm{k}_{off,PI}$ corresponds to a thermally activated process, then $\mathrm{k}_{off,PI} \propto \ e^{-\Delta E/kT}$ and therefore, a linear heating of the QD or the ITO substrate by the excitation intensity would not explain the observed exponential behavior.

## 6.5 Conclusions

Photoluminescence blinking of $Zn_{0.42}Cd_{0.58}Se$ quantum dots was measured for the first time. The length of the on- and off-periods present the power-law probability density that was universally observed in other QDs of different compositions and structures. This further supports the idea of a common blinking mechanism for all semiconducting QDs.

The blinking behavior of QDs on glass (insulator) and on ITO-coated glass (semiconductor) substrates was studied under different excitation intensities.

The probability density of the off-times shows a power-law that spans up to 8 decades in probability density and 4 decades independently of the excitation intensity and the nature of the substrate. In contrast, the probability of the on-times shows the same power-law for short times but long on-times become less probable as the excitation intensity increases. The decrease in the number of long on-times, and as a consequence of the on-time fraction, is much more pronounced for the QDs on glass. Then it can be concluded that there are two different processes governing the lifetime of the on- and the off-times, at least for the long times.

At very low excitation intensities, the QDs spend approximately half the time in the on-state and the other half in the off-state. As the excitation intensity increases, the fraction of time that the QDs spend in the on-state reduces. This is in agreement with the ionization model that states that a positively charged QD is a dark QD and a neutral QD is a dark QD, supported by the electrostatic measurements on single QDs performed by Krauss et al [112]. They reported that, at room temperature and in air, half of the QDs were positively charged and half were neutral, and that the fraction of charged dots increased upon illumination with light of energy above the band-gap of the dots.

A careful observation of the correlation between adjacent on- and off-times shows a weak residual memory effect for consecutive on-times and for the consecutive off-times. No dependence of this correlation on the excitation power was observed. No memory effect was observed between an on-time and the adjacent off-time. This supports the idea of the two different process, one ruling the on-times and another ruling the off-times. Although such a memory effect was predicted by the model of ionization through fluctuating tunnelling barriers proposed by Kuno [110], it was never observed in experiments.

From the analysis of the intensity distributions, it is found that the QDs present a Poisson-distributed off-intensity with average equal to the background intensity showing that the QDs indeed stop emitting during the off-periods. In contrast, the on-intensity distribution is in general not Poissonian. Some kinetic traces (or parts of kinetic traces) can be found in which the on-intensity is practically Poisson distributed. Even in those cases the on- and off-times show a very clear power-law probability density. It can be concluded then that the observed power-law is not a product of the analysis of a non-Poissonian on-intensity. The power-law reflects the

statistics of an underlying real process.

A Monte-Carlo procedure was set-up to simulate the blinking of the QDs. The model behind considers a random switch between an on- and an off-state, both with respective Poisson-distributed intensities, and an additional independent pathway from the on-state to the off-state to account for the photo-induced shortening of the on-times. This independent on→off transition introduces an exponential probability for the on-times with a consequent characteristic lifetime for the on-state.

The simulated kinetic traces do not show any correlation between adjacent times as it is expected because the time periods are randomly generated. This gives evidence that the on- and off-times are not completely random and that the physical processes behind the blinking needs to introduce a slight memory effect.

It was suggested that the deviations of the on-intensity from the Poisson behavior was due to the fact that very short on-times, which are highly probable due to the power-law probability, were partly detected [119]. The simulated kinetic traces show a Poisson-distributed on-intensities in all cases. This allows to refute the hypothesis of the partly detected on-times and indicates that the QDs posses several emitting states, supporting the results of Schlegel [113] and Fisher [114].

Except for the on-intensity and the weak memory effect, the Monte-Carlo model can reproduce all the experimental characteristics of the blinking. The only input parameter that was varied in order to reproduced the experimental data is the characteristic lifetime of the on-times $\tau_{PI}$. Three experimental photoinduced characteristics of the blinking (decrease of the on-time fraction, increase of the cycles per second and decrease of the maximum on-time) could be reproduced quantitatively by $\tau_{PI}$. This lifetime of the on-state shows a completely different behavior as function of the excitation intensity for the QDs on glass and on ITO-coated glass. In the case of QDs on glass, $\tau_{PI}$ can be satisfactorily fitted by a power-law with exponent -1, providing evidence of a one-photon photo-induced shortening of the on-times. In the case of ITO, $\tau_{PI}$ can be fitted satisfactorily with a single exponential dependence on the excitation intensity but no theoretical support was found for this dependence. Nevertheless, given the so different dependencies of $\tau_{PI}$ on the excitation intensity for the QDs on glass and on ITO, it is most likely that two completely different photo-induced mechanisms are involved.

# Chapter 7

# Confocal microscopy measurements of light scattering from single metallic nano-structures

This chapter is meant to demonstrate the performance of the home-built confocal microscope for light scattering measurements. First, colloidal gold nanoparticles are used as a test sample to proof the light scattering measurement principle and to characterize the size of the smallest detectable scatterer. Then, light scattering images and spectra are acquired from two C-shaped gold nanoparticles. Excitation with two polarization states is employed to try to identify different resonances.

## 7.1 Introduction

The interest in metallic nanoparticles is nowadays driven by the phenomenon of surface enhancement of optical spectroscopies, where the signals of molecules adsorbed on rough metal surfaces or metallic nanoparticles can be strongly enhanced. In the case surface enhanced Raman scattering (SERS), the enhancement factor can reach values above $10^{12}$, allowing for single molecules detection [5, 120, 121]. Even though the adsorption of the molecule on the metal can participate chemically in the Raman enhancement [122], it is believed that the greatly enhanced local electromagnetic fields generated upon excitation of surface plasmons in the metallic nanoparticles are responsible for the major contribution to the SERS effect. Fluorescence can be also enhanced by the strong surface plasmon fields. Alterations of the local photonic mode density can lead to an higher quantum efficiency and shorter lifetime [45,62] of a chromophore, and in molecular fluorescence can lead to a higher number of excitation/de-excitation cycles before irreversible photo-bleaching occurs.

In order to successfully implement the plasmon resonances in practical applications, it is necessary to tailor the resonance frequencies and the field localization in a controlled manner. To achieve this, the investigation of nanoparticles of different shapes and materials is of fundamental importance.

In recent years, a great progress has been made in the fabrication of metallic nano-structures of different shapes [123–127]. Theoretical investigations have been also developed [128, 129] but accurate solutions for the local fields of plasmon resonant particles of arbitrary shape remains however a theoretical challenge. For this reason, experimental investigations are very important.

The aim of this chapter is to demonstrate the capabilities of the home-built SCOM to perform light scattering measurements, with particular application to the study of surface plasmon resonances of metallic nanoparticles. For this purpose, two different gold nanoparticles were studied: spherical colloidal nanoparticles and C-shaped nano-structures.

## 7.2 Light scattering of individual colloidal gold nanoparticles

Colloidal gold nano-particles have been deeply studied and can be readily available, thus they provide an ideal test sample to characterize the performance of the home-build SCOM for light scattering measurements. For this reason, the first experiments were performed with gold nanoparticles with an average size of 20 nm, which due to background limitations, is near the minimum detectable size with this kind of far-field instruments.

### 7.2.1 Experimental

#### Colloidal gold synthesis

Colloidal gold particles nanoparticles were prepared by citrate reduction of gold chloride. The method is well documented [130, 131] and produces gold particles with a narrow size distribution.

The synthetic procedure is as follows: in a 500 ml 2-neck round-bottom flask, 300 ml of a 0.01% Milli-Q water solution of $HAuCl_4$ (*Aldrich GmbH*) are brought to boiling temperature under refluxing and stirring, then 10.5 ml of 1% trisodium citrate (*Aldrich GmbH*) in Milli-Q water is injected rapidly. After the change of color, accomplished within 3 to 5 minutes, the mixture is kept boiling for another 20 minutes. After that, the heating source is removed but the stirring is continued until the solution reaches room temperature. The so prepared colloidal suspension has a conductivity of $380 \pm 20$ mS/cm, and an initial pH of $6.0 \pm 0.3$. The particle size

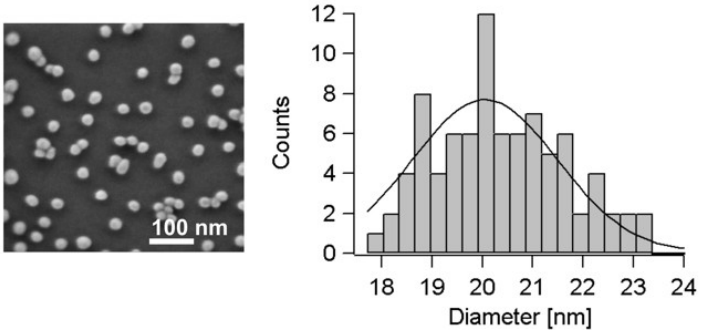


**Figure 7.1:** Size distribution (right) of the colloidal gold particles obtained by analysis of the SEM image (left).

distribution was obtained by analyzing scanning electron microscopy (SEM) images of the gold particles deposited on silicon wafers as described in [57](see figure 7.1).

### Sample preparation

Colloidal gold nanoparticles were physisorbed on thin ($0.13-0.16$ mm) glass coverslips (*N° 1, Menzel-Gläser*). The glass substrates were cleaned successively with Hellmanex 2%, Milli-Q water and ethanol ($\geq$ 98%, *Riedel - de Haën*). In addition, to remove any rest of organic material, the coverslips were heated for two hours at 500 °C in air. To deposit the particles, the gold colloid was let in contact with the coverslips for a certain waiting time and then spin-casted. The waiting time was adjusted in order to obtain a surface density suitable for single particle measurements; the best results were found between 10 and 60 seconds.

### Measurement

Light scattering images and spectra were acquired with the home-built SCOM described in chapter 2 set up for light scattering measurements. A blocking disc with a diameter of 6 mm was used to produce annular illumination (section 2.2.1) and the pinhole size was adjusted in order to optimize the signal to background as explained below.

Images were acquired under laser illumination (Ar-ion, $\lambda = 514.5$ nm) and white light illumination (Xe-arc lamp) was used to acquire the spectra.

## 7.2.2 Images of colloidal gold nanoparticles

Figure 7.2 shows a light scattering image of the 20 nm size gold nanoparticles obtained with circularly polarized, 514.5 nm (Ar-ion laser) illumination. Light-scattering images can be effectively acquired. All the observed scatterers present

a diffraction limited signal with enhanced Airy discs because of the annular illumination.

The signals present different intensities spanning around an order of magnitude. Figure 7.2 (right) also shows representative maximum and minimum signals (obtained from the vertical white lines in the main image), the ratio of the maximum to minimum signal is $(1940 - 120)/(280 - 120) = 12.9$. The scattering cross-section of the particles is proportional to the sixth power of their diameter [132]. From the size distribution of the particles (figure 7.1), the minimum particle size is approximately 17.5 nm and the maximum 23.5 nm. This size range can account only for a ratio of maximum to minimum signal of 5.8. The signals with intensities beyond this range belong probably to small conglomerates of particles or more than one particle lying close to each other within the diffraction limited focal spot.

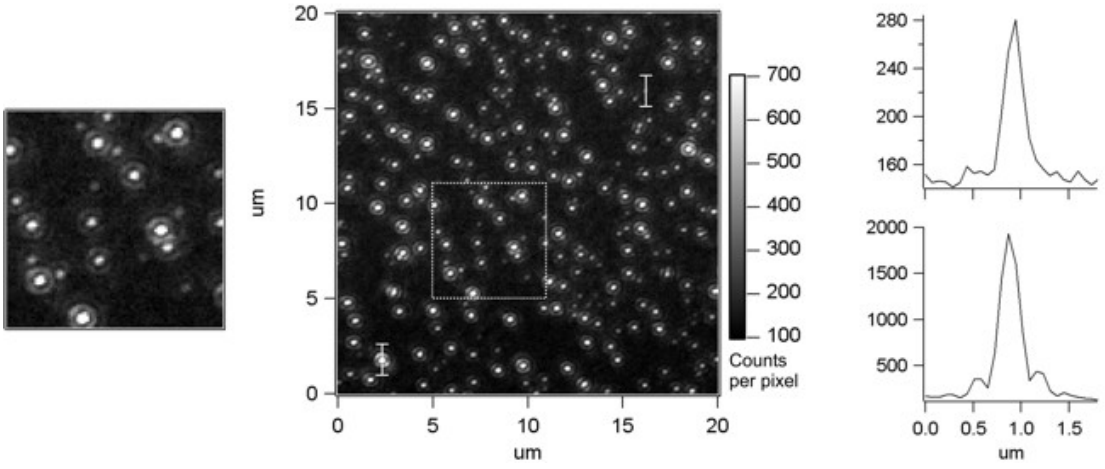


**Figure 7.2:** Light scattering of individual Au-nanoparticles. In the center, a scattered light image of single gold nanoparticles. On the left, a detail of the main image corresponding to the dash-line square. On the right, profiles of the strongest (bottom) and the weakest (top) signals of the main image (marked by the white vertical lines).

Figure 7.3 is meant to show that the measured signals indeed correspond to scattered light. The sample area was scanned from bottom to top. During the first lines the sample was not illuminated, thus the image appears dark to a background intensity level. The next two dark areas were produced by placing a notch filter for the illumination wavelength ($\lambda = 514.5$ nm) in the detection channel. The notch filter renders the image dark to background level showing that the signals are composed of scattered light.

The effect of different sizes of the detection diaphragm aperture was also tested during the scanning for the image of figure 7.3. A large diaphragm aperture allows more reflected light to pass and be detected, therefore the background intensity is higher. Reducing the diaphragm aperture, makes the overall signal less intense and the signal to background ratio higher. There is an optimum size for the diaphragm

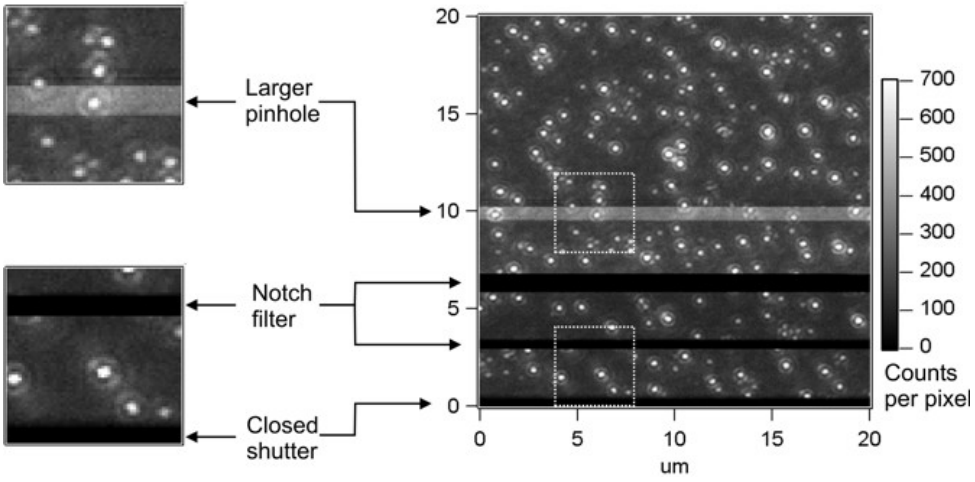


**Figure 7.3:** Light scattering image of individual gold particles. The detail images on the left correspond to the dashed-line squares in the main image

aperture beyond which the signal reduces without any further increase of the signal to background.

### 7.2.3 Spectra of colloidal gold nanoparticles

Using white light illumination, the scattering spectra of individual nanoparticles were recorded. In order to account for the spectral behavior of the system (Xe-arc lamp, lenses, mirrors and CCD-camera), the spectrum of the light reflected at the glass/air interface was recorded from an empty area of the samples and used as reference. The scattering spectral response of a single particle $S(\lambda)$ was obtained by:

$$S(\lambda) = \frac{S_{part}(\lambda) - S_{ref}(\lambda)}{S_{ref}(\lambda)} \tag{7.1}$$

where $S_{part}(\lambda)$ is the intensity of scattered light by a given particle and $S_{ref}(\lambda)$ is the reflected intensity, both for the wavelength $\lambda$.

Spectra from a number of particles were acquired. All the spectra present a single peak corresponding to the excitation of the surface plasmon resonance (SPR) in the quasi-spherical particles [132]. Different SPR wavelengths were found with the trend that longer SPR wavelengths correspond to stronger signals (i.e. larger particles). No further studies were carried out because the aim of the present experiments is to provide a proof of principle for the light scattering measurements and to characterize the resolution of the home built microscope. Figure 7.4.a shows a typical scattering spectra of the colloidal gold particles showing a resonance at

533 nm. Figure 7.4.b shows a spectra of one of the weakest detected signals. This spectra is expected to correspond to the smallest detectable particle and presents a SPR at 520 nm indicating a size of approximately 20 nm [132].

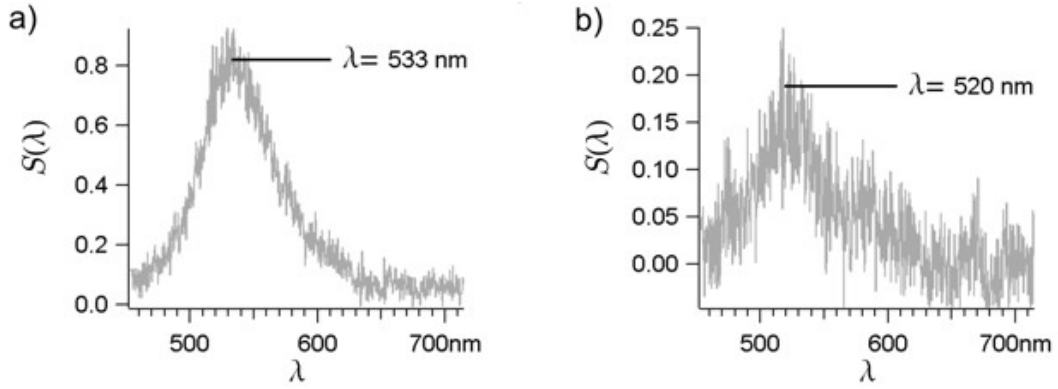


**Figure 7.4:** Light scattering spectra of individual gold particles.

## 7.3 Light scattering of individual C-shaped gold nanoparticles

Metallic nano-structures of more complex shape are more interesting than spherical nano-particles because they can present several surface plasmon resonances and stronger field localization effects. C-shaped nano-structures are supposed to present at least two resonances and a strongly enhanced field localization within the open gap. Far-field investigations should allow to characterize the resonances of these particles and get some understanding of the local field enhancement.

### 7.3.1 Experimental

#### Substrate preparation

Thin glass cover slips (*N° 1, Menzel-Gläser*) were cleaned by immersing them in freshly prepared piranha solution [7:3 concentrated sulfuric acid (*Aldrich GmbH*) 30% hydrogen peroxide(*Aldrich GmbH*)] for 1 hour and then sonicated for 15 minutes. The slides were rinsed copiously with Milli-Q water and dried under a stream of nitrogen. The cover slips were used immediately after this process.

### Fabrication of the C-shaped nano-structures

The fabrication of the C-shaped nanoparticles consists of four steps: deposition of polystyrene (PS) colloids on glass substrates, evaporation of a thin gold film, ion milling and removal of the PS colloids.

PS colloidal nano-spheres (*Polysciences Inc.*) with a Ø=400 nm were physisorbed on the glass coverslips by immersing the substrates for 30 minutes in the PS colloid. Stock solutions of the PS colloid (2.1% solids in water) were stored at 4°C. Before deposition, the PS colloid was allowed to warm to room temperature, sonicated for 5 minutes and then diluted 10 times in ethanol. The coverslips with adsorbed colloids were rinsed with ethanol and dried with a stream of nitrogen. Next, a process of subsequent deposition of a thin gold film was carried out twice followed by ion milling. The samples were mounted in a home-built holder that allows to control the angle of evaporation with respect to the metal source (tilting angle) as well as the rotation angle of the cover slips. A 15 nm gold film was thermally evaporated (thermal evaporator: *Edwards A100*) with a tilting angle of 30°. After that, the samples were rotated by 90° and a second gold film of 15 nm was deposited with the same tilting angle. The thicknesses of the evaporated films were controlled by monitoring the deposited mass with a quartz crystal microbalance. Then, Argon-ion milling (Ion-beam etching machine: *Microsys400, Roth und Rau Oberflächentechnik GmbH*) was performed with a beam perpendicular to the substrate surface in order to remove all the gold not masked by the colloidal PS spheres. Optimization of the ion milling process (8 minutes, $I = 0.1\,mA, V = 100\,V$) is important for removing the gold film while preserving the structure of the polystyrene sphere (i.e. avoiding sphere melting). Finally, the PS spheres were removed (lift off) from both sides of the coverslips by using adhesive tape (*Scotch Magic Tape, 3M Inc.*).

The diameter of the colloidal spheres controls the diameter of the metallic C-shaped nano-structure and the evaporated metal film thickness determines the nanoparticle thickness. The rotation angle between the two evaporations determines the opening angle of the C-structure.

### Measurement

Light scattering images and spectra were acquired with the home-built SCOM described in 2 set up for light scattering measurements. A blocking disc with a diameter of 6 mm was used to produce annular illumination (section 2.2.1) and the pinhole size was adjusted in order to optimize the signal to background.

The images and the spectra were acquired under white light illumination (Xe-arc lamp). A polarizing film was used to linearly polarized the illumination beam.

### 7.3.2 Images and spectra of C-shaped gold nanoparticles

Figure 7.5 shows an SEM image of the gold C-shaped nano-structures (top-right) and a light scattering image (bottom-right). In contrast to the spherical, and much smaller, gold nanoparticles, the signals from the individual C-shaped nano-particles present all very similar intensities.

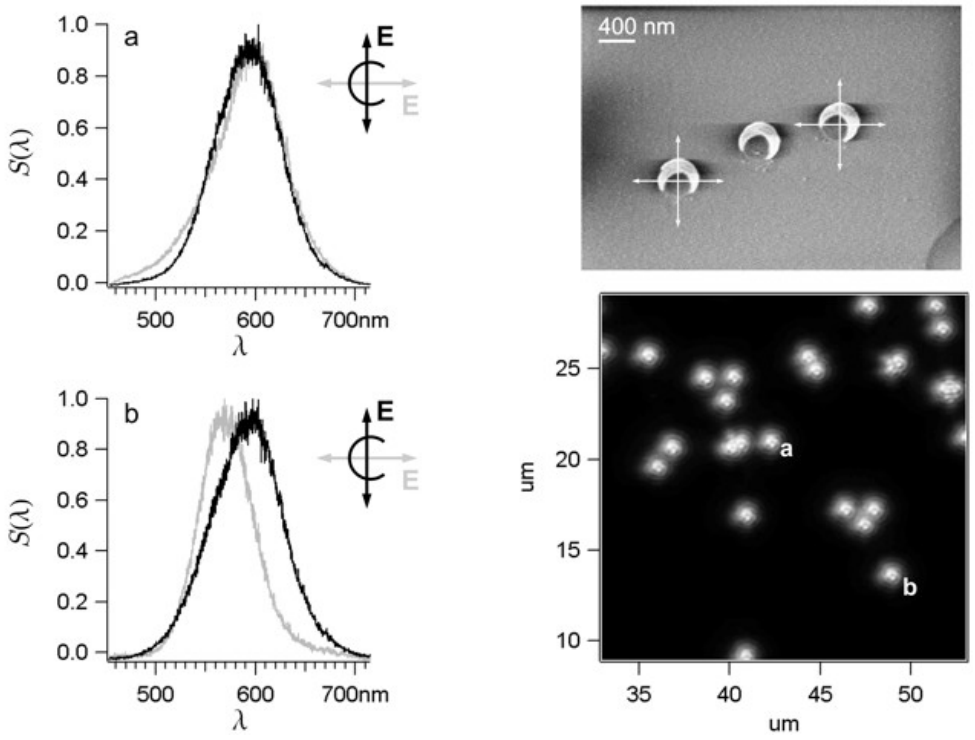


**Figure 7.5:** Light scattering of C-shaped gold nanoparticles. On the right, SEM (top) and scattered light (bottom) images of the particles. On the left, spectra of particles a and b for the two polarization states of the illumination beam.

Light scattering spectra were recorded from several particles with the illumination beam polarized along the symmetry axis of the C-particles and along the perpendicular direction. Some particles showed different behavior for the two polarizations and some particles showed almost indistinguishable spectra. As example, the spectra from the particles marked as a and b are shown on the left of figure 7.5. Particle a does not show a noticeable difference between the two polarizations. The spectra differ slightly from each other in the short-wavelength range but in both cases the maximum lies at around 596 nm. In contrast, particle b presents a clearly different behavior for the two illumination polarizations. When illuminated with light polarized along the symmetry axis of the C, the resonance is found at around 570 nm, and for the perpendicular polarization at around 596 nm. This effect can be explained by the fact that, even though the fabrication process should lead to particles with uniform orientation, the C-shaped particles do not all have the exact same

orientation. As it can be observed in the SEM image of figure 7.5, for the particle on the left, the two polarization states represent two different situations but for the particle on the right, both polarizations constitute almost identical situations.

The previous experimental results represent a nice example to show how important is to investigate these particles individually. In an ensemble measurement, the polarization effects would be hidden by averaging the response of particles with slightly different orientations.

## 7.4 Conclusions

The constructed home-built SCOM can perform light scattering measurements with high sensitivity. Individual scatterers with a sub-wavelength size can be easily detected and studied. For example, colloidal gold particles can be detected down to a size of approximately 20 nm.

The light scattering behavior of C-shaped gold nano-structures was studied for two polarization states: the electric field parallel and perpendicular to the symmetry axis of the C. The two polarization states correspond in some particles to two different resonances but some other particles showed the same spectra for both polarizations. This controversy, which shows the importance of performing studies on a single particle level, might be explained by taking into account that the particles have slightly different orientations. Further measurements and complementary experiments will be carried out to test this hypothesis.

In combination with the results presented in the previous chapters, the results presented here envisage combined measurements of light scattering and fluorescence (or Raman scattering) on a single particle level. Such measurements can be useful to perform a quantitative study of the SERS or enhanced fluorescence in well defined geometries.

# Chapter 8

# Summary

A sample scanning confocal optical microscope (SCOM) was designed and constructed in order to perform local measurements of fluorescence, light scattering and Raman scattering. The components of the SCOM and their functions were described and instructions for the alignment and operation of the microscope were given. This instrument allows to measure time resolved fluorescence, Raman scattering and light scattering from the same diffraction limited spot. Fluorescence from single molecules and light scattering from metallic nanoparticles with a minimum size around 20 nm can be studied.

Two theoretical methods were presented. First, a theoretical method for the description of the electric field distribution in the focus of the SCOM. This enables the design of illumination modes for different purposes, such as the determination of the three-dimensional orientation of single chromophores or the excitation of particular resonances in metallic structures. Second, a method for the calculation of the de-excitation rates of a chromophore. This permits to compare different detection schemes and experimental geometries in order to optimize the collection of fluorescence photons. Both methods were combined to calculate the SCOM fluorescence signal of a chromophore in a general layered system.

The fluorescence excitation and emission of single molecules through a thin gold film was investigated experimentally and modelled. Chromophores were placed at a controlled separation distance from the gold film by means of a polyelectrolyte spacer layer.

It was demonstrated that, due to the mediation of surface plasmons, single molecule fluorescence near a thin gold film can be excited and detected with an epi-illumination scheme through the film. Single molecule fluorescence as close as 15 nm to the gold film was studied in this manner.

In comparison to the detection from the air side, the surface plasmon mediated detection through the gold film resulted more efficient. In comparison to the

case without gold, the number of detectable photons emitted by perpendicular fluorophores was found to be enhanced by a factor of 1.4. The latter is a consequence of the increased photo-stability produced by the surface plasmon enhanced total de-excitation rate.

An excellent quantitative agreement between the experimental and modelled single molecule fluorescence signals was found if the molecules were considered to behave optically as on the air side of the interface.

The fluorescence dynamics (fluorescence blinking and excited state lifetime) of single molecules was studied in the presence and in the absence of a nearby gold film in order to investigate the influence of the metal on the electronic transition rates.

Two methods (trace-histogram and autocorrelation) for the analysis of single molecule fluorescence blinking were presented and evaluated. The trace-histogram method was improved with respect to previously reported algorithms in order to systematically find the best compromise between time resolution and accuracy in distinguishing between on- and off-states. A Monte-Carlo procedure to simulate single molecule fluorescence blinking was set-up and used to compare the performance of the two analysis methods. The autocorrelation method was found to be more reliable, specially for the analysis of short kinetic traces.

The influence of the nearby gold on the total decay rate $\Gamma_{21}$ was clearly observed. Comparison to theoretical calculations showed that the observed distribution of $\Gamma_{21}$ in the absence of gold can be explained if the chromophores behave optically as on the air side of the interface, confirming the results obtained from the intensity distribution of the fluorescence signals.

No influence of the gold presence on the ISC rate from the excited state to the triplet $\Gamma_{23}$ was observed. In contrast, the gold presence produced a 2-fold (in average) increase of the transition rate from the triplet to the singlet ground state $k_{on}$ ($= \Gamma_{31}$). Furthermore, a positive correlation between $\Gamma_{21}$ and $k_{on}$ was found which indicates that the gold film influences $\Gamma_{31}$ and $\Gamma_{21}$ in a similar way; i.e. the triplet-singlet and the singlet-singlet transition dipoles have similar orientations.

The photoluminescence blinking of $Zn_{0.42}Cd_{0.58}Se$ QDs on glass and ITO substrates was investigated experimentally as a function of the excitation power ($P$). At low $P$, it was observed that the probability of a certain on- or off-time follows a negative power-law with exponent $m$ near to 1.6. As $P$ increased, the on-time fraction reduced on both substrates whereas the off-times did not change. A weak residual memory effect between consecutive on-times and consecutive off-times was observed but not between a given on-time and the adjacent off-time. All of this suggests the presence of two distinct mechanisms governing the lifetimes of the on- and off-states.

The photoluminescence of quantum dots presented a variety of on-intensity distributions, in general broader than a Poissonian. The probability of the on- and

off-times followed the same power-law regardless of the shape of the on-intensity distribution.

The blinking of the QDs was modelled via Monte-Carlo simulations. The QDs were thought to switch between a dark state and an emitting state with power-law probability. The simulated kinetic traces showed Poisson-distributed off- and on-intensities, demonstrating that the non-Poissonian on-intensity of the QDs is not a product of the underlying power-law probability of the on- and off-times and that the blinking of QDs occurs between a non-emitting off-state and a distribution of emitting on-states with different intensities.

In order to account for the photo-induced shortening of the on-times, an independent single-rate transition from the on- to the off-state was introduced in the simulations. Exclusively by means of this transition it was possible to reproduce the experimentally observed photo-induced effects (shortening of the on-time fraction and maximum on-time, and increase of the cycles per second) and to assign a characteristic photo-induced lifetime $\tau_{PI}$ to the on-state of QDs on glass and on ITO. The QDs on glass presented a $\tau_{PI}$ proportional to $P^{-1}$ suggesting the presence of a one-photon process. In the case of the QDs on ITO, the dependence of $\tau_{PI}$ on $P$ could be reasonably fitted by an single exponential.

Light scattering images and spectra of colloidal and C-shaped gold nano-particles were acquired. From the studies on colloidal gold nano-particles it was possible to determine that the minimum size of a metallic scatterer detectable with the SCOM lies around 20 nm.

The C-shaped gold nano-particles were studied under excitation with two polarization states. Some particles showed two distinct resonances for the different polarization states and some particles did not. These experiments showed the potential of the SCOM to investigate surface plasmon resonances in metallic nano-particles and the importance of studying them on a single particle basis.

In conclusion, experimental and theoretical contributions were made for the quantitative understanding of the influence of locally enhanced electromagnetic fields on single molecule fluorescence.

# Appendix A

# Set-up control and data acquisition software

In this appendix, the programmed code for the control of the home-built SCOM and the data acquisition is presented. The routines are commented and some important characteristics of the programming languages are explained.

All the computer controlled functions of the home-built SCOM are driven by signals provided by the Analog-Digital/Digita-Analog (AD/DA) PC-Card. Operations to be performed by the AD/DA card can be controlled by routines loaded in its local CPU. These routines are programmed in AD-Basic and can be found in the section A.1.

The user interface was programmed with Igor in order to use Igor's built-in capabilities for data treatment. The code of the user interface functions is presented in section A.2.

Since the AD-Basic language has no drivers for Igor, intermediate routines in C++ were needed to complete the communication flow between the user and the local CPU of the AD/DA card. The corresponding C++ routines can be found in the section A.3.

## A.1 AD-Basic routines

### ScanInit.BAS

*Prozeßnummer = 4*

*Delay = 1000*

*Eventsource = 0*

*Number of Loops = 0*

*Priorität = 1*

*Version = 1*

*FastStop = 0*

*AdbasicVersion = 2000000*

```
ATSRAM = 0
OPT_LEVEL = 1
SAVECOMPIL = 0
DIM i,check,X,Y AS INTEGER
DIM DATA_1[10000] AS LONG
DIM DATA_2[10000] AS LONG
DIM DATA_3[10000] AS LONG
DIM DATA_4[10000] AS LONG
DIM DATA_5[10000] AS LONG
DIM DATA_11[10000] AS LONG
DIM DATA_12[10000] AS LONG
DIM DATA_13[10000] AS LONG
DIM DATA_14[10000] AS LONG
DIM DATA_15[10000] AS LONG
DIM DATA_31[10000] AS LONG
DIM DATA_32[10000] AS LONG
DIM DATA_21[100000] AS LONG
DIM DATA_22[100000] AS LONG
DIM DATA_23[100000] AS LONG
#DEFINE Xi PAR_1
#DEFINE Yi PAR_2
#DEFINE X PAR_7
#DEFINE Y PAR_8
EVENT:
    GLOBALDELAY=1
    i=0
    X=PAR_7
    Y=PAR_8
    IF(X<32768)THEN
        X=32768
    ENDIF
    IF(Y<32768)THEN
        Y=32768
    ENDIF
    IF(X>65535)THEN
        X=65535
    ENDIF
    IF(Y>65535)THEN
        Y=65535
    ENDIF
    IF(X<>Xi)THEN
        IF (Xi<X) THEN
            IF(X-Xi<1900)THEN
                DO
                    i=0
                    DEC(X)
```

```
                    DO
                        DAC(1,X)
                        i=i+1
                    UNTIL(i=2000)
                UNTIL(X=Xi)
            ELSE
                DO
                i=0
                DEC(X)
                DO
                    DAC(1,X)
                    i=i+1
                UNTIL(i=150)
            UNTIL(X=Xi)
        ENDIF
    ELSE
        IF(Xi-X<1900)THEN
            DO
                i=0
                INC(X)
                DO
                    DAC(1,X)
                    i=i+1
                UNTIL(i=2000)
            UNTIL(X=Xi)
        ELSE
            DO
                i=0
                INC(X)
                DO
                    DAC(1,X)
                    i=i+1
                UNTIL(i=150)
            UNTIL(X=Xi)
        ENDIF
    ENDIF
ENDIF
i=0
IF(Y<>Yi)THEN
    IF (Yi<Y) THEN
        IF(Y-Yi<1900)THEN
            DO
                i=0
                DEC(Y)
                DO
                    DAC(2,Y)
```

```
                    i=i+1
                UNTIL(i=2000)
            UNTIL(Y=Yi)
        ELSE
            DO
                i=0
                DEC(Y)
                i=0
                DO
                    DAC(2,Y)
                    i=i+1
                UNTIL(i=150)
            UNTIL(Y=Yi)
        ENDIF
    ELSE
        i=0
        IF(Yi-Y<1900)THEN
            DO
                i=0
                INC(Y)
                DO
                    DAC(2,Y)
                    i=i+1
                UNTIL(i=2000)
            UNTIL(Y=Yi)
        ELSE
            i=0
            DO
                INC(Y)
                DO
                    DAC(2,Y)
                    i=i+1
                UNTIL(i=150)
                i=0
            UNTIL(Y=Yi)
        ENDIF
    ENDIF
ENDIF
PAR_21=0
PAR_22=0
PAR_23=0
i=1
DO
    DATA_1[i]=0
    DATA_2[i]=0
    DATA_3[i]=0
```

```
    DATA_4[i]=0
    DATA_5[i]=0
    DATA_11[i]=0
    DATA_12[i]=0
    DATA_13[i]=0
    DATA_14[i]=0
    DATA_15[i]=0
    DATA_31[i]=0
    DATA_32[i]=0
    INC(i)
UNTIL(i=10000)
i=1
DO
    DATA_21[i]=0
    DATA_22[i]=0
    DATA_23[i]=0
    INC(i)
UNTIL(i=100000)
check=1
END
```

## HP-Pixel.BAS

```
 Prozeßnummer = 2
Delay = 1
Eventsource = 0
Number of Loops = 0
Priorität = 0
Version = 1
FastStop = 0
AdbasicVersion = 2000000
ATSRAM = 0
OPT_LEVEL = 1
SAVECOMPIL = 0
DIM delay, time1, time2, time, Pixeltime AS long
DIM X, j, Counts AS INTEGER
DIM DATA_3[10000]AS LONG 'Counts'
DIM DATA_4[10000]AS LONG 'time0'
DIM DATA_5[10000]AS LONG 'time3'
#DEFINE Pixeltime PAR_5
#DEFINE flag PAR_55
#INCLUDE C:\ADwin\ADbasic3\Inc\adwgcnt.inc
INIT:
    Globaldelay=1
```

```
EVENT:
    Pixeltime=PAR_5
    X=PAR_7
    j=PAR_9
    flag=0
    time1=READ_TIMER()
    IF(j>1)THEN
        time1=DATA_5[j-1]
    ENDIF
    DO
        DAC(1,X)
        time=READ_TIMER()
        delay=(time-time1)
    UNTIL(delay>=Pixeltime)
    time2=READ_TIMER()
    Counts=CNT_READ(1)
    CNT_CLEAR(1)
    DATA_3[j]=Counts
    DATA_4[j]=time1
    DATA_5[j]=time2
END
FINISH:
    flag=1
```

## LP-HP-LineScan.BAS

```
 Prozeßnummer = 1
Delay = 1
Eventsource = 0
Number of Loops = 0
Priorität = 1
Version = 1
FastStop = 0
AdbasicVersion = 2000000
ATSRAM = 0
OPT_LEVEL = 1
SAVECOMPIL = 0
DIM test,Tpixels,j AS INTEGER
DIM DATA_1[10000]AS LONG 'X'
DIM DATA_2[10000]AS LONG 'Y'
DIM DATA_6[10000]AS LONG 'Monitor X'
#DEFINE Xi PAR_1
#DEFINE Yi PAR_2
#DEFINE Scanrange PAR_3
```

```
#DEFINE Pixels PAR_4
#DEFINE Pixeltime PAR_5
#DEFINE Pixelsize PAR_6
#DEFINE X PAR_7
#DEFINE Y PAR_8
#DEFINE j PAR_9
#DEFINE terminated PAR_11
#DEFINE flag PAR_55
#INCLUDE C:\ADwin\ADbasic3\Inc\adwgcnt.inc
INIT:
    terminated=0
    globaldelay=1
    test=0
    IF(test=1)THEN
        Xi=32768
        Yi=32768
        Scanrange=32768
        Pixels=5
        Pixeltime=200
        Y=45000
    ENDIF
EVENT:
    PAR_11=0
    Pixelsize=Scanrange/Pixels
    Pixeltime=Pixeltime*40 'usec'
    X=Xi-(Pixelsize/2)
    Y=PAR_8
    flag=1
    j=0
    CNT_ENABLE(1)
    CNT_CLEAR(1)
    DAC(2,Y)
    DO
        j=j+1
        X=X+Pixelsize
        DATA_1[j]=X
        DATA_2[j]=Y
        START_PROCESS(2)
        DO
            'X=PAR_7'
        UNTIL(flag=1)
        DATA_6[j]=ADC(1)
    UNTIL(j=Pixels)
    DO
        j=j+1
        START_PROCESS(2)
```

```
        DO
            'X=PAR_7'
        UNTIL(flag=1)
        DATA_1[j]=X
        DATA_2[j]=Y
        X=X-Pixelsize
        DATA_6[j]=ADC(1)
    UNTIL(j=2*Pixels)
    X=X+Pixelsize
END
FINISH:
PAR_11=1
```

## LP-HP-LineScan_Calibration.BAS

```
 Prozeßnummer = 7
Delay = 1       Eventsource = 0
Number of Loops = 0
Priorität = 1* Version = 1
FastStop = 0* AdbasicVersion = 2000000
ATSRAM = 0
OPT_LEVEL = 1
SAVECOMPIL = 0
DIM test,Tpixels,j,k AS INTEGER
DIM DATA_1[10000]AS LONG 'X'
DIM DATA_2[10000]AS LONG 'Y'
DIM DATA_11[10000]AS LONG 'X'
DIM DATA_12[10000]AS LONG 'Y'
DIM DATA_31[10000]AS LONG 'Xmon'
DIM DATA_32[10000]AS LONG 'Xmon'
#DEFINE Xi PAR_1
#DEFINE Yi PAR_2
#DEFINE Scanrange PAR_3
#DEFINE Pixels PAR_4
#DEFINE Pixeltime PAR_5
#DEFINE Pixelsize PAR_6
#DEFINE X PAR_7
#DEFINE Y PAR_8
#DEFINE j PAR_9
#DEFINE terminated PAR_11
#DEFINE flag PAR_55
#INCLUDE C:\ADwin\ADbasic3\Inc\adwgcnt.inc
INIT:
    terminated=0
```

```
    GLOBALDELAY=1
    SET_MUX(0)
    test=0
    IF(test=1)THEN
        Xi=32768
        Yi=32768
        Scanrange=3277
        Pixels=128
        Pixeltime=5000
        Y=45000
    ENDIF
EVENT:
    PAR_11=0
    Pixelsize=Scanrange/Pixels
    Pixeltime=Pixeltime*40 'usec'
    X=Xi-(Pixelsize/2)
    Y=PAR_8
    flag=1
    j=0
    CNT_ENABLE(1)
    CNT_CLEAR(1)
    DAC(2,Y)
    DO
        j=j+1
        X=X+Pixelsize
        DATA_1[j]=X
        DATA_2[j]=Y
        START_PROCESS(2)
        DO
            X=PAR_7
        UNTIL(flag=1)
        DATA_31[j]=ADC(1)
    UNTIL(j=Pixels)
    DO
        j=j+1
        START_PROCESS(2)
        DO
            X=PAR_7
        UNTIL(flag=1)
        DATA_31[j]=ADC(1)
        DATA_1[j]=X
        DATA_2[j]=Y
        X=X-Pixelsize
    UNTIL(j=2*Pixels)
    X=X+Pixelsize
END
```

```
FINISH:
    PAR_11=1
```

## HP-Pixel-Vert.BAS

```
 Prozeßnummer = 8
Delay = 1
Eventsource = 0
Number of Loops = 0
Priorität = 0
Version = 1
FastStop = 0
AdbasicVersion = 2000000
ATSRAM = 0
OPT_LEVEL = 1
SAVECOMPIL = 0
DIM delay, time1, time2, time, Pixeltime AS long
DIM Y,j, Counts AS INTEGER
DIM DATA_3[10000]AS LONG 'Counts'
DIM DATA_4[10000]AS LONG 'time0'
DIM DATA_5[10000]AS LONG 'time3'
#DEFINE Pixeltime PAR_5
#DEFINE flag PAR_55
#INCLUDE C:\ADwin\ADbasic3\Inc\adwgcnt.inc
INIT:
    Globaldelay=1
EVENT:
    Pixeltime=PAR_5
    Y=PAR_7
    j=PAR_9
    flag=0
    time1=READ_TIMER()
    IF(j>1)THEN
        time1=DATA_5[j-1]
    ENDIF
    DO
        DAC(2,Y)
        time=READ_TIMER()
        delay=(time-time1)
    UNTIL(delay>=Pixeltime)
    time2=READ_TIMER()
    Counts=CNT_READ(1)
    CNT_CLEAR(1)
    DATA_3[j]=Counts
```

```
    DATA_4[j]=time1
    DATA_5[j]=time2
END
FINISH:
    flag=1
```

## LP-HP-LineScan-Vert.BAS

```
 Prozeßnummer = 3
Delay = 1
Eventsource = 0
Number of Loops = 0
Priorität = 1
Version = 1
FastStop = 0
AdbasicVersion = 2000000
ATSRAM = 0
OPT_LEVEL = 1
SAVECOMPIL = 0
DIM test,Tpixels,j AS INTEGER
DIM DATA_1[10000]AS LONG 'X'
DIM DATA_2[10000]AS LONG 'Y'
DIM DATA_6[10000]AS LONG 'Monitor X'
#DEFINE Xi PAR_1
#DEFINE Yi PAR_2
#DEFINE Scanrange PAR_3
#DEFINE Pixels PAR_4
#DEFINE Pixeltime PAR_5
#DEFINE Pixelsize PAR_6
#DEFINE Y PAR_7
#DEFINE X PAR_8
#DEFINE j PAR_9
#DEFINE terminated PAR_11
#DEFINE flag PAR_55
#INCLUDE C:\ADwin\ADbasic3\Inc\adwgcnt.inc
INIT:
    terminated=0
    globaldelay=1
    test=0
    IF(test=1)THEN
        Xi=32768
        Yi=32768
        Scanrange=32768
        Pixels=5
```

```
            Pixeltime=200
            Y=45000
        ENDIF
    EVENT:
        PAR_11=0
        Pixelsize=Scanrange/Pixels
        Pixeltime=Pixeltime*40 'usec'
        Y=Yi-(Pixelsize/2)
        X=PAR_8
        flag=1
        j=0
        CNT_ENABLE(1)
        CNT_CLEAR(1)
        DAC(1,X)
        DO
            j=j+1
            Y=Y+Pixelsize
            DATA_1[j]=X
            DATA_2[j]=Y
            START_PROCESS(8)
            DO
            UNTIL(flag=1)
            DATA_6[j]=ADC(1)
        UNTIL(j=Pixels)
        DO
            j=j+1
            START_PROCESS(8)
            DO
            UNTIL(flag=1)
            DATA_1[j]=X
            DATA_2[j]=Y
            Y=Y-Pixelsize
            DATA_6[j]=ADC(1)
        UNTIL(j=2*Pixels)
        Y=Y+Pixelsize
    END
    FINISH:
        PAR_11=1
```

## HP-KineticPixel.BAS

```
 Prozeßnummer = 6
Delay = 1
Eventsource = 0
```

```
Number of Loops = 0
Priorität = 0
Version = 1
FastStop = 0
AdbasicVersion = 2000000
ATSRAM = 0
OPT_LEVEL = 1
SAVECOMPIL = 0
DIM DATA_21[100000] AS LONG
DIM DATA_22[100000] AS LONG
DIM DATA_23[100000] AS LONG
DIM time,time1,time2,delay,counts AS LONG
DIM test AS INTEGER
#DEFINE Pixeltime PAR_5
#DEFINE j PAR_9
#DEFINE flag PAR_55
#DEFINE Xi PAR_1
#INCLUDE C:\ADwin\ADbasic3\Inc\adwgcnt.inc
INIT:
    globaldelay=1
    test=0
    IF(test=1)THEN
            PAR_5=500000
    ENDIF
EVENT:
    Pixeltime=PAR_5
    flag=0
    time1=READ_TIMER()
    j=PAR_9
    'CNT_ENABLE(1)'
    'CNT_CLEAR(1)'
    time1=READ_TIMER()
    IF(j>1)THEN
        time1=DATA_22[j-1]
    ENDIF
    DO
        time=READ_TIMER()
        delay=(time-time1)
    UNTIL(delay>=Pixeltime)
    time2=READ_TIMER()
    Counts=CNT_READ(1)
    CNT_CLEAR(1)
    DATA_23[j]=Counts
    DATA_21[j]=time1
    DATA_22[j]=time2
    j=j+1
```

```
        flag=1
END
```

## LP-HP-PointKinetic.BAS

```
 Prozeßnummer = 5
Delay = 1
Eventsource = 0
Number of Loops = 0
Priorität = 1
Version = 1
FastStop = 0
AdbasicVersion = 2000000
ATSRAM = 0
OPT_LEVEL = 1
SAVECOMPIL = 0
DIM DATA_21[100000] AS LONG
DIM DATA_22[100000] AS LONG
DIM DATA_23[100000] AS LONG
DIM j,test AS INTEGER
DIM time0,time3,time,delay,Kineticduration AS LONG
#DEFINE Xi PAR_1
#DEFINE Yi PAR_2
#DEFINE Pixeltime PAR_5
#DEFINE j PAR_9
#DEFINE Kineticduration PAR_15
#DEFINE flag PAR_55
#INCLUDE C:\ADwin\ADbasic3\Inc\adwgcnt.inc
INIT:
    globaldelay=1
    flag=0
    test=0
    IF(test=1)THEN
        PAR_1=32768
        PAR_2=32768
        PAR_5=100
        PAR_15=2
    ENDIF
EVENT:
    globaldelay=1
    PAR_11=0
    Xi=PAR_1
    Yi=PAR_2
    CNT_ENABLE(1)
```

```
        CNT_CLEAR(1)
        Pixeltime=PAR_5
        Pixeltime=Pixeltime*40 'usec'
        PAR_5=Pixeltime
        time0=READ_TIMER()
        Kineticduration=Kineticduration*10000
        DAC(2,Yi)
        DAC(1,Xi)
        time0=READ_TIMER()
        j=1
        DO
            START_PROCESS(6)
            DO
                flag=PAR_55
            UNTIL(flag=1)
            time=READ_TIMER()
            delay=time-time0
        UNTIL(delay>=Kineticduration)
        time3=READ_TIMER()
        PAR_11=1
    END
    FINISH:
```

## A.2 Igor routines

Igor routines are called *Function, Macro or Window* and are grouped in *Procedures*. Igor can also call external routines programmed in other languages, these external routines are called *XOPs* [133] and in this case were programmed in C++ (see A.3). Any set of data, i.e. an array of numbers, is called *Wave* in Igor; a *Wave* can be one-, two-, three- or four-dimensional. In this section, all the *Procedures* programmed to control the operation of the home-build confocal microscope are presented. Every Procedure and individual routine is explained and commented (in Igor the symbol "//" is used to add comments in the code). Most of Igor commands have self-explaining names and the code can be easily followed and in case of doubts, there is a complete lexicon with all the programming commands in Igor's manual. However, it is worth to make a remark regarding the way Igor treats global variables. If at the beginning of a Procedure reads:
*#pragma rtGlobals=0*
then, global variables and *Waves* do not need to be declared to be accessed in any function. On the other hand, if at the beginning of an Igor procedure states:
*#pragma rtGlobals=1*
then, all the global variables need to be declared in the corresponding functions

with the commands *Nvar* and *Svar*. *Waves*, have to be declared as well with the command *Wave*.

### Procedure ADWinInitiation

ADWinInitiation Procedure has two functions. The one, via the *ADWinBoot2 XOP*, boots and loads all the necessary routines to the local CPU of the AD/DA PC-card. And the other, via the *ADWinInit2 XOP*, sends the stage to a initial position

```
#pragma rtGlobals=1

Function Boot()
    Nvar,Xi,Yi,Xi_prev,Scanrange_prev,Pixels_prev
    Xi=32768 // 0 Volt
    Yi=32768 // 0 Volt
    Xi_prev=0
    Yi_prev=0
    Scanrange_prev=0
    Pixeltime_prev=0
    Pixels_prev=0
    Pixeltime_prev=0
    Init()
    Execute "ADWinBoot2" //ADWinBoot2 is an XOP written in C++
End

Function Init()
    Variable result,t1,t2
    Execute "ADWinInit2, Xi, Yi" //ADWinInit2 is an XOP written in C++
    t1=DateTime
    Do
        t2=DateTime
    While(t2-t1<14)
    Return result
End
```

### Procedure Calibration

This procedure realizes all the necessary corrections for the delay of the piezoelectric drivers. *ScanCalib* scans, via the Function *ExecuteScanCalib* and the *ScanCalibration XOP*, three lines with the set parameters and records the capacitive monitor signal from the amplifier. Then it calls *CalibrationDisplay* which calculates the corrected position and displays it together with the driving signal and the capacitive monitor signal. The corrected position is calculated from the monitor signal

with the calibration parameters. The function *CheckValues* belongs to Procedure Confocal Imaging A.2.

```
#pragma rtGlobals=0


Function ScanCalib()
    Variable paramctrl, j, Offset
    Xi_um=Xi_um_display
    Yi_um=Yi_um_display
    Pixels=Pixels_display
    Scanrange_um=Scanrange_um_display
    If (CheckValues()==0)
        Abort "Scan aborted. Parameters out of range"
    Endif
    DoUpdate
    CalculateParametersForADWin()
    Init()
    DoWindow/B PointKinetic
    DoWindow/F Calibration
    Make /O/I/U/N=(2*Pixels) Xdisplay
    Make /O/I/U/N=(2*Pixels) Xmondisplay
    Make /O/I/U/N=(2*Pixels) t2display
    Make /O/I/U/N=(2*Pixels) Corr_Xmondisplay
    CompleteImage[][]=0
    Xdisplay=0
    Xmondisplay=0
    t2display=0
    Make/O/I/U/N=(2*Pixels,4) calibrationwave
    ActualY=Yi+(Pixelsize/2)
    XminusXmon=0
    RemoveFromGraph/Z fit_Xmondisplay, fit_Xdisplay, fit_XmondisplayB
    RemoveFromGraph/Z fit_XmondisplayF, PrevXdisplay
    j=0
    Do
        ExecuteScanCalibration()
        CalibrationDisplay()
        j+=1
    While (j<3)
    Return 1
End


Function ExecuteScanCalibration()
    Execute "ScanCalibration, Xi, Yi, Scanrange, Pixels, Pixeltime, ActualY, 'calibrationwave'"
End
```

```
Function CalibrationDisplay()
    Variable TimeZero,Offset
    Wave Xdisplay, Xmondisplay, t2display, Corr_Xmondisplay, Calibrationwave
    Xdisplay = Calibrationwave[p][0]
    Xmondisplay = Calibrationwave[p][1]
    t2display= Calibrationwave[p][3]
    TimeZero= t2display[0]
    t2display= t2display-TimeZero
    Offset= Xdisplay[0]-Xmondisplay[0]
    Xmondisplay= Xmondisplay+Offset
    Corr_Xmondisplay[0,Pixels-1]= Xmondisplay[p] + (10852*Pixelsize / Pixeltime + 299665*(Pixelsize/Pixeltime)^2)
    Corr_Xmondisplay[Pixels,2*Pixels-1]= Xmondisplay[p] - (10852*Pixelsize / Pixeltime + 299665*(Pixelsize/Pixeltime)^2)
End
```

*FitLinearRange* fits the linear range of the corrected monitor signal and calculates how many pixels have to be added and the initial position for the measurement scan in order to have the desired number of pixels and scanning range in the linear range of the stage position. The *CorrectParameters* function sets the scanning global variables to the values calculated by *FitLinearRange*. And the function *RestoreDisplayValues* gives the user the possibility to recover the uncorrected parameters.

```
Function FitLinearRange()
    Wave Xdisplay, Xmondisplay, t2display, Corr_Xmondisplay, W_coef
    Variable a, b, Yup, Ydwn, i, j, difference, Pixels_aux
    RemoveFromGraph /Z fit_Corr_XmondisplayF
    RemoveFromGraph /Z fit_Corr_XmondisplayB
    XiF=0.4*Pixels
    XfF=Pixels-1
    Cursor /P A Corr_Xmondisplay XiF
    Cursor /P B Corr_Xmondisplay XfF
    CurveFit/Q/N line Xdisplay[0,Pixels-1] //a+bx
    CurveFit/Q/N/H="01" line Corr_Xmondisplay[XiF,XfF] //a+bx
    a=W_coef[0]
    b=W_coef[1]
    Make/O/N= (Pixels*1.20) fit_Corr_XmondisplayF
    fit_Corr_XmondisplayF= a+b*p
    AppendToGraph fit_Corr_XmondisplayF vs t2display
    XiB=1.4*Pixels
    XfB=2*Pixels-1
    Cursor /P A Corr_Xmondisplay XiB
    Cursor /P B Corr_Xmondisplay XfB
    CurveFit/Q/N line Xdisplay[Pixels,2*Pixels-1] //a+bx
    CurveFit /Q/N/H="01" line Corr_Xmondisplay[XiB,XfB]
    a=W_coef[0]
    b=W_coef[1]
```

```
Make/O/N=(Pixels) fit_Corr_XmondisplayB
fit_Corr_XmondisplayB=a+b*(p+Pixels)
Duplicate /O/R=[Pixels, 2*Pixels-1] t2display t2displayB
AppendToGraph fit_Corr_XmondisplayB vs t2displayB
j=0
Do
    difference=Corr_Xmondisplay[j]-fit_Corr_XmondisplayF[j]
    j+=1
While (difference>Pixelsize)
XiF=j-1
j=0
Do
    difference= fit_Corr_XmondisplayB[j] - Corr_Xmondisplay[j+Pixels]
    j+=1
While (difference>Pixelsize)
XiB=j-1+Pixels
If (Corr_Xmondisplay[XiF]== Corr_Xmondisplay[2*Pixels-1])
    XfB=2*Pixels-1
Elseif (Corr_Xmondisplay[XiF]> Corr_Xmondisplay[2*Pixels-1])
    j=2*Pixels-1
    Do
        difference=Corr_Xmondisplay[XiF] - Corr_Xmondisplay[j]
        j-=1
    While (difference>Pixelsize)
    XfB=j+1
Else
    XfB=2*Pixels-1
    j=XiF
    Do
        difference=Corr_Xmondisplay[2*Pixels-1] - Corr_Xmondisplay[j]
        j+=1
    While (difference>Pixelsize)
    XiF=j-1
Endif
If (Corr_Xmondisplay[Pixels-1]== Corr_Xmondisplay[XiB])
    XfF=Pixels-1
Elseif (Corr_Xmondisplay[Pixels-1]> Corr_Xmondisplay[XiB])
    j=Pixels-1
    Do
        difference=Corr_Xmondisplay[j] - Corr_Xmondisplay[XiB]
        j-=1
    While(difference>Pixelsize)
    XfF=j+1
Else //should never happen aber...
    j=XiB
    Do
```

```
            difference=Corr_Xmondisplay[j] - Corr_Xmondisplay[Pixels-1]
            j+=1
        While(difference>Pixelsize)
        XiB=j-1
        XfF=Pixels-1
    Endif
    PixelsToDiscard=XiF
    Ydwn=Corr_Xmondisplay[XiF-1]
    j=XiF
    Do
        j-=1
    While (Xdisplay[j]>Ydwn)
    PixelsToCorrectInX=j+1
    XminusCorr_X_F = Sum(Xdisplay,XiF,XfF) / (XfF-XiF) - Sum(Corr_Xmondisplay,XiF,XfF) / (XfF-XiF)
    XminusCorr_X_B = Sum(Xdisplay,XiB,XfB) / (XfB-XiB) - Sum(Corr_Xmondisplay,XiB,XfB) / (XfB-XiB)
End

Function CorrectParameters()
    Variable result, Pixels, Pixels_display, PixelsToDiscard, Pixelsize
    Variable Scanrange, Xi, Xi_um, PixelsToCorrectInXScanrange_um
    Xi=Xi-PixelsToCorrectInX*Pixelsize
    Scanrange= Scanrange + PixelsToDiscard*PixelSize
    Pixels= round(Scanrange/Pixelsize)
    Scanrange_um=Scanrange*80/32768
    Xi_um=(Xi-32768)*80/32768
    result=1
    If (Xi_um<0)
        DoAlert 0, "X is out of range after calibration"
        result=0
    Endif
    If (Scanrange_um>80)
        DoAlert 0, "Scan range is too big after calibration"
    result=0
    Endif
    Return result
End

Function RestoreDisplayValues(RestoreDisplayValues):ButtonControl
    String RestoreDisplayValues
    Xi_um=Xi_um_display
    Yi_um=Yi_um_display
    Scanrange_um=Scanrange_um_display
    Pixels=Pixels_display
    Xi=Xi_um*32768/80+32768 //Piezo-table in closed loop moves 80um
    Yi=Yi_um*32768/80+32768 // for the 0-10V (32768 ADWin units) range
    Scanrange=Scanrange_um*32768/80
```

```
    Xf=Xi+Scanrange
    Yf=Yi+Scanrange
    Xf_um=Xi_um+Scanrange_um
    Yf_um=Yi_um+Scanrange_um
End
```

Once the corrected parameters are calculated, a new set of 3 scans is performed by *ScanFinalCalib* with the corrected parameters. Then, through *FitFinalLinear-Range*, it is verified that with the new parameters, an image with the desired number of pixels and position can be constructed within the linear range of the piezo-stage trajectory.

```
Function ScanFinalCalib()
    Variable paramctrl,j,Offset
    Wave Xdisplay, t2display, Xmondisplay, Corr_Xmondisplay
    DoWindow/B PointKinetic
    DoWindow/F Calibration
    ControlInfo /W=ControlPanel KeepPrevFit
    If (V_value==1)
        Duplicate/O Xdisplay PrevXdisplay
        Duplicate/O t2display Prevt2display
    Endif
    Redimension /N=(2*Pixels) Xdisplay
    Redimension/N=(2*Pixels) Xmondisplay
    Redimension/N=(2*Pixels) t2display
    Redimension/N=(2*Pixels) Corr_Xmondisplay
    Xdisplay=0
    Xmondisplay=0
    Corr_Xmondisplay=0
    t2display=0
    Make/O/I/U/N=(2*Pixels,4) calibrationwave
    Init()
    ActualY=Yi+(Pixelsize/2)
    XminusXmon=0
    j=0
    Do
        ExecuteScanCalibration()
        CalibrationDisplay()
        j+=1
    While (j<3)
    Return 1
End

Function FitFinalLinearRange()
    Wave Xdisplay, Xmondisplay, t2display
    Wave Corr_Xmondisplay, W_coef, PrevXdisplay
```

```
Variable a, b, Yup, Ydwn, i, j, difference, Pixels_aux
RemoveFromGraph /Z fit_Corr_XmondisplayF
RemoveFromGraph /Z fit_Corr_XmondisplayB
ControlInfo /W=ControlPanel KeepPrevFit
If (V_value==1)
    AppendToGraph/C=(10000,65535,10000) PrevXdisplay vs t2display
Endif
XiF=0.4*Pixels
XfF=Pixels-1
Cursor /P A Corr_Xmondisplay XiF
Cursor /P B Corr_Xmondisplay XfF
CurveFit/Q/N line Xdisplay[0,Pixels-1] //a+bx
CurveFit/Q/N/H="01" line Corr_Xmondisplay[XiF,XfF] //a+bx
a=W_coef[0]
b=W_coef[1]
Make /O/N=(Pixels*1.20) fit_Corr_XmondisplayF
fit_Corr_XmondisplayF=a+b*p
AppendToGraph fit_Corr_XmondisplayF vs t2display
XiB=1.4*Pixels
XfB=2*Pixels-1
Cursor /P A Corr_Xmondisplay XiB
Cursor /P B Corr_Xmondisplay XfB
CurveFit/Q/N line Xdisplay[Pixels,2*Pixels-1] //a+bx
CurveFit /Q/N/H="01" line Corr_Xmondisplay[XiB,XfB]
a=W_coef[0]
b=W_coef[1]
Make/O/N=(Pixels) fit_Corr_XmondisplayB
fit_Corr_XmondisplayB= a+b*(p+Pixels)
Duplicate /O/R=[Pixels, 2*Pixels-1] t2display t2displayB
AppendToGraph fit_Corr_XmondisplayB vs t2displayB
j=0
Do
    difference=Corr_Xmondisplay[j] - fit_Corr_XmondisplayF[j]
    j+=1
While (difference>Pixelsize)
XiF=j-1
If (Corr_Xmondisplay[XiF]==Corr_Xmondisplay[2*Pixels-1])
    XfB=2*Pixels-1
Elseif (Corr_Xmondisplay[XiF]>Corr_Xmondisplay[2*Pixels-1])
    j=2*Pixels-1
    Do
        difference= Corr_Xmondisplay[XiF] - Corr_Xmondisplay[j]
        j-=1
    While (difference>Pixelsize)
    XfB=j+1
Else
```

```
        XfB=2*Pixels-1
        j=XiF
        Do
            difference= Corr_Xmondisplay[2*Pixels-1] - Corr_Xmondisplay[j]
            j+=1
        While (difference>Pixelsize)
        XiF=j-1
    Endif
    j=0
    Do
        difference= fit_Corr_XmondisplayB[j] - Corr_Xmondisplay[j+Pixels]
        j+=1
    While (difference>Pixelsize)
    XiB=j-1+Pixels
    If (Corr_Xmondisplay[Pixels-1]== Corr_Xmondisplay[XiB])
        XfF=Pixels-1
    Elseif (Corr_Xmondisplay[Pixels-1]>Corr_Xmondisplay[XiB])
        j=Pixels-1
        Do
            difference= Corr_Xmondisplay[j] - Corr_Xmondisplay[XiB]
            j-=1
        While(difference>Pixelsize)
        XfF=j+1
    Else //should never happen aber...
        j=XiB
        Do
            difference=Corr_Xmondisplay[j] - Corr_Xmondisplay[Pixels-1]
            j+=1
        While(difference>Pixelsize)
        XiB=j-1
        XfF=Pixels-1
    Endif
    //Lines for future(if needed)improvement to consider the case in which Calibration fails
    //If (XfF-XiF<GoodPixels || XfB-XiB<GoodPixels)
    // return 0
    //endif
    If (XfF-XiF>GoodPixels)
        Do
            XfF-=1
        While(XfF-XiF>GoodPixels)
    Endif
    If (XfB-XiB>GoodPixels)
        Do
            XiB+=1
        While(XfB-XiB>GoodPixels)
    Endif
```

```
    XminusCorr_X_F=Sum(Xdisplay,XiF,XfF)/(XfF-XiF)-Sum(Corr_Xmondisplay,XiF,XfF)/(XfF-XiF)
    XminusCorr_X_B=Sum(Xdisplay,XiB,XfB)/(XfB-XiB)-Sum(Corr_Xmondisplay,XiB,XfB)/(XfB-XiB)
End
```

## Confocal Imaging

All the routines employed for imaging are grouped in the Confocal Imaging Procedure. The function *CheckValues* checks that the input values from the *ControlPanel* are proper; i.e. the initial position, scanning range, the scanning speed and number of pixels are whitin the possible limits.

```
#pragma rtGlobals=0

Function CheckValues()
    Variable result
    Result=1
    If (Xi_um<0 || Xi_um>80)
        DoAlert 0,"Xi must be between 0 and 80 um"
        Result=0
    Endif
    If (Yi_um<0 || Yi_um>80)
        DoAlert 0,"Yi must be between 0 and 80 um"
        Result=0
    Endif
    If ((Xi_um+Scanrange_um)>80 || (Yi_um+Scanrange_um)>80 || Scanrange_um < 0)
        DoAlert 0,"The Scan Range is not valid"
        Result=0
    Endif
    If (Pixels <= 0 || Pixels>4096)
        DoAlert 0,"The number of Pixels is not valid or makes no sense"
        Result=0
    Endif
    ControlInfo /W=ControlPanel PixeltimeUnits
    If (V_value==1)
        Pixeltime=Pixeltime_display*1000
    Else
        Pixeltime=Pixeltime_display
    Endif
    If (Pixeltime < 300)
        DoAlert 0,"The Time per Pixel is not valid"
        Result=0
    Endif
    Return result
End
```

Once controlled that the set of scanning parameters is within the possible limits, *CalculateParametersForAdwin* translate the parameters into terms of AD digits for the AD/DA card.

```
Function CalculateParametersForAdwin()
    Xi=Xi_um*32768/80+32768 //Piezo-table in closed loop moves 80um
    Yi=Yi_um*32768/80+32768 // for the 0-10V (32768 ADWin units) range
    Scanrange=Scanrange_um*32768/80 //The 80 should be calibrated
    Xf=Xi+Scanrange
    Yf=Yi+Scanrange
    Pixelsize=Scanrange/Pixels
    Xf_um=Xi_um+Scanrange_um
    Yf_um=Yi_um+Scanrange_um
End
```

*ExecuteSAC2ForScan()* executes the *Sac2 XOP*, which then calls the routines to move the piezo-stage

.

```
Function ExecuteSAC2ForScan()
    scantype=0
    Execute "Sac2, Xi, Yi, Scanrange, Pixels, Pixeltime, ActualY, scantype, k, 'transferdatawave'"
End
```

The collected data for each line is displayed by *DataForDisplay* in both the forward and backward images as well as in the on-line line display.

```
Function DataForDisplay()
    Wave CtsDisplayF, CtsDisplayB, transferdatawave, LineCtsDisplay
    CtsdisplayF[][k] = transferdatawave[p+XiF][q][2]-1
    CtsdisplayB[][k] = transferdatawave[XfB-p][q][2]-1
    LineCtsdisplay=CtsdisplayB[p][k]
    AvCounts=sum(LineCtsDisplay, 0, GoodPixels-1) / GoodPixels
    AvCPS=AvCounts*1000000/Pixeltime
    DoUpdate
End
```

The function *Scan* is the main function for image scanning and it coordinates all the previously presented functions.

```
Function Scan (Start) : ButtonControl
    String Start
    SetDataFolder root:
    Variable paramctrl, XiScale, XfScale, YiScale, YfScale
    Wave fit_LineCtsDisplay
```

```
If(saved!=1)
    DoAlert 2, "The displayed data is not saved! Do you want to save it?"
    Switch (V_flag)
    Case 1:
        dataname=SaveCompleteData(dataname)
        break
    Case 3:
        Abort
    Endswitch
Endif
saved=0
XiScale=Xi_um_display
XfScale=Xi_um_display+Scanrange_um_display
YiScale=Yi_um_display
YfScale=Yi_um_display+Scanrange_um_display
XiF=0
XiB=Pixels
ControlInfo /W=ControlPanel Calibrate
If (V_value==1)
    CheckBox KeepPrevFit, value=0,win=ControlPanel
    ScanCalib()
    FitLinearRange()
    GoodPixels=Pixels
    If(CorrectParameters()==0)
        Abort "Scan aborted. Parameters out of range after calibration"
    Endif
    DoUpdate
    ScanFinalCalib()
    FitFinalLinearRange()
    DoUpdate
Else
    PixelsToDiscard=0
    Xi_um=Xi_um_display
    Yi_um=Yi_um_display
    Scanrange_um=Scanrange_um_display
    Pixels=Pixels_display
    GoodPixels=Pixels
    If (CheckValues()==0)
        Abort "Scan aborted. Parameters out of range"
    Endif
    DoUpdate
    CalculateParametersForAdWin()
    Init()
Endif
Xi_prev=Xi_um_display
Yi_prev=Yi_um_display
```

```
    Scanrange_prev=Scanrange_um_display
    Pixels_prev=Pixels_display
    Pixeltime_prev=Pixeltime
    DoWindow/B PointKinetic
    DoWindow/B Calibration
    DoWindow/F SurfaceScanF
    DoWindow/F SurfaceScanB
    DoWindow/F LineScan
    ValDisplay Width,disable=1,win=LineScan
    Make/O/I/U/N=(GoodPixels,GoodPixels) CtsdisplayF
    Make/O/I/U/N=(GoodPixels,GoodPixels) CtsdisplayB
    ControlInfo /W=ControlPanel Cleandata
    If (V_value==1)
        CtsdisplayF=0
        CtsdisplayB=0
    Endif
    SetScale x, XiScale, XfScale ,"um" ,CtsdisplayF
    SetScale y, YiScale, YfScale ,"um" ,CtsdisplayF
    SetScale x, XiScale, XfScale ,"um" ,CtsdisplayB
    SetScale y, YiScale, YfScale ,"um" ,CtsdisplayB
    Make/O/I/U/N=(2*Pixels,GoodPixels,6) transferdatawave
    transferdatawave=0
    Make/O/I/U/N=(GoodPixels) LineCtsDisplay
    LineCtsDisplay=0
    fit_LineCtsDisplay=0
    SetScale x, XiScale, XfScale ,"um" ,LineCtsDisplay
    SetScale x, XiScale, XfScale ,"um" ,fit_LineCtsDisplay
    ControlUpdate /A /W=LineScan
    k=0
    ActualY=Yi-(Pixelsize/2)
    OpenShutter()
    Do
        ActualY=ActualY+Pixelsize
        ExecuteSAC2ForScan()
        DataForDisplay()
        k+=1
        DoUpdate
    While(k<GoodPixels)
    CloseShutter()
    Beep
End
```

### Confocal Line

The Confocal Line Procedure groups the routines for line scanning. The Igor function *ExecuteSAC2ForLine* calls the *XOP SAC2* with the required parameters.

```
#pragma rtGlobals=0

Function ExecuteSAC2ForLine()
    k=0
    Execute "Sac2, Xi, Yi, Scanrange, Pixels, Pixeltime, ActualY, scantype, k, 'transferdatawaveL'"
End
```

The collected data for each line is displayed on the on-line line display by *DataForDisplay*.

```
Function DataForLineDisplay(graphname)
    String graphname
    Wave LineCtsDisplay,transferdatawave,transferdatawaveL
    If(cmpstr(graphname,"SurfaceScanF")==0)
        LineCtsDisplay = transferdatawaveL[p+XiF][q][2]-1
    Endif
    If(cmpstr(graphname,"SurfaceScanB")==0)
        LineCtsDisplay = transferdatawaveL[XfB-p][q][2]-1
    Endif
    ControlInfo /W=ControlPanel FitGauss
    If (V_value==1)
        ValDisplay Width, disable=0,win=LineScan
        Fit()
    Else
        ValDisplay Width,disable=1,win=LineScan
    Endif
    AvCounts=sum(LineCtsDisplay,0,Pixels-1)/Pixels
    AvCPS=AvCounts*1000000/Pixeltime
    DoUpdate
End
```

With the function *Fit*, it is possible to fit on-line a Gaussian curve to the scanned line and display the FWHM.

```
Function Fit()
    Wave LineCtsDisplay,W_coef
    CurveFit /N/Q/W=0/M=0 gauss LineCtsDisplay(0,GoodPixels) /D /A=0 /F=0.990000, 4
    width=W_coef[3]
End
```

*LineScanH* scans repetitively a line horizontally on the sample until the user

aborts. The data from every scanned line is displayed on the on-line display.

```
Function LineScanH(StartLineH) : ButtonControl
    String StartLineH
    SetDataFolder root:
    String graphname, message
    Variable aux,finish,paramctrl
    Wave fit_LineCtsDisplay
    graphname=winname(0,1)
    If (cmpstr(graphname,"SurfaceScanF")!=0)
        If (cmpstr(graphname,"SurfaceScanB")!=0)
            message= "Parameters are taken from the top graph. At the moment the top graph is '"+graphname+"'. Be sure that one of the surface scan images is the top graph"
            Abort message
        Endif
    Endif
    Xi_um=xcsr(A,"")
    Yi_um=vcsr(A,"")
    Scanrange_um= xcsr(B,"")-xcsr(A,"")
    Pixels=Pixels_display
    If (CheckValues()==0)
        Abort "Scan aborted. Parameters out of range"
    Endif
    CalculateParametersForAdwin()
    DoWindow/B PointKinetic
    DoWindow/F SurfaceScanF
    DoWindow/F SurfaceScanB
    DoWindow/F LineScan
    Xi=Xi-PixelsToCorrectInX*Pixelsize //Correction using previous calibration parameters
    Scanrange=Scanrange+PixelsToDiscard*Pixelsize //Correction using prev calibration parameters
    Pixels=round(Scanrange/Pixelsize)
    Make/O/I/U/N=(2*Pixels,2*Pixels,5) transferdatawaveL
    transferdatawaveL=0
    Make/O/I/U/N=(Pixels) LineCtsDisplay
    LineCtsDisplay=0
    fit_LineCtsDisplay=0
    SetScale x, Xi_um, Xf_um ,"um" ,LineCtsDisplay
    SetScale x, Xi_um, Xf_um ,"um" ,fit_LineCtsDisplay
    DoUpdate
    ActualY=Yi
    Scantype=1
    Init()
    OpenShutter()
    Do
        ExecuteSAC2ForLine()
        DataForLineDisplay(graphname)
```

```
    While (1)
End
```

*LineScanV* scans repetitively a line vertically on the sample until the user aborts. The data from every scanned line is displayed on the on-line display.

```
Function LineScanV(StartLineV) : ButtonControl
    String StartLineV
    SetDataFolder root:
    String graphname,message
    Variable aux,finish,paramctrl
    Wave fit_LineCtsDisplay
    graphname=winname(0,1)
    If (cmpstr(graphname,"SurfaceScanF")!=0)
        If (cmpstr(graphname,"SurfaceScanB")!=0)
            message= "Parameters are taken from the top graph. At the moment the top graph is '"+graph-
name+"'. Be sure that one of the surface scan images is the top graph"
            Abort message
        Endif
    Endif
    Xi_um=xcsr(A)
    Yi_um=vcsr(A)
    Scanrange_um= vcsr(B,"")-vcsr(A,"")
    Pixels=Pixels_display
    If (CheckValues()==0)
        Abort "Scan aborted. Parameters out of range"
    Endif
    CalculateParametersForAdwin()
    DoWindow/B PointKinetic
    DoWindow/F SurfaceScanF
    DoWindow/F SurfaceScanB
    DoWindow/F LineScan
    Yi=Yi-PixelsToCorrectInX*Pixelsize //Correction using previous calibration parameters
    Scanrange=Scanrange+PixelsToDiscard*Pixelsize //Correction using prev calibration parameters
    Pixels=round(Scanrange/Pixelsize)
    Make/O/I/U/N=(2*Pixels,2*Pixels,5) transferdatawaveL
    transferdatawaveL=0
    Make/O/I/U/N=(Pixels) LineCtsDisplay
    LineCtsDisplay=0
    fit_LineCtsDisplay=0
    SetScale x, Yi_um, Yf_um ,"um" ,LineCtsDisplay
    SetScale x, Yi_um, Yf_um ,"um" ,fit_LineCtsDisplay
    DoUpdate
    ActualY=Xi
    Scantype=2
    Init()
```

```
    OpenShutter()
    Do
        ExecuteSAC2ForLine()
        DataForLineDisplay(graphname)
    While (1)
End
```

## Confocal Kinetic

This procedure groups the necessary routines to accomplish fixed position measurements. In particular, fluorescence vs. time traces. The main function is *MainKinetic*, which via the *ExecuteKinetic* and the *Kinetic XOP* drives the piezo-stage to the measurement position and collects the data. The data is displayed in intervals fixed by the global variable *Kinetic Duration*.

```
#pragma rtGlobals=0

Function ExecuteKinetic()
    Execute "Kinetic, Xi, Yi, PixeltimeforKinetic, Kineticduration, Points, 'transferkineticwave'"
End

Function MainKinetic(StartKinetic) : ButtonControl
    String StartKinetic
    Variable PxlXi,PxlYi,cambio,n,T0
    String graphname
    graphname=winname(0,1)
    If (cmpstr(graphname[0,(strlen(graphname)-2)],"SurfaceScan")!=0)
        Abort "The position input is given by the position of round cursor in the top SurfaceScan image.At the
moment, no scan image is the top graph. The process will be aborted."
    Endif
    cambio=0
    If(Xi_um!=hcsr(A))
        Xi_um=hcsr(A)
        cambio=1
    Endif
    If (Yi_um!=vcsr(A))
        Yi_um=vcsr(A)
        cambio=1
    Endif
    Xi=Xi_um*32768/80+32768
    Yi=Yi_um*32768/80+32768
    DoUpdate
    PixeltimeForKinetic=PixeltimeForKinetic_display*1000
    If (cambio==1)
```

```
        Init()
    Endif
    Kineticduration=Kineticduration_display
    Points=Kineticduration*1000000/PixeltimeForKinetic
    If (Points>50000)
        Abort "Too many data points per cycle. The ADWin card - Igor comunication process might fail. Please
set a shorter repetition time or a longer pixel time"
    Endif
    Make/O/U/N=(Points,3) transferkineticwave
    transferkineticwave=Nan
    Make/O/U/N=0 KineticCtsDisplay
    Make/O/U/N=0 KineticTimeDisplay
    DoWindow/F SurfaceScanF
    DoWindow/F SurfaceScanB
    DoWindow/F PointKinetic
    SetAxis /W=PointKinetic /A
    If (V_flag!=1)
        Execute "PointKinetic()"
    Endif
    n=0
    OpenShutter()
    Do
        ExecuteKinetic()
        InsertPoints (n*Points),(Points), KineticCtsDisplay
        InsertPoints (n*Points),(Points), KineticTimeDisplay
        KineticCtsDisplay[n*Points,(n+1)*Points-1]=transferkineticwave[p-n*Points][2]-1
        If (n==0)
            T0=transferkineticwave[0][1]
        Endif
        KineticTimeDisplay[n*Points,(n+1)*Points-1] = (transferkineticwave[p-n*Points][1]-T0)*25/1e9
        DoUpdate
        n+=1
    While(1)
End
```

## A.3 C++ routines

In this section all C++ programmed *XOP* routines are presented. *The ADWin-Boot2 XOP* boots the local CPU of the AD/DA PC-card and loads in it all the ADBasic routines for the operation of the microscope.

## ADWinBoot2.c

```
#include "XOPStandardHeaders.h"
/*Include ANSI headers, Mac headers, IgorXOP.h, XOP.h and XOPSupport.h*/
#include "ADWinBoot2.h"
#include "C:\ADwin\Developer\C\Microsoft_VisualC\Adwin.c"
#include "C:\ADwin\Developer\C\Microsoft_VisualC\Adwin.h"
/*All structures are 2-byte-aligned.*/
#if GENERATINGPOWERPC
#pragma options align=mac68k
#endif
#ifdef _WINDOWS_
    #pragma pack(2)
#endif
static void
XOPEntry(void)
{    long Xi,Yi,firstrun;
    switch (GetXOPMessage())
    {    case CMD: /*CMD is the only message we care about*/
            Boot("D:\\Doktorarbeit\\Control\\ADBasic\\adwin9.btl",800000); /*Boot ADwin */
            ADBPrLoad("D:\\Doktorarbeit\\Control\\CompleteRoutines\\Scan-Acquisition-Control\\ADBasic
\\LP-HP-LineScan.T91");
            ADBPrLoad("D:\\Doktorarbeit\\Control\\CompleteRoutines\\Scan-Acquisition-Control\\ADBasic
\\HP-Pixel-Forth.T92");
            ADBPrLoad("D:\\Doktorarbeit\\Control\\CompleteRoutines\\Scan-Acquisition-Control\\ADBasic
\\HP-Pixel-Back.T93");
            ADBPrLoad("D:\\Doktorarbeit\\Control\\CompleteRoutines\\Scan-Acquisition-Control\\ADBasic
\\ScanInit.T94");
            ADBPrLoad("D:\\Doktorarbeit\\Control\\CompleteRoutines\\Scan-Acquisition-Control\\ADBasic
\\LP-HP-PointKinetic.T95");
            ADBPrLoad("D:\\Doktorarbeit\\Control\\CompleteRoutines\\Scan-Acquisition-Control\\ADBasic
\\HP-KineticPixel.T96");
            ADBPrLoad("D:\\Doktorarbeit\\Control\\CompleteRoutines\\Scan-Acquisition-Control\\ADBasic
\\LP-HP-LineScan_Calibration.T97");
        break; } }
/* main(ioRecHandle) This is the initial entry point at which the host application calls XOP. The message sent by
the host must be INIT.main() does any necessary initialization and then sets the XOPEntry field of the ioRecHandle
to the address to be called for future messages.*/
    HOST_IMPORT void
    main(IORecHandle ioRecHandle)
    {    #ifdef XOP_GLOBALS_ARE_A4_BASED
            #ifdef __MWERKS__ /* For CodeWarrior 68K XOPs.*/
                SetCurrentA4(); /* Set up correct A4. This allows globals to work.*/
                SendXOPA4ToIgor(ioRecHandle, GetA4()); /*And communicate it to Igor.*/
            #endif
        #endif
```

```
    XOPInit(ioRecHandle); /* do standard XOP initialization */
    SetXOPEntry(XOPEntry); /* set entry point for future calls */
    SetXOPResult(0L); }
/*All structures are 2-byte-aligned.*/
    #if GENERATINGPOWERPC
        #pragma options align=reset
    #endif
    #ifdef _WINDOWS_
        #pragma pack()
    #endif
```

*ADWinInit* sends the piezoelectric stage to a given position via the *ScanInit.BAS* (A.1).

## ADWinInit2.c

```
     #include "XOPStandardHeaders.h"
/*Include ANSI headers, Mac headers, IgorXOP.h, XOP.h and XOPSupport.h*/
    #include "ADWinInit2.h"
    #include "C:\ADwin\Developer\C\Microsoft_VisualC\Adwin.c"
    #include "C:\ADwin\Developer\C\Microsoft_VisualC\Adwin.h"
/*All structures are 2-byte-aligned.*/
    #if GENERATINGPOWERPC
        #pragma options align=mac68k
    #endif
    #ifdef _WINDOWS_
        #pragma pack(2)
    #endif
    static void
    XOPEntry(void)
    {     long Xi,Yi;
        char* varname;
        switch (GetXOPMessage()) {
        case CMD:
            GetLong(&Xi); /*Initial X*/
            GetLong(&Yi); /*Initial Y*/
            SetPar(1,Xi);
            SetPar(2,Yi);
            ADBStart(4);
        break; } } /*CMD is the only message I care about.*/
/* main(ioRecHandle) This is the initial entry point at which the host application calls XOP. The message sent by
the host must be INIT.main() does any necessary initialization and then sets the XOPEntry field of the ioRecHandle
to the address to be called for future messages.*/
    HOST_IMPORT void
    main(IORecHandle ioRecHandle)
```

```
    {       #ifdef XOP_GLOBALS_ARE_A4_BASED
                #ifdef __MWERKS__ /* For CodeWarrior 68K XOPs.*/
                    SetCurrentA4(); /*Set up correct A4. This allows globals to work.*/
                    SendXOPA4ToIgor(ioRecHandle, GetA4()); /* And communicate it to Igor.*/
                #endif
            #endif
            XOPInit(ioRecHandle); /* do standard XOP initialization */
            SetXOPEntry(XOPEntry); /* set entry point for future calls */
            SetXOPResult(0L); } }
/*All structures are 2-byte-aligned.*/
    #if GENERATINGPOWERPC
        #pragma options align=reset
    #endif
    #ifdef _WINDOWS_
        #pragma pack()
    #endif
```

All types of scanning are controlled by the XOP Sac2.c. The parameter scantype defines which kind of scan will be performed; scantype=0 for image scan, scantype=1 for horizontal line scan and scantype=2 for a vertical line scan.

### Sac2.c

```
    #include "XOPStandardHeaders.h" /*Include ANSI headers, Mac headers, IgorXOP.h, XOP.h and XOPSup-
port.h*/
    #include "Sac2.h"
    #include "C:\ADwin\Developer\C\Microsoft_VisualC\Adwin.c"
    #include "C:\ADwin\Developer\C\Microsoft_VisualC\Adwin.h"
/*All structures are 2-byte-aligned.*/
    #if GENERATINGPOWERPC
        #pragma options align=mac68k
    #endif
    #ifdef _WINDOWS_
        #pragma pack(2)
    #endif

    static void
    DataTransfer(waveHndl transferdatawaveF,waveHndl transferdatawaveB, long Pixels, long k)
    {     int i;
        long dataXf[10000];
        long dataYf[10000];
        long dataCtsf[10000];
        long datat1f[10000];
        long datat2f[10000];
        long dataXb[10000];
        long dataYb[10000];
        long dataCtsb[10000];
        long datat1b[10000];
        long datat2b[10000];
        long indices[3]; /*dimensions of the wave*/
        double value[1]; /*dimensions of the value*/
        GetlData(1,dataXf,1,Pixels); /*transfers points 1 to Pixels of ADW:data_1 to dataXf*/
        GetlData(2,dataYf,1,Pixels);
        GetlData(3,dataCtsf,1,Pixels);
        GetlData(4,datat1f,1,Pixels);
        GetlData(5,datat2f,1,Pixels);
        i=0;
```

```
while(i<Pixels)
{       indices[0]=i; /*row number*/
        indices[1]=k; /*column number*/
        indices[2]=0; /*layer number*/
        value[0]=dataXf[i];
        MDSetNumericWavePointValue(transferdatawaveF,indices,value);
        i++; }
i=0;
while(i<Pixels)
{       indices[0]=i; /*row number*/
        indices[1]=k; /*column number*/
        indices[2]=1;
        value[0]=dataYf[i];
        MDSetNumericWavePointValue(transferdatawaveF,indices,value);
        i++; }
i=0;
while(i<Pixels)
{       indices[0]=i; /*row number*/
        indices[1]=k; /*column number*/
        indices[2]=2;
        value[0]=dataCtsf[i];
        MDSetNumericWavePointValue(transferdatawaveF,indices,value);
        i++; }
i=0;
while(i<Pixels)
{       indices[0]=i; /*row number*/
        indices[1]=k; /*column number*/
        indices[2]=3;
        value[0]=datat1f[i];
        MDSetNumericWavePointValue(transferdatawaveF,indices,value);
        i++; }
i=0;
while(i<Pixels)
{       indices[0]=i; /*row number*/
        indices[1]=k; /*column number*/
        indices[2]=4;
        value[0]=datat2f[i];
        MDSetNumericWavePointValue(transferdatawaveF,indices,value);
        i++; }
GetlData(11,dataXb,1,Pixels); /*transfers points 1 to Pixels of ADW:data_1 to dataXb*/
GetlData(12,dataYb,1,Pixels);
GetlData(13,dataCtsb,1,Pixels);
GetlData(14,datat1b,1,Pixels);
GetlData(15,datat2b,1,Pixels);
i=0;
while(i<Pixels)
{       indices[0]=i; /*row number*/
        indices[1]=k; /*column number*/
        indices[2]=0; /*layer number*/
        value[0]=dataXb[i];
        MDSetNumericWavePointValue(transferdatawaveB,indices,value);
        i++; }
i=0;
while(i<Pixels)
{       indices[0]=i; /*row number*/
        indices[1]=k; /*column number*/
        indices[2]=1;
        value[0]=dataYb[i];
        MDSetNumericWavePointValue(transferdatawaveB,indices,value);
        i++; }
i=0;
while(i<Pixels)
{       indices[0]=i; /*row number*/
        indices[1]=k; /*column number*/
        indices[2]=2;
        value[0]=dataCtsb[i];
        MDSetNumericWavePointValue(transferdatawaveB,indices,value);
i++; }
i=0;
while(i<Pixels)
```

```
        {       indices[0]=i; /*row number*/
                indices[1]=k; /*column number*/
                indices[2]=3;
                value[0]=datat1b[i];
                MDSetNumericWavePointValue(transferdatawaveB,indices,value);
                i++; }
        i=0;
        while(i<Pixels)
        {       indices[0]=i; /*row number*/
                indices[1]=k; /*column number*/
                indices[2]=4;
                value[0]=datat2b[i];
                MDSetNumericWavePointValue(transferdatawaveB,indices,value);
                i++; } }

    DataTransferLine(waveHndl transferdatawaveL, long Pixels)
    {       int i;
        long DataCts[10000];
        long indices[3]; /*dimensions of the wave*/
        double value[1]; /*dimensions of the value*/
        GetlData(3,DataCts,1,Pixels);
        i=0;
        while(i<Pixels)
        {       indices[0]=i; /*row number*/
                indices[1]=0; /*column number*/
                indices[2]=2;
                value[0]=DataCts[i];
                MDSetNumericWavePointValue(transferdatawaveL,indices,value);
                i++; } }


    static void
    Scan(long Xi, long Yi, long Scanrange, long Pixels, long Pixeltime, long Y, long scantype, long k, waveHndl
transferdatawaveF, waveHndl transferdatawaveB)
    {       int check;
        SetPar(1,Xi); /*Xi->PAR_1*/
        SetPar(2,Yi); /*Yi->PAR_2*/
        SetPar(3,Scanrange); /*Scanrange->PAR_3*/
        SetPar(4,Pixels); /*Yf->PAR_4*/
        SetPar(5,Pixeltime); /*Scanrate->PAR_5*/
        SetPar(8,Y); /*Y->PAR_8*/
        check=1;
        switch (scantype)
        {       case 0:
                        ADBStart(1);
                        check=GetPar(11);
                        while (check==0)
                        {       check=GetPar(11); }
                                DataTransfer(transferdatawaveF, transferdatawaveB, Pixels, k);
                        break; }
                case 1:
                        ADBStart(1);
                        check=GetPar(11);
                        while (check==0)
                        {       check=GetPar(11); }
                        DataTransferLine(transferdatawaveF,Pixels);
                        break; } }


    static void

    XOPEntry(void)

    {       long Xi, Yi, Scanrange, Pixels, Pixeltime, Y, scantype, k;

        waveHndl transferdatawaveF, transferdatawaveB;

        switch (GetXOPMessage())

        {       case CMD:

                        GetLong(&Xi); /*Initial X*/
```

```
                GetLong(&Yi); /*Initial Y*/
                GetLong(&Scanrange);
                GetLong(&Pixels);
                GetLong(&Pixeltime);
                GetLong(&Y);
                GetLong(&scantype);
                GetLong(&k);
                transferdatawaveF=GetWave();
                transferdatawaveB=GetWave();
                Scan(Xi, Yi, Scanrange, Pixels, Pixeltime, Y, scantype, k, transferdatawaveF, transferdatawaveB);
            break; } } /*CMD is the only message I care about*/
/*main(ioRecHandle) This is the initial entry point at which the host application calls XOP. The message sent by
the host must be INIT. main() does any necessary initialization and then sets the XOPEntry field of the ioRecHandle
to the address to be called for future messages.*/
    HOST_IMPORT void
    main(IORecHandle ioRecHandle)
    {     #ifdef XOP_GLOBALS_ARE_A4_BASED
            #ifdef __MWERKS__
                /*For CodeWarrior 68K XOPs.*/
                SetCurrentA4(); /*Set up correct A4. This allows globals to work.*/
                SendXOPA4ToIgor(ioRecHandle, GetA4()); /*And communicate it to Igor.*/
            #endif
        #endif
        XOPInit(ioRecHandle); /*do standard XOP initialization*/
        SetXOPEntry(XOPEntry); /*set entry point for future calls*/
        SetXOPResult(0L); }
/*All structures are 2-byte-aligned.*/
    #if GENERATINGPOWERPC
        #pragma options align=reset
    #endif
    #ifdef _WINDOWS_
        #pragma pack()
    #endif
```

# List of Tables


2.1 Light sources . . . . . 10
2.2 Single photon counting detectors . . . . . 18
2.3 Spectrograph components . . . . . 19

4.1 Properties of the sample layers . . . . . 70
4.2 Influence of the gold film on the decay rates . . . . . 75

5.1 Trace-histogram and autocorrelation analysis of TCSPC-data . . . . . 96
5.2 Comparison of the trace-histogram and autocorrelation methods. . . . 97
5.3 Total EM decay rate in the samples with and without gold . . . . . 102
5.4 Detectable decay rate in the samples with and without gold . . . . . 105

# List of Figures


2.1 Confocal principle . . . . . 6
2.2 Confocal image formation . . . . . 7
2.3 Schematic of the home-built confocal microscope . . . . . 9
2.4 Focusing angles in the microscope objective . . . . . 11
2.5 Scanning process . . . . . 12
2.6 Scanning delay . . . . . 13
2.7 Scanning correction . . . . . 15
2.8 Light scattering set-up . . . . . 17
2.9 Time correlated single photon counting principle . . . . . 20
2.10 Collimation and alignment of the illumination beam . . . . . 24
2.11 Alignment of the dichroic mirror and microscope objective . . . . . 26
2.12 Huygenian ocular . . . . . 27
2.13 Alignment of the spectrograph . . . . . 28
2.14 Control panel of the PC user interface . . . . . 29
2.15 Sample holder . . . . . 30
2.16 Calibration screen . . . . . 31
2.17 Scanning screen . . . . . 32
2.18 Line scan screen . . . . . 33
2.19 Fluorescence lifetime imaging . . . . . 35
2.20 Kinetic trace screen . . . . . 37

3.1 Coordinate system . . . . . 41
3.2 Parameters for the TMA coordinate system . . . . . 43
3.3 Calculation of the electric field near a geometric focus . . . . . 49
3.4 Symmetry considerations in the focal plane . . . . . 52
3.5 Electric fields along an arbitrary direction . . . . . 53

4.1 Experimental configuration . . . . . 58
4.2 Reflectivity of the sample system . . . . . 62
4.3 Full beam illumination images . . . . . 63
4.4 Dye-molecules on glass and under annular illumination . . . . . 64
4.5 Different modes of illumination . . . . . 65
4.6 Influence of the separation distance to the gold film . . . . . 66

4.7 Quenching behavior . . . 67
4.8 Schematic of the excitation and de-excitation rates . . . 69
4.9 Electromagnetic decay rates . . . 72
4.10 Detectable fraction of the fluorescence vs. spacer thickness . . . 73
4.11 Detectable fraction of the fluorescence vs. dipole orientation . . . 74
4.12 Electric field distribution in the samples . . . 76
4.13 Electric field distribution in a sample without the gold film . . . 77
4.14 Modelled FB illumination fluorescence signals . . . 78
4.15 Modelled FL illumination fluorescence signals . . . 79
4.16 Modelled TL illumination fluorescence signals . . . 80
4.17 Modelled and experimental fluorescence signals . . . 82
4.18 Profiles of the experimental and modelled fluorescence signals . . . 83

5.1 Three-level description of molecular fluorescence . . . 86
5.2 TCSPC photon detection times . . . 88
5.3 Autocorrelation . . . 89
5.4 Effect of the bin-width on the kinetic trace histogram . . . 91
5.5 Inter-photon times histogram . . . 92
5.6 Kinetic trace histogram . . . 94
5.7 Histograms of the length of the on- and off-periods . . . 95
5.8 Monte-Carlo simulated photon detection times . . . 96
5.9 Analysis of the simulated data . . . 98
5.10 $k_{on}$ and $k_{off}$ by histogram and autocorrelation methods . . . 99
5.11 Experimental configuration . . . 100
5.12 Distributions of $\Gamma_{21}$, $k_{on}$ and $k_{off}$ . . . 101
5.13 Distribution of $k_{off}/(I_{on} - I_{off})$ . . . 104
5.14 $k_{on}$ as a function of $\Gamma_{21}$ . . . 105

6.1 Absorption and emission of $Zn_{0.42}Cd_{0.58}Se$ QDs . . . 112
6.2 Image of the sample with individual QDs . . . 113
6.3 QDs kinetic traces . . . 114
6.4 Histograms of the length of the on- and off-periods on glass . . . 116
6.5 Histogram of the on- and off-times of a single kinetic trace . . . 117
6.6 Histograms of the length of the on- and off-periods on ITO . . . 118
6.7 On- and off-intensities . . . 119
6.8 Power-law exponent . . . 119
6.9 Cycles per second . . . 120
6.10 On-time fraction . . . 121
6.11 Correlations of adjacent on- and off-times . . . 122
6.12 Correlation coefficient vs. the excitation intensity . . . 123
6.13 Simulated and detected on- and off-periods . . . 127
6.14 Simulated QD kinetic trace . . . 128
6.15 Histograms of simulated on- and off-times for QDs on glass . . . 128

6.16 Histograms of simulated on- and off-times for QDs on ITO . . . . . 129
6.17 Correlations between simulated adjacent on- and off-times . . . . . 130
6.18 Photo-induced lifetime of the on-state vs. excitation intensity . . . . 131

7.1 Size distribution and SEM of the gold particles . . . . . 137
7.2 Light scattering of individual Au-nanoparticles . . . . . 138
7.3 Light scattering imaging . . . . . 139
7.4 Light scattering spectra of individual gold particles . . . . . 140
7.5 Light scattering of C-shaped gold nanoparticles . . . . . 142

# Abbreviations

| | |
|---|---|
| AD/DA | analog-digital / digital-analog |
| APD | avalanche photo-diode |
| $\alpha,\ \beta,\ \phi,\ \varphi,\ \theta,\ \psi$ | angles |
| CCD | charge-coupled device |
| $\mathbf{E}$ | electric field |
| $\epsilon$ | dielectric constant |
| FB | full-beam |
| FL | forbidden light |
| FWHM | full width at half maximum |
| $\Gamma$ | transition rate |
| $I$ | intensity |
| $k$ | transition rate |
| $\mathbf{k}$ | wavevector |
| $\lambda$ | wavelength |
| $\mu$ | transition dipole |
| NA | numerical apperture |
| $\eta$ | refractive index |

| | |
|---|---|
| PMT | photomultiplier tube |
| QD | quantum dot |
| $QE$ | fluorescence quantum efficiency |
| $\mathbf{r}$ | position |
| $R$ | radius, linear correlation coefficient |
| $R_rl$ | radius of the objective rear lens |
| $\rho$ | radius in polar coordinates |
| $SBR$ | signal to background ratio |
| SCOM | scanning confocal optical microscope |
| SERS | surface enhanced Raman scattering |
| SM | single molecule |
| SPR | surface plasmon resonance |
| TCSPC | time correlated single photon counting |
| TEM00 | transverse electromagnetic mode 00 |
| $t$ | time |
| TMA | transfer matrix algorithm |
| TL | transmitted light |
| TTL | transistor-transistor logic |
| VPH | volume phase holographic |
| $\tau$ | characteristic time |
| $x,\ y,\ z$ | Cartesian coordinates |
| $\parallel$ and $\perp$ | parallel and perpendicular |
| $\langle\rangle$ | average |

# Bibliography


[1] M. Fleischmann, P. J. Hendra, and A. J. McQuillan, "Raman spectra of pyridine adsorbed at a silver electrode," *Chem. Phys. Lett.*, vol. 26, pp. 163–166, 1974.

[2] D. L. Jeanmaire and R. van Duyne, "Surface raman spectroelectrochemistry. Part I. heterocyclic, aromatic, and aliphatic amines adsorbed on the anodized silver electrode.," *J. Electroanal. Chem.*, vol. 84, pp. 1–20, 1977.

[3] M. Albrecht and J. Creighton, "Anomalously intense raman spectra of pyridine at a silver electrode," *J. Am. Chem. Soc.*, vol. 99, pp. 5215–5217, 1977.

[4] M. R. Philpott, "Effect of surface plasmons on transitions in molecules," *J. Chem. Phys.*, vol. 62, pp. 1812–1817, 1975.

[5] S. Nie and S. R. Emory, "Probing single molecules and single nanoparticles by surface-enhanced raman scattering," *Science*, vol. 275, pp. 1102–1106, 1997.

[6] K. T. Shimizu, W. K. Woo, B. R. Fisher, H. J. Eisler, and M. G. Bawendi, "Surface-enhanced emission from single semiconductor nanocrystals," *Phys. Rev. Lett.*, vol. 89, p. 117401, 2002.

[7] M. Minsky, "U.s. patent 3013467, microscopy apparatus," vol. 1961, pp. Filed Nov. 7, 1957, Dec. 19.

[8] M. Minski, "Memoir on inventing the confocal scanning microscope," *Scanning*, vol. 10, pp. 128–138, 1988.

[9] C. J. R. Sheppard and T. Wilson, "Image formation in confocal scanning microscopes," *Optik*, vol. 55, no. 4, pp. 331–342, 1980.

[10] W. Lukosz, "Optical systems with resolving powers exceeding classical limit," *J. Opt. Soc. Am.*, vol. 56, no. 11, p. 1463, 1966.

[11] W. Lukosz, "Optical systems with resolving powers exceeding classical limit .2.," *J. Opt. Soc. Am.*, vol. 57, no. 7, p. 932, 1967.

[12] J. C. Knight and P. S. J. Russell, "Photonic crystal fibers: New ways to guide light," *Science*, vol. 282, pp. 1476–1478, 1998.

[13] P. Russell, "Photonic crystal fibers," *Science*, vol. 199, pp. 358–392, 2003.

[14] M. Born and E. Wolf, *Principles of optics*. Oxford, England: Pergamon Press, 6th ed., 1980.

[15] T. Wilson, "Techniques of optical scanning microscopy," *J. Phys. E: Sci. Instrum.*, vol. 22, pp. 532–517, 1989.

[16] T. Wilson, *Theory and practice of scanning optical microscopy*. London: Academic Press, 1st ed., 1984.

[17] D. V. O'Connor and D. Phillips, *Time-Correlated Single Photon Counting*. London: Academic Press, 1984.

[18] L. M. Bollinger and G. E. Thomas, "Measurement of the time dependence of scintilation intensity by delayed-coincidence method," *The Review of Scientific Instruments*, vol. 32, no. 9, pp. 1044–1150, 1961.

[19] Becker und Hickl GmbH, "SPCM-630 User manual." http://www.becker-hickl.de (Last accessed in Jan 2004).

[20] Jäger GmbH, "ADwin AD/DA converters." http://www.adwin.de (Last accessed in Jan 2004).

[21] Wavemetrics inc., "IGOR v. 4.02." http://www.wavemetrics.com (Last accessed in Jan 2004).

[22] PCO imaging GmbH. http://www.pco.de (Last accessed in Jan 2004).

[23] Melles Griot inc., "Shear plate collimation tester theory." http://beammeasurement.mellesgriot.com/tut_ shear_ plate_ test.asp (Last accessed in Jan 2004).

[24] P. I. GmbH, *Tittle!!*

[25] Wavemetrics inc., *Igor Pro v4. Programming and reference manual*, 2000.

[26] A. Sommerfeld, "Über die ausbreitung der wellen in der drahtlosen telegraphie," *Annalen der Physik*, vol. 28, no. 4, pp. 665–736, 1909.

[27] R. R. Chance, A. Prock, and R. Silbey, "Molecular fluorescence and energy transfer near interfaces," *Adv. Chem. Phys.*, vol. 37, pp. 1–65, 1978.

[28] H. Weyl, "Ausbreitung elektromagnetischer wellen über einem ebenem leiter," *Annalen der Physik*, vol. 60, no. 22, pp. 481–500, 1919.

[29] G. W. Ford and W. H. Weber, "Electromagnetic interactions of molecules with metal surfaces," *Phys. Rep.*, vol. 113, no. 4, pp. 195–287, 1984.

[30] W. Lukosz, "Theory of optical-environment-dependent spontaneous-emission rates for emitters in thin layers," *Phys. Rev. B*, vol. 22, no. 6, pp. 3030–3038, 1980.

[31] R. E. Collins, *Field Theory of Guided Waves*. John Wiley and Sons, 1990.

[32] R. J. Potton, "Reciprocity in optics," *Rep. Prog. Phys.*, vol. 67, pp. 717–754, 2004.

[33] P. Yeh, *Optical waves in layered media*. John Wiley and Sons, 1st ed., 1988.

[34] L. Novotny, *Light Propagation and light confinement in near field optics*. PhD thesis, Swiss Federal Institute of Technology, Zurich, 1996.

[35] L. Novotny, "Allowed and forbidden light in near-field optics. i. a single dipolar light source," *J. Opt. Soc. Am. A*, vol. 14, pp. 91–104, 1997.

[36] E. Wolf, "Electromagnetic diffraction in optical systems. i. an integral representation of the image filed.," *Proc. Roy. Soc. London A*, vol. 253, no. 1274, pp. 349–357, 1959.

[37] B. Richards and E. Wolf, "Electromagnetic diffraction in optical systems ii. structure of the image filed in an aplanatic system.," *Proc. Roy. Soc. London A*, vol. 253, no. 1274, pp. 358–379, 1959.

[38] E. Engel, N. Huse, T. A. Klar, and S. W. Hell, "Creating $\lambda/3$ focal holes with a mach zehnder interferometer," *App. Phys. B*, vol. 77, pp. 11–17, 2003.

[39] B. Sick, B. Hecht, and L. Novotny, "Orientational imaging of single molecules by annular illumination," *Phys. Rev. Lett.*, vol. 85, no. 21, pp. 4482–4485, 2000.

[40] M. Kreiter, M. Prummer, B. Hecht, and U. Wild, "Orientation dependence of fluorescence lifetimes near an interface," *J. Chem. Phys.*, vol. 117, p. 9430, 2002.

[41] K. H. Drexhage, M. Fleck, H. Kuhn, F. P., and W. Sperling, "Beeinflussung der fluoreszenz eines europiumchelates durch einen spiegel," *Ber. Bunsenges. Phys. Chem.*, vol. 70, no. 9-10, p. 1179, 1966.

[42] K. Drexhage, H. Kuhn, and F. Schäfer, "Variation of fluorescence decay time of a molecule in front of a mirror," *Ber. Bunsenges. Phys. Chem.*, vol. 72, no. 2, p. 329, 1968.

[43] K. Drexhage, "Monomolecular layers and light," *Sci. Am.*, vol. 222, no. 3, p. 108, 1970.

[44] H. Kuhn, "Classical aspects of energy transfer in molecular systmes," *J. Chem. Phys.*, vol. 53, no. 1, pp. 101–108, 1970.

[45] W. L. Barnes, "Fluorescence near interfaces: the role of photonic mode density," *Journal of Modern Optics*, vol. 45, no. 4, pp. 661–699, 1998.

[46] K. Vasilev, W. Knoll, and M. Kreiter, "Fluorescence intensities of chromophores in front of a thin metal film," *J. Chem. Phys.*, vol. 120, no. 7, pp. 3439–3445, 2004.

[47] K. Vasilev, F. D. Stefani, V. Jacobsen, W. Knoll, and M. Kreiter, "Reduced photobleaching of chromophores close to a metal surface," *J. Chem. Phys.*, 2004.

[48] X. S. Xie and R. C. Dunn, "Probing single molecule dynamics," *Science*, vol. 265, no. 5170, pp. 361–364, 1994.

[49] X. S. Xie and J. K. Trautman, "Optical studies of single molecules at room temperature," *Annu. Rev. Phys. Chem.*, vol. 49, pp. 441–480, 1998.

[50] H. Yokota, K. Saito, and T. Yanagida, "Single molecule imaging of fluorescently labeled proteins on metal by surface plasmons in aqueous solution," *Phys. Rev. Lett.*, vol. 80, no. 20, pp. 4606–4609, 1998.

[51] J. Enderlein, "Single-molecule fluorescence near a metal layer," *Chemical Physics*, vol. 247, pp. 1–9, 1999.

[52] G. Binning, H. Rohrer, C. Gerber, and E. Weibel, "Surface studies by scanning tunnelling microscopy," *Phys. Rev. Lett.*, vol. 49, no. 1, pp. 57–60, 1982.

[53] G. Binning, C. F. Quate, and C. Gerber, "Atomic force microscope," *Phys. Rev. Lett.*, vol. 56, no. 9, pp. 930–933, 1986.

[54] D. M. Kolb, "An atomistic view of electrochemistry," *Surf. Sci.*, vol. 500, pp. 772–740, 2002.

[55] G. Decher, "Fuzzy nanoassemblies: Toward layered polymeric multicomposites," *Science*, vol. 277, no. 5330, pp. 1232–1237, 1997.

[56] A. Tronin, Y. Lvov, and C. Nicolini, "Ellipsometry and x-ray reflectometry characterization of self-assembly process of polystyrenesulfonate and polyallylamine," *Colloid Polym. Sci.*, vol. 272, pp. 1317–1321, 1994.

[57] K. Vasilev, *Fluorophores near metal interfaces.* PhD thesis, Martin-Luther-Universität Halle-Wittenberg, Halle, Germany, 2004.

[58] W. Knoll, "Interfaces and thin films as seen by bound electromagnetic waves," *Ann. Rev. Phys. Chem.*, vol. 49, pp. 569–638, 1998.

[59] L. Novotny, M. R. Beversluis, K. S. Youngworth, and T. G. Brown, "Longitudinal field modes probed by single molecules," *Phys. Rev. Lett.*, vol. 86, no. 23, pp. 5251–5254, 2001.

[60] I. Pockrand, A. Brillante, and D. Möbius, "Nonradiative decay of excited molecules near a metal surface," *Chem. Phys. Lett.*, vol. 69, no. 3, pp. 499–504, 1980.

[61] H. Knobloch, H. Brunner, A. Leitner, F. Aussenegg, and W. Knoll, "Probing the evanescent field of propagating plasmon surface polaritons by fluorescence and raman spectroscopies," *J. Chem. Phys.*, vol. 98, no. 12, pp. 10093–10095, 1993.

[62] J. R. Lakowicz, "Radiative decay engineering: Biophysical and biomedical applications," *Analytical Biochemistry*, vol. 298, pp. 1–24, 2001.

[63] B. N. J. Persson and N. D. Lang, "Electron-hole-pair of excited states near a metal," *Phys. Rev. B*, vol. 26, no. 10, pp. 5409–5415, 1982.

[64] B. N. J. Persson and E. Zaremba, "Electron-hole pair production at metal surfaces," *Phys. Rev. B*, vol. 31, no. 4, pp. 1863–1872, 1985.

[65] P. W. Atkins, *Physical Chemistry*. W.H. Freeman & Company, 6th ed., 1997.

[66] K. D. Weston, P. J. Carson, J. A. DeAro, and S. K. Buratto, "Single-molecule detection fluorescence of surface-bound species in vacuum," *Chemical Physics Letters*, vol. 308, pp. 58–64, 1999.

[67] J. Widengren, Ü. Mets, and R. Rigler, "Fluorescence correlation spectroscopy of triplet states in solution: A theoretical and experimental study," *J. Phys. Chem.*, vol. 99, pp. 13368–13379, 1995.

[68] J. Bernard, H. Talon, and M. Orrit, "Photon bunching in the fluorescence from single molecules: A probe for intersystem crossing," *J. Chem. Phys.*, vol. 98, no. 2, pp. 850–859, 1993.

[69] A. Zumbusch, L. Fleury, R. Brown, J. Bernard, and M. Orrit, "Probing individual two-level systems in a polymer by correlation of single molecule fluorescence," *Phys. Rev. Lett.*, vol. 70, no. 23, pp. 3584–3587, 1993.

[70] R. M. Dickson, A. B. Cubitt, R. Y. Tsien, and W. E. Moerner, "On/off blinking and switching behavior of single molecules fo green fluorescent protein," *Nature*, vol. 388, pp. 355–358, 1997.

[71] K. D. Weston, P. J. Carson, H. Metiu, and S. K. Buratto, "Room-temperature characteristics of single dye molecules adsorbed on a glass surface," *J. Chem. Phys.*, vol. 109, no. 17, pp. 7474–7485, 1998.

[72] M. Orrit, J. Bernard, R. Brown, and B. Lounis, *Progress in Optics*, vol. XXV, ch. Optical spectrocopy of single molecules in solids, pp. 61–144. Amsterdam, The Netherlands: Elsevier, 1996.

[73] S. Y. Kilin, T. M. Maevskaya, A. P. Nizovtsev, V. N. Shatokhin, P. R. Berman, C. von Borczyskowski, J. Wrachtrup, and L. Fleury, "Stochastic dynamics of a single impurity molecule from the viewpoint of continuous measurement theory," *Phys. Rev. A*, vol. 57, pp. 1400–1411, 1998.

[74] A. N. Kapanidisa and S. Weiss, "Fluorescent probes and bioconjugation chemistries for single-molecule fluorescence analysis of biomolecules," *J. Chem. Phys.*, vol. 117, pp. 10953–10964, 2002.

[75] S. Weiss, "Measuring conformational dynamics of biomolecules by single molecule fluorescence spectroscopy," *Nat. Struct. Biol.*, vol. 7, pp. 724–729, 2000.

[76] B. Lounis and W. E. Moerner, "Single photons on demand from a single molecule at room temperature," *Nature*, vol. 407, pp. 491–493, 2000.

[77] V. L. Colvin, M. C. Schlamp, and A. P. Alivisatos, "Light-emitting diodes made from cadmium selenide nanocrystals and a semiconducting polymer," *Nature*, vol. 370, pp. 354–357, 1994.

[78] N. Tessler, V. Medvedev, M. Kazes, S. Kan, and U. Banin2, "Efficient near-infrared polymer nanocrystal light-emitting diodes," *Science*, vol. 295, pp. 1506–1508, 2002.

[79] V. I. Klimov, A. A. Mikhailovsky, S. Xu, A. Malko, J. A. Hollingsworth, C. A. Leatherdale, H.-J. Eisler, and M. G. Bawendi, "Optical gain and stimulated emission in nanocrystal quantum dots," *Science*, vol. 290, pp. 314–317, 2000.

[80] M. V. Artemyev, U. Woggon, R. Wannemacher, H. Jaschinski, and W. Langbein, "Light trapped in a photonic dot: Microspheres act as a cavity for quantum dot emission," *Nano Lett.*, vol. 1, no. 6, pp. 309–314, 2001.

[81] M. Bruchez, M. Moronne, P. Gin, S. Weiss, and A. P. Alivisatos, "Light-emitting diodes made from cadmium selenide nanocrystals and a semiconducting polymer," *Science*, vol. 281, pp. 2013–2016, 1998.

[82] W. C. W. Chan and S. Nie, "Quantum dot bioconjugates for ultrasensitive nonisotopic detection," *Science*, vol. 281, pp. 2016–2018, 1998.

[83] M. Y. Han, X. H. Gao, J. Z. Su, and S. M. Nie, "Quantum-dot-tagged microbeads for multiplexed optical coding of biomolecules," *Nat. Biotechnology*, vol. 19, pp. 631–635, 2001.

[84] B. Dubertret, P. Skourides, D. J. Norris, V. Noireaux, A. H. Brivanlou, and A. Libchaber, "In vivo imaging of quantum dots encapsulated in phospholipid micelles," *Science*, vol. 298, pp. 1759–1762, 2002.

[85] K. Kalyanasundaram, E. Borgarello, D. Duonghong, and M. Grätzel, "Cleavage of water by visible-light irradiation of colloidal cds solutions; inhibition of photocorrosion by ruo2," *Angewandte Chemie International Edition in English*, vol. 20, no. 11, pp. 987–988, 1981.

[86] D. Duonghong, J. Ramsden, and M. Grätzel, "Dynamics of interfacial electron transfer processes in colloidal semiconductor systems," *J. Am. Chem. Soc.*, vol. 104, no. 11, pp. 2977–2985, 1982.

[87] L. E. Brus, "A simple model for the ionization affinity, and aqueous redox potentials of small semiconductor crystallites," *J. Chem. Phys.*, vol. 79, no. 11, pp. 5566–5571, 1983.

[88] L. E. Brus, "Electron-electron and electron-hole interactions in small semiconductor crystallites: The size dependence of the lowest excited state," *J. Chem. Phys.*, vol. 80, no. 9, pp. 4403–4409, 1984.

[89] R. Rossetti, J. L. Ellison, J. M. Gibson, and L. E. Brus, "Size effects in the excited electronic states of small colloidal CdS crystallites," *J. Chem. Phys.*, vol. 80, no. 9, pp. 4464–4469, 1984.

[90] R. Rossetti, R. Hull, J. M. Gibson, and L. E. Brus, "Excited electronic states and optical spectra of ZnS and CdS crystallites in the $\approx$ 15 to 50 å size range:

Evolution from molecular to bulk semiconducting properties," *J. Chem. Phys.*, vol. 82, no. 1, pp. 552–559, 1985.

[91] N. Chestnoy, T. D. Harris, R. Hull, and L. E. Brus, "Luminescence and photophysics of CdS semiconductor clusters: The nature of the emitting electronic state," *J. Phys. Chem.*, vol. 90, no. 15, pp. 3393–3399, 1986.

[92] C. B. Murray, D. J. Noms, and M. G. Bawendi, "Synthesis and characterization of nearly monodisperse cde (e = s, se, te) semiconductor nanocrystallites," *J . Am. Chem. Soc.*, vol. 115, pp. 8706–8715, 1993.

[93] Z. A. Peng and X. Peng, "Formation of high-quality cdte, cdse, and cds nanocrystals using cdo as precursor," *J. Am. Chem. Soc.*, vol. 123, pp. 183–184, 2001.

[94] X. Peng, "Green chemical approaches toward high-quality semiconductor nanocrystals," *Chem. Eur. J.*, vol. 8, pp. 334–339, 2002.

[95] L. Qu, Z. A. Peng, and X. Peng, "Alternative routes toward high quality cdse nanocrystals," *Nano Lett.*, vol. 1, pp. 333–337, 2001.

[96] L. Qu and X. Peng, "Control of photoluminescence properties of cdse nanocrystals in growth," *J. AM. CHEM. SOC.*, vol. 124, p. 2049, 2002.

[97] M. G. Bawendi *et al.*, "Electronic structure and photoexcited-carrier dynamics in nanometer-size CdSe clusters," *Phys. Rev. Lett.*, vol. 65, no. 13, pp. 1623–1626, 1990.

[98] E. Hilinski and P. A. Lucas, "A picosecond bleaching study of quantum confined cadmium sulfide microcrystallites in a polymer film," *J. Chem. Phys.*, vol. 89, no. 6, pp. 3435–3441, 1988.

[99] A. L. Efros and M. Rosen, "The electronic structure of semiconductor nanocrystals," *Annu. Rev. Mater. Sci.*, vol. 30, pp. 475–521, 2000.

[100] "Observation of the ´´Dark Exciton" in CdSe quantum dots," *Phys. Rev. Lett.*, vol. 75, pp. 3728–3731, 1995.

[101] A. L. Efros and M. Rosen, "Band edge exciton in quantum dots of semiconductors with a degenerate valence band: Dark and bright exciton states," *Physical Review B*, vol. 54, no. 7, pp. 4543–4856, 1996.

[102] M. Nirmal, B. O. Dabbousi, M. G. Bawendi, J. J. Macklin, J. K. Trautman, T. D. Harris, and L. E. Brus, "Fluorescence intermittency in single CdSe nanocrystals," *Nature*, vol. 383, pp. 802–804, 1996.

[103] M. Danek, K. F. Jensen, C. B. Murray, and M. G. Bawendi, "Synthesis of luminescent thin-film cdse/znse quantum dot composites using cdse quantum dots passivated with an overlayer of znse," *Chem. Mater.*, vol. 8, pp. 173–180, 1996.

[104] B. O. Dabbousi, J. Rodriguez-Viejo, F. V. Mikulec, J. R. Heine, H. Mattoussi, R. Ober, K. F. Jensen, and M. G. Bawendi, "(cdse)zns core-shell quantum dots: Synthesis and characterization of a size series of highly luminescent nanocrystallites," *J. Phys. Chem. B*, vol. 101, pp. 9463–9475, 1997.

[105] W. Guo, J. J. Li, Y. A. Wang, and X. Peng, "Luminescent cdse/cds core/shell nanocrystals in dendronboxes: Superior chemical, photochemical and thermal-stability," *J. Am. Chem. Soc.*, vol. 125, pp. 3901–3909, 2003.

[106] D. S. English, L. E. Pell, Z. Yu, P. F. Barbara, and B. A. Korgel, "Size tunable visible luminescence from individual organic monolayer stabilized silicon nanocrystal quantum dots," *Nano Lett.*, vol. 2, pp. 681–685, 2002.

[107] M. Kuno, D. P. Fromm, H. F. Hamann, A. Gallagher, and D. J. Nesbitt, "Nonexponential "blincking" kinetics of single CdSe quantum dots: A universal power law behavior," *J. Chem. Phys.*, vol. 112, no. 7, pp. 3117–3120, 2000.

[108] R. G. Neuhauser, K. T. Shimizu, W. K. Woo, S. A. Empedocles, and B. M. G., "Correlation between fluorescence intermittency and spectral diffusion in single semiconductor quantum dots," *Phys. Rev. Lett.*, vol. 85, no. 15, pp. 3301–3304, 2000.

[109] K. T. Shimizu, R. G. Neuhauser, C. A. Leatherdale, S. A. Empedocles, W. K. Woo, and M. G. Bawendi, "Blincking statistics in single semiconductor nanocrystal quantum dots," *Phys. Rev. B*, vol. 63, no. 205316, 2001.

[110] M. Kuno, D. P. Fromm, H. F. Hamann, A. Gallagher, and D. J. Nesbitt, ""On/Off" fluorescence intermittency of single semiconductor quantum dots," *J. Chem. Phys.*, vol. 115, no. 2, pp. 1028–1040, 2001.

[111] M. Kuno, D. P. Fromm, S. T. Johnson, A. Gallagher, and D. J. Nesbitt, "Modeling distributed kinetics in isolated semiconductor quantum dots," *Phys. Rev. B*, vol. 67, p. 125304, 2003.

[112] T. D. Krauss and L. E. Brus, "Charge, polarizability, and photoionization of single semiconductor nanocrystals," *Phys. Rev. Lett.*, vol. 83, no. 23, pp. 4840–4843, 1999.

[113] G. Schlegel, J. Bohnenberger, I. Potapova, and A. Mews, "Fluorescence decay time of single semiconductor nanocrystals," *Phys. Rev. Lett.*, vol. 88, p. 137401, 2002.

[114] B. R. Fisher, H. J. Eisler, N. E. Stott, and M. G. Bawendi, "Emission intensity dependence and single-exponential behavior in single colloidal quantum dot fluorescence lifetimes," *J. Phys. Chem. B*, vol. 108, pp. 143–148, 2004.

[115] S. Hohng and T. Ha, "Near-complete suppression of quantum dot blinking in ambient conditions," *J. Am. Chem. Soc.*, vol. 126, pp. 1324–1325, 2004.

[116] X. Zhong, M. Han, Z. Dong, T. J. White, and W. Knoll, "Composition-tunable $Zn_xCd_{1-x}Se$ nanocrystals with luminescence and stability," *J. Am. Chem. Soc.*, vol. 125, no. 8, pp. 8589–8594, 2003.

[117] Y. Park, V. Choong, Y. Gao, B. R. Hsieh, and C. W. Tang, "Work function of indium tin oxide transparent conductor measured by photoelectron spectroscopy," *Appl. Phys. Lett.*, vol. 68, pp. 2699–2701, 1996.

[118] H. M. Wadsworth, *The Handbook of Statistical Methods for Engineers and Scientists*. McGraw-Hill, 2nd ed., 1998.

[119] M. Kuno, D. P. Fromm, A. Gallagher, D. J. Nesbitt, O. I. Micic, and A. J. Nozik, "Fluorescence intermittency in single InP quantum dots," *Nano Lett.*, vol. 1, pp. 557–564, 2001.

[120] E. J. B. H. Xu, M. Käll, and L. Börjesson, "Spectroscopy of single hemoglobin molecules by surface enhanced raman scattering," *Phys. Rev. Lett.*, vol. 83, pp. 4357–4360, 1999.

[121] J. Jiang, K. Bosnick, M. Maillard, and L. Brus, "Single molecule raman spectroscopy at the junctions of large ag nanocrystals," *J. Phys. Chem. B*, vol. 107, pp. 9964–9972, 2003.

[122] P. Kambhampati, C. M. Child, M. C. Foster, and A. Campion, "On the chemical mechanism of surface enhanced raman scattering: experiment and theory," *J. Chem. Phys.*, vol. 108, pp. 5013–5026, 1998.

[123] K. Bromann, C. Félix, H. Brune, W. Harbich, R. Monot, J. Buttet, and K. Kern, "Controlled deposition of size-selected silver nanoclusters," *Science*, vol. 274, pp. 956–958, 1996.

[124] D. M. Kolb, R. Ullmann, and T. Will, "Nanofabrication of small copper clusters on gold(111) electrodes by a scanning tunneling microscope," *Science*, vol. 275, pp. 1097–1099, 1997.

[125] Y.-Y. Yu, S.-S. Chang, C.-L. Lee, , and C. R. C. Wang, "Gold nanorods: Electrochemical synthesis and optical properties," *J. Phys. Chem. B, Vol. 101, No. 34, 1997*, vol. 101, pp. 6661–6664, 1997.

[126] J. Bosbach, D. Martin, F. Stietz, T. Wenzel, and F. Träger, "Laser-based method for fabricating monodisperse metallic nanoparticles," *Appl. Phys. Lett.*, vol. 74, pp. 2605–2607, 1999.

[127] R. Jin, Y. Cao, C. A. Mirkin, K. L. Kelly, G. C. Schatz, and J. G. Zheng, "Photoinduced conversion of silver nanospheres to nanoprisms," *Science*, vol. 294, pp. 1901–1903, 2001.

[128] J. P. Kottmann and O. J. F. Martin, "Spectral response of plasmon resonant nanoparticles with a non-regular shape," *Optics Express*, vol. 6, pp. 213–219, 2000.

[129] L. A. Blanco and F. J. G. de Abajo, "Spontaneous light emission in complex nanostructures," *Phys. Rev. B*, vol. 69, p. 205414, 2004.

[130] T. Turkevich, P. C. Stevenson, and J. Hillier, "A study of the nucleation and growth processes in the synthesis of colloidal gold," *Discuss. Faraday Soc.*, vol. 11, pp. 55–75, 1951.

[131] G. Frens, "Controlled nucleation for the regulation of the particle size in monodisperse gold suspensions," *Nature Phys. Sci.*, vol. 241, pp. 20–22, 1973.

[132] U. Kreibig and M. Vollmer, *Optical properties of metal clusters*. Springer-Verlag, 1st ed., 1995.

[133] Wavemetrics inc., *Igor XOP Toolkit Reference Manual v.3.1*, 1998.

# Acknowledgements

This lines are dedicated to express my gratitude the people who made my research possible and my stay at the MPI-P pleasant.

In first place, I want to thank the supervisor of my dissertation Prof. Dr. Wolfgang Knoll. Thank you for giving me the opportunity of carrying out my Ph. D. programm at your group at the MPI-P. I am greatly thankful for the support and freedom you gave me during these years.

Dr. Maximilian Kreiter, thank you for your scientific support you gave me and the confidence you deposited on me. I profited greatly from your advice and enjoyed all the discussions with you. Special thanks for your critical proof reading of my dissertation.

Prof. Dr. Wolfram Baumann, thank you very much for supervising my dissertation.

Dr. Herr Volker Jacobsen, thanks for the nice time in Mainz, your help in all the imaginable fields such as science, lab-tools, German translations, etc. The keine Experimente times are gone for good!

Dr. Krasimir Vasilev, thank you for the great work you did in preparing the samples with the polyelectrolyte spacers. Will those polymers be so clean again? Thank you also for the nice time in the lab and in the office and for stopping kicking me in the football matches.

Dr. Kaloian Koynov, thanks for your help during the construction of the confocal microscope.

Herr Pilz and his "Haustechnik" team, thank you for helping me to adapt so quickly the laboratory for the experiments of this dissertation.

Herr Richter and his "Elektroniklabor" team, thank you for you support with the electronic problems.

Thanks to Jennifer Shumaker and Heiko Rochholz for the scattering samples (C-shaped nanoparticles).

Andreas Scheller, thank you for the computer support.

Dr. Christian Hübner, thank you. You were a very valuable scientific partner during these years.

I want to thank Tatiana Dimitrova, Volker Jacobsen, Kaloian Koynov, Katy Lovejoy, Joe and Gale Robertson, Heiko Rochholz, Jennifer Shumaker and Krasimir Vasilev for proof-reading parts of my thesis.

Dr. Rodolfo Acosta, thank you for the mates in between experiments.

I want to thank all the AK-Knoll members for the nice working atmosphere at the MPI-P and the unforgettable moments in Mainz. I want to thank in particular: Steffen Berg, Tatiana Dimitrova, Stuart Fraser, Lisa Henke, Volker Jacobsen, Thomas Jakob, Gleb Jakubov, Toby Jenkins, Ralf Kügler, Alessandro Manni, Bernhard Menges, Thomas Neumann, Kirstin Petersen, Rashmi Sahoo, Marco Stemmler and Angela Vogt.

Special thanks to my father Daniel, my mother Inés, my brothers Gustavo and Julian and my sister Leticia. Thank you for your love and being there for me, always.

Finally but above all, thank you Silke for your support and love and for being my partner in everything.

# Curriculum Vitae

PERSONAL INFORMATION

Name: FERNANDO DANIEL STEFANI
Gender: Male
Date of birth: 19th of November, 1975
Place of birth: Buenos Aires, Argentina
Citizenship: Argentine and Italian

EDUCATION

| | |
|---|---|
| 1989-1994 | High school studies at Instituto Tecnológico Philips Argentina. Awards: silver medal (1992) and honours (1994) in the Olimipíada Argentina de Química. Title: Electromechanic Technician |
| 1995-1997 | Chemical Engineering studies at Universidad Tecnológica Nacional, Buenos Aires. Average grade: 7.7 (scale from 0 to 10) |
| 1997-2000 | Materials Engineering studies at Instituto de Tecnología Prof. J. Sabato, Buenos Aires. Scholarship granted by the Comisión Nacional de Energía Atómica. Average grade 9.0 (scale from 0 to 10). Awards: Iron and Steel Society annual scholarship (1999). Thesis: *Surface plasmon resonance spectroscopy applied to the detection and study of DNA hybridization reactions* - Experimental part carried out at the Max-Planck-Institut für Polymerforschung under the direction of Prof. Dr. W. Knoll. Title: Materials Engineer. |
| 2000–2004 | Ph. D. program at Johannes Gutenberg Universität Mainz and Max-Planck-Intitut für Polymerforschung. |